THE UNIVERSITY OF WISCONSIN—MILWAUKEE

CENTER
FOR
GREAT LAKES STUDIES

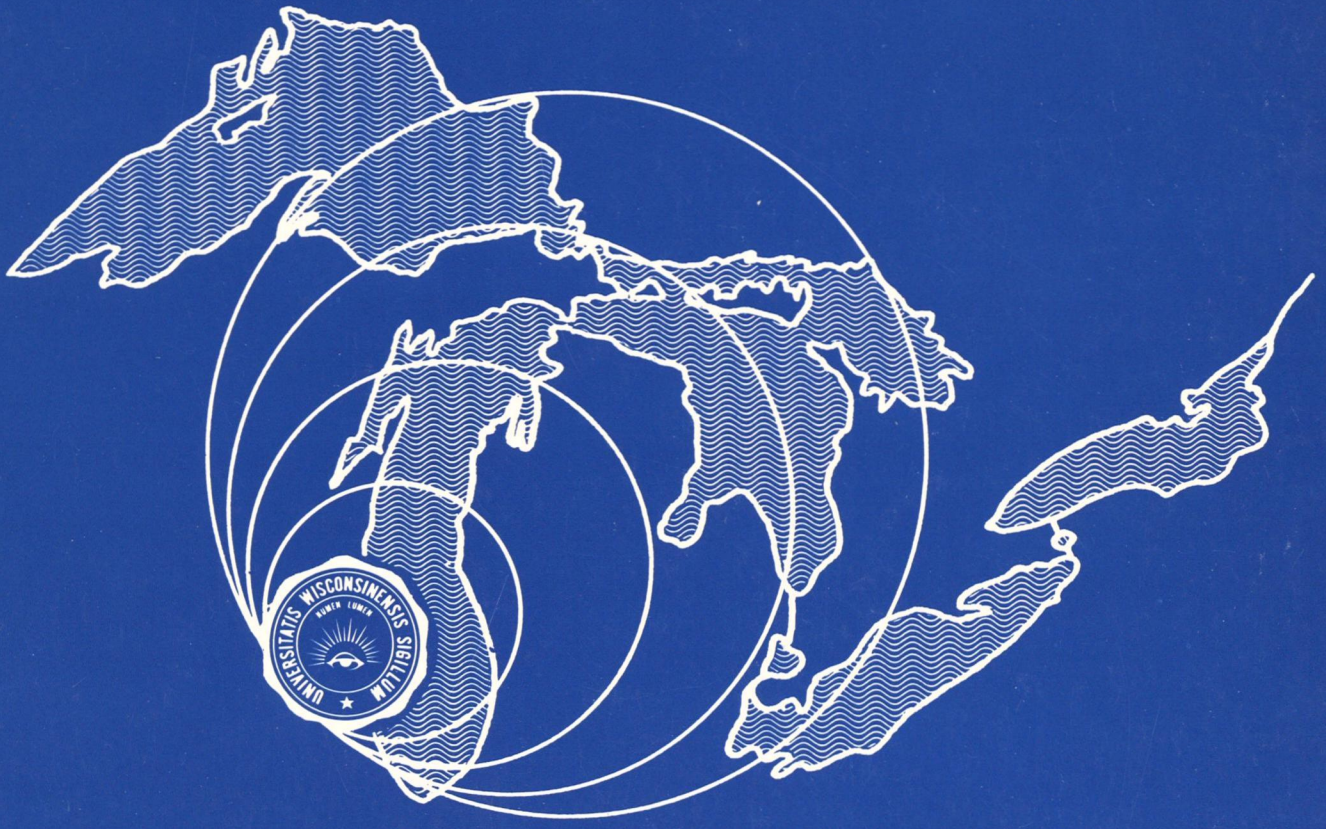

MILWAUKEE, WISCONSIN 53201 U.S.A.

To Bob Rickett,
with the author's good wishes

SPECIAL REPORT NO. 37

Inertial Motion and Related Internal Waves in Lake Michigan and Lake Ontario as Responses to Impulsive Wind Stresses.

I. Introduction, Descriptive Narrative, and Graphical Archive of IFYGL* Data.

by

C. H. MORTIMER

in fulfillment of
Contract No. NOAA-03-78-B01-21
with U.S. Department of Commerce,
National Oceanic and Atmospheric Administration

*International Field Year for the Great Lakes, 1972, Lake Ontario.

Center for Great Lakes Studies
The University of Wisconsin-Milwaukee
Milwaukee, Wisconsin, USA, 53201

1980

ABSTRACT

"Continuous" current and temperature records from instruments moored at various depths and stations in Lake Michigan and in Lake Ontario (International Field Year for the Great Lakes) are here assembled and examined for evidence of inertial oscillations and related internal wave responses to impulsive wind stress. Prefaced by a brief, illustrated recapitulation of well-known linear channel-wave theory, this report (Part I) assembles and performs a preliminary analysis on records from a single Lake Michigan station (August to October, 1976) and from twenty stations in Lake Ontario (June to November, 1972). The timing and magnitude of wind stresses are estimated from records at shore stations (Lake Michigan) or at offshore moorings (Lake Ontario). The IFYGL moored stations and in-lake towers are grouped along four cross-basin sections; and the results are presented in 14-day composite diagrams displaying, for each cross-section, the current and temperature records from all stations and depths compared with the wind record from 4 m above the water surface at one station. In three of the cross-sections, the cross-basin temperature structure was also explored by sensors towed by vessels on continuous transect shuttles occupying four days in July, August, and October.

Whenever the record displays more or less regular oscillations, seen as current rotations or as temperature fluctuations at particular depths, selected episodes (typically calmer intervals following impulses of wind stress) are fitted by eye to one of the following "average period bands" (APB) centered on the local inertial period (17.4 h) and on periods of Poincaré wave-modes in a two-layered channel model with parameters adjusted to mean conditions during the stratified season in the real lake, i.e., to 17.0, 15.8, 14.4 and 13.0 h in Lake Ontario. With an APB of 16.5 h added for convenience, this subjective method of period-fitting is adopted, because spectral methods fail to distinguish satisfactorily between the periods of "pure" inertial oscillations and Poincaré-type near-inertial responses, if present. Combining the APB estimates with knowledge of the modelled structure of individual Poincaré wave-modes, it is sometimes possible to draw useful inferences from interstation comparisons, which provide clues to the response structure or mixed-response structure following wind impulses in particular episodes. (Interstation coherence and presence or absence of whole-basin structure will be further examined in Part II.)

Preliminary findings disclose three types of response, occurring sometimes singly or sometimes in combination: (i) regular clockwise rotation of the current vector at inertial frequency, commonly seen as a local response during spring, before thermal stratification fully extends over the whole basin, and during autumn, when stratification is breaking down; (ii) near-inertial current and temperature oscillations associated with strong downwelling of the thermocline near one shore, which also generates internal solitary waves (solitons?) travelling away from that shore; and (iii) oscillations, also at near-inertial periods, corresponding to one or more of the whole-basin free baroclinic (inertial seiche) modes, here interpreted as "basin-tuned", near-intertial Poincaré-type responses.

ACKNOWLEDGEMENTS

This report, and the second part which will follow, review and analyze a very large body of physical data from Lake Ontario, produced by the efforts and skills of very many individuals who took part in the planning and execution of the bi-national program IFYGL. Also reviewed are similar data from Lake Michigan, produced by the efforts and skills of members of the Center for Great Lakes Studies (CGLS), University of Wisconsin-Milwaukee. To all of those individuals, and to the government agencies, research institutes, and universities which supported these programs in physical limnology on the Great Lakes, I express my appreciation and gratitude. In doing so, I also wish to record special thanks to F.M. Boyce and J.A. Bull of the Canada Centre for Inland Waters for providing plots of isotherm motions at thermistor chain moorings, to F.W.N. Bates and G.M. Thoenes for their long labors in data reduction, to Delpfine Welch and Joan Flores for manuscript preparation, and particularly to R.J. Ristic for the monumental output of illustrations, to which this and previous reports bear witness. Where previously published figures are used, their sources are acknowledged in the legend.

The work has greatly benefitted from discussions with J.H. Saylor and D.J. Schwab of NOAA's Great Lakes Environmental Research Laboratory (GLERL), Ann Arbor, Michigan, and with G.W. Platzman, University of Chicago. Assistance and comments were also generously given by D.L. Cutchin and G.O. Marmorino during their tenure of post-doctoral fellowship in CGLS.

Finally, it is gratefully noted that the work leading to this report was supported by the National Oceanic and Atmospheric Administration by means of research contracts administered by GLERL.

CONTENTS

INERTIAL MOTION AND RELATED INTERNAL WAVES IN LAKE MICHIGAN AND LAKE ONTARIO AS RESPONSES TO IMPULSIVE WIND STRESS :

PART I, INTRODUCTION, DESCRIPTIVE NARRATIVE, AND GRAPHICAL ARCHIVE OF IFYGL DATA.

1. INTRODUCTION

Before 1962, little attention had been paid to the hydrodynamics of lakes large enough to be conspicuously influenced by the earth's rotation. The decade which followed, saw an upsurge of investigations on the Laurentian Great Lakes using oceanographic concepts and techniques and culminating in a large-scale, eighteen-month, multidisciplinary field program carried out jointly by Canadian and United States investigators on Lake Ontario during 1972-73, the International Field Year for the Great Lakes (IFYGL). The findings are still being analyzed; and some related to long internal waves were reviewed in previous reports in this series (Mortimer 1977, Marmorino and Mortimer 1977), also Mortimer (1978) and G.T. Csanady in Lerman (1978). The physical data base was provided by: (i) a network of current and temperature sensors moored at various depths at over thirty lake stations and on nearshore towers, all recording every 10 min (Canadian) or 6 min (U.S.); (ii) meteorological sensors including anemometers at lake buoys and land stations; (iii) airborne radiation thermometry; (iv) regular two-weekly bathythermometry at over 90 stations; (v) current and temperature profiles obtained at buoyed flag stations along five "coastal chain" lines 12 km in length and aligned perpendicular to shore; (vi) moored and towed thermistor chains; and (vii) depth-undulating ("porpoising") thermographs towed by vessels continuously shuttling to and fro across three selected cross-sections during 5-day intervals in July, August, and October, 1972 (Boyce and Mortimer 1977).

In Lake Michigan, an extended series of current and temperature records were obtained at 34 stations during 1962-64 by the (then) U.S. Federal Water Pollution Control Administration (U.S. Dept. Interior 1967, Mortimer 1971) and at 10 stations in a nearshore region by Sato and Mortimer (1975). And in 1976, the records reported on here were obtained from instruments moored approximately 30 km offshore.

The Michigan and Ontario data sets were initially examined for responses to applied wind stress, i.e. for changes in current or temperature structure and, in particular, for long internal waves representing free modes of oscillation excited by the wind-induced perturbations. Observed waves were compared with and fairly well described by the well-known models of tidal (i.e. long) waves in straight, rotating channels of uniform depth and rectangular cross-section, first applied to interpretation of the responses of large lakes by Mortimer (1963, with more detailed treatment in 1971). The rotating channel waves, in the simplest two-layered models corresponding to the dimensions and internal density structure of the Great Lakes, fall into two classes, well-separated in frequency. The first class is represented by internal Kelvin waves of low frequency (much less than the local inertial frequency, f) with activity confined to a nearshore "corridor" of about 10 km width. The second class is represented by internal Poincaré waves, i.e. a set of cross-channel internal seiche modes involving the whole thermocline and with frequencies close to but greater than f. The wider the channel, or the smaller the density difference between the two model layers, the closer do the Poincaré mode frequencies approach f. Tidal wave theory, including its application to internal waves, has been extensively treated elsewhere (Krauss 1966, Platzman 1970, LeBlond and Mysak 1978). Therefore, Section 2 of this report is confined to a brief illustrated recapitulation of those particular models which are

helpful in the interpretation of motions observed in large lakes and shallow seas.

Internal waves of the Kelvin and Poincaré type are not the only responses to impulsive wind stress. Another is the related response of inertial motion, in which the acquired momentum of a water mass causes motion to continue after the wind impulse has ceased. In the simplest model of such motion, no forces, except the Coriolis force, act on the mass after the initiating disturbance has passed. With acquired inertia, the mass continues to move at steady speed, s, and follows a horizontal circular track (the inertial circle) imposed by the Coriolis force, fs, in which $f = 2\Omega \sin \phi$; Ω denotes the angular speed of the earth's rotation and ϕ the latitude. That circle, respectively traversed in clockwise and counterclockwise directions in the N and S hemispheres, is completed in an inertial period of $12/\sin \phi$ hours. Its radius is s/f; and with current speeds of order 10 cm s^{-1} at mid-latitudes, inertial circle radii are of order 1 km. The feature of this model of "inertial motion proper," further treated in Section 2, is that all horizontal gradients, vertical motions, and friction are eliminated and the energy is entirely in kinetic form. It may also be viewed as an "inertial oscillation," a limiting case of wave motion when the wave frequency σ becomes equal to f and the potential energy content falls to zero.

It is obvious that inertial motion proper or even close approximations to such motion, cannot take place very near an obstructing shoreline. And, indeed, approximateions to inertial motion in the Great Lakes are not seen closer than about five inertial circle diameters from shore. The model described in the previous paragraph is modified by the presence of the shore barrier. The frequency is increased slightly, and some vertical motion is introduced. The potential energy content of the oscillation is therefore no longer zero; and current rotation is

commonly accompanied by internal thermocline waves of the same frequency, attributable to the presence of shore boundaries.

Difficulties arising in the analysis attempted in this report stem from the fact that -- depending on the strength, timing, and variations of the wind stress impulse -- the water response in a particular region of the basin is a combination of pre-existing motions and newly generated components, which may include: local inertial motion, one or more internal Poincaré wave modes corresponding to basin topography, and (if near shore) contributions from Kelvin waves. Two approaches toward unravelling this complexity have been taken: (i) spectral analysis and (ii) visual inspection of records from many episodes and many stations, in the hope of encountering particular events during which one or the other of the response components was dominant and in which interstation coherence is detectable. Approach (i), using maximum entropy spectral analysis for example, met with only limited success (Marmorino and Mortimer 1977) because of short duration of the free response episodes and because of small frequency separation between the inertial and Poincaré mode responses. This report attempts the second approach and, as explained in the abstract, is divided into two parts.

2. RECAPITULATION OF SOME THEORETICAL RESULTS

2.1 Inertial motion proper and observed approximations to it.

As mentioned in the introduction, a characteristic response of the upper layers of the ocean or a large lake to suddenly imposed or suddenly changed wind stress is motion in a horizontal circle, clockwise in the northern hemisphere, counterclockwise in the southern. If, as a result of a wind impulse, a water mass has acquired a speed s and if friction and all horizontal pressure gradients can be ignored, the mass will continue to move under its own momentum (inertia) at speed s after the wind stops. Then the only force acting is a

deflecting force, fs, the Coriolis force arising from the earth's rotation, in which f is the Coriolis parameter defined in the introduction. The Coriolis force is directed always perpendicular to the direction of motion, so that the inertial track is a circle (the inertial circle) of radius s/f, which is completed in an inertial period (siderial day/2 sin ϕ = 11.97/sin ϕ h). At latitudes (ϕ) of interest in this report, the inertial period, P_i, is near 17.5 h, and the inertial circle radius is about 1 km if s is 10 cm s^{-1}. If the current vector is resolved into horizontal components, u (x-directed) and v (y-directed), the x and y equations of motion for "inertial motion proper," as described above, reduce to:

$$\partial u/\partial t = fv \qquad \text{and} \qquad \partial v/\partial t = -fu \tag{1}$$

which have solutions:

$$u = s \sin (ft) \qquad \text{and} \qquad v = s \cos (ft) \tag{2}$$

which define circular motion and in which $s^2 = u^2 + v^2$.

Approximations to this simplified model of proper or pure inertial motion are often seen in the oceans (examples on pp. 158-9 in Neumann and Pierson 1966) and in large lakes when not masked by a variety of similar motions, termed "near-inertial," which arise when boundaries are present, as described later.

A further complicating factor in real oceans and lakes is the presence of currents generated by mechanisms other than those causing inertial motion, for example, whole-basin circulations or individual eddies and gyres, or nearshore geostrophic currents and low-frequency internal waves. Such low-frequency motions combine, as relatively steady unidirectional currents, with the inertial or near-inertial rotations, to produce a current pattern, which may be looping, cusping, or meandering (Figure 1) depending on the relative proportions of the "steady" and rotating components. Such patterns, changing with time and with the incidence of wind impulses, are seen as a characteristic and universal

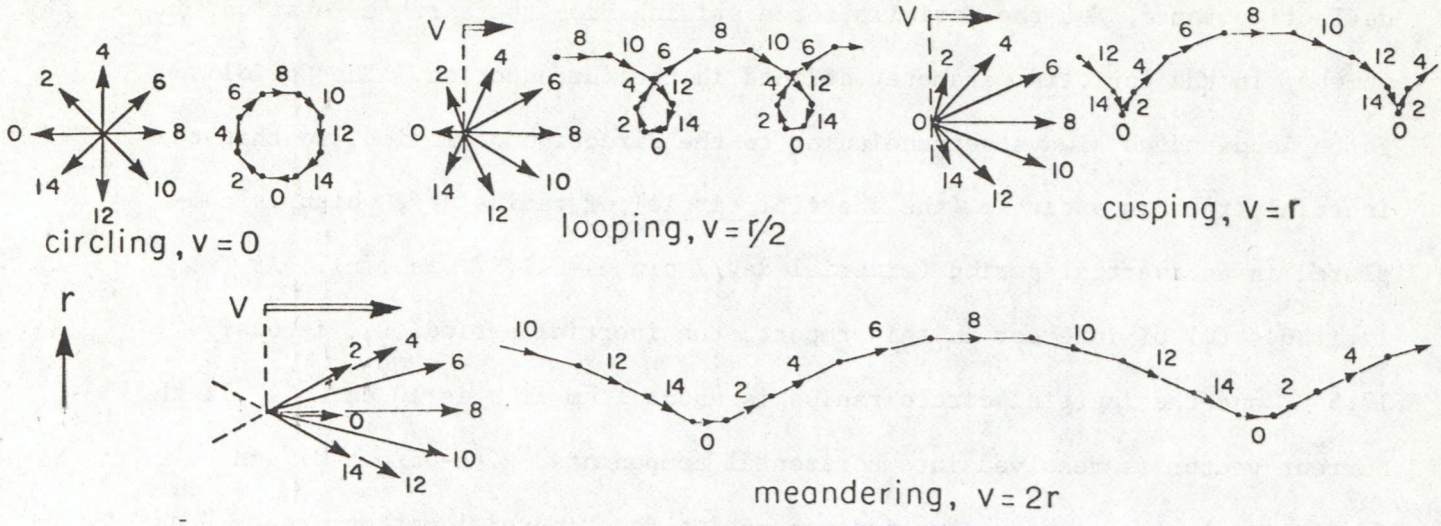

Fig. 1. Combinations of inertial currents (rotating vector of constant speed, r, and unidirectional currents at various constant speeds, v) illustrated at 2 h intervals for a P_i of 16 h and for the following cases: $v = 0$ (motion in inertial circle); $v = r/2$ (looping track); $v = r$ (cusping track); $v = 2r$ (meandering track). The hodographs (vectors with common origin) are plotted on twice the scale of the progressive vector (track) diagrams.

response to wind forcing in large stratified basins, under many different circumstances. The upper-left example in Figure 2 is a well-known textbook example of inertial motion.

Pollard (1970) conclusively demonstrated that inertial motion in the ocean is generated by wind impulses acting initially on the upper mixed layer. In his model, the wind stress is simulated as a body force with harmonic horizontal dependence of wavelength L acting for time interval T on the mixed layer. In the response of the mixed layer to the body force, partition between energy E_i in inertial motions (rotating currents) and energy E_g in geostrophic motions ("steady unidirectional" currents) is strongly dependent on the duration of T. As expected, the E_i component is large when T is $P_i/2$ (or an odd number multiple of $P_i/2$, Table 1) and small when T is a multiple of a whole inertial

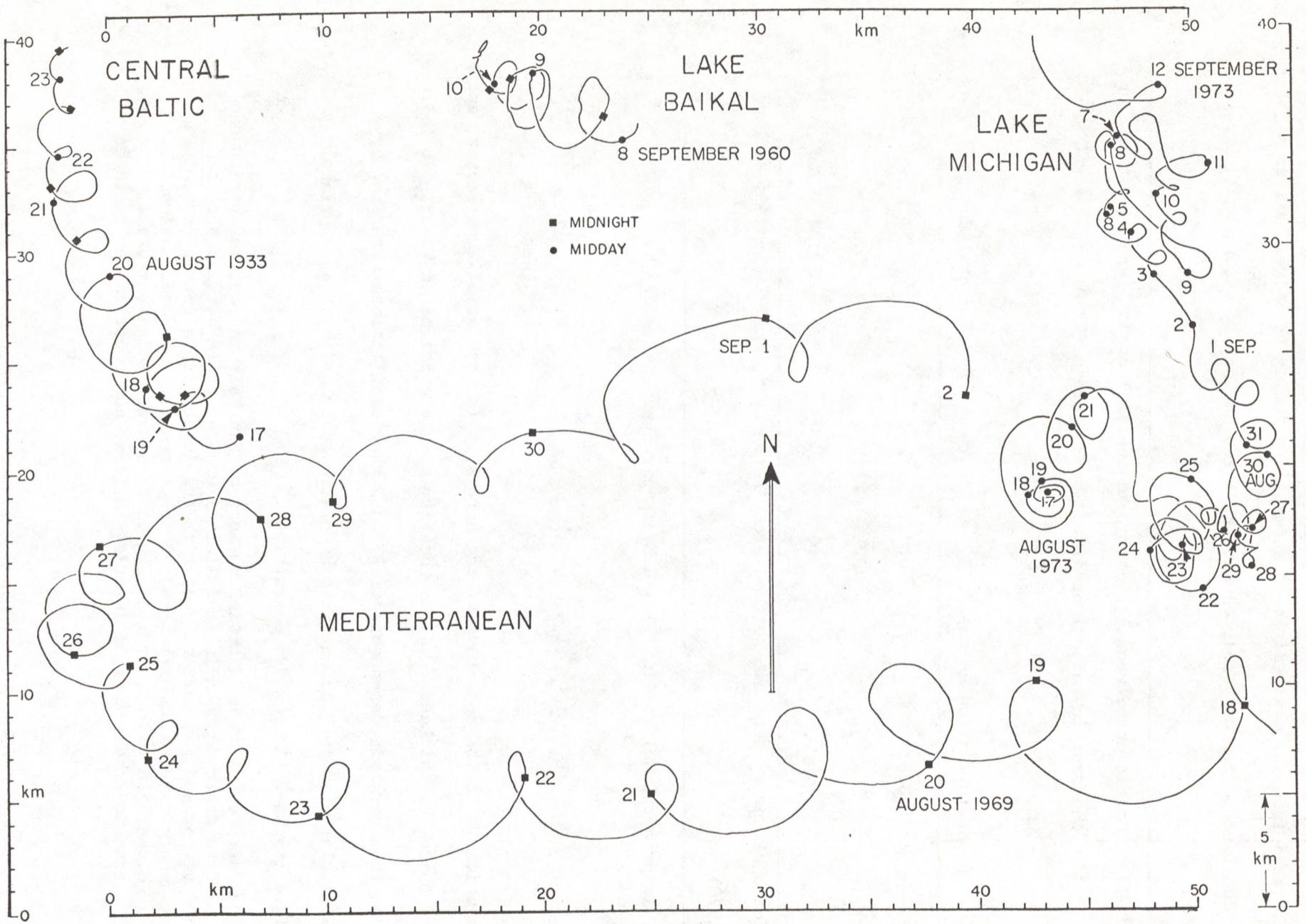

Fig. 2. Examples of looping current tracks (plotted on a common scale and with distances from shore and depths indicated in brackets) from: Central Baltic (31 km, 14 m, Gustafson and Kullenberg 1936); Lake Baikal (6 km, 10 m, Galazii 1969); Lake Michigan (12 km, 12 m, Sato and Mortimer 1975); Mediterranean (100 km, 10 m, Gonella 1974).

period. The physical reason is clear. Motion in the inertial circle is accelerated if a uniformly-directed stress acts during the first half of P_i, but is decelerated if the stress continues to act during the second half.

TABLE 1. Partition between E_i (energy in inertial motion) and E_g (energy in geostrophic motion) predicted by Pollard's (1970) model for L = 500 km.

T (inertial period units)	E_i*	E_g*	E_i/Total Energy
0.5	8.8	2.0	0.81
1	0.1	8.0	0.01
1.5	8.6	18.0	0.32

*Units of energy per unit surface area, K-erg cm^{-2}, from Table 2 in Pollard (1970).

E_g is proportional to $(\tau_o T)^2$, and E_i is given approximately by:

$$E_i = \frac{\tau_o^2}{2\bar{\rho} a f^2}(1 - \cos fT) \qquad (3)$$

in which τ_o is the amplitude of the stress, f is the Coriolis parameter, and a and $\bar{\rho}$ are the thickness and mean density of the upper mixed layer. It follows from this harmonic dependence of E_i on T that oscillations generated by a particular wind impulse can also be destroyed by another appropriately-timed impulse. As Pollard notes, the

> "stress builds up inertial motions within half an inertial period and then destroys them in a similar time. The angle between the wind vector and the current vector is the important factor in determining whether momentum will be added to or removed from oscillations.... Dispersion out of a forced region is not sufficient to explain the transient behaviour of inertial motions, nor their rather rapid decay

> rates. It is probable that wind stress must be invoked to destroy as well as create them."

Several of the above predictions were confirmed in a comparison between a simpler version of Pollard's model and a long series of current and wind observations at an ocean mooring (Pollard and Millard 1970). The main purpose of the comparison was to determine whether the observed rapid changes in amplitude of inertial oscillations could be reproduced by incorporating observed wind stresses in the model. It was found, in fact, that

> "the phase, amplitude, and intermittency of bursts of inertial oscillations in the mixed layer are surprisingly well reproduced, considering the simplicity of the model, and one concludes that such oscillations are predominantly locally generated by surface winds [, and] that the features in the wind field which are most efficient in changing [increasing or reducing] the amplitude of inertial motions are (i) a strong wind blowing in one direction for a few hours up to half an inertial period, and (ii) a strong wind combined with a fairly sudden shift in direction." [ ] indicate my inserts.

Examples from Lake Ontario, which also support these conclusions, will be described in later sections.

2.2 Inertial response to wind impulses in the presence of a shore boundary.

In the model of inertial motion proper, the flow is frictionless and exclusively horizontal and the period P_i and diameter of the perfectly circular track ($2\ s/f$) do not change. Close approximations to this model are seen in large lakes and seas, as responses to short wind impulses, particularly when a steep density gradient has developed in the thermocline, permitting the upper mixed layer to move easily as a slab on the "slippery" thermocline surface. But even under these circumstances, deviations from the simple model are observed. The period is often a few percent less than P_i and must therefore be described as near-inertial; the circle diameter decreases with time under the influence of friction (see Fig. 2); vertical motions are present in the form of internal waves of near-inertial period on the thermocline; and the near-inertial motion is not confined to the surface layer, but penetrates to deep

layers often exhibiting a nearly 180° phase difference across the thermocline.

This behaviour is a consequence of the fact that the motion takes place in a closed basin of non-uniform depth. Although the inertial flow is predominantly horizontal, progress over a sloping bottom generates some vertical motion; and onshore/offshore movements during the initiating wind impulse and during the subsequent oscillation also generate horizontal pressure gradients to which the whole water column must adjust. Thus, Crépon (1974) showed that the coastline could be a source of near-inertial motions propagating in the course of a geostrophic adjustment process; and the fact that inertial (or near-inertial) motion is seen in the lower layers of the Baltic Sea, typically out of phase with inertial motion in the surface layers, was also interpreted by Krauss (1979) as a consequence of geostrophic adjustment of the inertial flow near a shore boundary. Millot and Crépon (1980) developed a model of a two-layered ocean with a single coastline to interpret the relationship between wind impulses and the inertial oscillations observed in both current and temperature records near the coast in the Mediterranean Sea. They linked the generation of those oscillations

> "to transient gusts of wind occurring in that region. Spectral analysis and the systematic study of many events show that the peak of the temperature spectrum is at a frequency ten per cent greater than the peak at f_c of current spectrum. Coherence analysis shows that current oscillations at the Coriolis frequency are in opposite phases in the two layers. These phenomena can be linked to the generation of internal dispersive waves at the shore during the geostrophic adjustment process which drives the upwelling. Furthermore, we are able to get the direction of propagation of these waves using coherence results between currents and a pseudo-temperature vector. These directions of propagation which are perpendicular to the nearest shore are in good agreement with the process above mentioned."

Millot and Crépon's findings demonstrate that a shore boundary imposes wavelike characteristics upon the inertial response; and this, as we shall see, can be abundantly demonstrated in large, stratified basins, in which some of the free internal modes of oscillation possess frequencies close to inertial,

so that the possibility of resonance exists. While large-scale horizontal coherence of inertial motion proper is not to be expected -- because inertial circle diameters are a few kilometers at most, and the strength and timing of the wind impulses vary from place to place -- the basin modes (internal, baroclinic seiches) involve the whole-basin thermocline or, at least, a large component section of it. Then, cross-basin coherence is commonly seen, and whole-basin coherence can sometimes be demonstrated; but the picture is complicated by the possibility of simultaneous generation of (i) an approximation to pure inertial motion in offshore regions, (ii) near-inertial motion interacting with one shoreline (cf. Millot and Crépon), and (iii) the basin-tuned or two-shore tuned near-inertial responses. The components of the mixed response are, therefore, difficult to distinguish from each other. Nevertheless, such distinction is attempted in this report and particularly in Part II, which examines selected wind-forced episodes in detail. Before embarking on this attempt, and because we must now deal with the wavelike properties of shore-dominated near-inertial motion, it will be helpful to review briefly some simple, linear models of long waves in straight, rotating channels of uniform rectangular cross-sections.

2.3 General equations for linear long-wave models, with rotation.

It can be shown that several of the observed characteristic features of long waves in lakes, responding to applied wind stress, are reproduced fairly closely in linear models of long waves in rotating channels of uniform depth (h) and that these models may be conveniently combined to yield solutions which fit particular boundary conditions (Platzman 1970, Mortimer 1971). Consider a long plane wave of horiztonal wavenumber k_h (wavelength $2\pi/k_h$, long compared with h) travelling with no restrictions on direction on the surface of an ocean of infinite extent and uniform depth. Adopting Cartesian coordinates in

a region sufficiently small to permit the Coriolis parameter f to be considered constant and the surface to be approximated by the local horizontal plane, the solution for wave elevation η assumes the form:

$$\eta = \eta \exp[i(kx + ly)] \tag{4}$$

in which η is an amplitude constant, i is $\sqrt{-1}$, and k and l are the horizontal wavenumber components in the x and y directions, respectively, such that $k_h^2 = (k^2 + l^2)$. The wave frequency σ is given by:

$$\sigma^2 = f^2 + gh(k^2 + l^2) \tag{5}$$

in which g is the acceleration of gravity and $\sqrt{gh}$ defines the phase velocity (phase speed or celerity c_o) of the wave when f is zero (no rotation). For a given value of h, c_o is therefore a constant and applicable to a long <u>surface</u> wave.

An equivalent no-rotation celerity, c_i, can be defined for long <u>internal</u> waves. Its magnitude, much smaller than that of c_o, depends on the structure of the vertical density profile. The simplest model of stratification, adopted here, divides the water column into an upper and lower layer (respectively designated by subscripts 1 and 2) of uniform densities ρ_1 and ρ_2 ($\rho_2 > \rho_1$) and of thicknesses h_1 and h_2. The interfacial density discontinuity models the thermocline in real oceans and lakes, and the interfacial wave celerity is given by

$$c_i = \sqrt{\frac{g(\rho_2 - \rho_1)h_1h_2}{\rho_2(h_1 + h_2)}} \tag{6}$$

This is analogous to $c_o(=\sqrt{gh})$, but with g and h replaced by a "reduced gravity," $g(\rho_2 - \rho_1)/\rho_2$ (typically 0.001 g or less), and a "reduced depth," $h_1h_1/(h_1 + h_2)$. The ratio of reduced to total depth (often < 1/10) cannot be > 1/4. Typical c_o and c_i values in the Great Lakes are 30 and 0.4 m s^{-1}, respectively. It is convenient to present the following outline of theory in terms of surface waves, using c_o. But the equations also apply to two-layer interfacial waves if c_i

is substituted for c_o. In that case elevations refer to elevations on the interface; and (where mentioned) velocities and transports refer to those in the lower layer. Continuity in the two-layered model requires that the vertically integrated transport in the lower layer is balanced by oppositely-directed vertically-integrated transport in the upper layer (neglecting small perturbations of the water surface, in phase opposition with the much larger perturbations on the interface). Therefore, upper-layer transports may be calculated by multiplying the lower-layer transports by $-h_2/h_1$.

The general wave equation (4) can be expanded to yield expressions, not only for η (elevation of the free surface or interface), but also for u and v (horizontal components of particle velocity in the x and y directions, respectively) and w (vertical component of particle velocity). An illuminating exposition of these expansions and of the special solutions for propagating waves derived from the general solution and described below, was given by Platzman (1970). The general solution is formally valid when k and l are complex; and k and l can be real or imaginary, subject to the condition for pure harmonic waves that σ and $(k^2 + l^2)$ must be real. If, for a wave travelling in the x-direction, k is real and positive and l is purely imaginary (to make this explicit, Platzman replaced the purely imaginary l by il', in which $i = \sqrt{-1}$), a special class of progressive wave solutions appears, which Platzman called "inhomogeneous plane waves," characterized by a sinusoidal variation of wave amplitude in the x-direction and an exponential variation in the y-direction. But, if both k and l are real (and for convenience the direction of propagation is made to coincide with the x-axis, so that $k = k_h$ and $l = 0$ in a plane wave) the Sverdrup wave solution emerges with sinusoidal amplitude variation along x and no amplitude variation along y ($l = 0$). Platzman summarized these results in a diagram (Fig. 3) which illustrates the relationship between σ and k for various values of $(l')^2$.

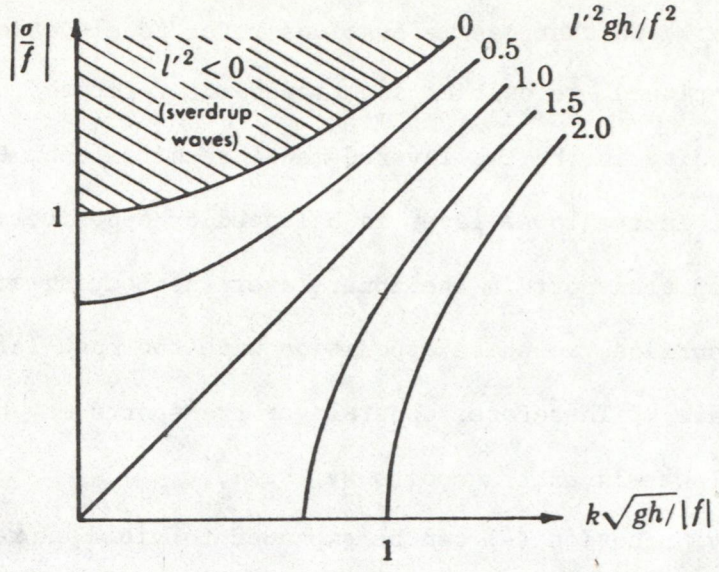

Fig. 3. Frequency versus wavenumber diagram from Platzman (1970). The unshaded portion is the domain of inhomogeneous plane waves, as explained in the text.

2.4 The Kelvin wave.

Platzman's inhomogeneous plane waves (unshaded domain in Fig. 3) are characterized by an exponential dependence of η and u along the y-axis. For given values of σ and k, and depending upon the sign of l', two wave types are possible. In one, η and u decrease to the right, in the other they decrease to the left when looking in the positive-x direction of wave progress. In one member of that pair the Coriolis force is counteracted by the pressure gradient (gravity acting on the $\partial\eta/\partial y$ slope); in the other it is not. In other words, complete or partial geostrophic equilibrium occurs only in left-decreasing waves in the N. hemisphere (right-decreasing in the S. hemisphere). The degree of geostrophic balance is determined by the ratio $-g(\partial\eta/\partial y)/fu$; and Platzman shows that the above ratio approaches unity as the frequency, σ, decreases from the Sverdrup frequency cut-off $\sigma^2 = (f^2 + c_o{}^2k^2)$ -- defined later and corresponding to the shaded/unshaded demarcation line in Figure 3 -- and approaches

($c_o^2 k^2$). At that point, corresponding to $l'^2 c_o^2 / f^2 = 1$ in Figure 3, the geostrophic balance is exact. There $l' = -f/c_o$, $k = \sigma/c_o$, and the wave solution takes the familiar Kelvin wave form. Platzman refers to this as the "prototype Kelvin wave," characterized by vertical polarization of the particle orbit (Fig. 4a) and by a non-dispersive celerity c_o, i.e. not influenced by rotation. Because of the vertical polarization, the prototype Kelvin wave solution satisfies the solid boundary condition at a vertical shore boundary aligned along the x-axis and lying on the righthand side (N. hemisphere) when looking in the direction of wave progress; elevation and current amplitudes decreases exponentially in the direction normal to the shore; v is zero; and flow u is everywhere directed shore-parallel. The consequent trapping of Kelvin waves to shore boundaries is very evident when internal Kelvin wave models are applied to conditions in large lakes; but these waves are not the subject of this report.

Observations, which may be interpreted as evidence for internal Kelvin waves, have been reviewed by G. T. Csanady in Lerman (1978). Also bearing on this subject is Clarke's (1977) review of evidence for shore-trapped long waves, including those seen in the Great Lakes, and Bennett's (1973) analysis of non-linear behaviour of large-amplitude internal Kelvin waves. Kanari's (1975) interpretation of observations in Lake Biwa is also relevant. For a review of the properties of "inhomogeneous plane waves" not in geostrophic equilibrium (i.e. not on line 1.0 in the white domain of Fig. 3) I refer the reader to Platzman (1970). In such cases the ratio $g(\partial\eta/\partial y)/fu$ deviates from unity; and the Coriolis force, not in exact balance, induces motion in the y-direction.

2.5 The Sverdrup wave.

When k and l are both real (shaded domain in Fig. 3) the elevation does not vary along the wavecrest; and there is, therefore, no gradient force (as in the "inhomogeneous" wave) to oppose the Coriolis force. Consequently that force generates particle motion transverse to the direction of wave progress.

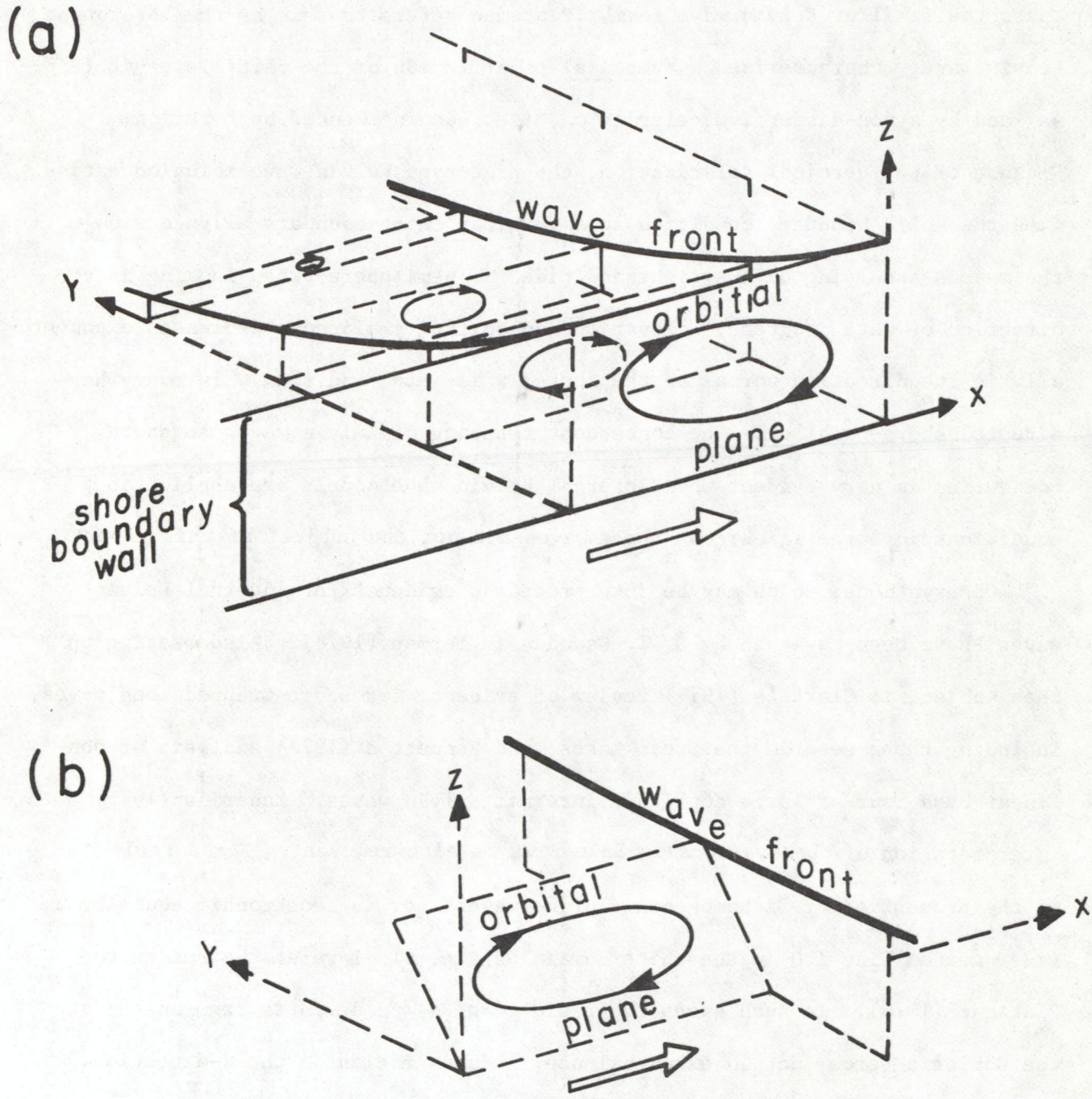

Fig. 4. Disposition of wave-fronts and of orbital planes of particle motion in (a) a prototype Kelvin wave and (b) a Sverdrup wave, with the vertical scale greatly magnified in both cases. The white arrows indicate direction of wave progress (along the x axis). The orbital plane at y = 0 in the Kelvin wave model coincides with a vertical solid boundary (shoreline). No such boundary is present in the Sverdrup wave model shown in Fig. 4b (modified from Platzman 1970).

The corresponding solutions and equations defining the polarization of the particle orbit were given by Platzman (1970, 3.2.1 to 3.2.3). To examine the properties of this "homogeneous" plane wave in detail, it is convenient to choose the direction of increasing x as the direction of wave progress, in which case $k > 0$ and $l = 0$. Taking real parts of the general solution, Platzman derived the following set of equations defining elevation (η), the horizontal components of particle motion (u and v, directed along the x and y axes, respectively), the vertical component of particle motion (w), and wave frequency (σ):

$$[\eta, u] = [h, \sigma/k]\cos(kx - \sigma t) \qquad (7)$$

$$[v, w] = [f/k, \sigma(z + h)]\sin(kx - \sigma t)$$

$$\sigma = \pm\sqrt{(f^2 + c_o{}^2k^2)}$$

For mathematical convenience, Platzman scaled wave amplitude (which is of course arbitrary and can be assigned any value) to make the amplitude of η equal to the depth h in the first equation of set (7). In the second equation the vertical velocity varies linearly from zero at the bottom ($z = -h$) to $\partial\eta/\partial t$ at the free surface. Together, the equation set defines a wave (illustrated in Fig. 4b) with the following properties, earlier treated by Sverdrup (1926).*

---

*The Sverdrup wave is, in fact, a member of a more general class treated by Poincaré (1910) and has been referred to as a Poincaré wave by some authors (LeBlond and Mysak, 1978, for example). However, others (Platzman 1970, Mortimer 1963, 1971) find it convenient to confine the designation "Poincaré" to waves which satisfy the boundary conditions at a straight vertical wall or walls in rotating uniform-depth models. As demonstrated later in this report, Poincaré waves so defined can be constructed as <u>combinations</u> of Sverdrup waves. To quote Platzman, the Sverdrup waves" may be regarded as an elemental propagator of tidal [i.e. long wave] signals", and it is convenient to retain the specific name to identify that property. The reference is Sverdrup (1926).

(i) The particle orbit in the Sverdrup wave (Fig. 4b) is polarized in a plane perpendicular to the wavefront. In the absence of rotation, the orbital plane is vertical; but with rotation it tilts from the vertical (inclining upward to the left of the direction of wave progress in the N. hemisphere) and the horizontal projection of the particle orbit is an ellipse with the major/minor axis ratio defined by σ/f, which also defines the speed ratio v max/u max. The equations for u and v in (7) define clockwise rotation of the horizontal current vector, illustrated for a particular case (σ/f = 3/2) in later Figure 5.

(ii) The third equation in (7) defines the frequencey dependence on f and wavenumber k and, for given k, sets a frequency limit below which σ is no longer real and below which Sverdrup waves cannot exist. The absolute low-frequency cut-off, when k decreases to zero, is f. Also, for given k, the third equation applies to a pair of waves, one forward-travelling ($\sigma > 0$, i.e., in the direction of increasing phase angle, $kx - \sigma t$) and the other backward-travelling ($\sigma < 0$). The two waves possess the same absolute frequency σ and therefore the same celerity σ/k. The dependence of the speed on k makes the wave dispersive, in contrast to the non-dispersive prototype Kelvin wave.

(iii) Compared with long plane waves in the absence of rotation (for which the phase speed and group speed are both equal $\sqrt{gh}$) the Sverdrup wave phase speed (celerity) and group speed are respectively increased and decreased by rotation, as follows:

$$\text{phase speed, } \sigma/k = \sqrt{gh}.\sigma/\sqrt{(\sigma^2 - f^2)} = c_o/\sqrt{(1 - f^2/\sigma^2)} \qquad (8)$$

$$\text{group speed, } \partial\sigma/\partial k = \sqrt{gh}.\sqrt{(\sigma^2 - f^2)}/\sigma = c_o.\sqrt{(1 - f^2/\sigma^2)}$$

in which $c_o = \sqrt{gh}$. The frequency dependence of k and of the phase and group speeds are illustrated by Platzman (1970) for surface Sverdrup waves in water depths ranging from 0.1 to 4.0 km and for f = 1 cycle per day, corresponding to latitude 29.91°.

(iv) The partition of potential and kinetic energy in the Sverdrup waves is also frequency-dependent, being governed by the ratio:

$$\frac{\text{kinetic energy density}}{\text{potential energy density}} = \frac{(\sigma^2 + f^2)}{(\sigma^2 - f^2)} \qquad (9)$$

At the limit $f = 0$ there is equipartition; but as σ approaches the limit f, the ratio approaches infinity (as does also the celerity, see 8), and more and more of the wave energy appears in the form of currents and less and less in the form of elevation change. Also, as σ approaches f, the polarization of the orbital plane (Fig. 4b) approaches horizontality; the elliptical track of the horizontal current vector approaches circularity ($v \rightarrow u$); and the limiting state of the Sverdrup wave is that of inertial motion (defined in Section 2.1) restricted to the horizontal plane, and appearing solely as a current of uniform speed u traversing an inertial circle in a clockwise direction (N. hemisphere) at angular frequency f.

2.6 The progressive Poincaré wave.

The single Sverdrup wave model (with $v > 0$) is obviously not a permissible solution in the presence of a shore boundary. However, perfect reflection of a Sverdrup wave at a straight vertical wall (model shore boundary) generates a second Sverdrup wave with amplitude and frequency (but not phase) unchanged (see Platzman 1970). This Sverdrup wave pair (incident and reflected) combine to form a type of wave (a progressive Poincaré wave) which satisfies the solid boundary condition at the wall. In the direction parallel to the wall the wave is a propagating sinusoid of wavenumber $k_s \cos \Theta$, in which k_s is the wavenumber of the Sverdrup wave and Θ is its angle of incidence at the wall. Perpendicular to the wall, the combined waveform is standing, with a series of wall-parallel nodal lines spaced at intervals $\pi/k_s \sin \Theta$. The combined wave -- now to be called a Poincaré wave -- retains the Sverdrup wave frequency, σ, and exhibits a

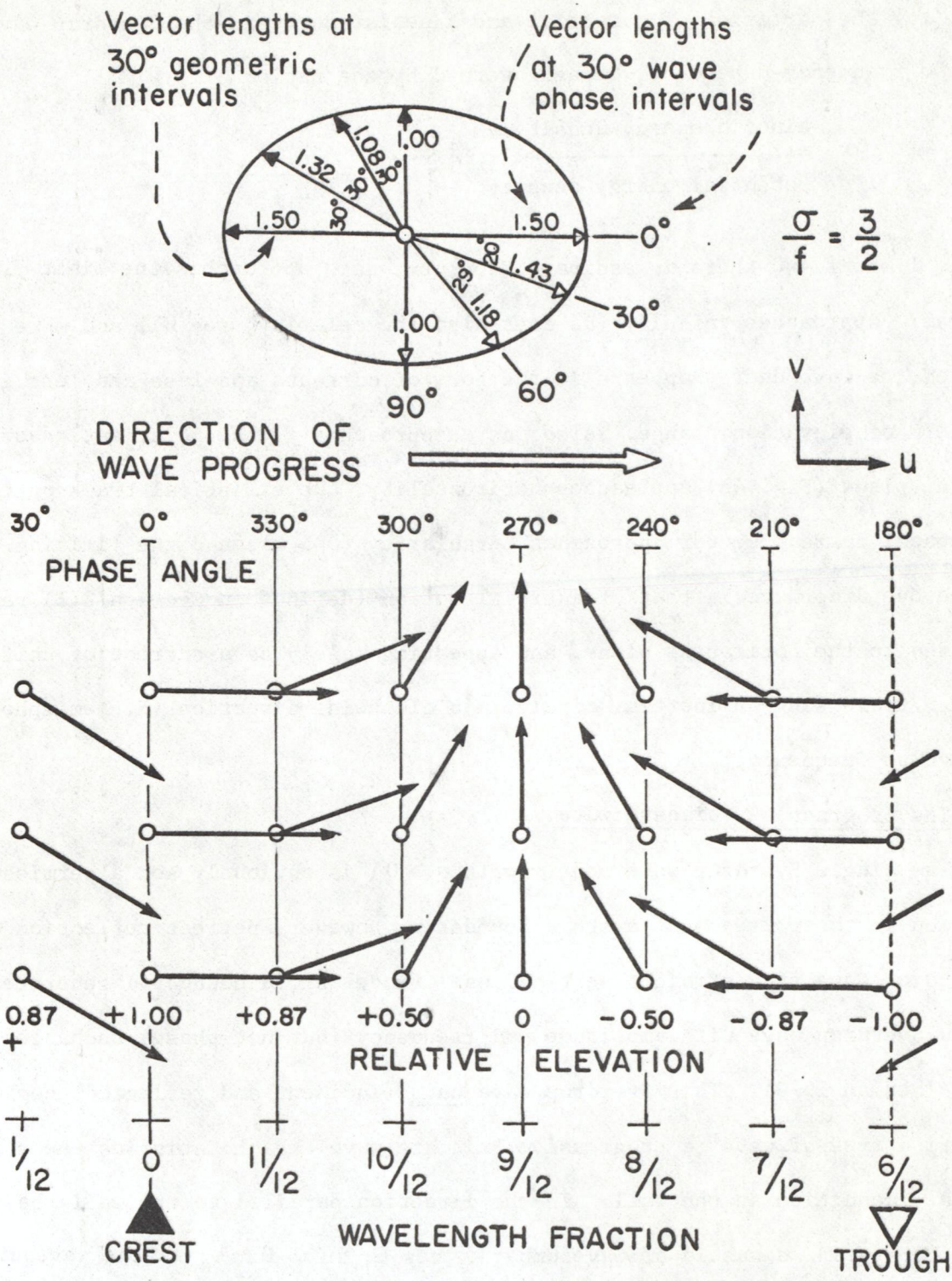

Fig. 5. Horizontal projections of current vectors in a half-wavelength portion of a Sverdrup wave progressing from left to right in the N. hemisphere, and for which $\sigma/f = u_{max}/v_{max} = 3/2$. The horizontal current vectors are plotted as arrows, and relative wave elevations are entered (as a row of numbers in the bottom third of the figure) at 1/12 wavelength (30° phase angle) intervals.

structure of cells within which the horizontal current vectors rotate clockwise (N. hemisphere) at frequency σ.

The wave equations which describe Sverdrup wave reflection and further combinations of Poincaré waves, introduced later, become somewhat unwieldly when written out and explained. Here I prefer to introduce the reader to the geometry of these combinations by means of diagrams, which illustrate their crest patterns (Fig. 6) and their current vector patterns (Figs. 7 to 9). The geometry of reflection at a vertical wall, with one Sverdrup wave incident at angle Θ and a second identical wave reflected at angle Θ, is illustrated by Platzman (1970). Approaching the same phenomenon in a different way, Figures 6 to 9 do not specify a wall at the outset, but commence with consideration of pairs of Sverdrup waves, identical in wavelength (λ_s) and frequency (σ), and differing only in the angle (2θ) between the directions along which the partners in each pair are propagating. Permissible locations for walls become evident when the combined horizontal vector fields of the pairs are inspected.

The "building brick" or component of each pair is the Sverdrup wave illustrated in Figure 5. In that particular example, the σ/f ratio was chosen to be 3/2, corresponding to a wave of 12 h period at latitude 41.8° (inertial period 18 h). The horizontal current vectors were plotted at $\lambda_s/12$ intervals (i.e. at hourly or 30° phase intervals)* and the wave elevations (relative to unit amplitude were also entered. The wave, as illustrated in Figure 5, progresses from left to right. A fixed observer therefore sees the current

---

*It should be noted that, for graphical convenience, the vectors in Figure 5 were drawn for 30° geometric intervals (as in the upper left portion of the ellipse) whereas the angular spacing of the vectors corresponding to $\lambda_s/12$ wavelength fractions, i.e. to 30° wave phase intervals, are not uniformly spaced. But the error thus introduced is unimportant in this demonstration.

vectors rotating clockwise. There is, however, no restriction of the direction of wave propagation; and pairs of Figure 5 waves can be superimposed and made to move (step by step for graphical combination) in directions which subtend any desired angle.

The current patterns of four such combinations (Θ chosen for geometrical simplicity to be the values listed in Table 2) are shown in Figure 6. In case

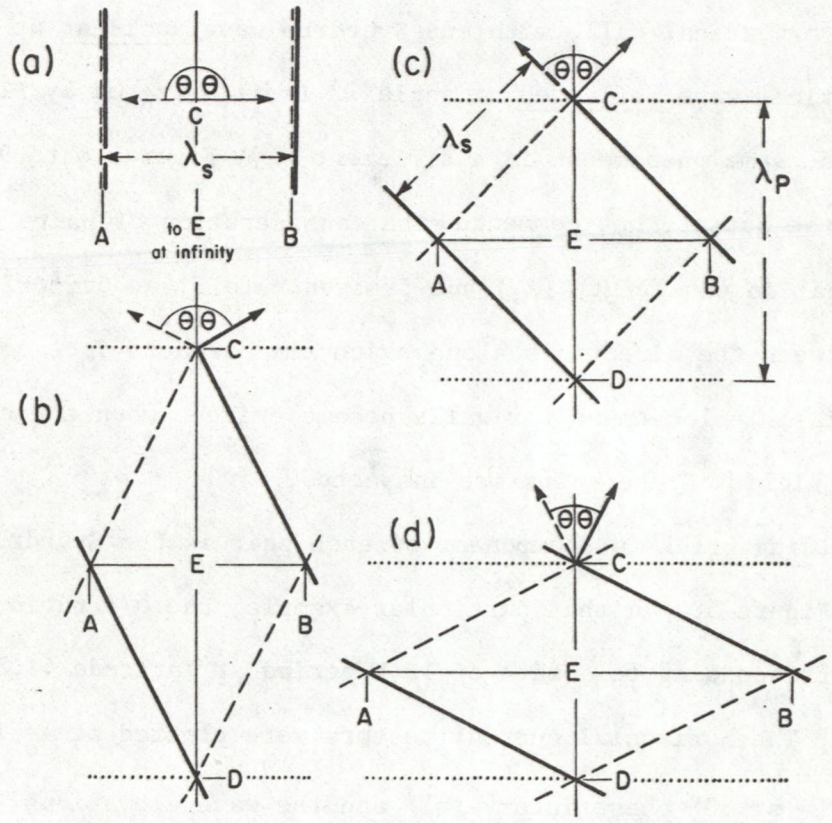

Fig. 6. Crest patterns produced by four pairs of Sverdrup waves. In pairs (a), (b), (c) and (d) the component waves are travelling in directions which subtend angle 2 Θ of 180°, 126.86°, 90°, and 53.14°, respectively (see Table 2). Crests of the right-propagating and left-propagating components are shown as unbroken and broken lines, respectively; and dotted lines indicate the crests of the combination (progressive Poincaré wave). The letters E, B, and D are repeated at corresponding positions in Figs. 7, 8, and 9.

(a), described in connection with Figure 7, Θ is 90° and the Sverdrup pair are moving in exactly opposed directions. In the other cases, $\Theta < 90°$, the wave crests (shown unbroken and broken for the right-propagating and the left-

propagating partner of the pair, respectively) form a network of parallelograms (only one of which is shown) of width AB and height CD. AB and CD intersect at E; AE = EB; and CD bisects the angle 2Θ. Passing through C and D are dotted lines perpendicular to CD which mark the crests of a combined wave formed by the paired Sverdrup combination. For later references, CD defines a Poincaré wavelength, λ_p, infinite in case (a); and EB defines the width (but not the position) of a channel (width b).

TABLE 2. Crest geometries of the Sverdrup wave pair combinations illustrated in Figure 6 and described in the text. The Sverdrup wavelength, λ_s, is the same in each case.

Case	CD/AB $= \lambda_p/2b$ $= \arctan \theta$	θ degrees	AB/λ_s $= 2b/\lambda_s$ $= 1/\sin \theta$	CD/λ_s $= \lambda_p/\lambda_s$ $= 1/\cos \theta$
a	infinity	90	1	infinity
b	2	63.43	$\sqrt{5}/2 = 1.118$	$\sqrt{5} = 2.236$
c	1	45	$\sqrt{2} = 1.414$	$\sqrt{2} = 1.414$
d	1/2	26.57	$\sqrt{5} = 2.236$	$\sqrt{5}/2 = 1.118$

The current and elevation patterns of combination (a) are shown on the left-hand and right-hand sides of Figure 7, respectively. The numbered rows correspond to hourly intervals in a 12 h cycle. The Sverdrup wave components, directly-opposed, propagate across the page, and their respective horizontal current vectors are shown as thin lines (unbroken right-going, broken left-going) in plan view. The vectors of the resultant wave are shown as thick arrows. The hourly elevations of the water surface are shown for the EB portion of the section aligned along the direction of Sverdrup wave propagation. The elevation sequence is that of a standing wave with a node at N and antinodes at E and B,

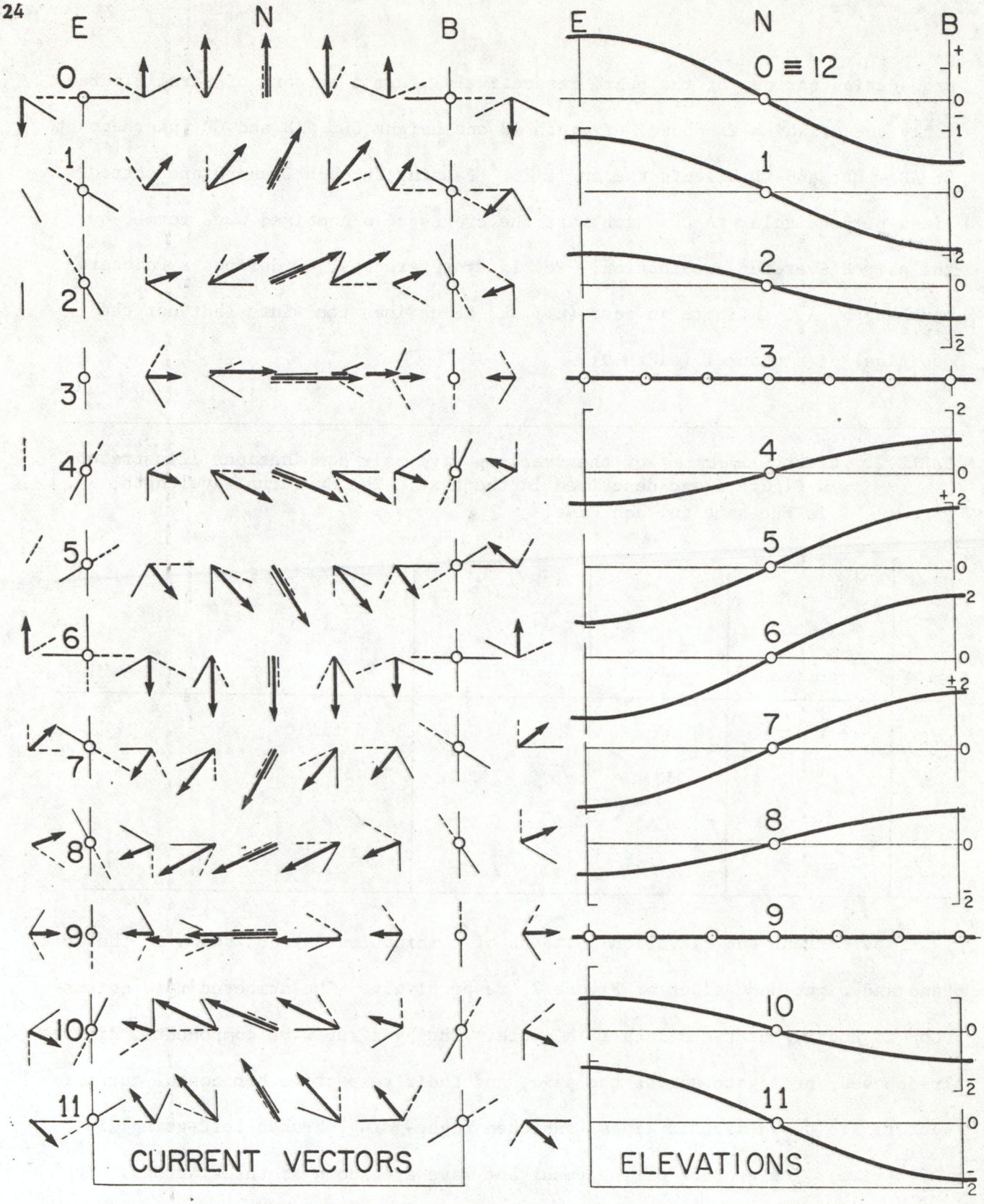

Fig. 7. Two oppositely-propagating but otherwise identical Sverdrup waves (horizontal current vectors shown as thin broken and unbroken lines, respectively) combined to form a "standing Sverdrup wave" corresponding to case (a) in Figure 6. The combined horizontal current vectors (thick arrows) and wave elevations across the section EB (see Fig. 6) are illustrated at 1/12 cycle intervals, i.e., hourly intervals for a wave of 12 h period. N marks the position of a node; E and B coincide with antinodes.

spaced (as can be seen by comparison with Figure 5) half a Sverdrup-wavelength apart. In the current field, the resultant current is always zero at the antinodes. Therefore this standing wave combination (termed "standing Sverdrup wave" by Mortimer 1963) can satisfy solid boundary conditions at any pair of vertical walls coinciding with antinodes, for example at E and B and aligned perpendicular to the direction of Sverdrup wave progress. Such a wall pair corresponds to an infintely long channel of rectangular cross section, which may contain a single nodal line (as at N in Fig. 7) or any integral number, n, of such lines. Each integer n corresponds to a normal mode of oscillation of the channel, i.e., cross-channel seiche modes; and any combination of such modes can co-exist. Figure 7 provides a set of hourly snapshots of the current field and surface elevation for the first seiche mode (n = 1) identically repeated at all points along the channel. Along-channel variation and the along-channel wavenumber are therefore zero; and the cross-channel wavenumber (later referred to as k_x) is equal to $2\pi n/\lambda_s$, in which λ_s is the component Sverdrup wave wavelength. That wavelength is twice the channel width (b) for the first mode and $2\ b/n$ in general. The corresponding general expression for the set of cross-channel wave numbers is $\pi n/b$, corresponding to frequencies, derived from (7) and given by:

$$\sigma^2 = f^2 + c_o^2 k_x^2 = f^2 + c_o^2(\pi^2 n^2/b^2) = f^2 + m^2 \qquad (10)$$

in which m is defined in the following paragraph.

If f is zero (no rotation), the channel modes take the form of simple cross-channel seiches with non-rotating current vectors and with frequencies (periods) determined by the well-known Merian equation. This yields a frequency set, $c_o \pi n/b$, which will later be referred to as the Merian (no rotation) frequency, m. Equation (10) defines a frequency limit below which a particular Sverdrup mode combination cannot exist in a particular channel. The importance of this limitation will be discussed later.

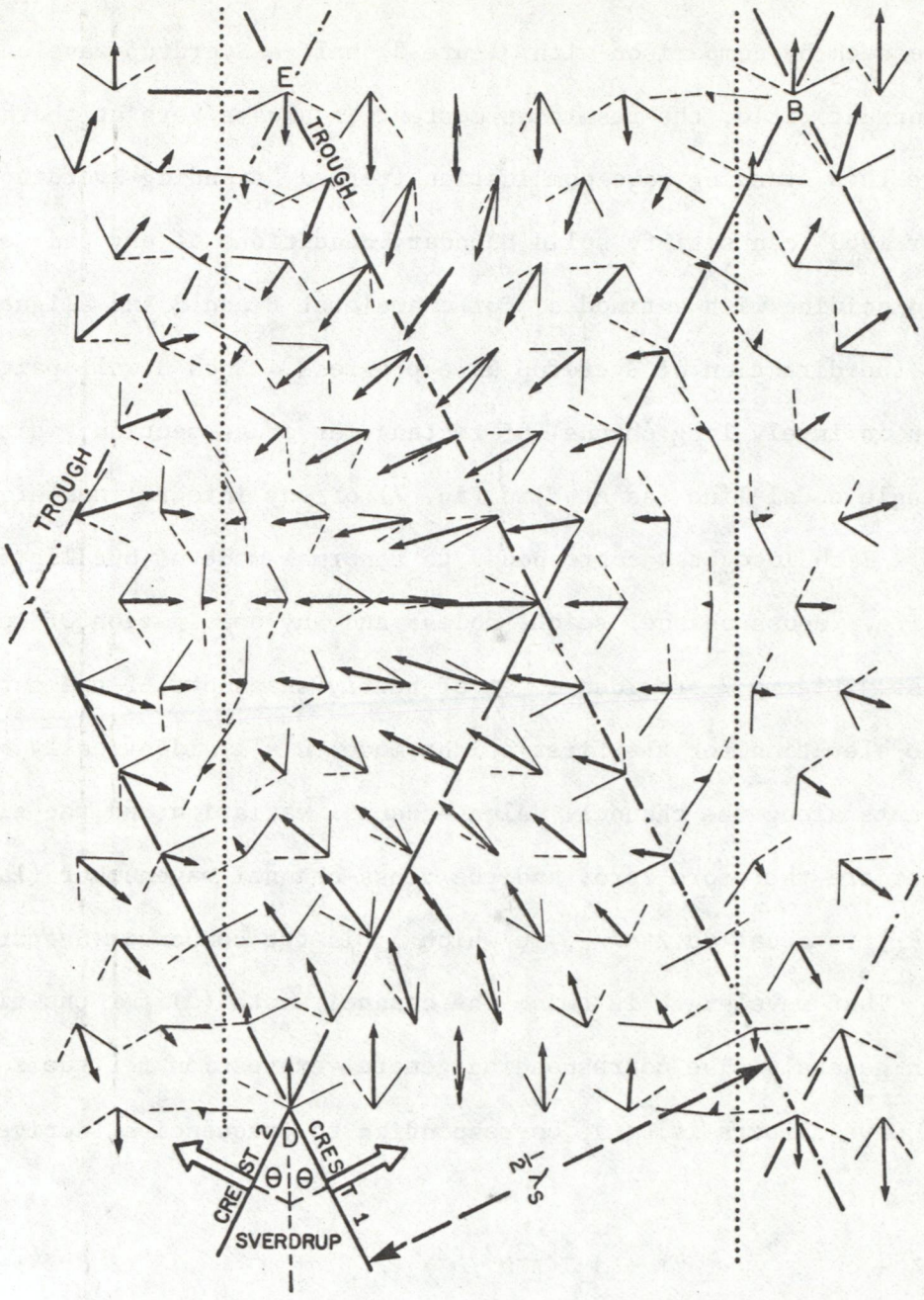

Fig. 8. A half-wavelength portion of the horizontal current vector field of a combined (Poincaré) wave made up of two identical Sverdrup waves travelling in directions defined by the angle 2 θ = 126.86° (arctan θ = 2, case b, Table 2, Fig. 6). The combined vectors (horizontal components of Poincaré wave current) are shown as thick arrows; the corresponding vectors of the two constituent Sverdrup waves are shown as thin broken and unbroken lines, respectively. Sverdrup wave crests and troughs are shown as thick continuous and broken lines, respectively, and the intersects E, B, and D occupy positions equivalent to those letters in Figure 6. The Poincaré (combined) wave progresses upward on the page; and vertical dotted lines indicate where vertical channel sides could be placed to satisfy solid boundary conditions, as described in the text.

The elevation and horizontal current patterns for combinations (a) and (b) in Figure 6 were illustrated in the preceeding figure (7) and in Figure 51 of Mortimer (1971), respectively. The horizontal current field of the latter combination (b) is also shown in Figure 8, relative to the crest and trough lines of the component Sverdrup waves and to the letters E, B, D, corresponding in position to those letters in Figure 6. Similarly, the horizontal current fields of combinations (c) and (d) are presented in Figure 9. The figures illustrate small portions of infinitely repeating cellular patterns, which should be viewed as propagating up the length of the page past a line fixed across it. The vertical ordinate may therefore be scaled either in time or length units (conveniently, Poincaré periods or wavelengths); and, because the pattern repeats with appropriate change of sign, it is only necessary to illustrate a half-wavelength portion (from E to D). During the upward passage of that portion, past a fixed observer, the current vectors of the component Sverdrup waves and the resultant Poincaré combination (thick arrows) execute a half-rotation clockwise. Examination of the Poincaré current vector field (thick arrows) discloses a set of lines parallel to ED (two of which are shown dotted in Figures 8 and 9) near which the currents are weak and across which the current direction reverses. In fact, as Figures 8 and 9 suggest, vertical walls could be placed along any of these lines (which are repeated at intervals of $\lambda_s/2 \sin \Theta$) without violating the solid boundary condition at the walls. One wall, so placed, does not restrict the choice of λ_s or Θ; but two such walls, forming a channel of width b, restrict the choices because of the interdependence of λ_s, Θ, and b evident from a comparison of Figures 6, 8, and 9. This point will be taken up again later.

Also evident from comparison of Figures 6, 8 and 9 is an increasing asymmetry of the Poincaré wave current pattern, relative to the channel defined by the vertical dotted lines, as Θ decreases from 90° (Fig. 6 in which the

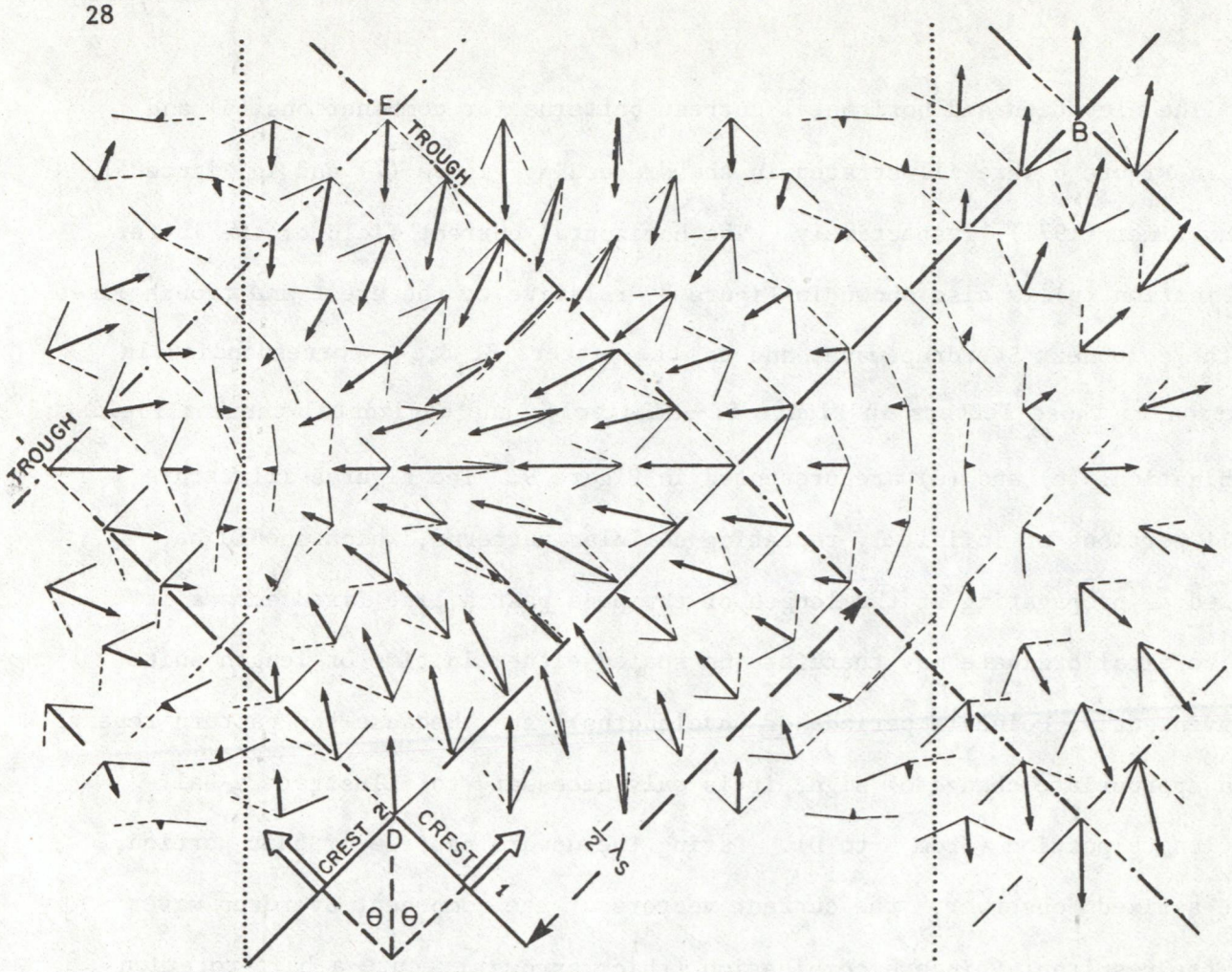

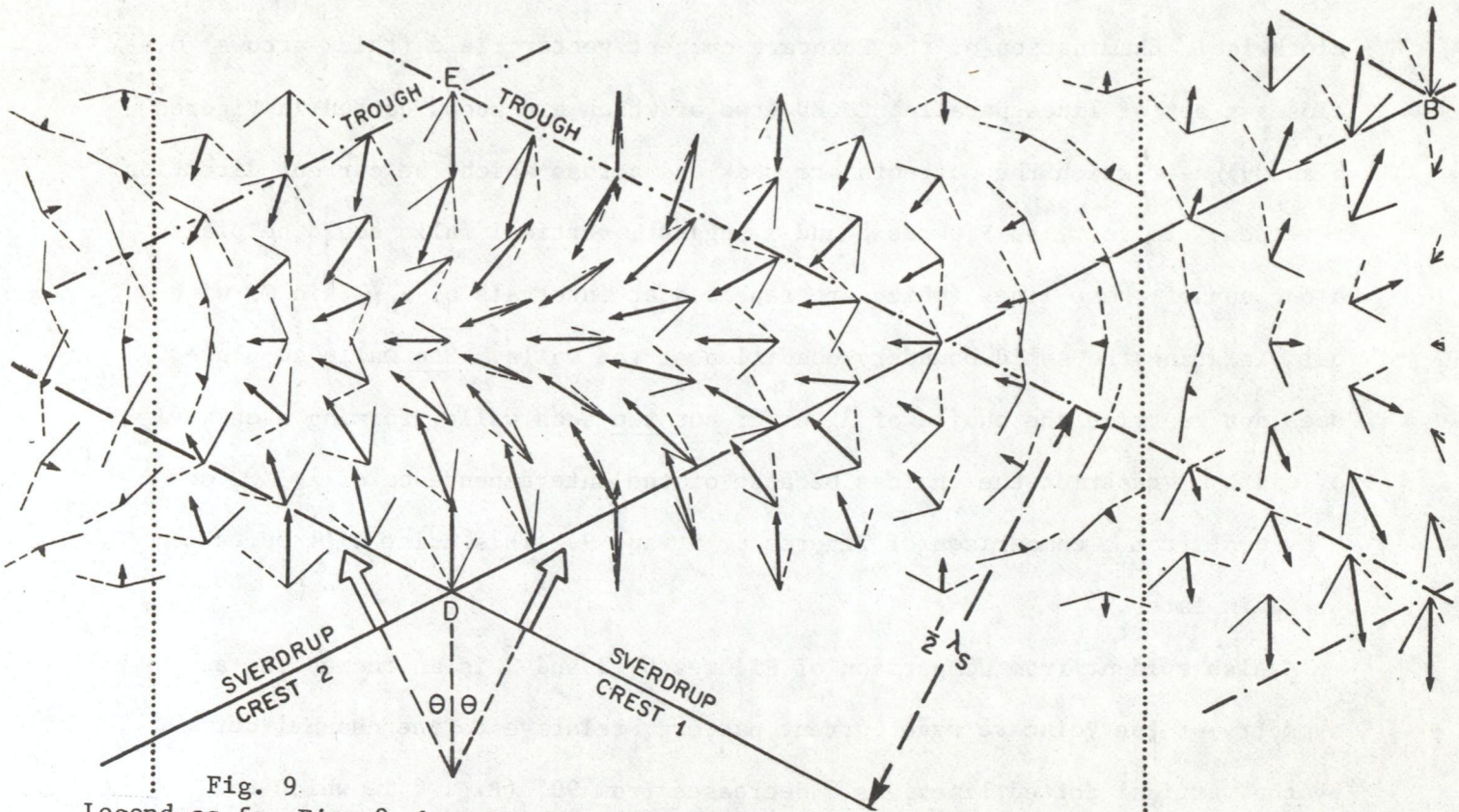

Fig. 9
Legend as for Fig. 8, but for two cases (upper and lower) corresponding to cases c and d in Table 2 and Fig. 6, i.e., 2 θ = 90° and 53.14°, respectively.

assymmetry is zero) to 27° (Fig. 9 lower part). Looking in the direction of wave progress, the region of strongest current is shifted to the left of the channel center line, while the line of maximum elevation change (ED, along which the Sverdrup crests and troughs intersect) is shifted to the right of the channel side by a distance which increases as θ decreases from 90°. This assymmetry, which was discussed and defined in Platzman (1970) and Mortimer (1971), is a consequence of the effect of rotation on the phase change which occurs when a Sverdrup wave is reflected at a wall. The effect is zero for normally incident waves, for example case (a) in Figure 7, i.e., the standing Sverdrup wave case illustrated in Figure 6. When θ is less than 90°, the resulting Poincaré wave is also standing across the channel (while propagating along it); but the nodal lines are displaced (to the right looking in the direction of wave progress) from the positions they occupy when θ = 90°. This rightward displacement* of the nodal line and leftward displacement of the maximum current line, relative to the channel centerline, is illustrated for progressive Poincaré waves of the first and third cross-channel mode (n = 1 and n = 3) in Figure 10.

Figures 6 to 9, which are based on paired combinations of Sverdrup waves of identical wavelength λ_s, demonstrate that decrease in Θ is accompanied by increase in the distance EB and therefore in b, the width of the channel into which the Poincaré wave will fit. In fact, as Table 2 shows, EB varies as $\lambda_s/2 \cos \Theta$, with the minimum spacing, $\lambda_s/2$, occurring at Θ = 90° (standing Sverdrup case). In other words, with λ_s fixed, Θ may take any value between 90° and 0°, as long as channel width is permitted to vary to accommodate the particular wave combination associated with that particular value of Θ.

---

*Displacement is b arctan $(f/\sigma \cot\Theta)/\pi n$ for the nth cross-channel mode in a channel of width b (Mortimer 1971).

Fig. 10. Cross-channel asymmetry of progressive Poincaré waves, illustrated in the upper (uninodal) example by shifts of the maximum current line (MCL) and of the nodal line (NL) from the channel center line (CCL). Similarly, looking in the direction of wave progress in the lower (trinodal) example, the position of maximum elevation range is shifted Δ_ζ to the right of the channel side, while MCL is shifted Δ_v to the left of the nodal line (N). Both shifts are defined in Mortimer (1971, in which the lower portion is Fig. 53a). The last sentence in the legend for Fig. 11 applies also here.

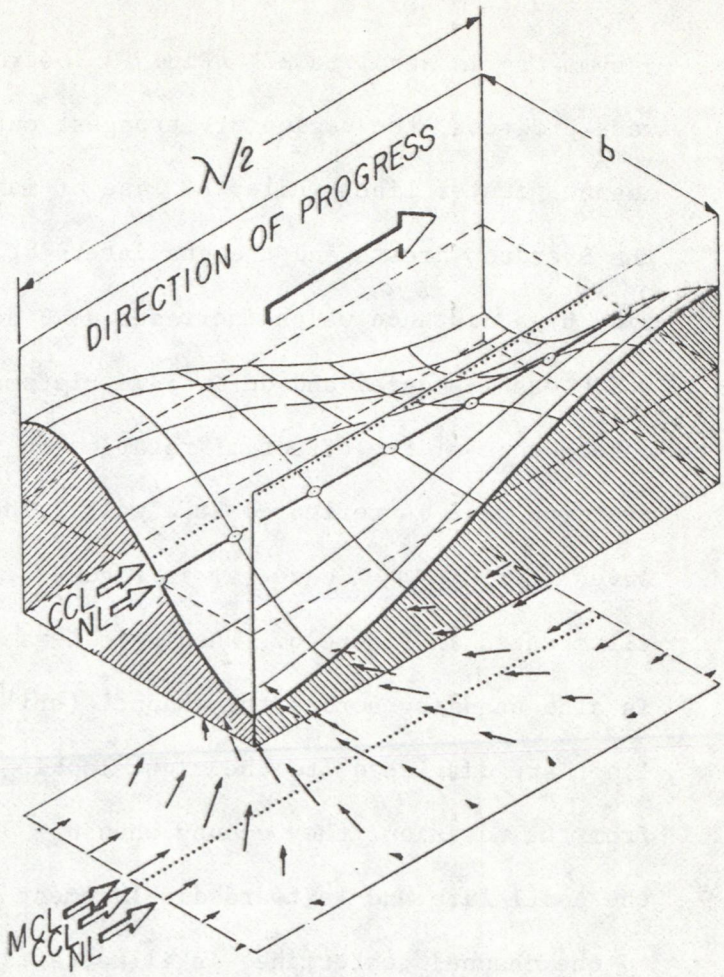

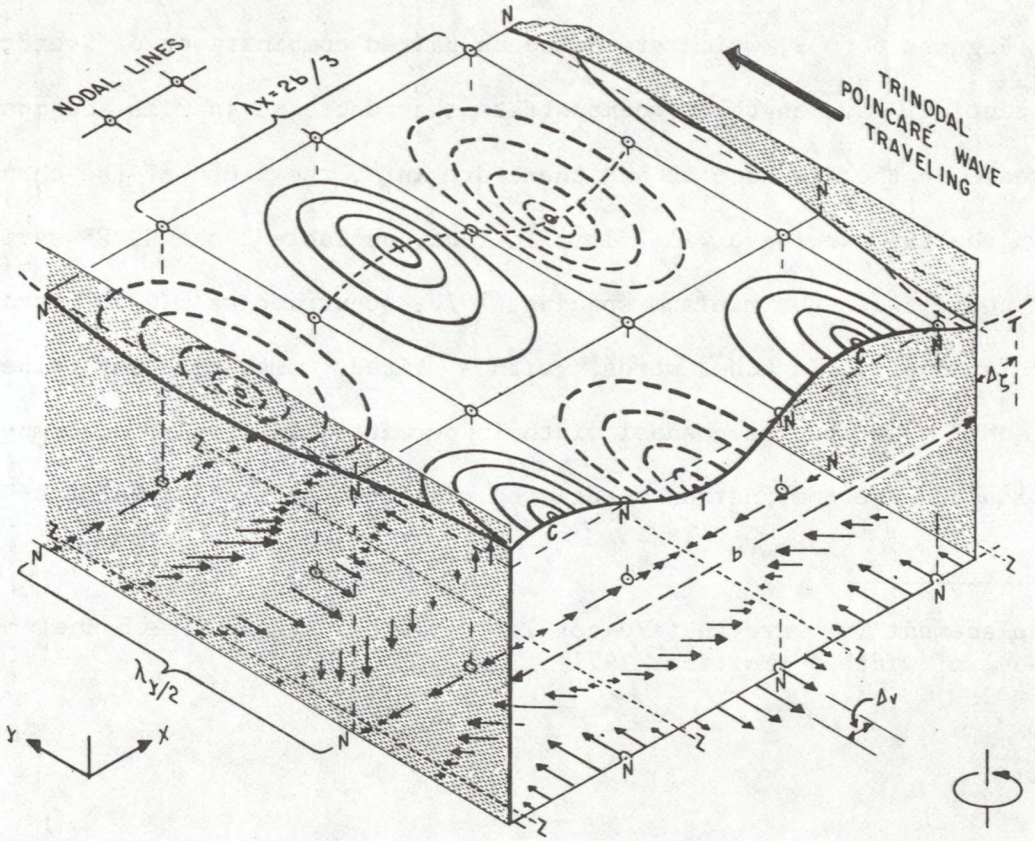

If, however, Figures 6 to 9 are interpreted on the basis of a fixed channel width (b, say) so that the distances between the dotted lines is set at b in all the figures, then λ_s is no longer fixed and becomes subject to a maximum limit, which is achieved in case (a) with $\Theta = 90°$, $\lambda_s = 2b$, and wavenumber $k = \pi/b$. This wavelength restriction corresponds to a frequency restriction, discussed below, which states that σ must be greater than the frequency defined by the third equation in (7), i.e. only Sverdrup (and therefore Poincaré) waves of σ^2 greater than $f^2 + (c_o\pi/b)^2$ can propagate in a channel of width b and depth h (which determines c_o). The effect of this limit on the propagation of tidal waves in restricted waters is described by Platzman (1970).

2.7 Poincaré waves combined in a channel.

The progressive Poincaré waves described in the previous section exhibit the properties of standing waves across the channel; and a pseudo-standing wave pattern can also be produced along the channel, if two identical but oppositely-propagating Poincaré waves are combined. Taking the cross-channel uninodal example from Figure 10 , half-wavelength portions of two such oppositely-propagating progressive Poincaré waves are shown in Figure 11(a). Eight phases in one oscillation cycle of the combined wave they produce are numbered in sequence in 11(b). Several features are evident: the cross-channel standing wave structure is maintained, but the assymmetry, described earlier for the progressive Poincaré wave (i.e. the displacement of NL and MCL from CCL), is cancelled out; an along-channel "standing" pattern emerges, dividing the wave structure into cells; clockwise rotation of the current vectors is maintained with highest speeds at the center of the cell; the solid boundary conditions are met at the channel sides, but not at the cell ends (therefore this is not a true standing wave, such as would be produced by a pair of oppositely-propagating plane waves in the absence of rotation); the current component normal to the cell end walls is small (very small as channel width increases) but does

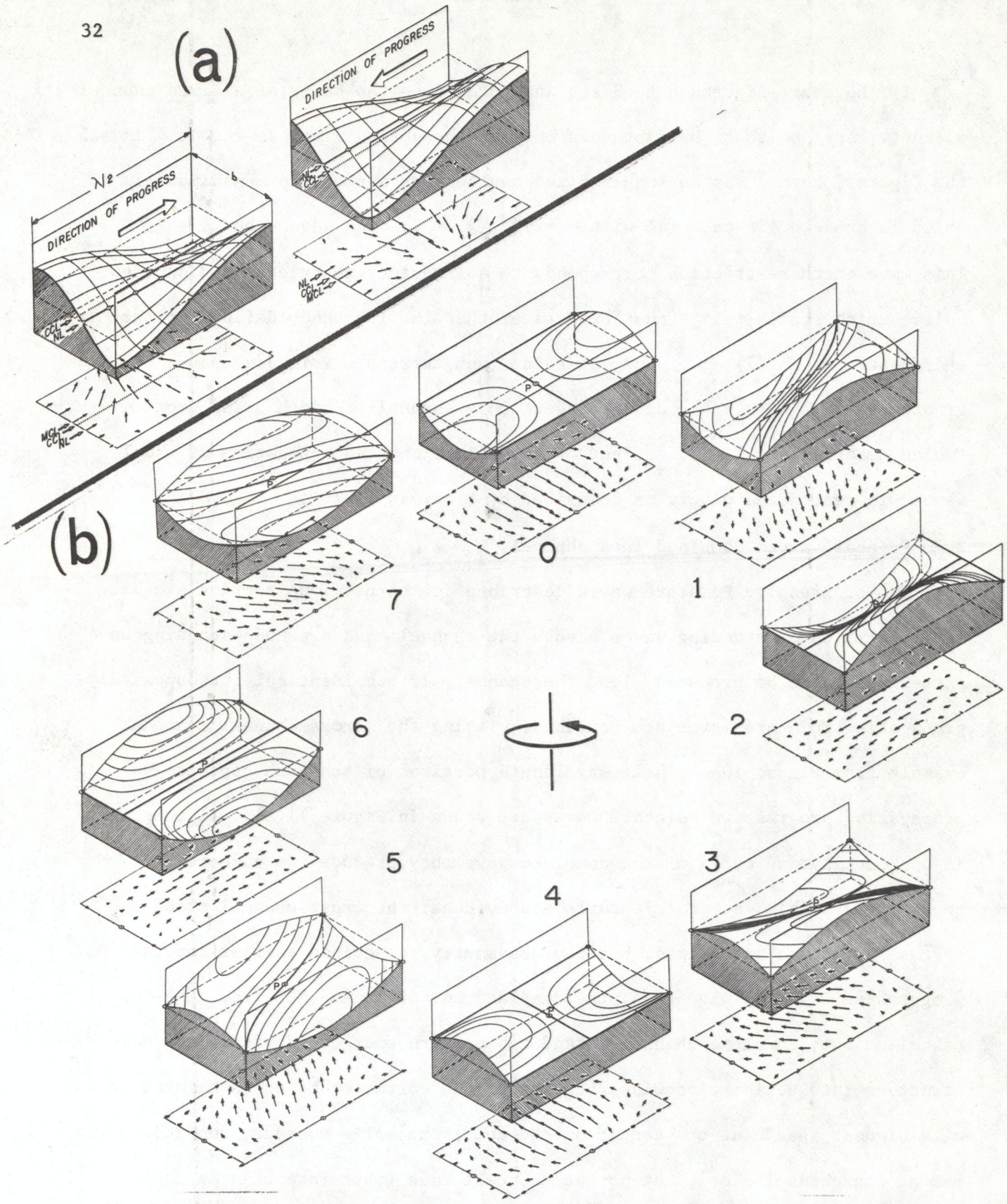

Fig. 11 (from Mortimer 1977). Two oppositely-propagating but otherwise identical progressive Poincaré waves, from Fig. 10 and shown here in (a), combine to produce the amphidromic "standing" Poincaré wave, half-wavelength cells of which are illustrated at 1/8-cycle intervals in (b). The combined wave, with amphidromic point P at the cell center, is truly standing (with one node in this case) across but quasi-standing along the channel, as explained in the text. Wave topography can be viewed either as that of a water surface or as that of a "thermocline" interface in a two-layered model, in which case the horizontal current vectors (illustrated beneath each cell) are those in the lower layer.

not fall to zero except at the center point; the wave elevation pattern progresses clockwise around cell-center point of no elevation change (the amphidromic point P): an amphidromic point is also located at each cell corner.

The model illustrated in Figure 11, when applied to whole-basin internal waves in large lakes, reproduces several observed features (Mortimer 1971), but as a basin (as opposed to a channel) model it is only complete with the addition of a pair of oppositely-propagating shore-trapped internal Kelvin waves. The cellular structure of the "standing" Poincaré wave is repeated along the channel (in this case with double the cross-channel wavelength); and depending on the number (n) of cross-channel nodes, n cells fit across the channel (cross-channel wavelength equals twice the cell width, i.e. $2b/n$ in a channel of width b). Figure 11 is an illustration of the first cross-channel Poincaré mode (n = 1); Figure 12 illustrates four phases in one oscillation cycle of the third cross-channel mode (n = 3). These paterns, it may be recalled, are all constructed from Sverdrup waves as elementary bricks, the sequence in these examples evolves through Figures 5, 8, 10, 11, 12.

2.8 Period/wavelength relationships of Poincaré waves.

In the following treatment it will be convenient to align the x and y axes across and along the channel respectively, i.e., the reverse of Platzman's (1970) convention used in earlier discussions. The cross-channel wavelength set is then defined by $\lambda_x = 2b/n$ (= $\lambda_s/n \sin\Theta$, Table 2) and as we have seen with width b fixed, x is restricted to particular values, namely those which adjust the distance EB to fit that particular channel width. The corresponding along-channel wavelength set, in the fixed-width channel, is therefore also fixed at $\lambda_y = \lambda_s/n \cos\Theta$ (= $\lambda_x/n \tan\Theta$). Cross-channel and along-channel wavenumbers, respectively k and l in the x and y directions and expressed generally for all modes, are: $k = 2\pi/\lambda_x = \pi n/b$ and $l = 2\pi n/\lambda_y = \pi n \cot\Theta/b$. The frequency of the Poincaré wave, already defined in equation (10), may be re-written:

$$\sigma^2 = f^2 + c_o{}^2(k^2 + l^2) = f^2 + (1 + r^2)(c_o \pi n/b)^2 \qquad (11)$$

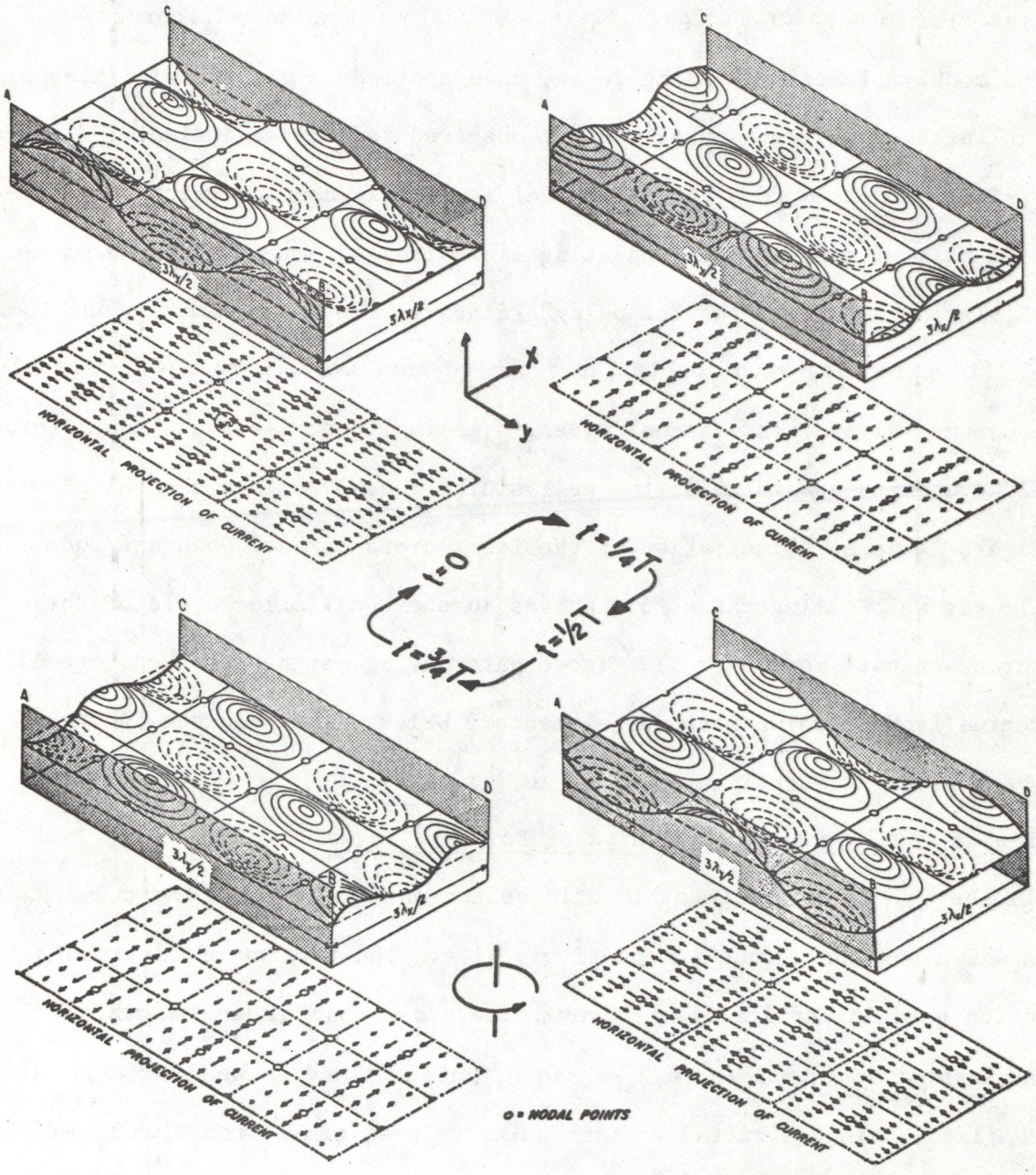

Fig. 12. A "standing" Poincaré wave of cross-channel nodality three, i.e., a trinodal equivalent of Fig. 11(b), but with only four phases of the oscillation cycle shown. The legend for Fig. 11 applies; and the progressive Poincaré wave component, contributing to this combination, is illustrated in Fig. 10 (lower part).

in which r = cot Θ denotes the ratio l/k (= λ_x/λ_y), and $c_o = \sqrt{gh}$. As pointed out earlier, our consideration is here confined to purely harmonic solutions of the general wave equation, solutions which require $(k^2 + l^2)$ to be real. In conformity with the cross-channel standing wave structure, k is always real for Poincaré waves, but l may be real or imaginary, depending on whether l^2 is positive or negative, respectively. This defines the above-mentioned frequency limit, $\sigma^2 = f^2 + c_o^2 k^2$, below which a channel of given width b and depth h (= c_o^2/g) cannot provide a wave-guide for progressive Poincaré waves. It follows from equation (11) that, at the frequency limit ($l^2 = 0$, the transitional standing Sverdrup wave case), r is zero, λ_y is infinite, and there is no amplitude variation along the channel. Above and below that limit ($l^2 > 0$ and $l^2 < 0$) the along-channel amplitude dependence is, respectively, sinusoidal (propagating Poincaré wave case) or exponential (evanescent Poincaré waves in the terminology of LeBlond and Mysak 1978). It should be noted that, in each of the three cases ($l^2 > 0, = 0, < 0$), the cross-channel standing wave pattern is maintained. As deduced by Taylor (1920), a complete set (n = 1 to infinity) of evanescent Poincaré modes, with exponential along-channel amplitude-decrease away from a cross-channel barrier, are the necessary adjuncts for perfect Kelvin wave reflection at that barrier and are therefore components of the combined Kelvin/Poincaré wave solution for closed basin models (Lauwerier 1960, Mortimer 1971). This (component assemblage) approach to closed basin solutions will later be compared with a more direct method of calculation, but before that is done some instructive graphical procedures are introduced, in which the frequency/wavenumber relationships embodied in equation (11) are applied to long internal wave responses in large lakes.

Recalling that $r = l/k$, and that m is the first cross-channel (Merian) mode frequency without rotation, and that n is an integer defining the number of cross-channel nodes in a particular mode structure, equation (11) may be rewritten

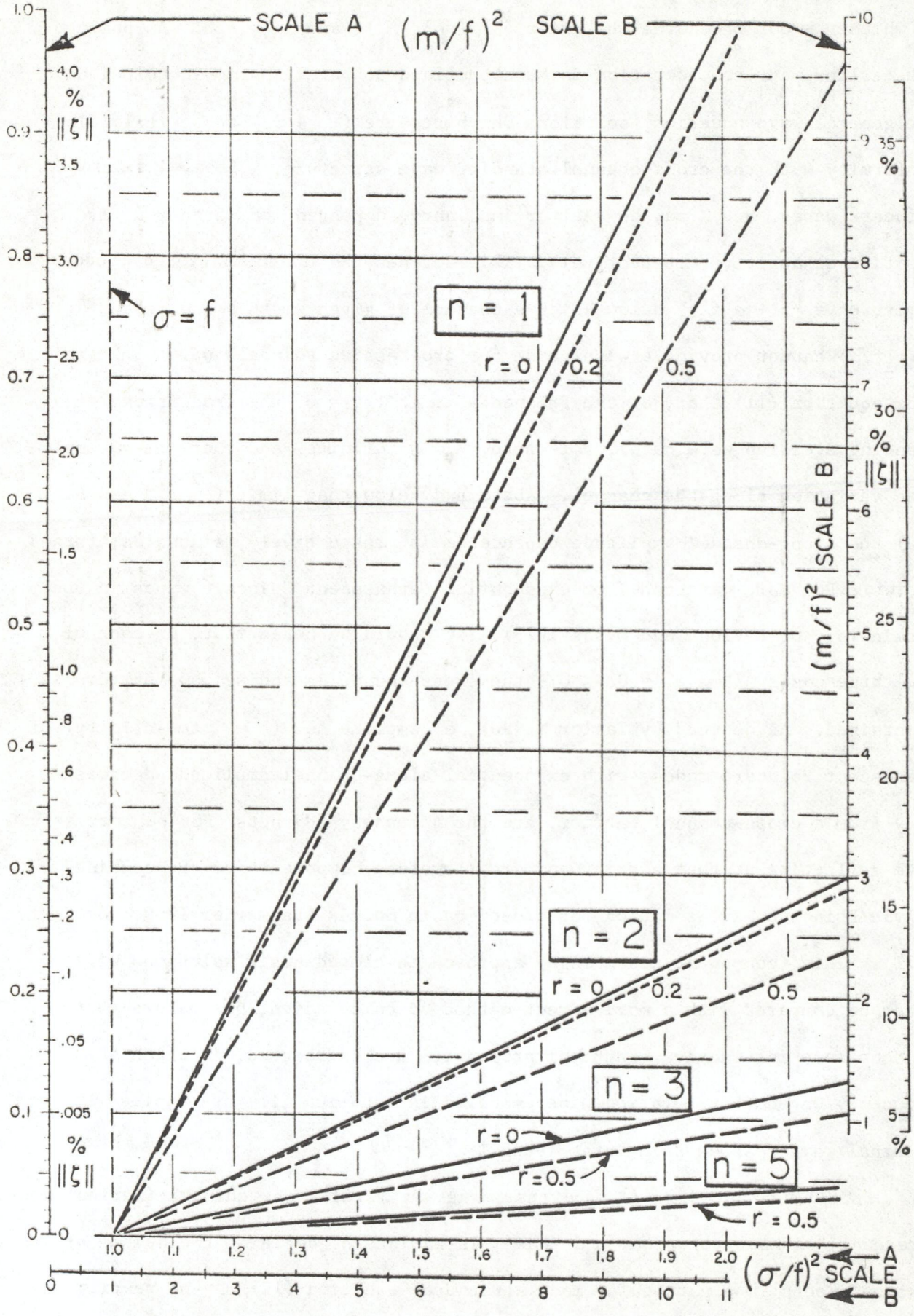

Figure 13. Legend on facing page, 37.

in nondimensional form:

$$(\sigma/f)^2 = 1 + (1 + r^2)\ (nm/f)^2 \qquad (12)$$

Recalling also from the discussion following equation (11) that y-propagating Poincaré waves of cross-channel mode number n are confined to the frequency domain defined by $\sigma^2 > f^2 + (1 + r^2)\ (nm^2)$, the low-frequency cut-offs for n-values 1, 2, 3 and 5 and for r = 0, 0.2, and 0.5 are displayed by the family of straight lines in Figure 13, defined by equation (12). Figure 13 can therefore be used to determine whether, for a given value of f, a particular Poincaré mode of frequency σ is progressive or evanescent along a channel of width b and depth h (b and h defining m). The domain to the left of line in question is that of evanescent waves; to the right is the domain of sinusoidal waves; the line itself marks standing Sverdrup wave transition.

[Although not relevant to this discussion of Poincaré wave properties, it may be noted in passing that the $\%\ \|\zeta\|$ scales in Fig. 13 enable the cross-channel amplitude decay in a Kelvin wave to be estimated if f, b, and c (and therefore m/f) are known. Looking along the channel in the direction of (N. hemisphere) wave progress, the amplitude at the lefthand side relative to 100 at the righthand side is given by: $\%\ \|\zeta\| = 100 \exp(-fb/c) = 100 \exp(-\pi f/m) = 100 \exp(-\pi P_m/P_i)$. Therefore the $(m/f)^2$ scales can be used to estimate $\%\ \|\zeta\|$.]

Defining P_i, P_m, and P_p as the inertial, Merian, and Poincaré periods, respectively, the scales in Figure 13 may also be labelled as follows: ordinate $(P_i/P_m)^2$; abscissa $(P_i/P_p)^2$; and when b, f, and c (c_o for a surface wave or c_i for an internal wave defined by equation (6), for example) are known or can be estimated for a particular case, it is instructive to recast Figure

---

Figure 13. See facing page, 36.

With σ defining the Poincaré wave frequency, f the inertial frequency, and m the (1st. mode) cross-channel Merian frequency, the output of equation (12) is plotted over ranges $(\sigma/f)^2$ 1 to 2.2 and $(m/f)^2$ 0 to 10, accommodated on two sub-ranges (scale parts A and B) and for values of n = 1, 2, 3, 5 and r = zero, 0.2, 0.5. For definitions and applications, and the use of the $\%\ \|\zeta\|$ scales, refer to the text.

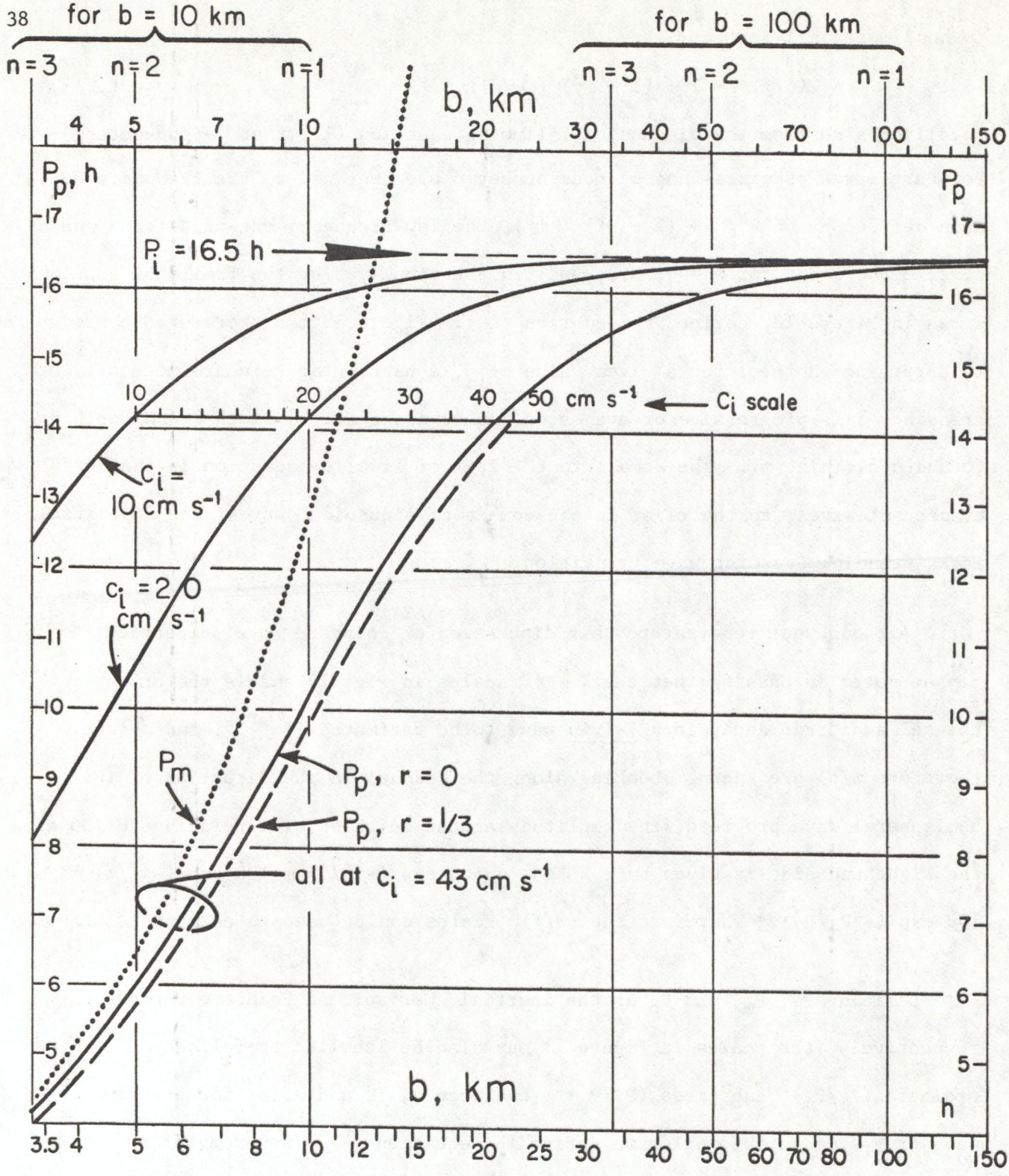

Figure 14. A linear/log plot (derived from equation 12) of Poincaré wave period, P_p, against channel width, b, for an inertial period, P_i, of 16 h and for particular values of internal celerity c_i. Curves for other c_i values can be produced by sliding the curve for c_i = 43 cm s^{-1} (and the appropriate value of r) laterally along the c_i scale. Vertical lines labelled n = 1, 2, 3 intersect the curves at the periods of the first three cross-channel modes in channels of 100 km and 10 km width. The first-mode Merian period, $P_m = 2b/c_i = 2\pi/m$, for c_i = 43 cm s^{-1} and for the b range 3.3 to 15 km is shown as a dotted line (period scale as for P_p); m is the Merian frequency defined in the text.

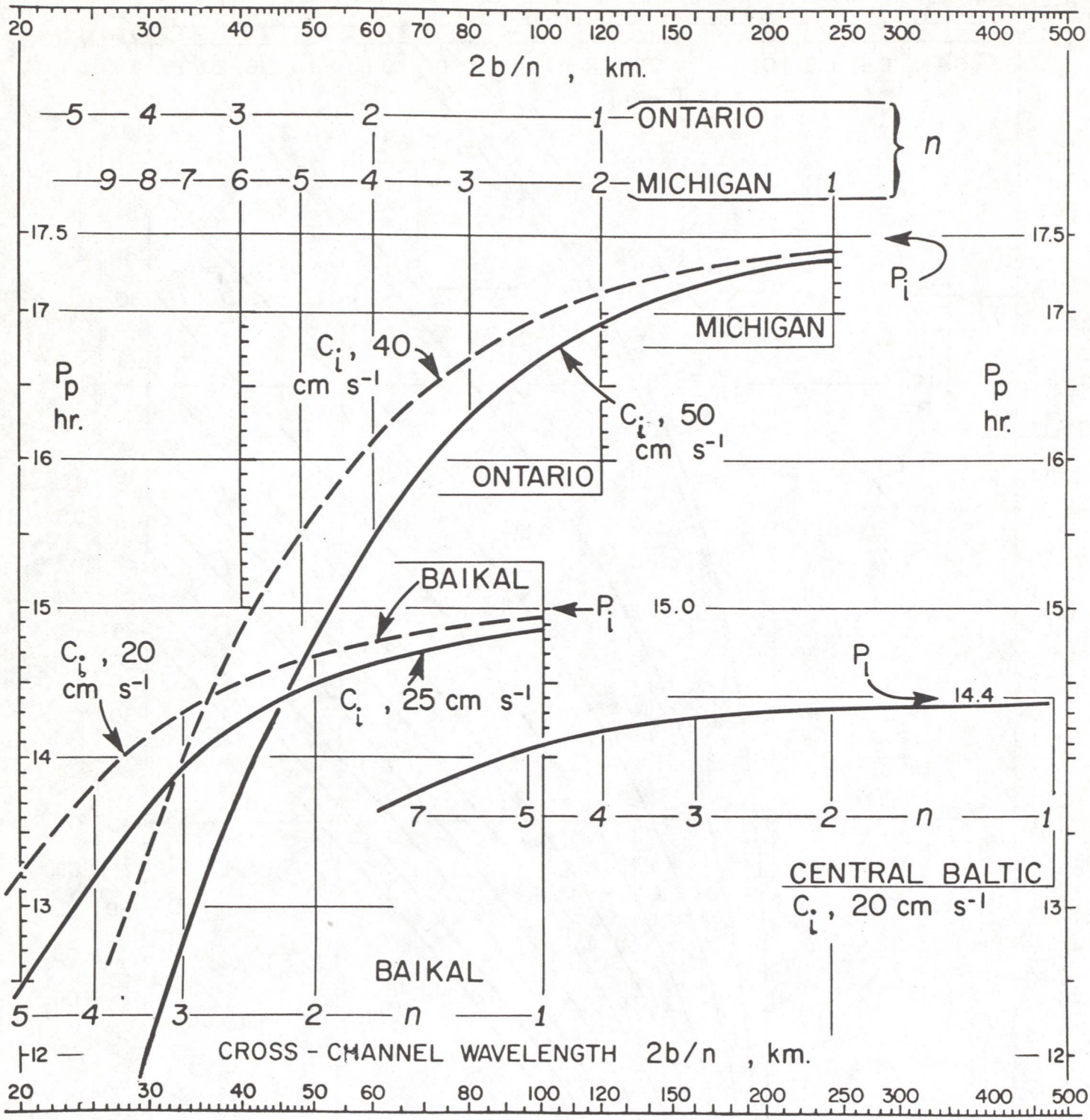

Figure 15. Poincaré wave period, P_p, versus cross-channel wavelength $2b/n$ in two-layered rotating channels fitted to dimensions and c_i values representative of conditions in the basins named (slightly modified from Fig. 13 in Mortimer 1977, which contains relevant parameters and references). The ratio $l/k = r$ is set to zero and vertical lines labelled n 1, 2, 3 etc., correspond to wavelength of mode numbers 1, 2, 3 etc., in the basins indicated.

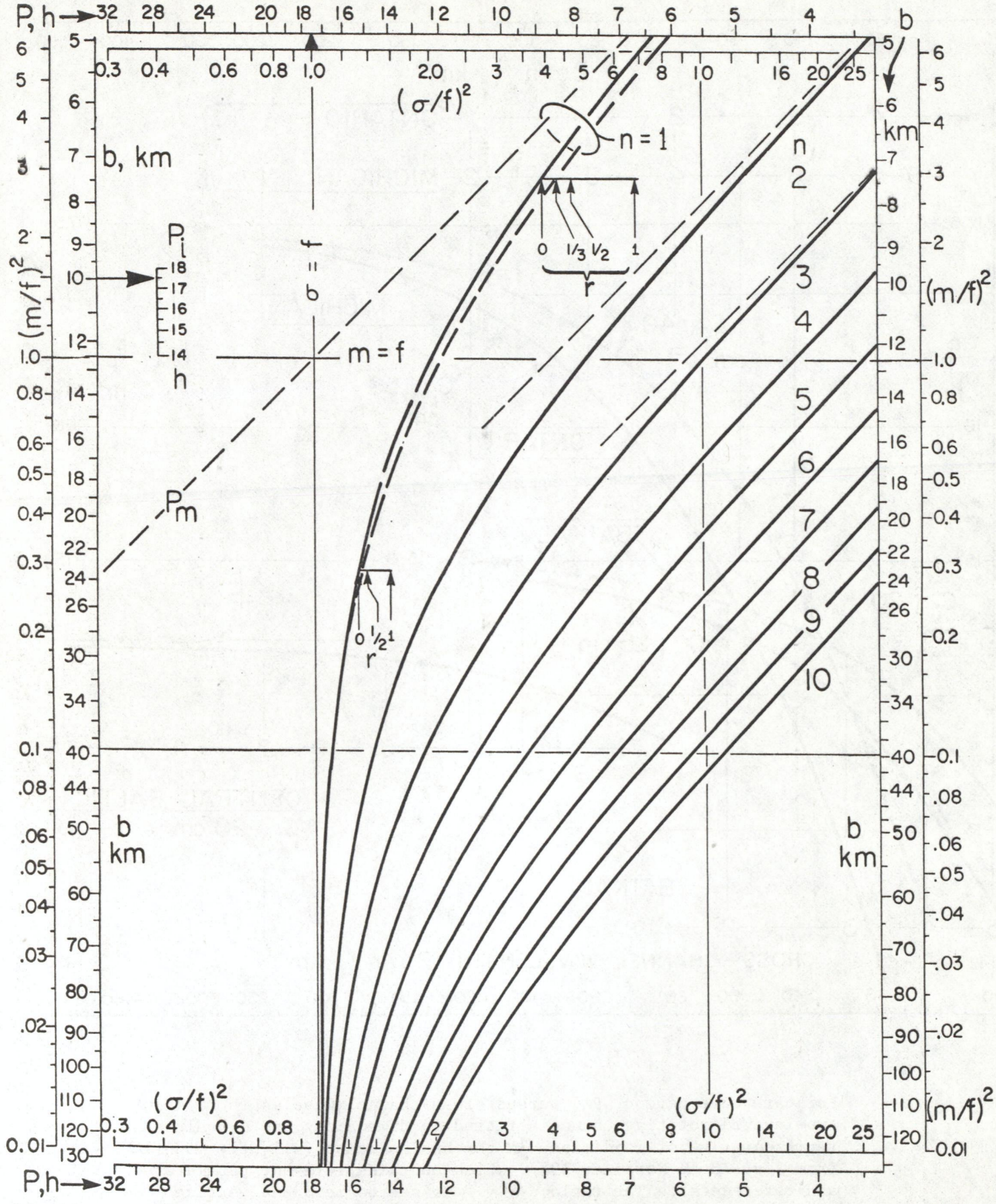

Figure 16. Legend on facing page, 41.

13 as a linear/log plot of P_p against b, as in Figure 14. That figure illustrates the influence of b and c_i on the period/wavelength relationship; the unbroken curves are for c_i values of 10, 20, and 43 cm s^{-1} (the latter, with P_i = 16.5 h, fitted to a Lac Léman case); but curves corresponding to other values of c_i can be produced by appropriate horizontal shifts along the c_i scale provided. The shift corresponding to r = 1/3 (broken curve) is relatively small; and observations in lakes suggest that models with r closer to zero are appropriate for elongated basins. Perhaps the ratio of basin width to length would be appropriate. For Lake Michigan that ratio is 1/6, and the factor $(1 + r^2)$ in equation (12) is therefore 1.028.

Figure 14 and Figures 15 and 16 which follow also illustrate the important result that the frequency (period) separation between modes decreases with

---

Figure 16. On facing page 40.
A log/log plot (derived from equation 12) of $(\sigma/f)^2$ versus $(m/f)^2$ for the first ten cross-channel modes (n = 1 to 10) of a Poincaré wave in two-layered rotating channels in which the internal wave celerity c_i is 40 cm s^{-1}. Also provided are scales of channel width, b, and Poincaré wave period, P, for the particular case, c_i = 40 cm s^{-1} and inertial period, P_i = 17.5 h. However, the diagram can be fitted to other particular cases, as follows:

(i) for P_i values other than 17.5 h, the whole P-scale (but not the $(\sigma/f)^2$ scale) is shifted horizontally to bring the desired value of P_i into line with the $\sigma = f$ vertical; and the b-scale (but not the $(m/f)^2$ scale) is shifted vertically to bring the arrowhead at b = 10 km to the desired value of P_i on the small scale inserted top-left in the figure.

(ii) adjustment of the figure to a celerity value other than 40 cm s^{-1} requires a vertical shift of or the application of a multiplication factor to the b-scale only. If the desired value is given as c_i cm s^{-1}, the b readings must be multiplied by $c_i/40$. This can be achieved by a vertical shift of the (logarithmic) b-scale, as follows. The desired value of c_i in cm s^{-1} units is located in km units on the b-scale, at point b^*, say. The b-scale is then shifted vertically until point b^* coincides with the position of 40 km on the present figure. The $(m/f)^2$ scale is not shifted.

The influence of the ratio $l/k = r$ in equation (12) is illustrated by the thick broken curve (for r = 1/3) and scales of r which accompany the curve for n = 1, as explained in the text. The thin broken straight lines indicate the Merian periods, P_m (i.e., read on the P scale), of the first three modes in a non-rotating channel, setting f to zero in equation 11.

increasing channel width. For example, vertical lines corresponding to n = 1, 2, and 3 are drawn in Figure 14 for two channel widths, 10 and 100 km, and a similar figure (15, reproduced from Mortimer 1977) illustrates the same result for channel models fitted to the dimensions and density distributions of Lakes Michigan, Ontario, Baikal and the central basin of the Baltic Sea.

A more generally applicable diagram (Figure 16) is a log/log plot of $n^2(m/f)^2$ against $(\sigma/f)^2$ scaled, in this example, in units of b (km) and P_p (h) for the case P_i = 17.5 h and c_i = 40 cm s^{-1}. As explained in the figure legend, the diagram can be adjusted for other values P_p and c_i by appropriate shifts of the scales. The family of unbroken curves illustrates the dispersive wavelength/frequency relationships of the first ten Poincaré modes with the ratio r in equation (12) set at zero. An additional curve is plotted (broken) for n = 1 and r = 1/3 and, to indicate the magnitude and sign of the correction, the corresponding points for other values of r are indicated by short insert scales attached to the n = 1, r = 0 curve at b = 7.5 and 24 km and corresponding to the $(m/f)^2$ values of 2.9 and 0.29, respectively. The correction can be calculated for other values of b and n by using equation (11); but in channel models applied to internal waves in large elongated lakes, the correction is expected to be small and can often be neglected in comparison with other sources of error. In that case, the curves in Figure 16 represent the (standing Sverdrup wave) transition, for each mode, between the left-hand and right-hand respective domains of evanescent and sinusoidal Poincaré waves.

Figure 16 displays the following results:

1. The separation between the Poincaré wave period P_p and the Merian wave period P_m (shown as dotted lines for the first three modes) increases with increasing b, illustrating the increasing influence of rotation as channel width increases.

2. Period separation between the modes decreases with increasing b; and the periods of all modes approach but do not exceed the inertial period P_i as b increases.

3. As already stated, the unbroken curves represent the first ten free mode (standing Sverdrup wave) periods in channels in the b range of 5 to 130 km. Internal Kelvin waves of period P_k can also be generated in the channel; and perfect Kelvin wave reflection at a vertical cross-channel barrier requires the corresponding P_k, b point to fall to the left of the $n = 1$ curve. But if the point falls to the right of that curve, reflection is not perfect, and the regular amphidromic pattern described by Taylor (1920) is not produced. Imperfect reflection would occur, for example, if P_k is 12 h and b 20 km, because only the Poincaré modes greater than $n = 1$ are evanescent. A more irregular pattern is produced combining the Kelvin wave and a sinusoidal first-mode Poincaré wave (as described by Brown 1973).

4. When, with Platzman* (1970), we consider a <u>forced</u> wave of given period P_f entering a channel of given width from an external "ocean," that channel cannot act as a waveguide for a wave of that period, if the P_f, b point falls to the left of curve $n = 1$. The wave would become evanescent in the channel and therefore could not propagate along it. Taking a specific example of an internal wave of 12 h period maintained by tidal forcing, entering a channel of 20 km width, and with P_i and c_i as in Figure 16, the wave could propagate as a first Poincaré mode, with appropriate adjustment of Θ and r in earlier equations to accommodate the fixed forced frequency. But, in this example, propagation in the form of higher Poincaré modes could not occur. And further, in a channel of 120 km width, the first nine Poincaré modes could propagate at this frequency, but higher modes could not.

---

*When comparing Platzman's treatment with present discussion, note that his along-channel and cross-channel wavenumber are k and l, respectively, i.e., the opposite convention to that adopted here.

5. The behavior of free internal waves, arising as a result of a disturbance within the channel (or basin) is not so clear and is, indeed, the principal subject of discussion in this report. We may suppose that the disturbance will generate forced waves with a range of frequencies, and we may expect that those which coincide with one or more of the free modes of the channel (or basin) will be preferentially selected by resonance. For a given channel width, we may therefore expect to see P_p, b points lying on one or more of the unbroken curves, or a little to the right of them if r is greater than zero. In that case a combination of propagating Poincaré modes would be excited, some more strongly than others, depending upon the frequency structure of the originating disturbance. This hypothesis has received some confirmation (some of which is presented here) from observations in large lakes; but further tests are needed to distinguish between the free baroclinic responses, modelled as whole-basin Kelvin- and Poincaré-type responses to wind impulses (usually excitation of the lowest modes is observed) and the local intermittent responses which approximate to pure inertial motion described in an earlier section.

2.9 Closed-basin model results compared with those given by combinations of channel-wave components.

The heuristic advantages of the above-described approach to modelling of baroclinic responses, i.e. the assembly of Kelvin and Poincaré channel-wave components, is offset by the fact that neither of those components alone provide exact solutions for closed basin cases. This is because the along-channel current component in "standing" Kelvin or Poincaré (Figure 11) wave cells does not fall to zero at the cell end-walls, although that component is very small for Poincaré waves fitted to the large stratified basin considered here (Mortimer 1971). As already noted, satisfaction of solid endwall (i.e. closed basin) boundary conditions (classical theory, Taylor 1920, Dantzig and Lauwerier 1960) requires particular combinations of a Kelvin wave and an infinite set of evanescent Poincaré modes.

This complicated combination of analytical models is avoided, and an identical result is obtained by direct calculation of the structure and frequencies of the normal modes of basins, as pioneered for barotropic cases by Rao and Schwab (1976); but extension to baroclinic cases is at present restricted to two-layered model basins of uniform depth. With rotation rates and dimensions fitted to Great Lakes examples, the frequencies and structures of the free baroclinic (two-layered) modes have been computed for rectangular basins by Rao (1977) and for a Lake Ontario model of irregular plan but uniform depth by Schwab (1977). The free modes fall into two distinct sets, analogous to the two components discussed above, namely a set of Kelvin-like modes of frequencies much less than f, and Poincaré-like modes with frequencies near to but greater than f. Schwab (1977) compares the Kelvin-like and Poincaré-like basin modes

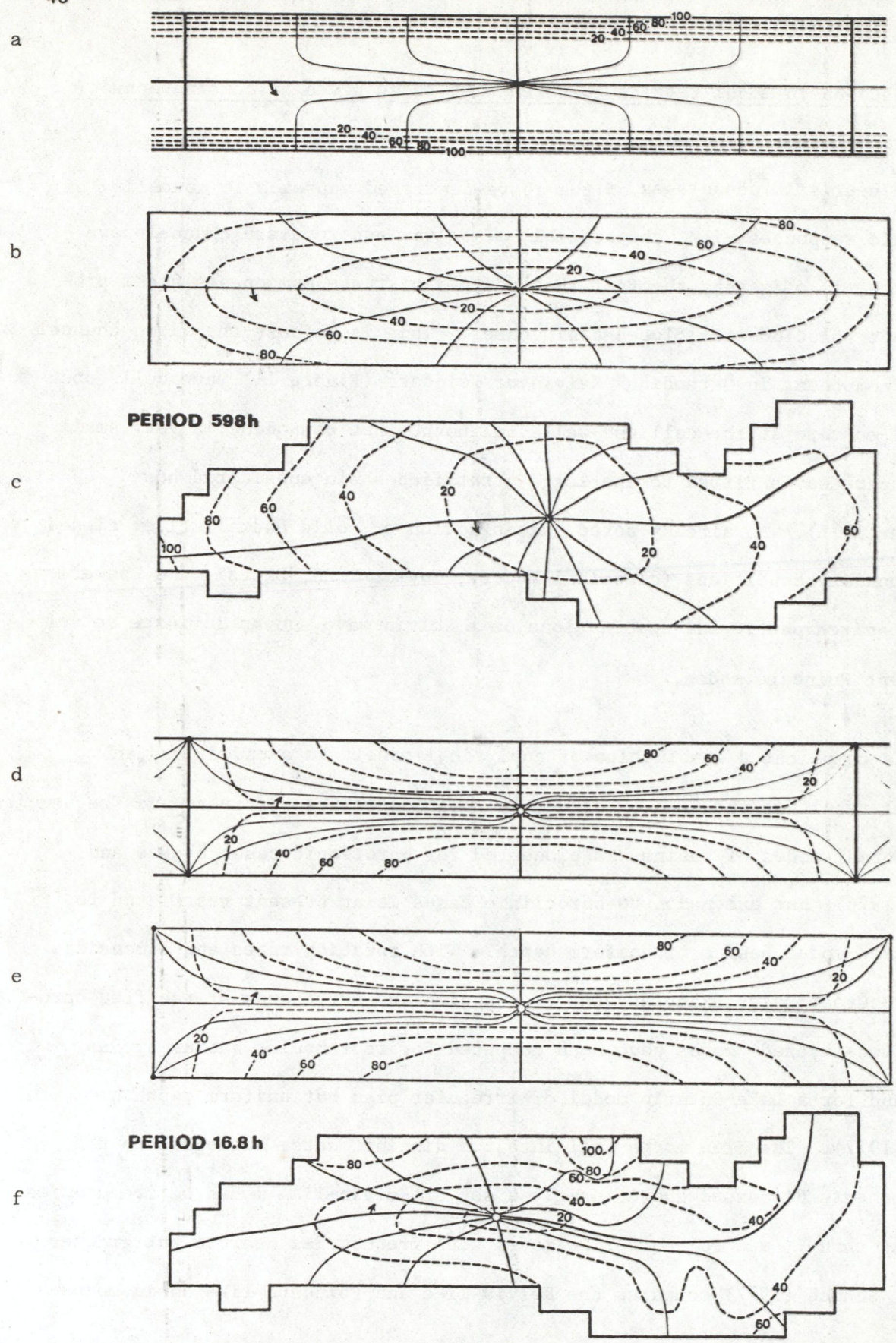

Figure 17. Legend on facing page, 47.

with their respective channel counterparts. Those comparisons are illustrated in Figure 17. The Kelvin-like basin mode exhibits a cyclonic phase progression as do its infinite channel and rectangular basin counterparts; but the distribution of wave amplitude differs, particularly near the basin ends and the frequency is decreased in the Ontario model. On the other hand, the lowest near-inertial Poincaré-type basin mode in the Ontario model is remarkably similar in amplitude distribution and anticyclonic (clockwise in N hemisphere) phase progression to the channel and rectangular basin equivalents; and the calculated period is close to that observed in cases of first-mode dominance, described later in this report.

Only the first Kelvin-type and Poincaré-type modes with n = 1 amphidromic points are shown in Figure 17. Schwab's model also discloses higher Kelvin modes with wavelengths and periods which are approximately simple fractions (1/2 for n = 2, 1/3 for n = 3, etc.) of those shown in Figure 17c. The n = 2 and n = 3 cases, with 2 and 3 amphidromic points, are illustrated in Schwab's paper. Also illustrated are the structures of the 2nd. and 3rd. along-basin Poincaré-type modes (also with 2 and 3 amphidromic points respectively). Their respective periods (16.7 and 16.6 h) differ little from 16.8 h calculated for the first mode. Structures of cross-basin modes higher than n = 1 were not illustrated.

Figure 17. See facing page, 46.

Free internal wave modes of Kelvin-type (a, b, c) and Poincaré-type (d, e, f) in two-layered models fitted to the dimensions and average density distribution observed in stratified Lake Ontario, calculated by Schwab (1977). Amplitude distributions (% of max) are shown by broken lines; phase progressions are shown by unbroken lines (at 30° increments, with 0° marked by an arrow indicating propagation direction). The first (i.e., lowest) cross-channel modes are shown for the following cases: an infinitely long channel (a, d); a rectangular basin (b, e); and a Lake Ontario model (c, f) with two layers of uniform equilibrium depth. Cases b and e were calculated but not published by Schwab (1977) and are included here with his permission.

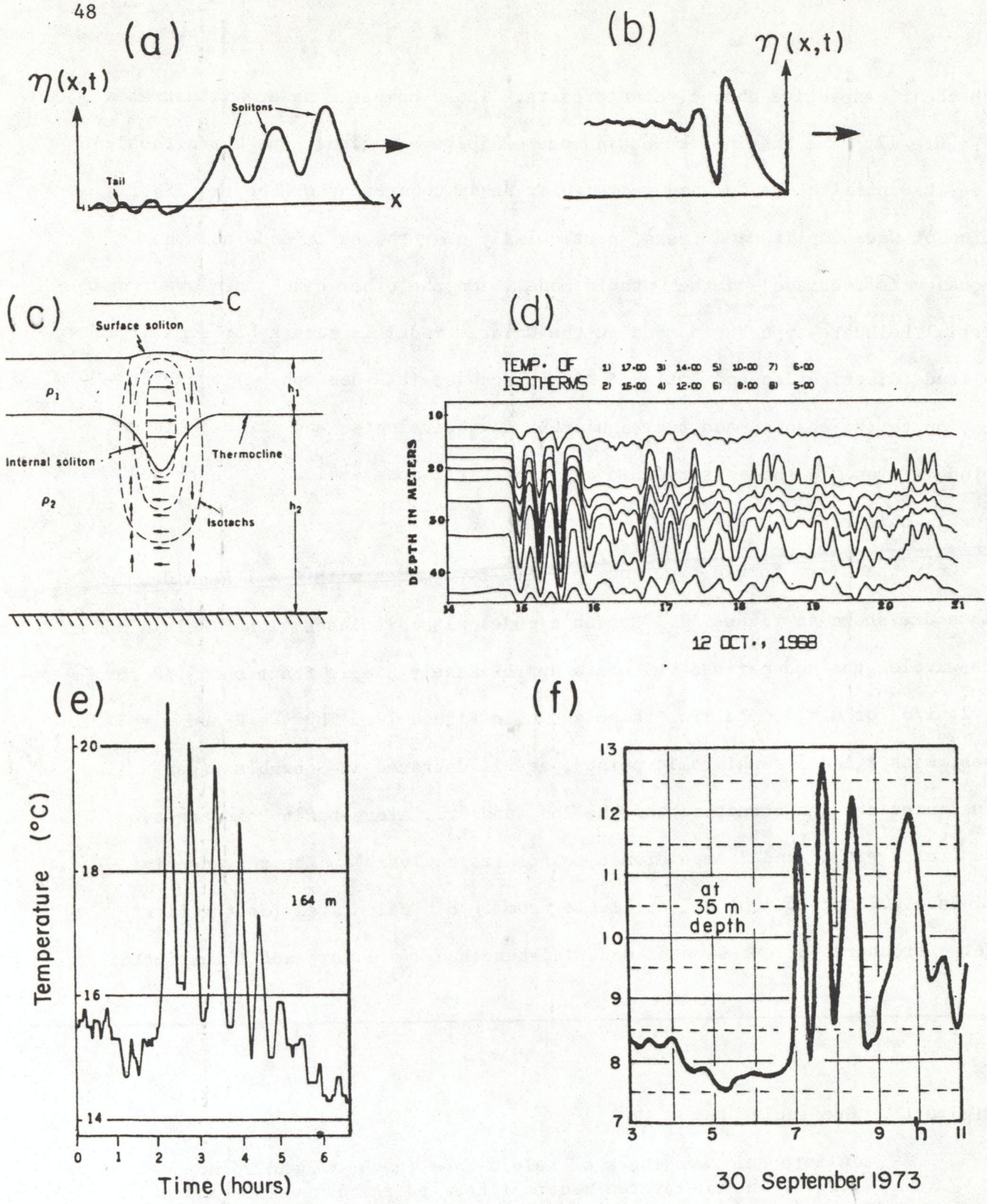

Figure 18. Models and observed examples of non-linear solitary waves (solitons) described in the text: surface and internal soliton modes (a, c,*); a surface soliton with friction (b,**); internal solitary waves observed in Seneca Lake (d,**); Andaman Sea (e,*) and Loch Ness (redrawn from Thorpe 1977).
*Osborne and Burch (1980). **Hunkins and Fliegel (1973).

2.10 Non-linear waves (solitons) described by the equation of Korteweg and de Vries.

The channel waves considered in earlier sections are, by definition, purely harmonic and are described by linear theory, which provides acceptable models of observed waves as long as their amplitudes are small compared with channel (or layer) depth. However that assumption often does not hold in the case of internal waves generated by large-scale upwelling and downwelling of the thermocline near shore, where the vertical excursion may be a large fraction of the water depth. The non-linear character of internal Kelvin waves, for example, has been treated by Bennett (1973). In general, large-amplitude internal waves assume non-linear characteristics which, if the wave length scale is large compared with layer depth and the upper-layer thickness less than that of the lower layer, are adequately described by the well-known Korteweg de Vries (K de V) equation (Osborne and Burch 1980). Examples are illustrated in Figure 18.

It has long been known that a localized elevation of the water surface or localized depression of a thermocline in a channel leads to the formation of solitary waves, on the surface or on the interface respectively, which are non-sinusoidal and non-linear in character. In 1965, Zabusky and Kruskal conducted a computer experiment in which two long K de V waves were made to collide. The result was unexpected in that, after collision, the individual waves retained their shape and propagation speed. This behaviour, reminiscent of that of elementary particles, earned these solitary waves the appellation "soliton." Subsequently the properties of surface and internal solitons were investigated, respectively, by Gardner et al. (1967) and Osborne and Burch (1980, whose treatment I have followed here with appropriate symbol changes). The latter authors describe and analyze a remarkable phenomenon involving tidally-generated internal solitons in the Andaman Sea (Fig. 18e) rendered visible in satellite

photographs because of interaction of local surface waves with the soliton-induced currents. Satellite photographs, suggesting a similar interpretation, have been obtained over Lake Superior (Bert Bennett, Canada Centre for Inland Waters, personal communication).

In a stable configuration, a surface K de V solitary wave in water depth h has the form:

$$\eta(x,t) = \eta_0 \operatorname{sech}^2[(x - ct)/L] \qquad (13)$$

in which η_0 is the maximum amplitude, the phase speed c is $c_0(1 + \eta_0/2h)$, and $L = \sqrt{4h^3/3\eta_0}$, the characteristic length. It should be noted that the phase speed varies with amplitude and is greater than c_0 defined earlier as $\sqrt{gh}$. Gardner et al. (1967) investigated the conditions under which a sufficiently localized elevation of the water surface evolves into one or more soliton waves (solitons) followed by a "tail" of dispersive waves (Fig. 18a). The rules governing this evolution of K de V waves in a channel of constant rectangular cross-section have been summarized by Hammack and Segur (1974) and by Osborne and Burch (1980). The essential conclusions, for the purposes of present discussion, are the following:

(a) Only when the initial wave form or portions of it are positive, do solitons evolve. Depressions of the water surface produce no solitons, only the "tail" of linear dispersive waves. Applied to internal solitons (Fig. 18c), with which we are here exclusively concerned, this rule states that internal solitons can only evolve from a depression of the thermocline, i.e., in a downwelling, but not in an upwelling region;

(b) As noted above, the soliton phase speed exceeds that of the associated linear wave by an amount which increases with wave amplitude. Therefore the largest and fastest-travelling solitons emerge at the head

of their group, creating a distinct front (Fig. 18a).

(c) The number of emerging solitons and their amplitudes (and therefore phase speeds) can be calculated (Osborne and Burch 1980); and the separation distance between them at any instant is therefore a measure of the distance travelled from their common source.

If the length scale of an internal soliton in a two layered channel is large compared with the upper layer depth, and if (as is usually the case) the lower layer is thicker than the upper layer, equation (13) is an adequate description of the waveform, and (following the notation of Figure 18c) c and L in that equation may be written (in a form equivalent to equations 15 and 16 of Osborne and Burch 1980) as follows:

phase speed, $$c = c_i(1 + \eta_0(h_2 - h_1)/2h_2h_1) \tag{14}$$

length scale, $$L = \frac{2h_1h_2}{[3\eta_0(h_2 - h_1)]^{\frac{1}{2}}} \tag{15}$$

in which

$$c_i^2 = \frac{g(\rho_2 - \rho_1)}{\rho_2} \qquad \frac{h_1,h_2}{h_1 + h_2} = \text{"reduced gravity" x "reduced depth"} \tag{16}$$

i.e., c_i is the phase speed of the equivalent linear wave in the same two-layered (non-rotating) channel. Equation (14) predicts that, if $h_2 > h_1$ (a condition for the validity of the K de V equation, according to Osborne and Burch 1980) the phase speed of the non-linear wave depends on its amplitude η_0 and is also sensitive to the value of $(h_2 - h_1)$.

Internal surges have been often observed in lakes (examples in Mortimer 1979) and, where these have been studied in detail, they are seen to be traveling away from regions of thermocline depression and often accompanied

by undulations in isotherm depth (or temperature) which follow a relatively abrupt front marked by suddenly rising temperature (example in Fig. 18f) or falling isotherms (Fig. 18d). This behavior suggests internal solitons as an explanation, particularly such as "organized" undulations always appear to be associated with a wave of thermocline depression. In Seneca Lake, deep at the southern end shallow at the north end, the surge (Fig. 18d) travels only from S to N, i.e. it is not reflected from the shallow end. In Loch Ness (Fig. 18f) it is "reflected" at the basin end, but the undulations disappear, and the front returns as a sudden temperature rise only (Thorpe 1977). At mid-lake stations, the surge passes and re-passes (Mortimer 1979) at regular intervals which correspond to the first mode internal seiche period (57h). This behavior may not, however, be the result of true reflection, but rather a consequence of the fact that the repeated downward swings of the thermocline are large at both ends of the basin, so that a surge is generated anew at each swing, as long as the seiche amplitude remains large enough.

The surge propagation speeds observed by Hunkins and Fliegel (1973) ranged between 35 and 40 cm s^{-1}; and equation (14) would predict an 11% increase in phase speed (above that of the equivalent linear wave) if η_0 is 5 m and the following representative values are estimated from illustrations in the authors' paper: t_1 17°C; t_2 6°; h_1 20 m; h_2 150 m; length of thermocline Talweg 50 km. The linear phase speed c_i, corresponding to these values is 40 cm s^{-1}. So the Seneca surge does not appear to travel faster in this case and may even travel slower. This result, particularly if it is confirmed by observations in other lakes, calls for a re-examination of the theory on which equation (14) is based.

It must also be remembered that the K de V equation as treated by Osborne and Burch (1980) neglects the effect of friction. When this is considered, the pattern of the front changes from the periodic form 18(a) to form

18(b) in which the solitons are suppressed as damping is increased (Kadomtsev and Karpman 1971, from which Hunkins and Fliegel took Fig. 18b). It appears likely therefore that the K de V equation as modified by Burgers may more appropriately describe internal surge fronts in lakes, perhaps in a form in which the frictional damping is small enough to permit a small number of soliton-like undulations to develop. The damping must have been very low in the oceanic case (Fig. 18e). Also it should be noted that solitons may appear under certain conditions when an internal wave moves from deep water onto a shelf (Djordjevic and Fedekopp 1978). Solitons formed in this way propagate away from the shelf.

Travelling temperature fronts have also been seen in the Great Lakes during the stratified season following downwelling events brought about by strong wind impulses. In all the Lake Ontario examples (Mortimer 1977, Figs. 58 to 63, and further examples described later in the present report) the initiating downwelling events occurred along the elongated, steep southern shore after the passage of strong eastward-directed wind impulses. Separating from the shore and propagating northwards at speeds consistent with equation (14) the fronts exhibit internal surge-like features and are repeatedly generated at near-inertial intervals, which suggests that the earth's rotation, as expressed in near-inertial oscillations in thermocline depth, plays an important part in their generation. In common with internal solitons, these surges are only seen propagating away from regions of strong downwelling (thermocline depression), never from upwelling regions of thermocline elevation. Simons (1978) has explored the relationship between these downwelling-generated surges and the near-inertial and quasi-geostrophic responses of nearshore stratified waters to wind forcing. He has developed a two-layer extension of Cahn's (1945) model of geostrophic adjustment and the more recent applications of Houghton (1969) and Crépon (1967) which deal resepectively with non-linear

effects and nearshore wind forcing. Simons obtained analytical and numerical solutions for the response of the two-layered model to a wind impulse of finite duration and showed that non-linear effects leading to internal surges could occur "without invoking excessive wind speeds." Numerical simulations, carried out for Lake Ontario conditions, showed satisfactory agreement with the behavior of the observed surges (Mortimer 1977) permitting the conclusion that the basic dynamics of that behavior can be explained by the non-linear wave properties of the model.

> "The recurrence of the front after an inertial period and the proper phase relationship between thermocline deflections and inertial currents, confirm that the observed downwelling fronts are intimately connected with the oscillatory action of the inertial motion in deep water. Thus, while less detailed observations of similar temperature distributions could easily be interpreted as manifestations of baroclinic jets, the fronts are to be visualized as part of the oscillatory rather than the quasi-geostrophic response of the Lake to wind. Although disturbances from the opposite upwelling shore may eventually combine with those from the downwelling shore to create standing Poincaré waves (Mortimer, 1977), the scale of the frontal zone is sufficiently small that it can be treated independently of this effect. Thus, similar phenomena can be expected to occur in any near-shore region for suitable stratification conditions."

3. PRESENTATION AND ANALYSIS OF WIND, CURRENT, AND TEMPERATURE OBSERVATIONS.

The main objective of this report is to compare the motions observed during the season of stratification in Lakes Michigan and Ontario and their responses to wind stress with the predictions of the simple, linear models of Poincaré and inertial oscillations described in Section 2. Anticipated responses are (i) approximations to whole-basin Poincaré-type internal seiches with discrete mode frequencies greater than but not far removed from f, and (ii) approximations to pure inertial oscillations of frequency f. Although both types of response have been previously recognized in Lake Ontario (Mortimer 1977), their separate identification on the basis of frequency and spatial coherence has proved difficult, because they often occur together and because the frequency separation of inertial oscillations and Poincaré-type modes is so small that conventional (power) spectral analysis fails to resolve discrete frequencies within that narrow, near-f spectral region which contains most of the energy. It was hoped that, because Lake Ontario is narrower than Lake Michigan, the somewhat greater frequency separation between Poincaré-type modes in the former basin (see Fig. 15) would make spectral resolution easier; but even those spectral techniques, which provide maximum resolution for relatively short time series, yielded disappointing results (Marmorino and Mortimer 1978). That publication should be consulted for a detailed discussion of methods and the precautions to be observed in applying them.

For example, maximum entropy spectral analysis (MESA) performed reasonably well in resolving four equal-amplitude sine waves of 14, 15, 16, and 17 h period in a 200 h-long record (Figs. 5-7 in Marmorino and Mortimer 1978) and in separating a near-inertial and a 15 h component (presumed Poincaré-type modes 1 and 5, Fig. 8 in that report) in a 5-day record of a relatively simple episode in Lake Michigan, but the application of MESA to 12 consecutive 5-day

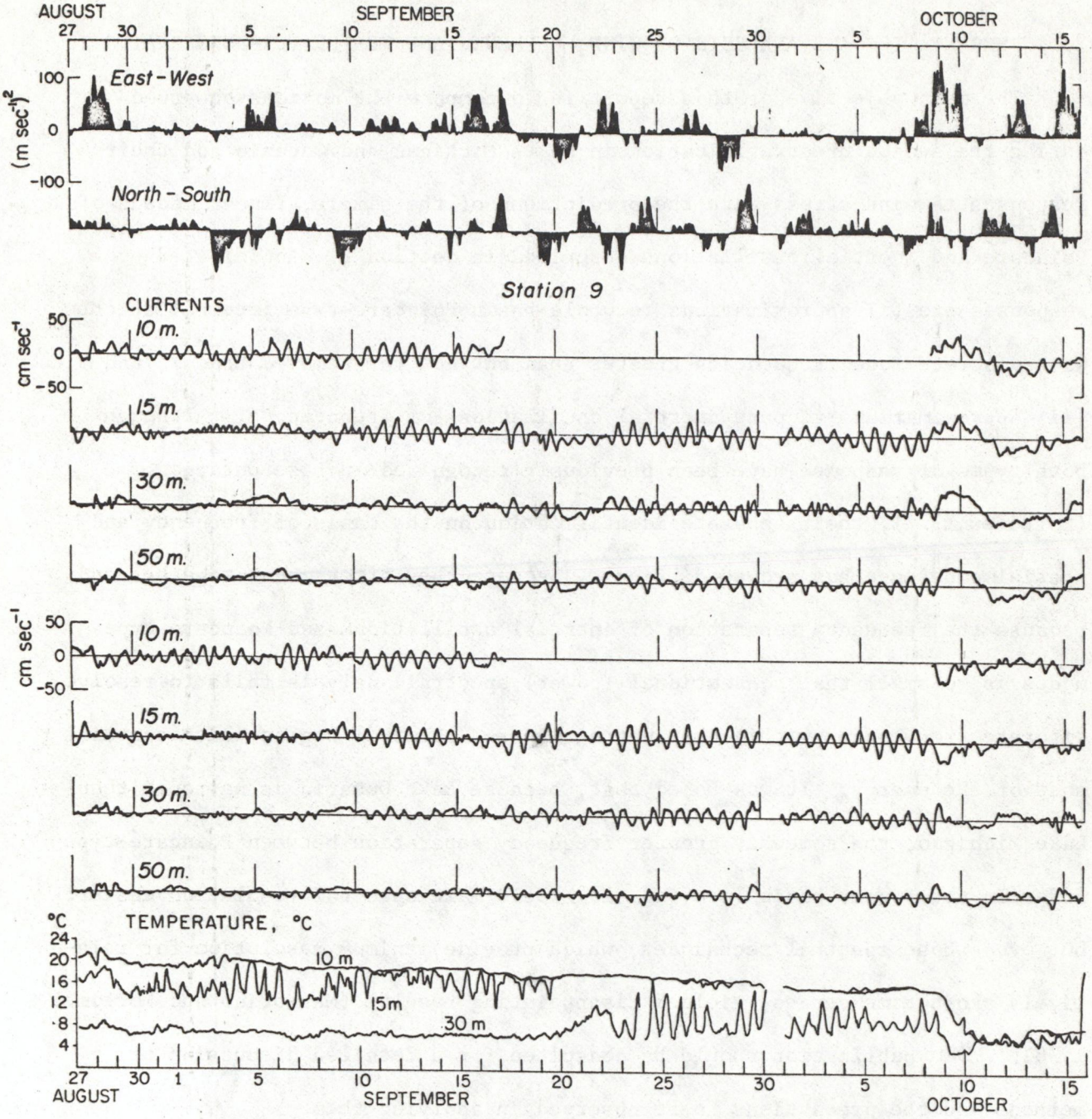

Figure 19. Wind components squared and components of current (upper set, east-west; lower set, north-south) at four depths and temperature at three depths at Station 9, Lake Ontario, 27 Aug. - 16 Oct., 1972.

sections of current records from Lake Ontario station 10 (IFYGL 1972) did not separate individual components (if present) in the large near-inertial peak (Fig. 15 of that report). The degree of resolution of MESA can be controlled by the user; but if it is increased beyond a certain limit, new peaks appear alongside or between those seen at lower resolutions, and there is no assurance that the new peaks are not spurious. Although MESA merits further exploration with longer time series, it apparently cannot give much assistance in the analysis of the short, episodic responses commonly seen in Lakes Michigan and Ontario after changes in force and direction of the wind and usually lasting not more than five days, before a fresh disturbance arrives on the scene.

The intermittent character of those responses is illustrated in Figure 19, in which the EW and NS components of squared wind-speed and the EW and NS components of current at four depths are displayed along with temperature at three depths, on a common time scale, for station 9 (Lake Ontario, IFYGL Sept.-Oct. 1972, see later Fig. 29 for position). Comparable figures for station 10, July-Aug. 1972, were presented by Marmorino and Mortimer (1978, Figs. 10 and 11). Wind speed squared, approximately proportional to wind stress on the wind surface, is used as a measure of the strength of the wind impulses in this and most of the later figures; but for some episodes stress is calculated in dyn cm^{-2} using the formula of Hamblin and Elder (1973).

Strong responses at near-inertial frequency are seen in Figure 19, particularly after strong, short wind impulses, for example on 10 and 23 September; but during the strong storm of relatively long duration (8-9 October) the inertial response was small and overshadowed by a steadier east-going current at all depths to 50 m. This behavior, and the weak inertial response to the long-lasting storm on 27-28 August, support the predictions of Pollard's model (Table 1, p. 8 in Section 2). The figure also shows that inertial currents

are stronger in the upper layer (10 m or 15 m) than below the thermocline (50 m) and also (although difficult to see on this scale) that the NS current component leads the EW component by about 90° (clockwise rotation of the current vector) and that the current at 10 m (or 15 m), above the thermocline, is generally in phase opposition to that at 50 m, below the thermocline. The energy in the near-inertial responses is obviously not entirely in kinetic form (as currents), as would be the case in pure inertial motion; some appears in potential form (as internal waves of near-inertial frequency concentrated in the thermocline).

3.1 Subjective fitting of an "average period band" (APB) to selected portions of record.

Because MESA could not be counted on to resolve the individual frequencies of inertial oscillations and Poincaré-type modes (if present), and because that method apparently requires considerable caution in its use, I had to fall back on the subjective and tedious technique of period-fitting to current and temperature records from individual episodes, usually selected to contain a wind impulse followed by calmer weather. As illustrated later, this period-fitting to the IFYGL episodes was carried out with transparent overlays (analogous to diffraction gratings) with vertical rulings corresponding to the local inertial period and to the periods of the first three Poincaré modes calculated for a two-layered channel model fitted to the average layer dimensions and density distribution during the stratified season. If an average P_i for Lake Ontario is taken as 17.4 h (it is 17.35 h at Lat. 43° 36') and b is taken as 60 km, and if the seasonal range of c_i is 40 to 50 cm s^{-1}, the channel-wave model (Fig. 15) predicts Poincaré period ranges of: 17.1 to 16.9 h (1st. mode); 16.1 to 15.4 h (2nd. mode) and 14.8 to 13.7 h (3rd. cross-channel mode). Adopting an average value of c_i = 43 cm s^{-1}, transparent ruled gratings were prepared for the following periods: 17.4 h (inertial) and 17.0, 15.8 and 14.4 approximating to the

periods calculated for the first three Poincaré modes. As it was also found by inspection that some IFYGL records showed a better period-fit with 16.5 h than with 17.0 or 15.8 h, a grating with 16.5 h ruling was added, making a set of five gratings in all. A 13 h (4th. mode?) grating was also prepared, but was only used once. In some instances, a 16 h grating (3 cycles in 2 days) was found to be convenient, but in practice is indistinguishable from the 15.8 h grating.

It will become obvious in many later examples that the precision of this method is rarely better than ± 0.2 h and that it is less for shorter episodes. Nevertheless the period-separation, indicated in the previous paragraph, between Ontario modes even when c_i ranges between 40 and 50 cm s^{-1} in Figure 15, promises the possibility of individual mode (or of inertial motion) identification during episodes in which that mode (or inertial motion) is dominant; and it will transpire later that a reasonable fit with one or other of the five gratings is achieved in the majority of the IFYGL episodes. Rare, shorter periodicities will be noted as they occur. But, to emphasize the approximate nature of the fit to an average period during an episode, the five gratings are taken to represent period bands with a spread of about ± 0.2 h, referred to as "average period bands" (APB).

In the case of Lake Michigan, Figure 15 shows that the period separation is considerably less than in the Lake Ontario case. Therefore, for analysis of records from the single station in section 4, the following gratings were ruled at 17.0, 16.5, 16.0 h intervals, in addition to 17.7 h corresponding to the local inertial period.

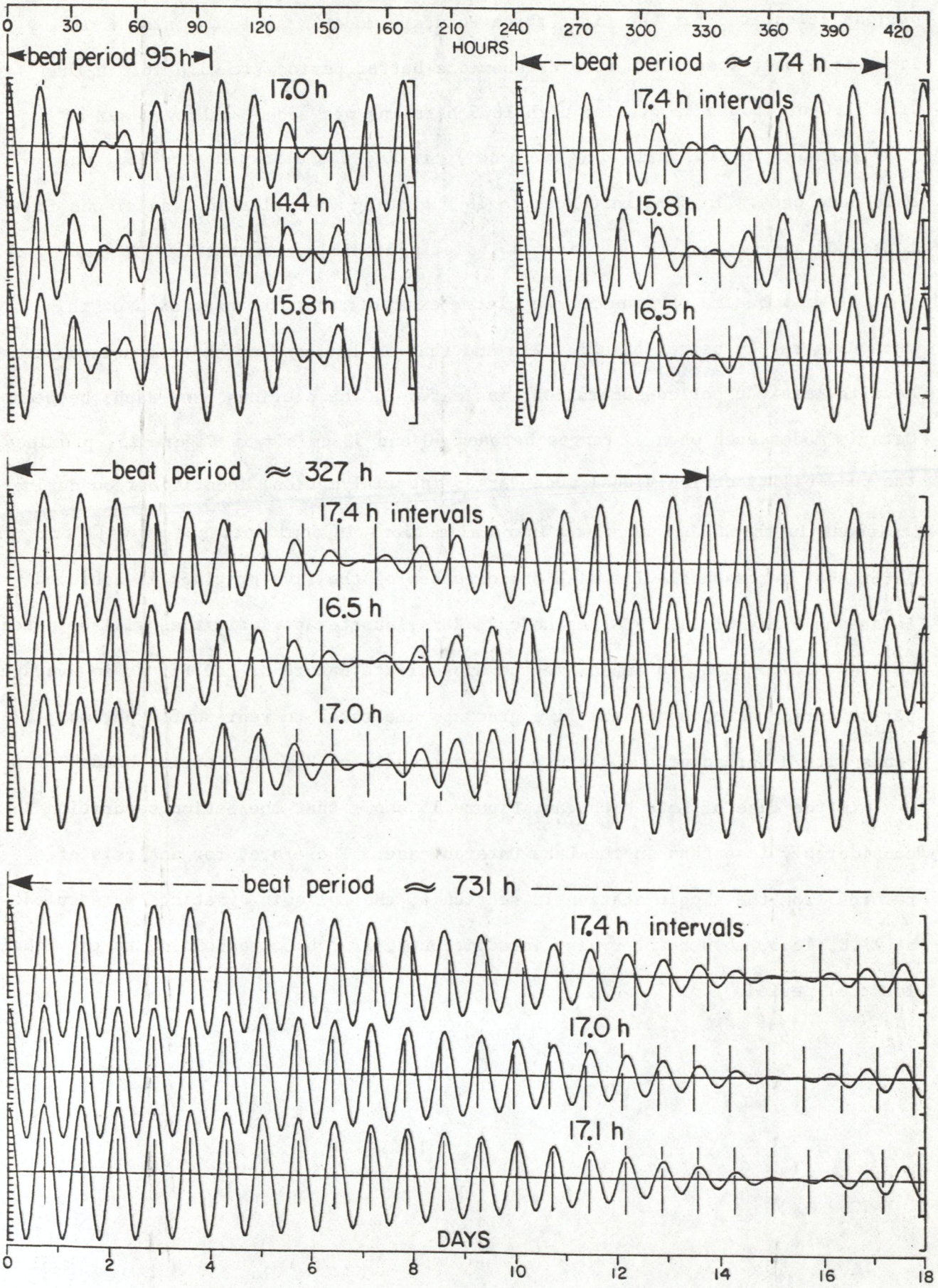

Figure 20. Legend on facing page, 61.

Further caution in the use of the gratings is prompted by examination of Figure 20, in which equal-amplitude sine waves, corresponding in period to the set of Ontario gratings referred to above, are combined in pairs to display beat oscillations. For each pair the pattern is repeated in three rows. On the top two rows are superimposed vertical rulings corresponding in period to the two components of the pair. To the bottom row is fitted one of the Ontario gratings as average period (APB) by eye, exactly as done for real records in later sections. Not surprisingly, the periods of the best-fitting APBs to the bottom rows lie between the periods of the sinusoid pairs; but more significant is the caution which Figure 20 engenders in the interpretation of amplitude and phase changes during episodes when two or more oscillation components may be present. There is, for example, a large phase change between the best-fit APB (bottom row) and the beat pattern on passing through the minimum; and in real episodes it may be difficult to distinguish between beat effects and between the effects of forcing and friction.

With the above cautions in mind, and because initially promising techniques of spectral and complex demodulation analysis show limited effectiveness in the analysis of short samples of record (Marmorino and Mortimer 1978), the remainder of this report explores the usefulness of the subjective period-fitting technique (coupled with the simple models described in section 2) in the interpretation of short episodes.

Figure 20. On facing page 60.

Beat patterns generated by combining pairs of equi-amplitude sinusoids of slightly differing period and with initial phase coincidence. Four examples are shown; and the beat pattern is repeated on three rows in each case. Vertical rulings fitted to the upper two rows correspond to the periods of the components selected for that case; and rulings on the bottom row represent the best fit (by eye) to the nearest "average period band" (APB) in the set constructed for fitting to IFYGL records in later figures, as explained in the text. The beat periods (i.e., intervals between recurring phase coincidences) are also indicated.

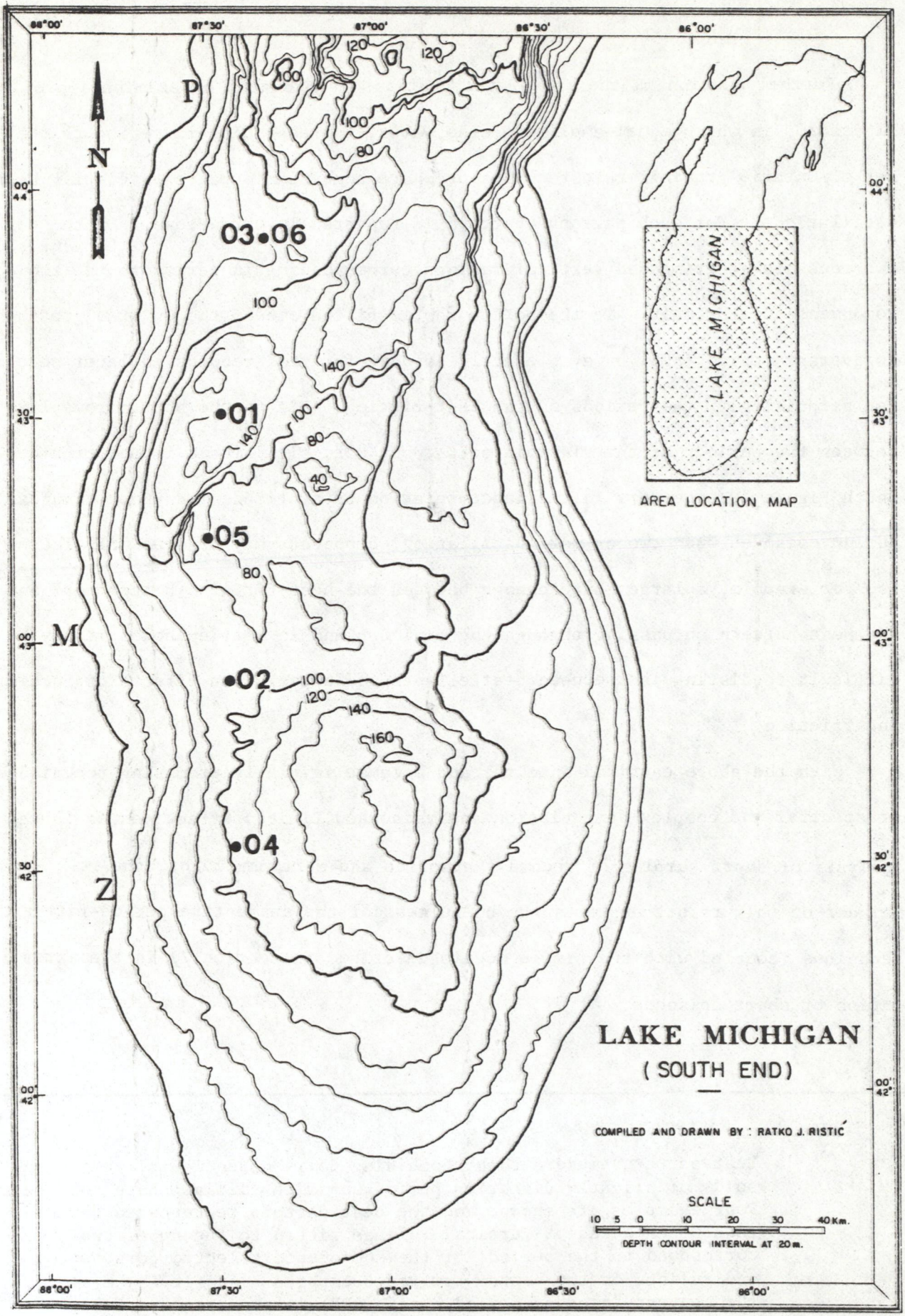

Fig. 21. Chart of Lake Michigan: positions of moored instruments, Aug. to Oct. 1976.

4. INERTIAL AND NEAR-INERTIAL RESPONSES TO WIND IMPULSES IN LAKE MICHIGAN, AUGUST TO OCTOBER 1976.

Figures 22 to 28 present consecutive 11-day sections of a series of current and temperature records from instruments moored 30 km E of Kenosha, Wisconsin (water depth 108 m, see Fig. 21) from 2 August to 11 October 1972. Contemporary wind records from a nearby anemometer on the shoreline at Zion, Illinois are also presented, as the NS and EW components of wind speed squared (upper panel), approximately proportional to wind stress. Current speed and direction was measured at 10 min intervals at 17 m depth, and the raw data is plotted in the second and third panels from the top. From hourly mean values of current speed and direction, the NS and EW components of the current were computed and plotted in the fourth panel. In the fifth panel are presented temperature data from 17 m (generally above the thermocline) and from 28 m (near the thermocline) and 33 and 38 m depth (below the thermocline). For selected episodes -- typically containing an initial wind impulse followed by calmer conditions -- a progressive vector diagram (PVD) was prepared (bottom panel) from the hourly means of current speed and direction. The PVD gives a useful indication of the current track, but as it is computed from measurements at a fixed point, its validity depends on how closely the recorder represents the current field in its neighborhood. It is unlikely, for example, that the westward drift often but not always seen in PVD's in these figures would persist into the nearshore region. That drift was probably part of a large and relatively persistent offshore eddy.

At the beginning of the record series (3-4 Aug., Fig. 22) a strong, regular inertial oscillation was in progress (mean speed about 45 cm s^{-1}) of period

---

Figure 22. See next page, 64.

Lake Michigan, 1976, station 04 (see Fig. 21); in descending order in the figure: NS and EW components of wind speed squared at Zion, Ill.; current direction and current speed at 17 m depth; NS and EW current components at 17 m; temperature at three depths; progressive vector diagram (PVD) for episode 1. Further details in the text.

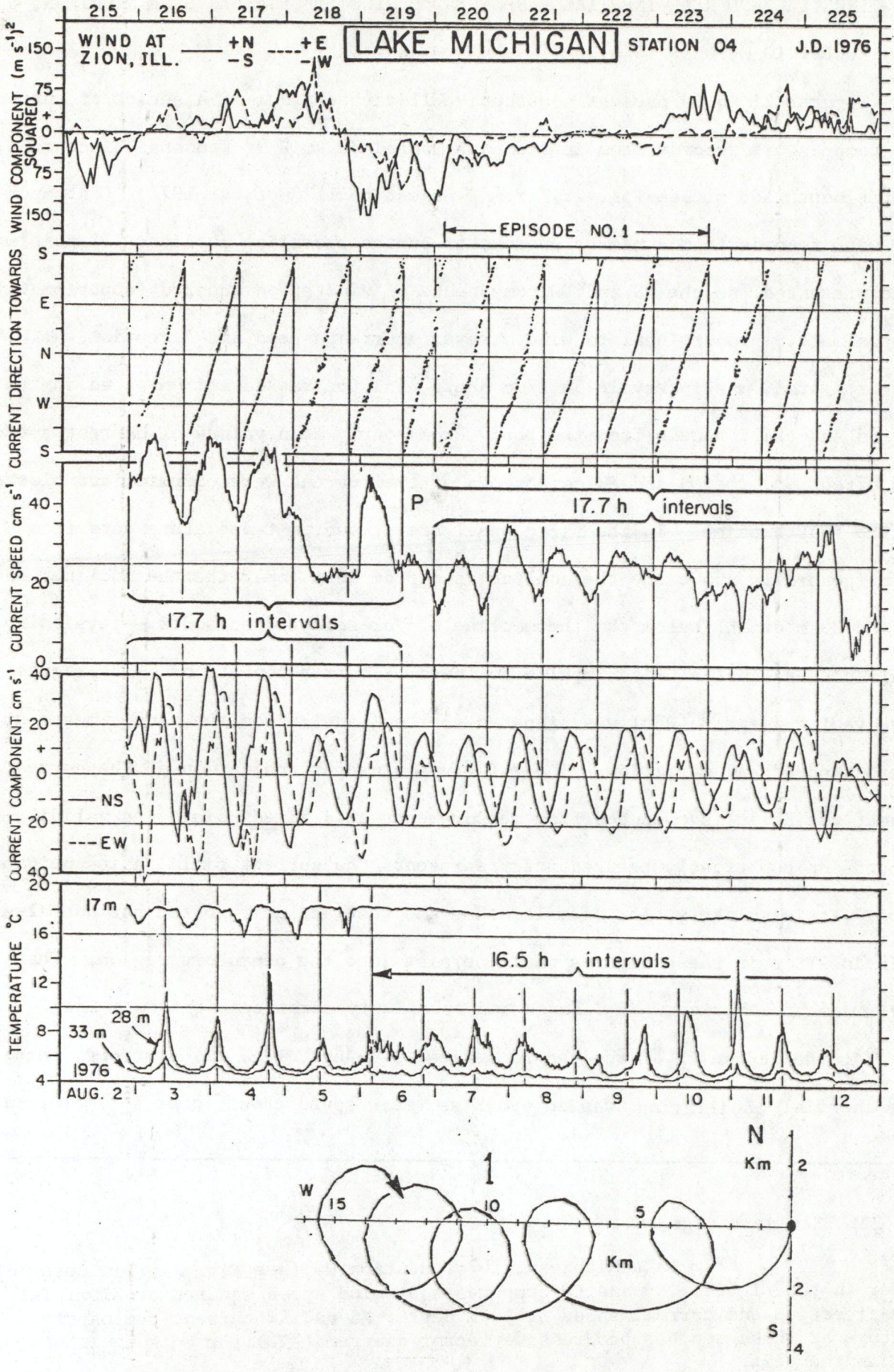

Figure 22. See legend at bottom of previous page, 63.

indistinguishable from the local inertial period (17.7 h) and modulated by the presence of a steadier current of about 10 cm s^{-1}, which produced speed maxima and minima in the directions NNW and SSE respectively. Probably disturbed by stronger wind impulses on 5-6 August, the current speed dropped to about half its previous mean value, and the regular phase progression of rotation was interrupted (P indicates phase change on 6 August). After the arrival of strong southgoing wind pulse, which peaked at midnight 6/7 August, there followed several days of relative calm (episode No. 1) marked by a very regular inertial oscillation (17.7 h APB, current speed about 20 cm s^{-1}) modulating a steadier westward current (averaging about 5 cm s^{-1}) to produce a looping PVD with a westward drift of about 15 km in five inertial cycles. In these examples, as in many others in Lake Michigan during the stratified season, the strongest currents were those arising from inertial or near-inertial oscillations; speeds of 30 cm s^{-1} were common, and 50 cm s^{-1} was occasionally attained.

Figure 22 and following figures illustrate another commonly observed feature. Whereas the current signal, expressing kinetic energy, displays a mean periodicity indistinguishable from inertial, the expression of potential energy (depth oscillations of the thermocline isotherms) is associated with a slightly but significantly shorter mean period, approximately 16.5 h in Figure 22. Bearing in mind (equation 9) that the ratio of kinetic to potential energy in the Sverdrup wave becomes very frequency-sensitive as the inertial frequency is approached, the oscillation illustrated in Figure 22 may be interpreted as a mixture of (i) a strong inertial response in the currents with little contribution at that frequency from thermocline waves, and (ii) a small-amplitude thermocline wave of shorter period (a higher Poincaré mode?) making little contribution to currents. That this is only one of several possible combinations is demonstrated by later examples.

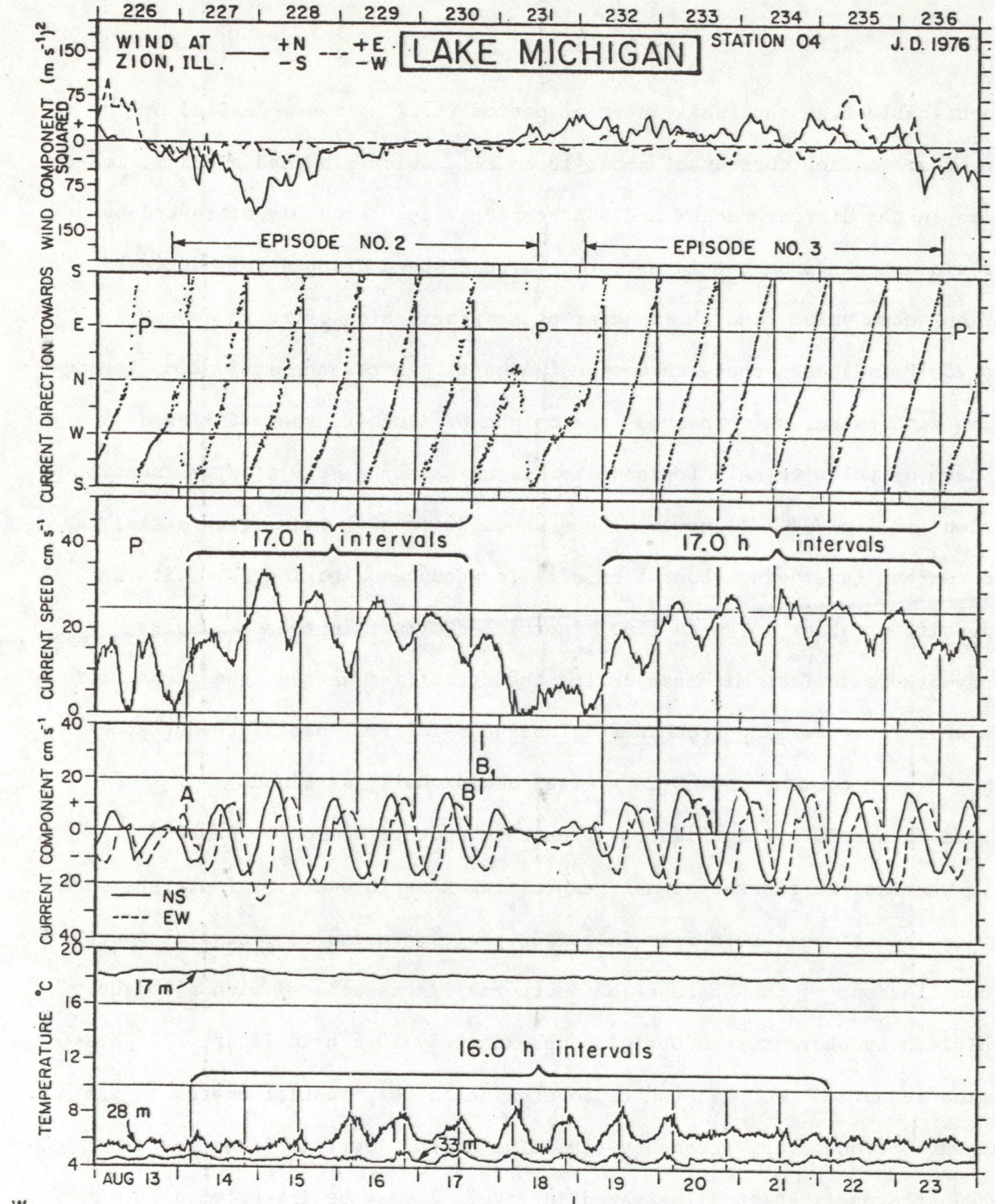

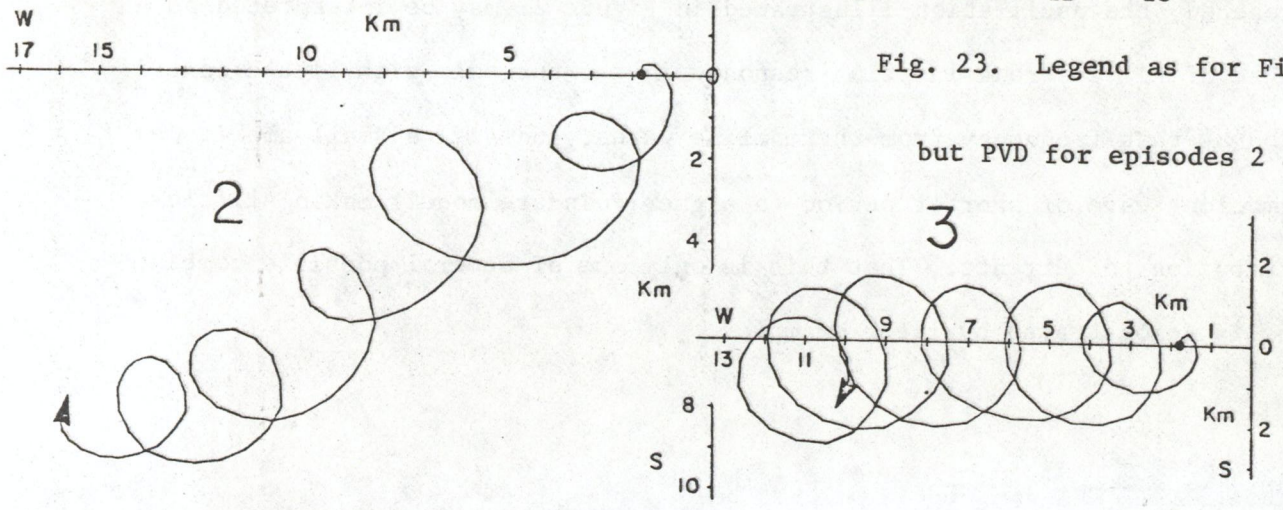

Fig. 23. Legend as for Fig. 22, but PVD for episodes 2 and 3.

Current patterns during the next two episodes, Figure 23, display a slightly but distinctly better fit to a 17.0 h periodicity than to the inertial period. (Compare distances AB and AB_1, corresponding to five cycles at 17.0 and 17.7 h, respectively.) A period of 17.0 is close to that predicted for the first Poincaré cross-channel mode, but there is no conspicuous thermocline oscillation of that period (comparable to that seen in episode 8, for example, in later Figure 26); the small-amplitude temperature oscillation observed in Figure 23 is a closer fit to 16 h. Episode 2, which combines a rotating component of about 20 cm s^{-1} speed and a SW-going drift of 5 cm s^{-1}, may be viewed as a response to the southgoing wind impulse on 14 August; but no strong impusle occurred to explain the phase change at P (18 Aug.) or the ensuing regular rotation during episode 3. This behavior could be the result of a beat interaction between two Poincaré modes of slightly differing periods or between a single Poincaré mode and inertial motion proper. In any case, the pattern displayed by the current components in Figure 23 is similar to the beat pattern illustrated at top right in Figure 20.

Current patterns during episode 4 (Fig. 24) also fit a 17.0 h periodicity, although the precision of fit is low for so short a sample; and the same is true for the 17.7 h fit to the middle section of episode 5. The first half of episode 4 coincides with a short westgoing wind pulse on 24 August followed by two days of negligible wind and displays a very regular 17.0 h rotation of the current at about 30 cm s^{-1}. A thermocline oscillation was not seen, although one might have occurred within the depth interval 17 to 28 m, in which case it would not appear in the record. Apparently the stronger winds, commencing on 27 August and continuing through and beyond episode 5 to September 3rd, first reduced the strength of the rotating current to below 20 cm s^{-1} (27 Aug.), then increased it to a mean of 35 cm s^{-1} for two cycles (29-30 Aug.) and then

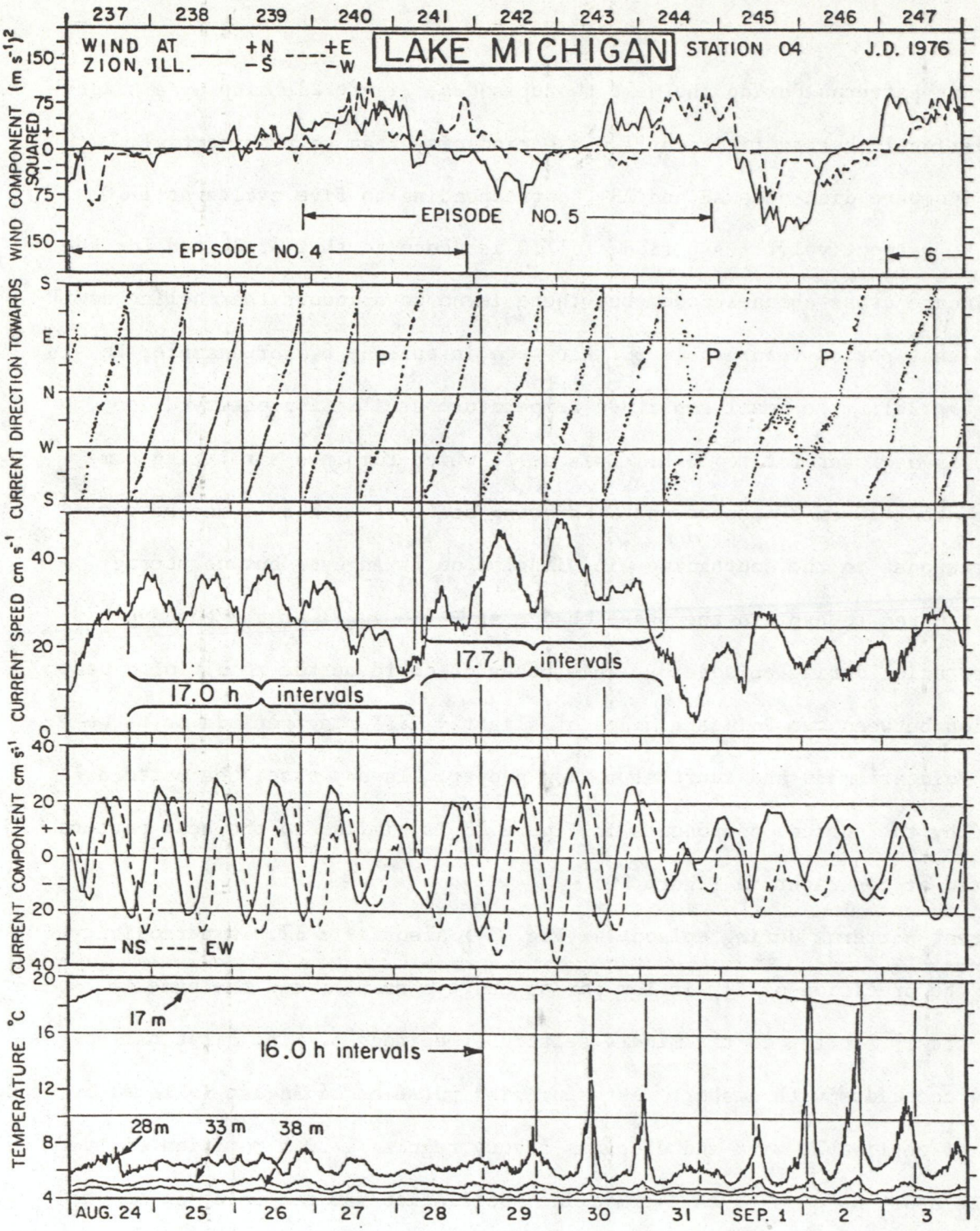

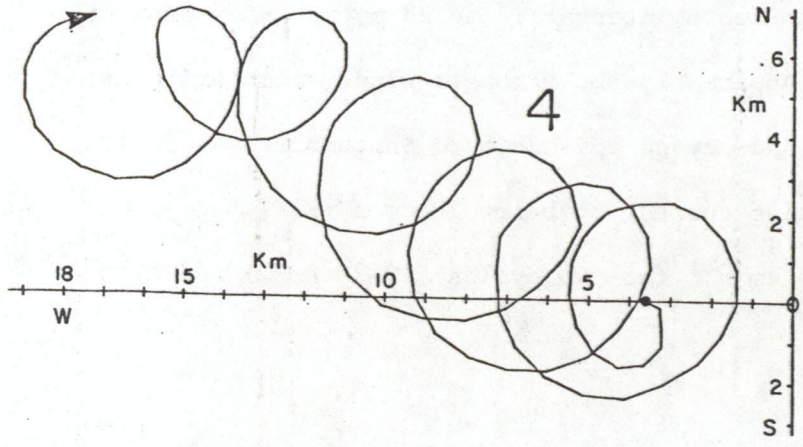

Fig. 24. Legend as for Fig. 22, but PVD for episode 4.

PVD for Episode 5 is inserted in Figure 28.

again reduced it to a mean of about 15 cm s^{-1} maintained for the following four days, in spite of the strong southgoing wind on 1 September. These details are mentioned to emphasize the complexity of the responses and the evident relationship, predicted by Pollard and Millard (1970), between the duration and timing of the wind impulses and their interactions with pre-existing current patterns. Compare, for example, what appears to have been a strong rotational response to the short (6 h) impulse on 24 August and the lack of response to a much stronger but longer (20 h) impulse on 1 September. Also note that, during the interval of marked variation in current speed and phase (29 Aug. to 3 Sept.) a regular thermocline oscillation persisted at about 16 h period, i.e., a distinctly shorter periodicity than that shown by the currents. In contrast to this behavior, episode 6 (Fig. 25) displays a periodicity indistinguishable from 17.7 h in current rotation and thermocline oscillation. A similar concurrence of a 17.7 h (inertial) APB in both current and temperature patterns is seen in episode 10 (later Fig. 28).

Episodes 6 and 7 (Fig. 25) show no unambiguous correlations with the strength or timing of wind impulses. Episode 6 -- four cycles of regular inertial oscillation (17.7 h) -- may owe its origin to changes in wind force and direction on 3 September. The speed of the rotational and drift components were 25 and 5 cm s^{-1}, respectively; and the corresponding PVD was contained within a relatively small region of about 9 km across. On the other hand, episode 7 (perhaps set in motion by a favorably-time sequence northward, eastward, and northward wind pulses starting on 8 Septmber) shows five cycles of very regular 17.0 h current rotation at high speeds (ca. 35 cm s^{-1}) bringing about a strong modulation of the westward drift, also illustrated in the PVD. During this episode the apparent period of the thermocline oscillations changed from near 17.7 to near 16.5 h, persisting at that periodicity until 15 September

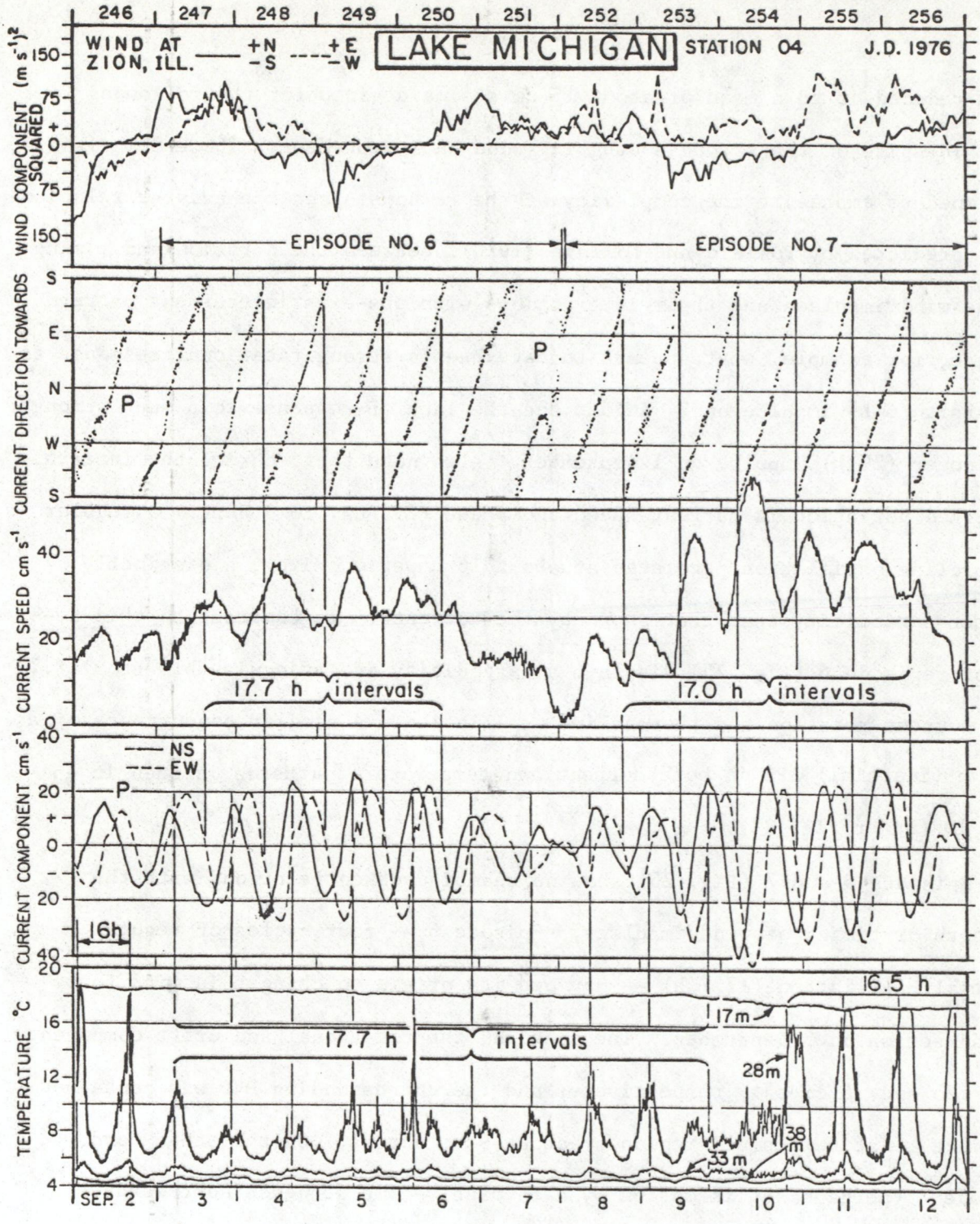

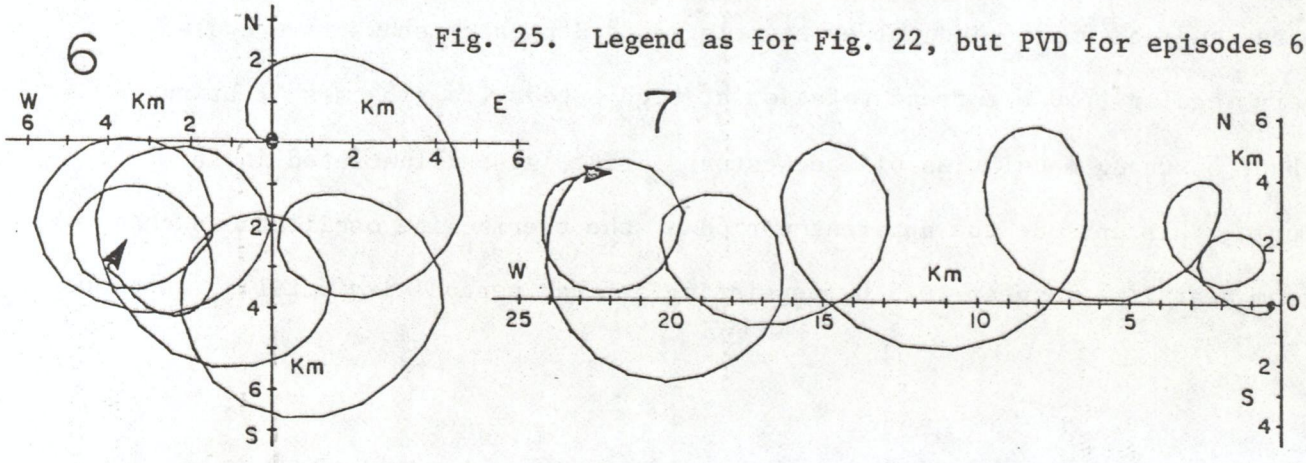

Fig. 25. Legend as for Fig. 22, but PVD for episodes 6 and 7.

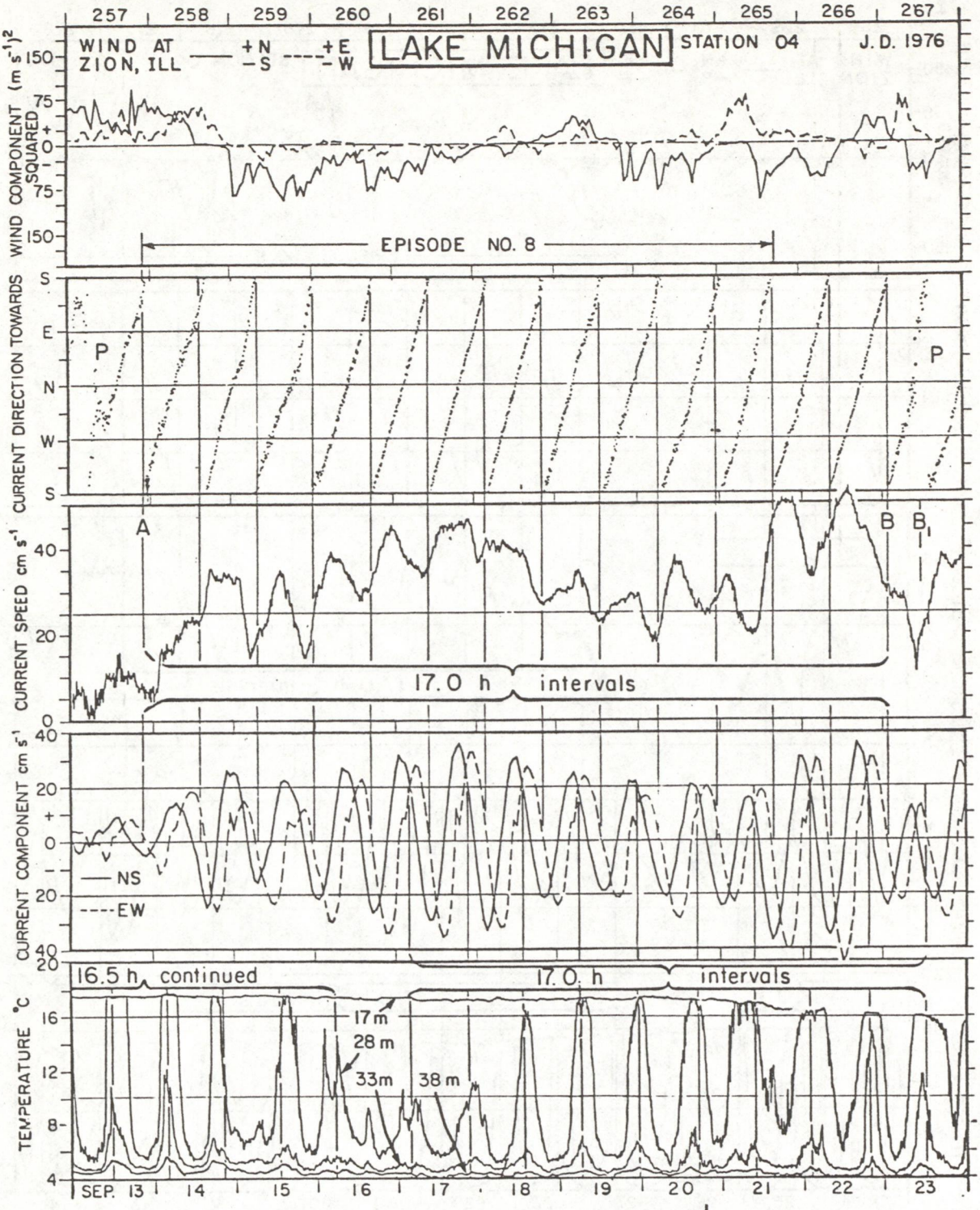

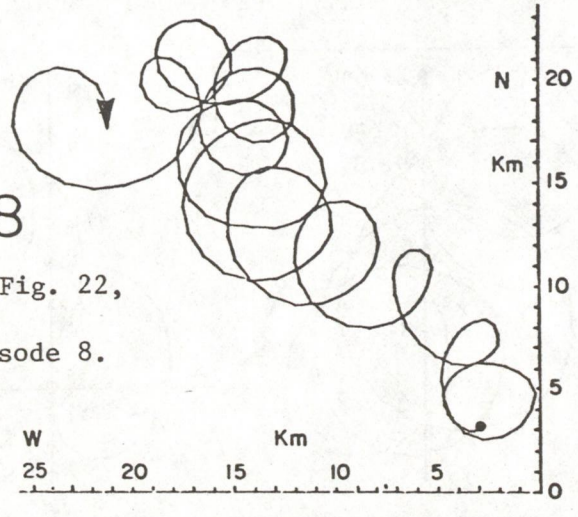

Fig. 26. Legend as for Fig. 22, but PVD for episode 8.

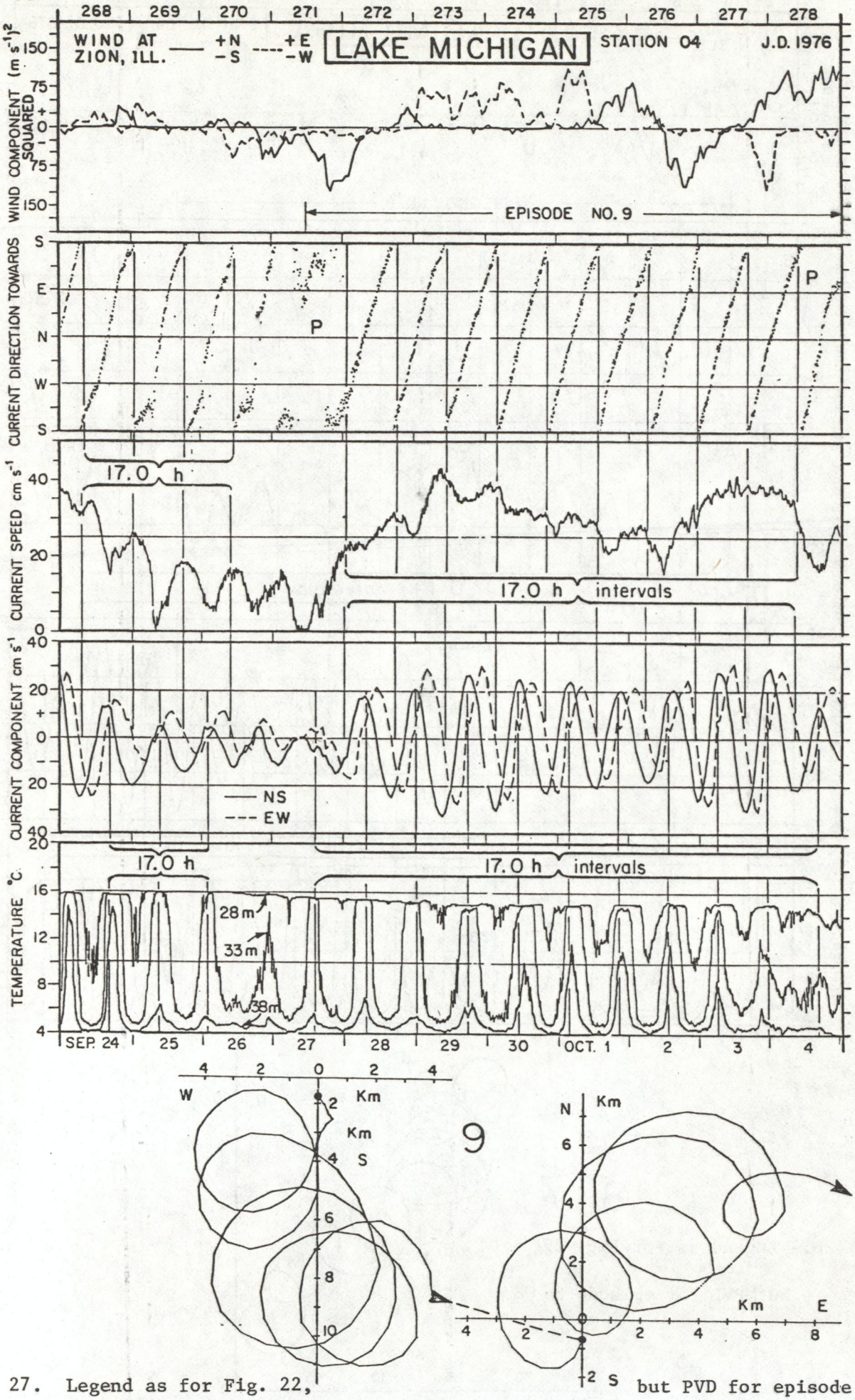

Fig. 27. Legend as for Fig. 22, but PVD for episode 9.

and close to the period calculated for the 2nd Poincaré cross-channel mode.

Later, during episode 8 (Fig. 26) the mean period fit for temperature was closer to 17.0 h (1st Poincaré mode?); and the same period also provided the best fit to the current rotations, particularly during the second two-thirds of the episode following the southgoing wind impulses in 15 September. It therefore appears reasonable to interpret episode 8 as an almost pure 1st Poincaré mode response; and perhaps the same may be said of episode 9 (Fig. 27). That response was clearly set in motion by the 12 h southgoing wind pulse starting on 2 October. Judging from the increase in current speed, the latter pulse appears to have reinforced the current oscillation (although the temperature oscillation decreased); but that increase was short-lived. It was brought to a halt by the timing of the westgoing wind pulse centered on midnight 3/4 October and followed by a northgoing pulse about eight hours later. If the pre-existing current pattern had been different, that wind pulse sequence might have generated a strong response rather than destroying an existing one. Again this confirms Pollard's (1970) conclusion that the duration and timing of the wind impulses, relative to pre-existing current patterns, exert a critically controlling influence.

In the final episode (10, Fig. 28) regular current rotation did not appear until after the wind impulses (5-6 Oct.) had died down. At the same time the drift current was strongly reduced. This episode is too short to be fitted to any period other than inertial (17.7 h).

The above series of records, from one station in Lake Michigan, discloses considerable variation between successive responses to wind action. One response may be almost purely inertial, while the next may be slightly but distinctly sub-inertial in period, suggesting dominance of one or more whole-basin (Poincaré) modes. With the method of period fitting employed here, this

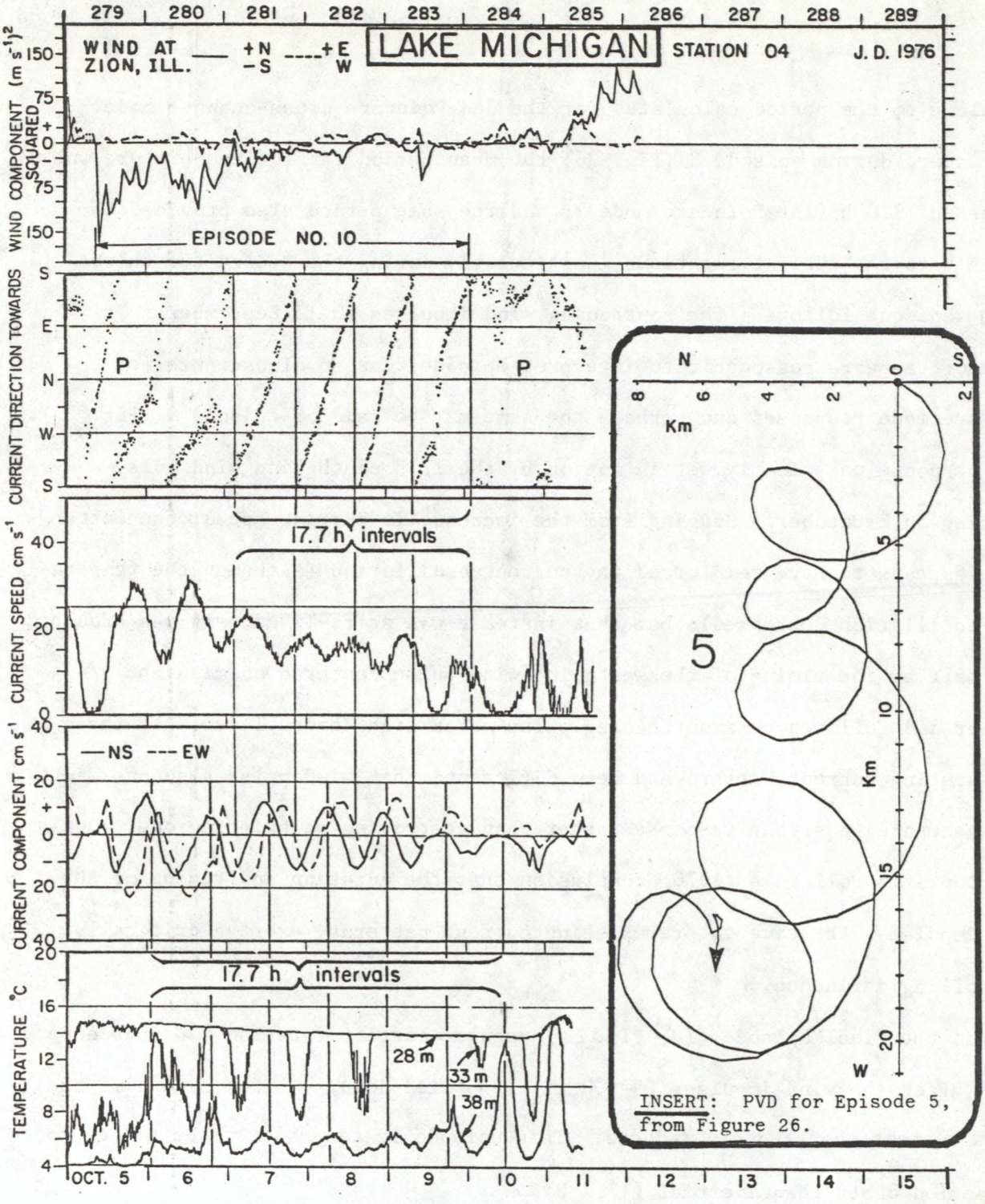

Fig. 28. Legend as for Fig. 22, but PVD for episode 10.

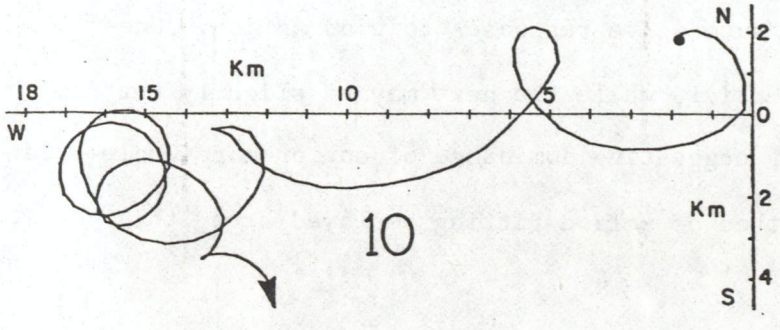

differentiation between inertial and sub-inertial responses is reliable when sufficient oscillation cycles have been recorded; but it is usually impossible to determine which Poincaré-type modes have been excited and in what proportion. Often the best-fit periods of the thermocline oscillations are slightly but significantly less than those of the current rotations; but other examples are seen in which the current and thermocline responses are indistinguishable in period, and in which that period may be either inertial (17.7 h), or 1st Poincaré-mode dominant (17.0 h), or perhaps a 1st. and 2nd. mode mixture.

Inspection of the wind structure, particularly with respect to direction, strength, duration, and timing of the wind impulses, sometimes provides clues to the types of water response are to be expected. These generally conform to Pollard's 1970 model; but exceptions to those expectations also occur; and this suggests that a more thorough application of Pollard's model (or of the simpler Pollard and Millard 1970 version) will be necessary to clarify causal relationships. Where, as is the case for Lake Ontario, wind, current, and temperature records are available from groups of stations, the differentiation between inertial responses (presumed to be relatively local) and "basin-tuned" Poincaré-type responses may become easier after study of the spatial structure of the response. This possibility will be examined in following sections and in Part II of this report.

5. INERTIAL AND NEAR-INERTIAL RESPONSES TO WIND IMPULSES IN LAKE ONTARIO, 1972.

5.1 Description of data sources and the method of presenting composite records for analysis.

The base map of the International Field Year for the Great Lakes (IFYGL), presented in Figure 29, shows depth contours and positions of moored instruments, nearshore towers (23 and 26) which, with additional land stations, made up the IFYGL observational network. A less detailed map, presented as Figure 30,

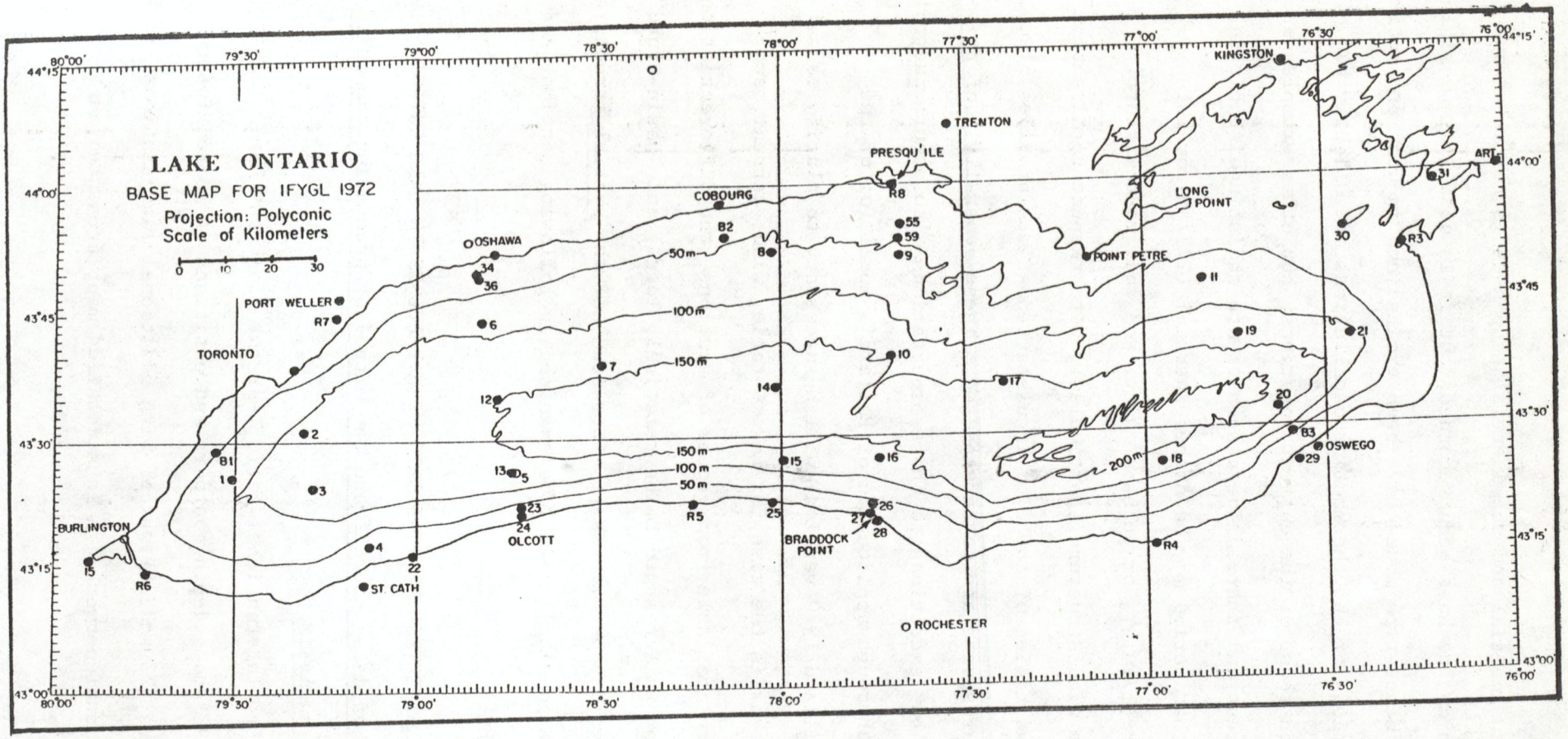

Fig. 29. Lake Ontario: Base map for IFYGL 1972, showing positions of moored instruments (measuring current and temperature at various depths and meteorological variables 4 m above the water surface at some stations); nearshore instrumented towers; and shore stations (at which water level and meterological variables were measured).

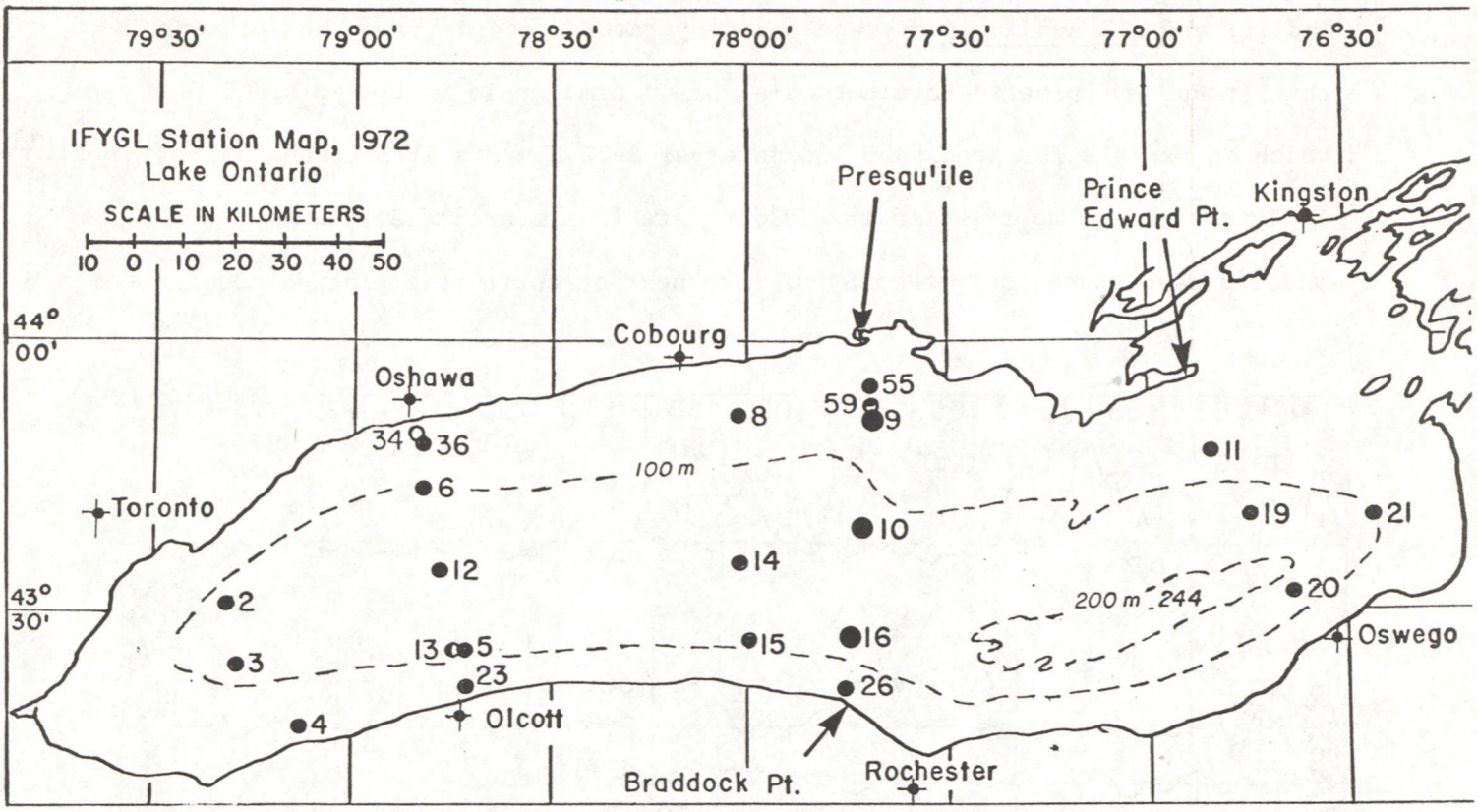

Figure 30. IFYGL 1972: Map of Lake Ontario showing positions of moored stations and transect lines from which records were selected for analysis in this report.

and referred to in later comparisons, indicates those stations which provided the records for this analysis. It also shows the positions of the three transect lines (Oshawa to Olcott, Presqu'ile to Braddock Pt., and Prince Edward Pt. to Oswego) along which the temperature structure was monitored in detail by continuously repeated crossings (see Introduction and Boyce and Mortimer 1977).

Records were selected from those stations which provided maximum continuity and which lay close to the transect lines. For the purposes of the present analysis, the stations are grouped in four cross-sections, the three transect lines already listed and a western one comprising stations 2, 3, and 4. For later reference purposes, each cross-sectional group is referred to by the station number from which the wind records were usually taken, i.e., 2, 6, 9,

and 11; and all available current and temperature records from the stations in that group are plotted together on a common time scale in 14-day blocks, of which an example for section 9 and interval 9-22 June is illustrated in Figure 31. It is convenient to refer to the Julian Date (day starting at midnight GMT); and, to save space, only the NS (v) component of current is plotted, designated

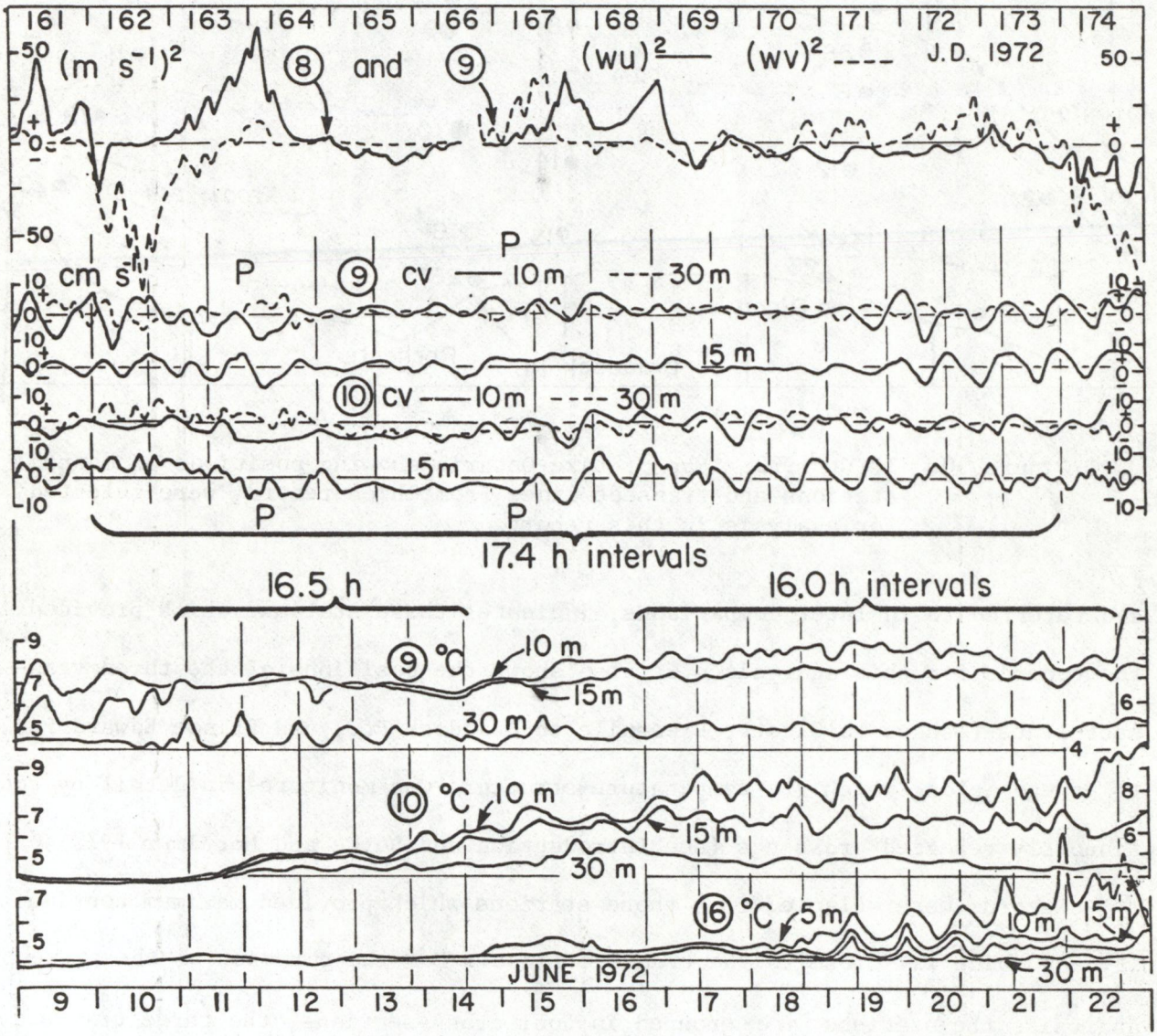

Figure 31. Lake Ontario, 9-22 June 1972: EW (continuous line) and NS (broken line) components of (wind-speed)^2 at stations 8 and 9; NS current components and temperature fluctuations at various depths at stations 9, 10, and 16 -- station numbers within circles; other details explained in the text.

as cv, at various depths. This entails no loss of information for the purposes of this analysis of near-inertial motions because, when oscillations are present, the current is predominantly rotary and the u component closely follows the v component in rotary amplitude with a lag very close to 90°, as may be confirmed by closer inspection of Figure 19. Of course, for a study of the drift currents or for preparation of progressive vector diagrams; information from the u component would also be needed. The current speed scales (in cm s^{-1}) are the same in Figure 31 and in all similar figures which follow. The same is true for the temperature scales, with a few obvious exceptions when the data was traced from microfilm rather than digital tape records.

In preparing the following composite diagrams in uniform format, the aim was to facilitate cross-referencing (for example 9/161-174 refers to Figure 31, by cross-section number and Julian date) and to present all usable records on a common cross-sectional display for initial comparison and period-and phase-fitting. This led, unavoidably in some cases, to congested diagrams; but individual station episodes will be later extracted for re-plotting on more convenient scales and groupings. All station numbers are circled and the usual plotting sequence, from top to bottom, is: wind; current; and temperature. In each cross-section, wind is plotted for one station only (there was often only one) and this is taken as the reference number for that cross-section. Where more than one wind record was available for a particular section, the small differences in the wind field (between stations 9 and 10, for example) were small enough to be neglected for the purposes of this initial exploration. In most cases, the EW and NS components of the wind speed squared are plotted, respectively, as $(wu)^2$ and $(wv)^2$ in (m s^{-1}) units, assumed to be proportional to the EW and NS components of wind stress. In some cases the EW (u) and NS (v) components of wind stress were calculated by the method of Hamblin and Elder

(1973) and plotted instead. Wind data from land stations, although available, was not used in this analysis, on the assumption that over-water wind measurements would more truly represent the stress on the water.

Period-fitting was carried out, where appropriate, on each diagram in the manner described in Section 3.1. Transparent vertically ruled gratings were prepared to correspond (on the time scale adopted for the composite diagrmas, 0.75 inches/day, full scale) to the following average period bands (APB) of 17.4 h (inertial period, assumed constant for the basin), 17.0 h, 16.5 h, 15.8 h, 14.4 h, and 13.0 h. The second and the last three members of that series were chosen to fit the first four Poincaré modes in a two-layered channel model fitted to average dimensions and density distribution in Lake Ontario during the interval 1 July to 30 September, as described in Section 3.1, in the expectation that one or other of those modes would occasionally dominate the record. The remaining APB, 16.5 h occasionally found to fit the record, may (as suggested by the patterns in Fig. 20) signal the presence of a 1st. and 2nd. mode mixture. The grating with 13.0 h intervals provided a best-fit in only one example. Occasionally it was convenient to apply 16.0 h intervals (3 cycles in 2 days) but the method of fitting is not precise enough to distinguish between 16.0 and 15.8 h. Nevertheless as discussed in Section 3.1 and as evident in later examples, many oscillation episodes of five cycles or more can be fitted unambiguously to either an inertial APB (17.4 ± 0.2 h), or to one member of the above sub-inertial APB series. The value of that fit lies in the clues it can supply to possible internal wave structures, which can then be further investigated by means of interstation comparisons, in this report and in Part II.

Because knowledge of the whole-basin or cross-sectional temperature structure can assist interpretation of the motions, additional inputs to the analysis are provided by (i) synoptic measurements of whole-lake surface temperature (airborne radiation thermometry, ART survey, Irbe and Mills 1976). (ii) plots of isotherm depth interpolated from thermistor-chain records obtained

at stations 6, 9, and 10 and kindly supplied by F.M. Boyce, and (iii) temperature distributions measured with an electronic bathythermograph (EBT) in selected cross sections during heat content surveys (Boyce, personal communication in advance of forthcoming report). The station positions, at which the EBT profiles were taken, are shown in Figure 32, upon which are indicated the cross-sections selected here for analysis (designated 2, 6, 9, and 11 as explained above). Those cross-sections correspond to the following sections in Boyce's heat content survey: A (heat content stations 8 to 12); B (stations 20 to 30); D (stations 49-59); and F (stations 79 to 90). Date, total elapsed time (hours) and central time (GMT) are indicated on each section diagram. Long elapsed

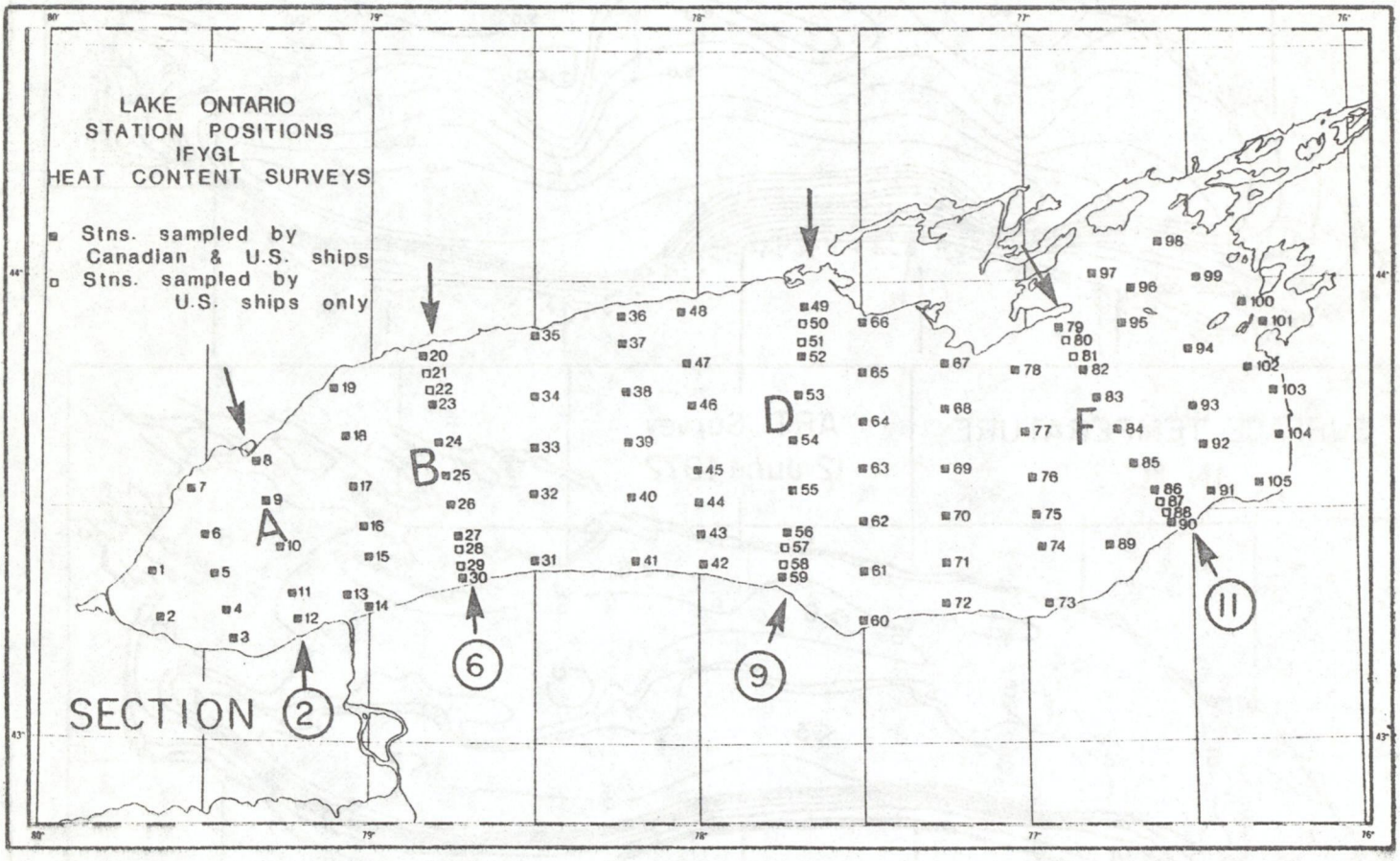

Figure 32. Station positions in IFYGL (1972) heat content surveys. Also indicated are: (by letters) the heat content sections, illustrated in later figures; and (by circled numbers and arrows) the four principal cross-sections (2, 6, 9 and 11) along which IFYGL station records are assembled in later composite diagrams.

times indicate that sections were worked in non-consecutive pieces. Individual station times are available on the EBT cards at the Canada Centre for Inland Waters, but are not quoted here. The central times indicate when most of the section was worked. Also shown, for comparion with the surface temperature maps prepared from the EBT surveys, are surface temperature maps prepared from

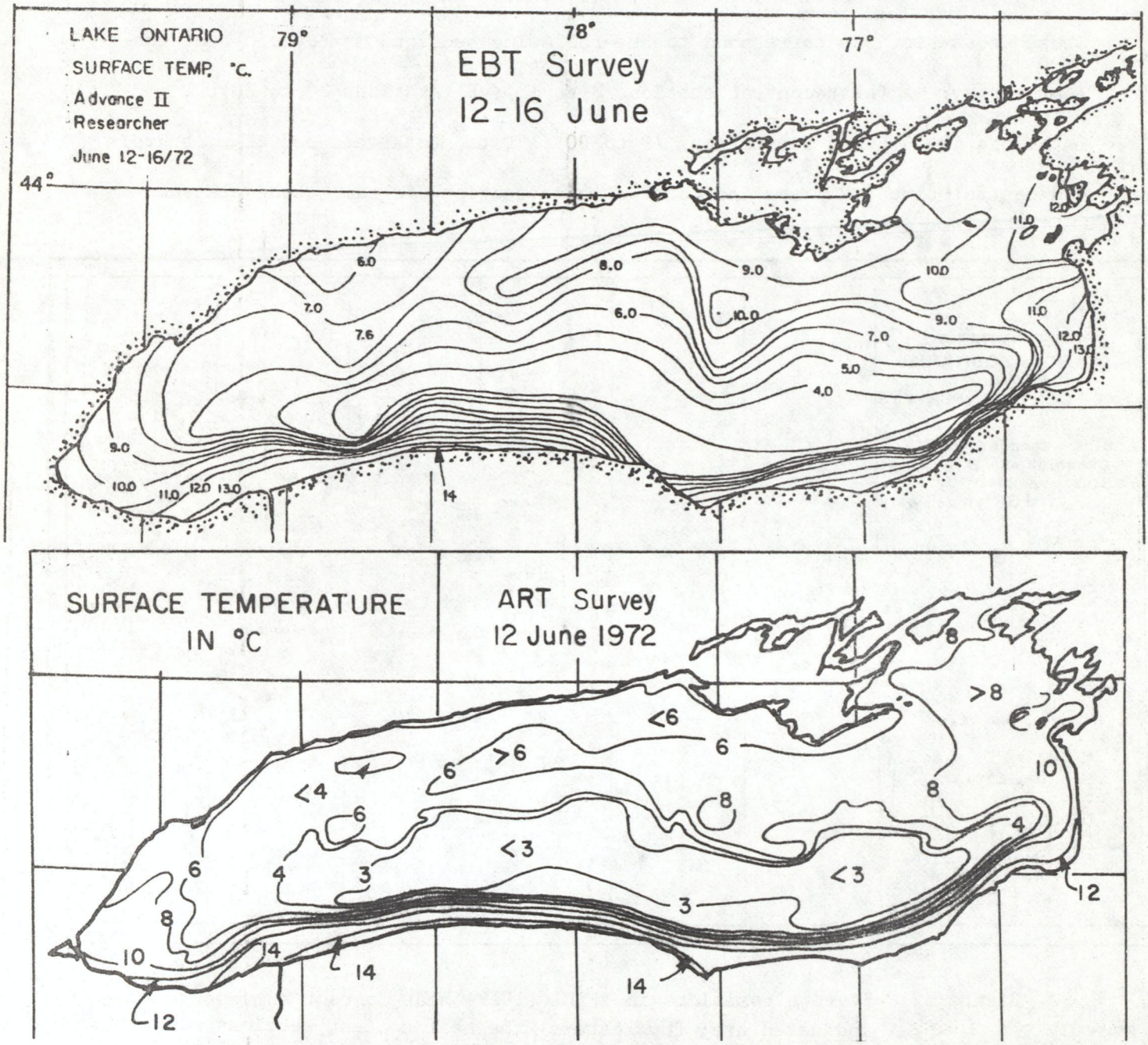

Fig. 33. Lake Ontario: surface temperature measured by electronic bathythermograph (EBT) survey (referred to in the text) 12-16 June 1972, compared with a "synoptic" measurement by airborne radiation thermometry (ART survey, Irbe and Mills 1976) on 12 June.

the airborne radiation thermometer surveys referred to above. The ART survey results are synoptic; the EBT survey is spread over several days required to complete the heat content cruise. A comparison between the two is made in Figure 33. Where appropriate, the cross-sectional temperature structures on sections 6, 9, and 11, explored on shuttle cruises during July, August, and October (Boyce and Mortimer 1977), are also illustrated.

The main bulk of the information, here reviewed chronologically, has been presented in the form of composite plots of wind, current, and temperature records from selected station groups, in the common format described above, and assembled on forty sheets. To keep this report within reasonable bounds, only a selection of those sheets are incorporated here as text figures; the remainder are assembled chronologically in Appendix 8.3. To simplify the correlation of individual portions of record it is important to keep in mind (see Fig. 30) the following station groupings: 2, 3, and 4 included in cross-section 2; 34, 36, 6, 12, 13, 5, and 23 included in cross-section 6; 55, 59, 9, 10, 16, and 26 included in cross-section 9; and 11, 19, and 20 included in cross-section 11. Individual portions of record are then referred to by section or station number, followed by /, then Julian date interval, and sometimes by depth and the text figure number, or by A if the corresponding sheet is in the appendix. For example, the onset of thermal stratification at station 10, seen in Figure 31, would be referred to as 10/163-166,Fig. 31; whereas the sudden descent of the thermocline at station 13, brought about by a storm on 7-8 October, would be referred to as 13/282-285 in 6/276-290 A, indicating that the corresponding record is to be found in the appendix in the sheet for cross-section 6 for the dates concerned. The Julian date in all the records, commences at midnight GMT. Calendar days are also shown commencing at midnight GMT on each sheet.

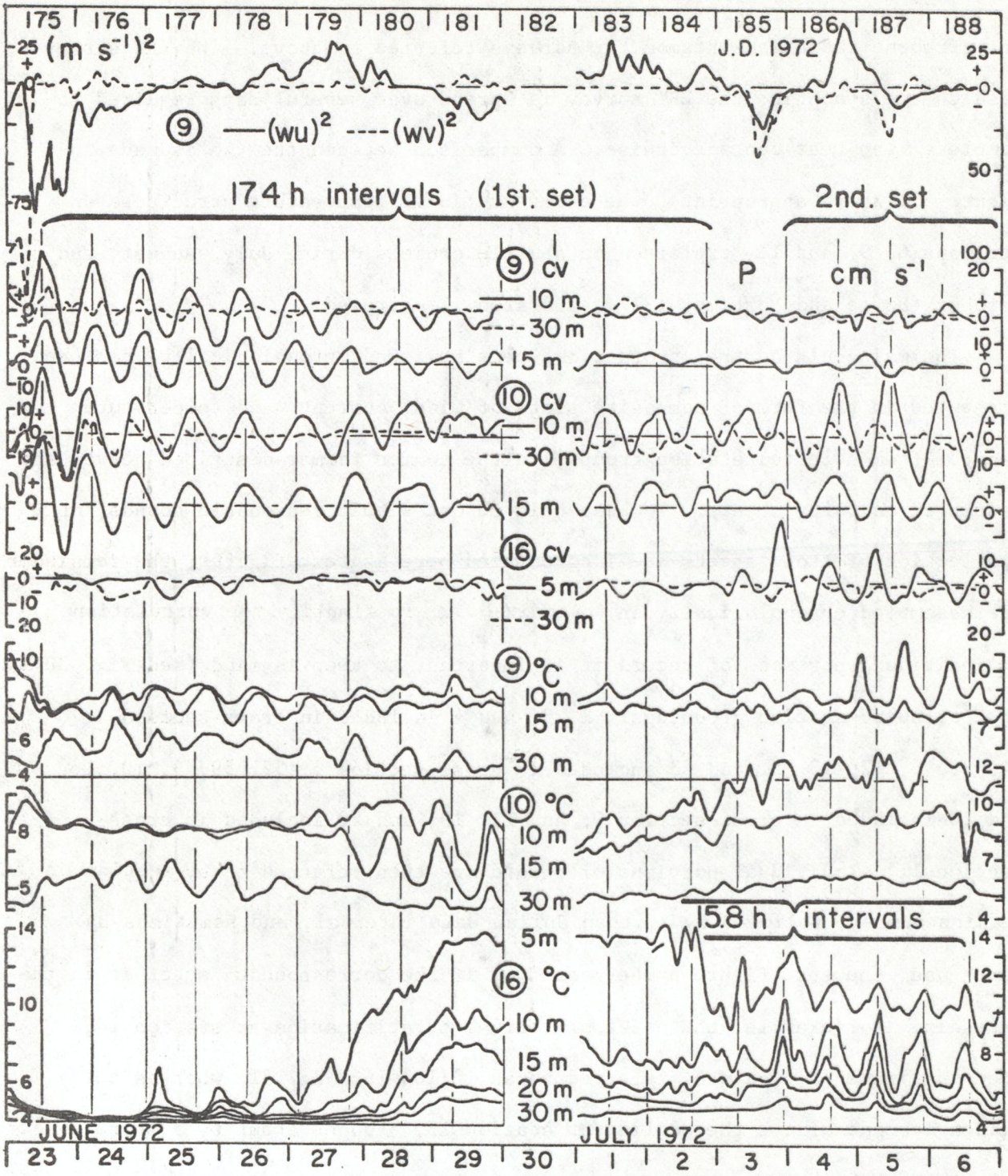

Fig. 34. Lake Ontario 1972 cross-section 9, Julian days 175 to 188 (23 June to 6 July), i.e., composite diagram 9/175-188: EW and NS components of wind speed squared, $(wu)^2$ and $(wv)^2$ respectively, 4 m above the water surface at station 9; NS components (cv) of current at various depths; and temperature at various depths at stations 9, 10, and 16. The intervals marked by vertically-ruled lines conform to the "average period bands" defined in Section 3.1; and P denotes an interruption or a phase change in the oscillation.

5.2 Inertial responses before whole-basin stratification had become established.

During the mid-June interval covered by Figure 31, stratification was confined to nearshore bands, bounded by a thermal bar, while the offshore water column remained cold and mixed from top to bottom (near 3° on 12 June, Fig. 33, near 4° on 21 June). Initially the warmest water was confined to a narrow band along the southern shore, presumably transported there by the eastgoing and southgoing wind pulses on 9 and 10 June. On 9 June, weak stratification was present at station 9, but stratification did not begin at stations 10 and 16 until a few days later. That stratification may have owed more to the advection of warm water from elsewhere than to local processes at 10 and 16.

Wind pulses on 167 and 168 were followed by weak oscillatory responses in the currents at 9 and 10, roughly fitting the inertial period, 17.4 h. These were the first, albeit weak, inertial responses of the season, indicating that some stratification must be present (to provide a low-friction base for inertial gyrations of the upper layer) although stratification need not be fully established across the basin for the inertial motion proper (as opposed to whole-basin near-inertial Poincaré-type-motion) to develop. If this interpretation is correct, it is puzzling to note that the thermocline oscillation 16/171-174 Fig. 31 displays a periodicity distinctly shorter than inertial. Equally puzzling is the current oscillation 11/165-169 A which fits a 16.5 h period (definitely not inertial) and which does not appear to have been initiated by wind. That oscillation is seen at 10 m and (in phase opposition) at 30 m depth. No contemporary temperature waves are visible. No strong or persistent inertial or near-inertial oscillations were seen at other stations (see 2/ and 6/161-174) A) during the 161-174 interval.

More striking examples of current and temperature oscillations with average period indistinguishable from 17.4 h -- therefore regarded as inertial motion proper -- occurred in cross-section 9 (Fig. 34) and 11 (11/175-188 A) after the

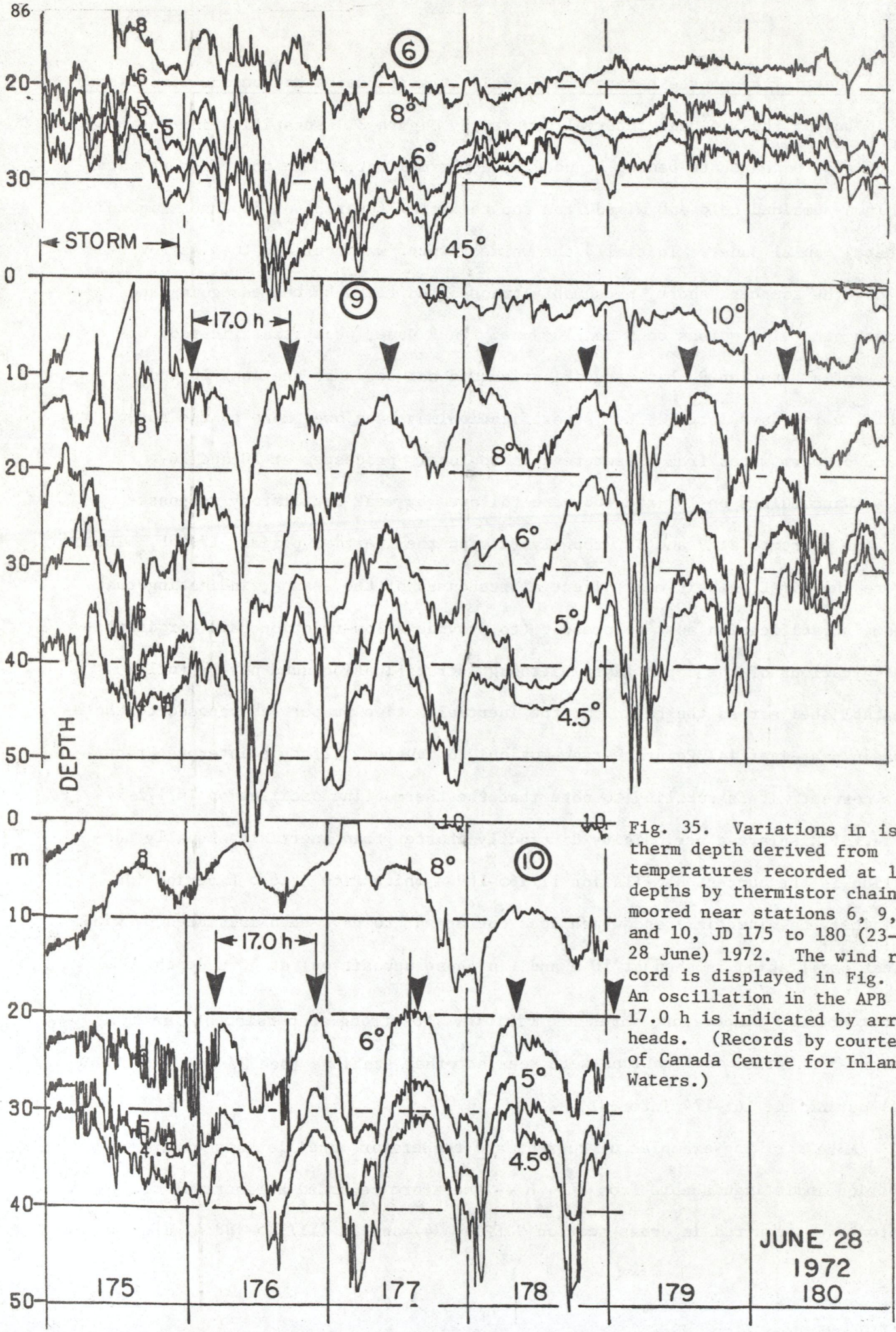

Fig. 35. Variations in isotherm depth derived from temperatures recorded at 19 depths by thermistor chains moored near stations 6, 9, and 10, JD 175 to 180 (23-28 June) 1972. The wind record is displayed in Fig. 34. An oscillation in the APB 17.0 h is indicated by arrowheads. (Records by courtesy of Canada Centre for Inland Waters.)

short, but strong burst of southgoing wind starting at midnight 174/175 (the aftermath of Hurricane "Agnes"). At other stations (2/6/175-188 A) the response was not as marked, although the weak response at 2 persisted for at least six cycles with little diminution in amplitude. Eight or more cycles of strong, regular inertial rotation of current at 10 m depth, starting at about 20 cm s^{-1} and decreasing gradually in amplitude, were seen at 9, 10, and 11, perhaps the clearest approximation to pure inertial response during the whole year.

At 16 (Fig. 34) the effect of the 175 storm was to mix the water column down to at least 30 m; but inertial oscillations began to show at higher levels on 177 to 179; and thereafter the thermocline rose to about 10 m. The storm did not disturb the stratification at 9, 10, 11, or 19; but the thermocline oscillations at those stations were (as was commonly the case) less regular than the current oscillations. However, there is no justification for fitting a period other than 17.4 h to those oscillations in Figures 34 and 11/175-188 A. But, when the higher-resolution isotherm-depth plots, obtained from thermistor chains at 6, 9, and 10, are examined (Fig. 35), no clear periodicity is evident at 6; and at 9 and 10 a better period fit is obtained with 17.0 h. The combined evidence suggests that, in cross-section 9 for which the most information is available, the mean periods of the current and temperature oscillations were closest to 17.4 and 17.0 h, respectively.

Figure 36. On next page, 88.

Phase comparisons between the NS components of current (cv) and temperature (°C) at various depths at stations 9, 10, 11 and 19, JD 175-181 (23-29 June) 1972. For further details, including explanation of the wind record, see legend of Fig. 34.

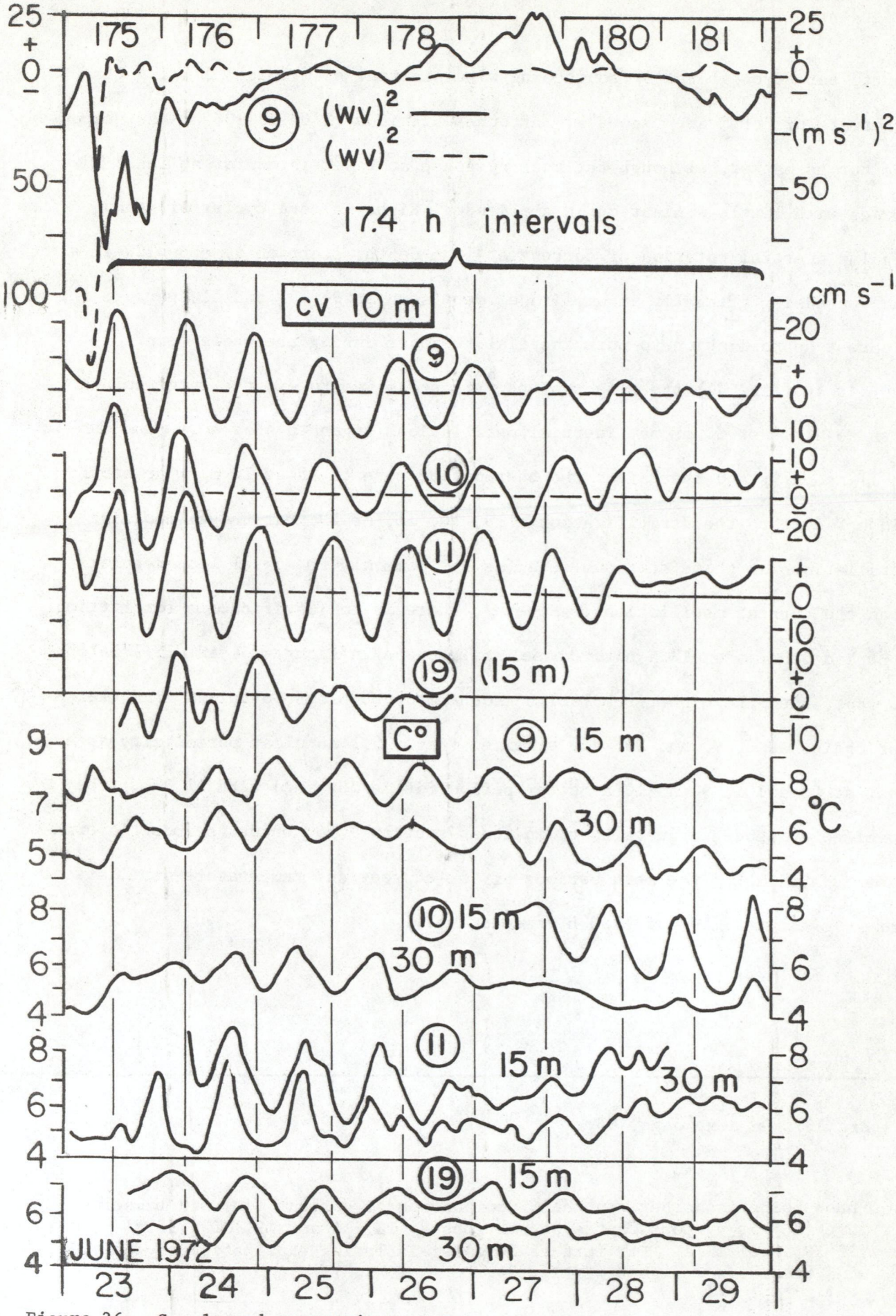

Figure 36. See legend on previous page.

A more detailed phase comparison in Figure 36 of current and temperature oscillations at stations 9, 10, 11, and 19 disclose strong current oscillations initiated in phase at 9, 10, and 11 by the strong southgoing wind pulse early on 175 which veered to westgoing later that day. During an almost windless spell which followed, the in-phase behavior at those stations was maintained for five cycles; but phase separation occurred thereafter, perhaps as a result of weak eastgoing wind on 179. Phase relationships between current rotation and thermocline oscillations differed from station to station. For example, the temperature wave at 9 was almost out-of-phase with that at 11; and 19 lagged by about a quarter-cycle.

At the time of the 175 storm, the thermocline was not yet fully established over the whole basin, although that storm probably assisted in the completion of the process. Surface temperature on 27 June (Fig. 37a) showed a central patch of <6° water, and on 28 June the heat content survey disclosed a dome-shaped thermocline (Fig. 37b) with the 6° isotherm very close to the surface in mid-lake (section D). By 5/6 July (Fig. 37c) a deeper thermocline had become established over the full extent of sections D and F, so that whole-basin internal responses became possible. The 15.8 h thermocline oscillation at 16/184-188 Fig. 34, perhaps set in motion by the wind impulse on 185, appears to be such a response. It was in phase with the oscillation at 10, but out of phase with 9. Over the same interval and continuing until 194, the period of the current oscillation at 11 was distinctly less than inertial; the best-fit APB was 17 h (see 11/175-188 A). These results should not suggest, however, that sub-inertial periodicities (Poincaré-type responses) constituted the sole response after the whole basin thermocline had become established. Examples of occasional and local approximations to pure inertial response during the summer and fall will be noted later.

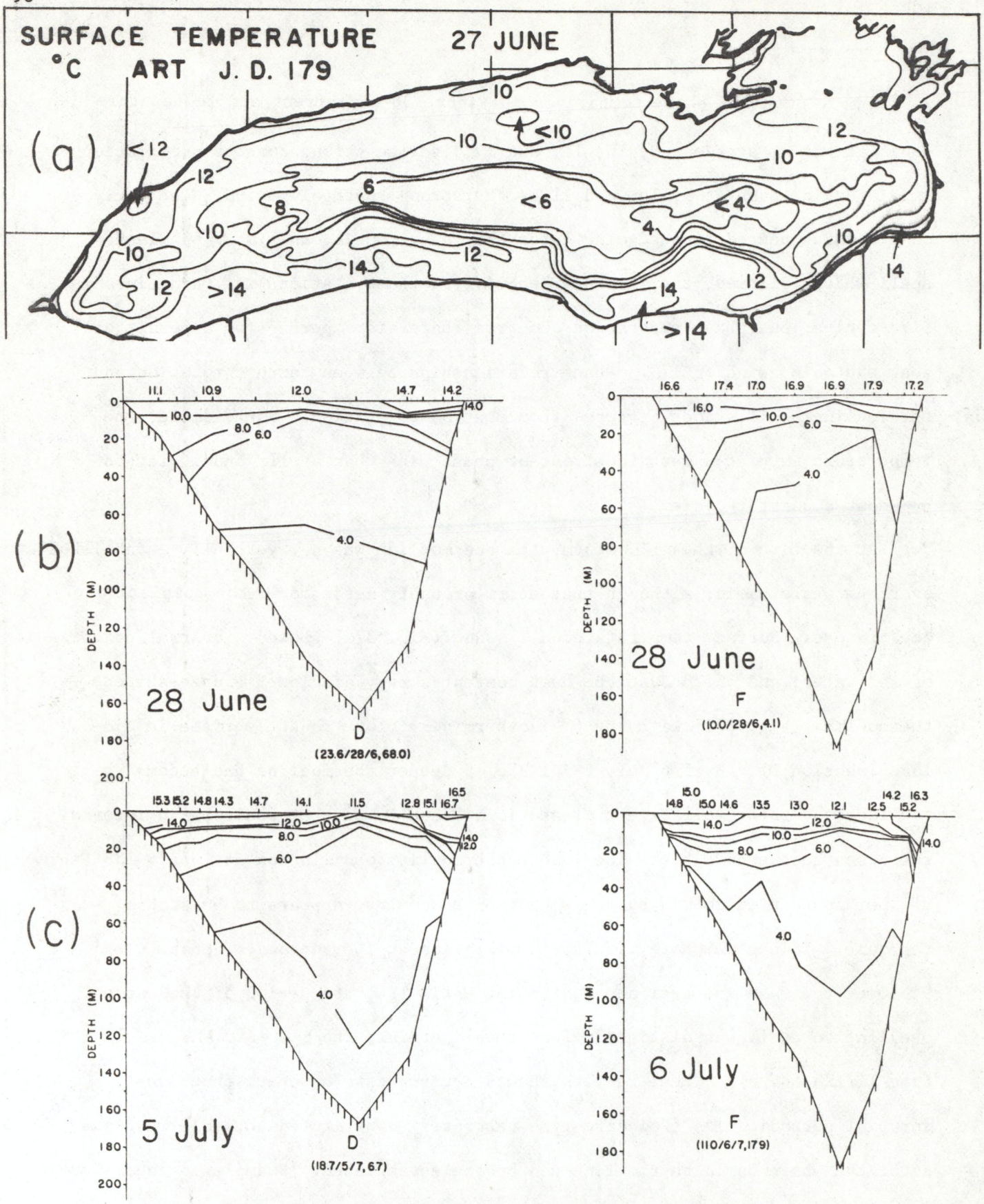

Fig. 37. Lake Ontario 1972: (a) surface temperature (ART survey, Irbe and Mills 1976) 27 June; sub-surface temperature distribution in sections D and F (heat content survey, see Fig. 32) , (b) 28 June and (c) 5 and 6 July.

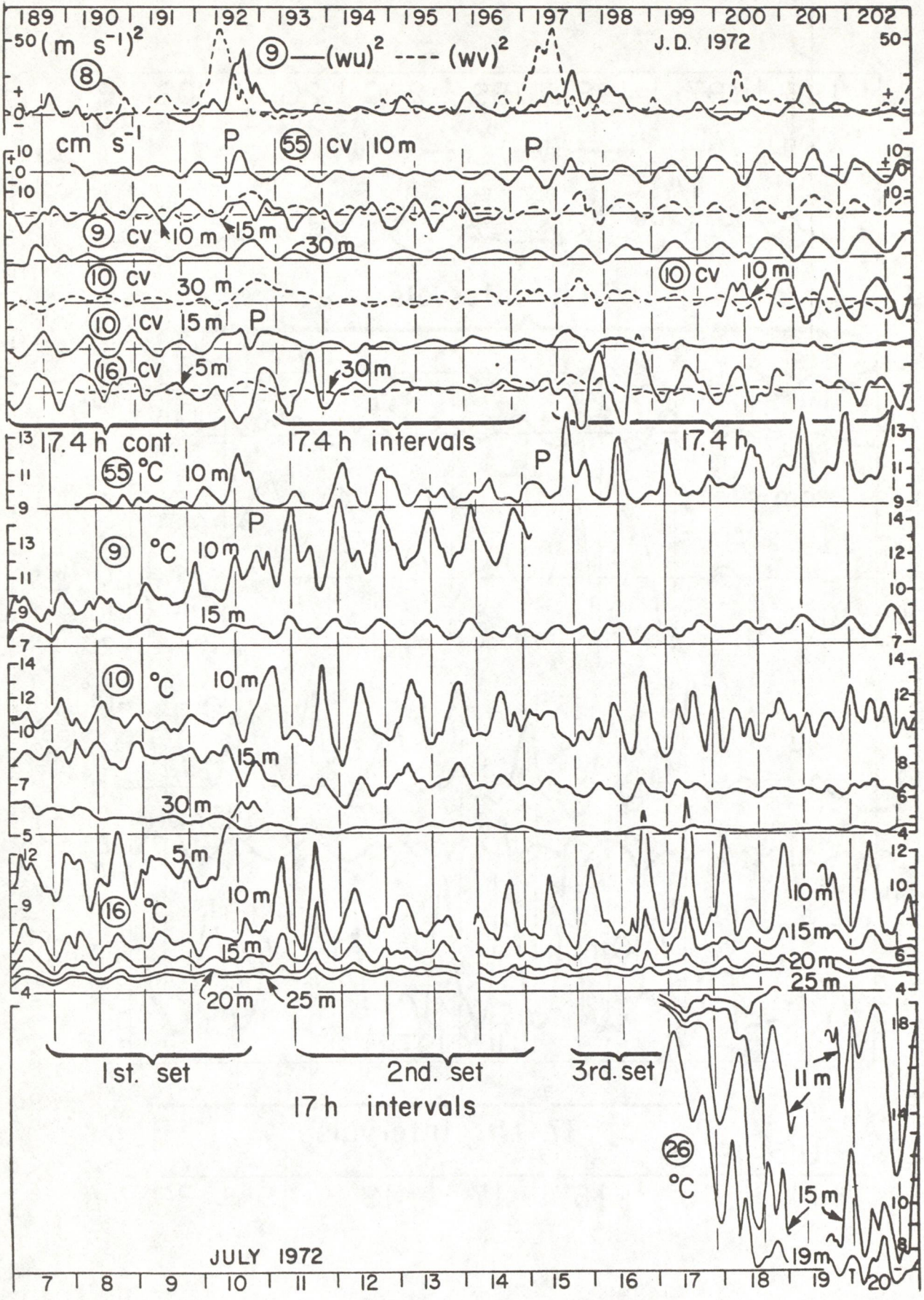

Figure 38. Composite diagram 9/189-202: wind components $(wu)^2$ and $(wv)^2$ at 9; current component (cv) and temperature (°C) at various depths at 55, 9, 10, 16 and 26. Further details in legend of Fig. 34.

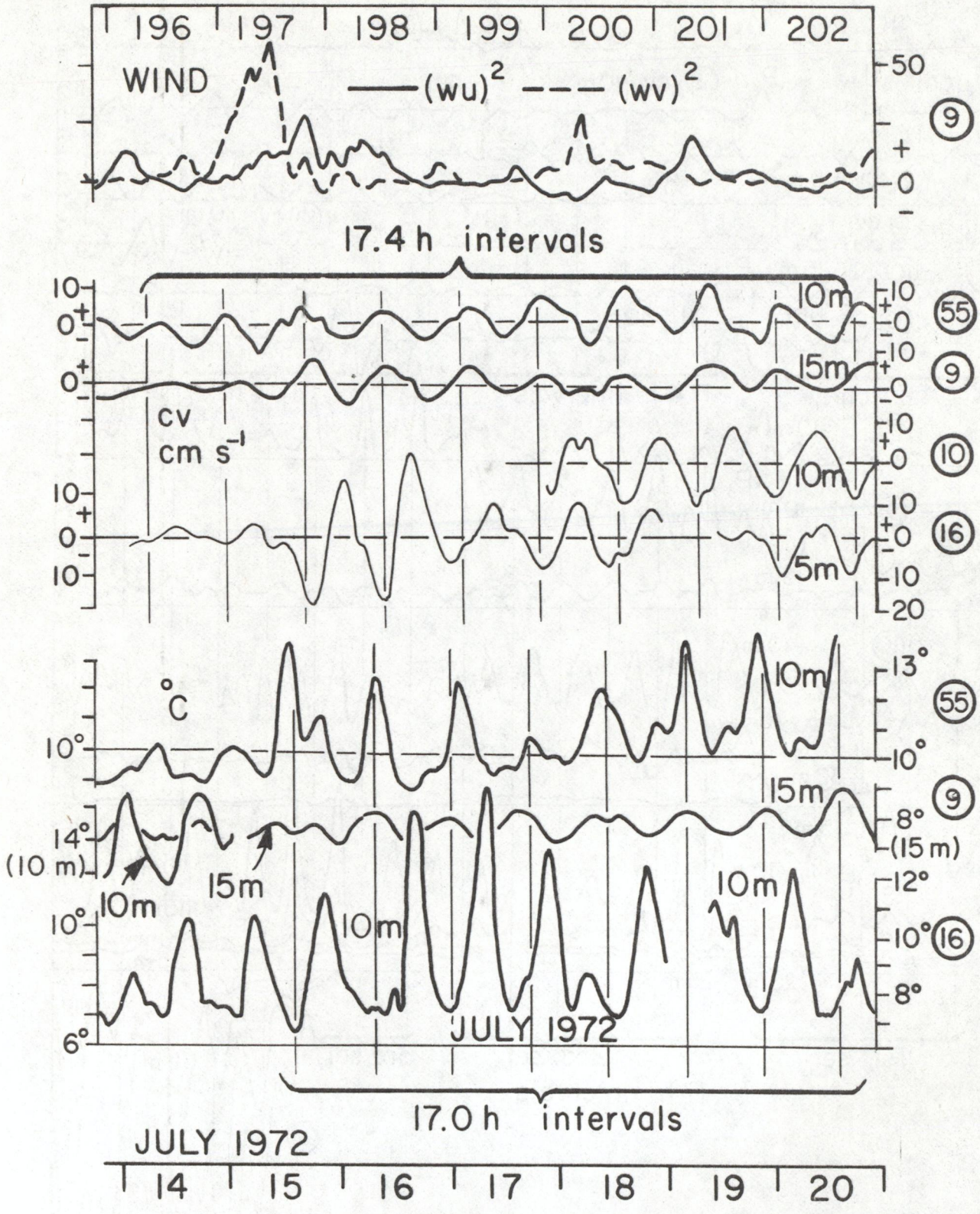

Fig. 39. Phase comparisons between near surface current and temperature records from stations 55, 9, 10 and 16, JD 196-202 (14-20 July) 1972. For further details, see legend of Fig. 34.

5.3 Responses after the establishment of whole-basin stratification.

During the interval 189-202 there were two wind pulses of medium strength, on 192 and 197; and also during that interval, weak but persistent inertial currents developed at a number of stations: 3 (2/189-202 A); 6 (6/189-202 A); 9 and 10 (Fig. 38). In each of those cases, the period of rotation was indistinguishable from 17.4 h. The contemporary thermocline oscillations, however, were either too irregular to be assigned a period, or were distinctly shorter than 17.4 h, for example 13 h at 4 (2/197-200 A), about 16 h at 6 (6/192-194) and about 17 h at 9 and 16 (Fig. 38). This again reinforces the finding that current oscillations are often dominated by longer periodicities than are thermocline waves; and a more detailed examination of current and temperature records from cross-section 9 (196-202, Fig. 39) immediately following the wind pulse on 197, suggests that thermocline motion was mainly controlled by a first cross-channel Poincaré mode (note the approximate in-phase behavior of 55 and 9 and the phase opposition between 9 and 16) of about 17 h period, whereas the 10 m current rotations were a better fit to 17.4 h.

In this connection, a comparison with section 11 is interesting (Fig. 40) because, although there is evidence of the presence of an internal seiche (first cross-basin mode, suggested by approximate phase opposition of temperature at 11 and 20, during days 196 to 199), the APB for current rotation at 11 (10 m) is distinctly less (about 16.5 h) than that already noted at stations on all other sections. Why a significant inertial component is lacking at 11 but present in other sections is not clear. The wind regime and stratification development was similar in all sections, although there was a deepening of the thermocline from west to east as seen in the lower portion of Fig. 40. Another puzzling feature is disclosed by phase comparisons of currents at stations in cross-section 9 (Fig. 39). Stations 9 and 55 are roughly in phase -- not surprising in view of their proximity -- but are approximately out of phase with

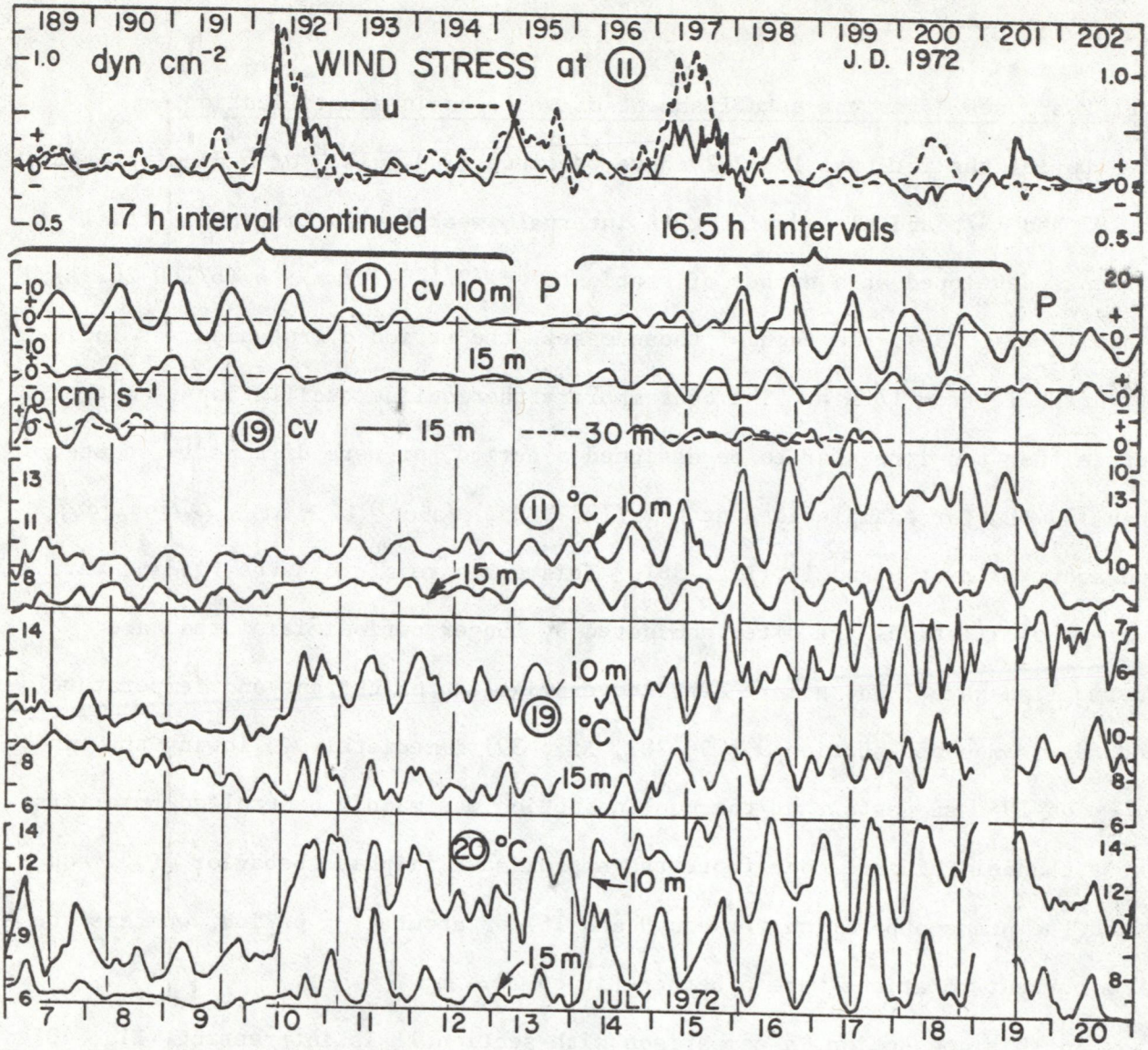

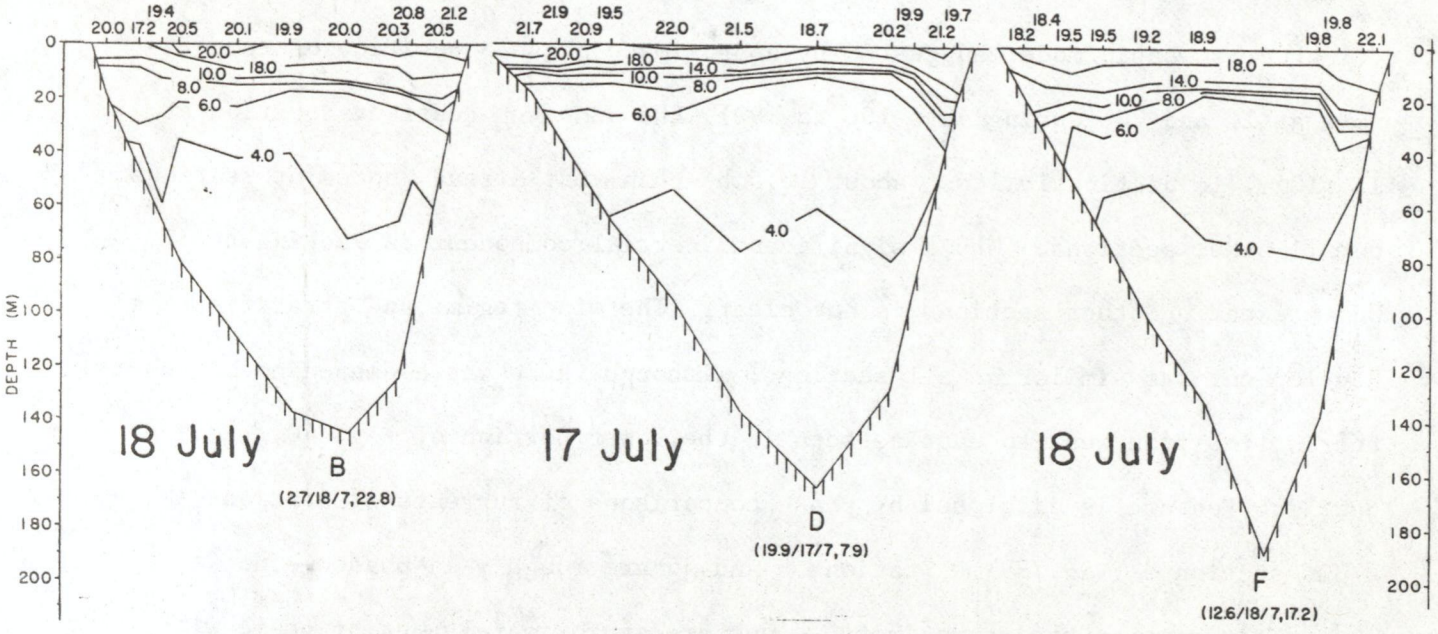

Figure 40. Legend on facing page, 95.

10 and 16. This is a current pattern to be expected in a second mode cross-channel Poincaré model (compare the first and third mode patterns in Figs. 11 and 12); but the temperature phases suggest a first mode response (best fit 17 h), and the best-fit period for the currents is 17.4 h. It is possible, although not particularly satisfying, to explain these phase relationships in terms of different phasing of an inertial response, on different sides of the lake, and the superposition of these on a first mode thermocline oscillation.

One of the most regular series of oscillations seen in the whole IFYGL data set, and therefore the most amenable to precise period fitting, occurred after a succession of windy days (205-208) with east-going pulses culminating in wind pulses on 208 particularly strong at the eastern end of the basin. At the western end (Fig. 41) current oscillations started suddenly (midnight 207/8) at 2, a little earlier at 3 and earlier and less conspicuously at 4. Station 2 recorded a regular 16.5 h oscillation for 11 cycles during a long calm spell until disturbed by a west-going wind pulse on 215. Temperature waves started at 2 at the same time as the currents during 207/8, and persisted for 10 cycles with a best-fit APB of 16.0 h. Also fitting 16.0 h was a shorter sequence of strong temperature oscillations, a sequence which would be consistent with a wave front travelling in direction 4, 3, 2 (i.e., anticycloncially) at an approximate speed of 15 km day^{-1} (17 cm s^{-1}). A more likely explanation is based on displacement of the thermocline at the western end of the basin from its equilibrium level, initially brought about by eastgoing wind impulses during 203-206. Extensive upwelling along the western and northern shores was dis-

Figure 40. See facing page, 94.

Composite diagram 11/189-202: wind components $(wu)^2$ and $(wv)^2$ at 11; current component (cv) and temperature (°C) at various depths at 11, 19, and 20 (further details on legend of Fig. 34). Lower portion: temperature distributions of sections B, D and F (heat content surveys, see Fig. 32) on 17 and 18 July.

closed by the ART survey (Fig. 42, upper portion) with concurrent downwelling along the southern shore and active mixing of the upper layer. That mixing produced a sharply defined thermocline across section 9 (Fig. 42, lower portion). Figure 41 can, therefore, be interpreted as the recovery of the thermocline

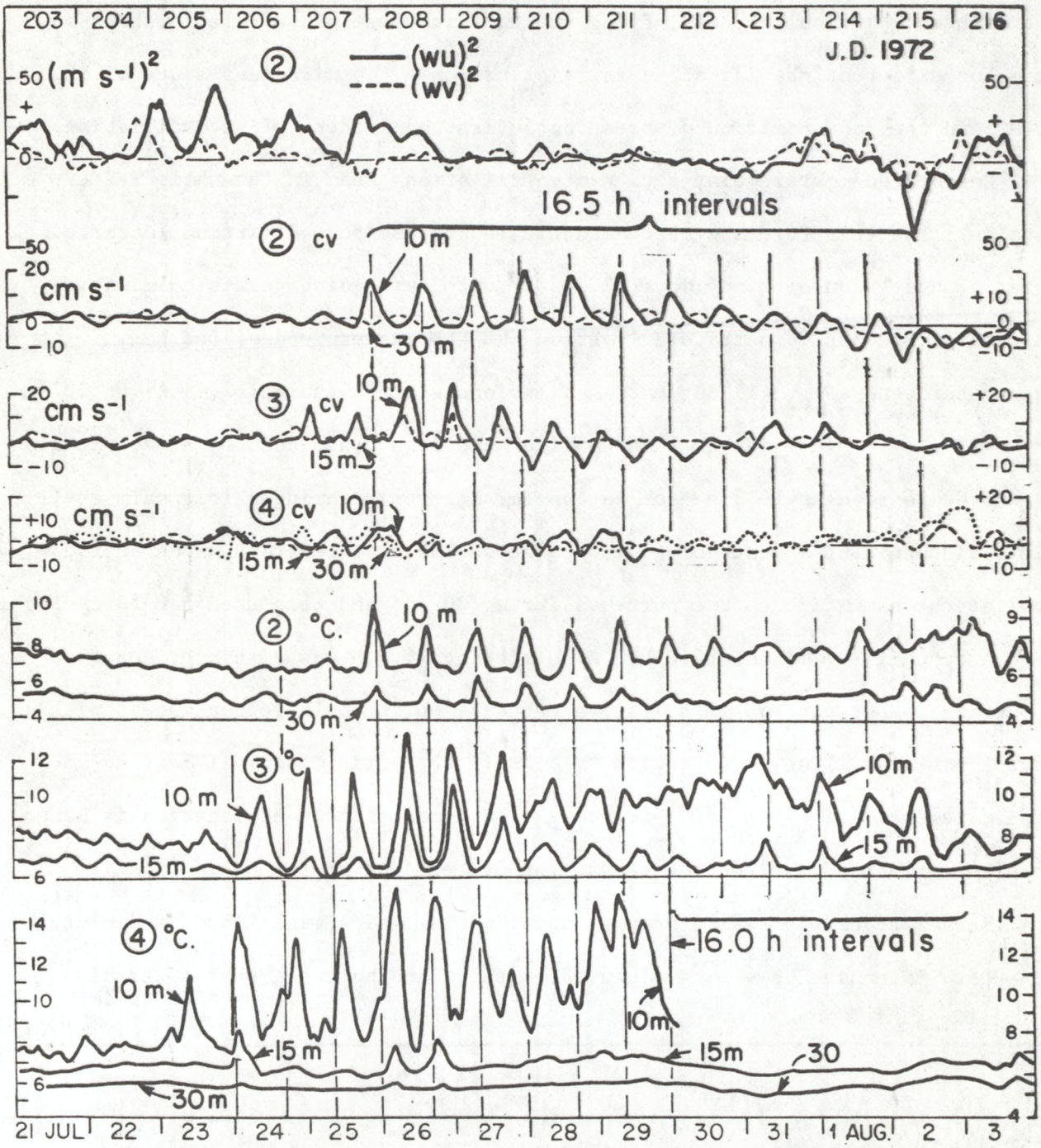

Fig. 41. Composite diagram 2/203-216: wind components $(wu)^2$ and $(wv)^2$ at 2; current component (cv) and temperature (°C) at various depths at 2, 3, and 4. For further details see legend of Fig. 34.

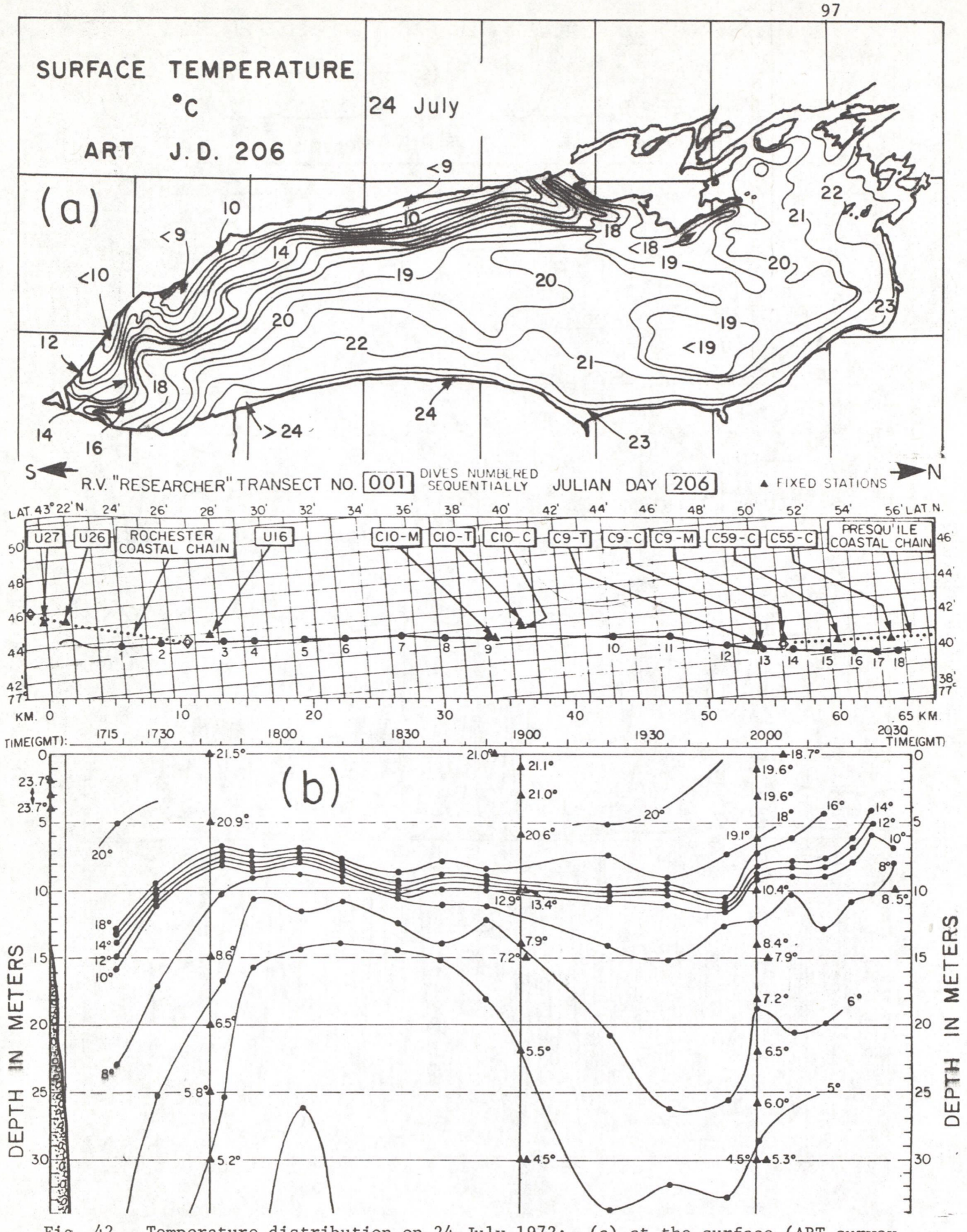

Fig. 42. Temperature distribution on 24 July 1972: (a) at the surface (ART survey, Irbe and Mills 1976) and (b) in cross-section 9.

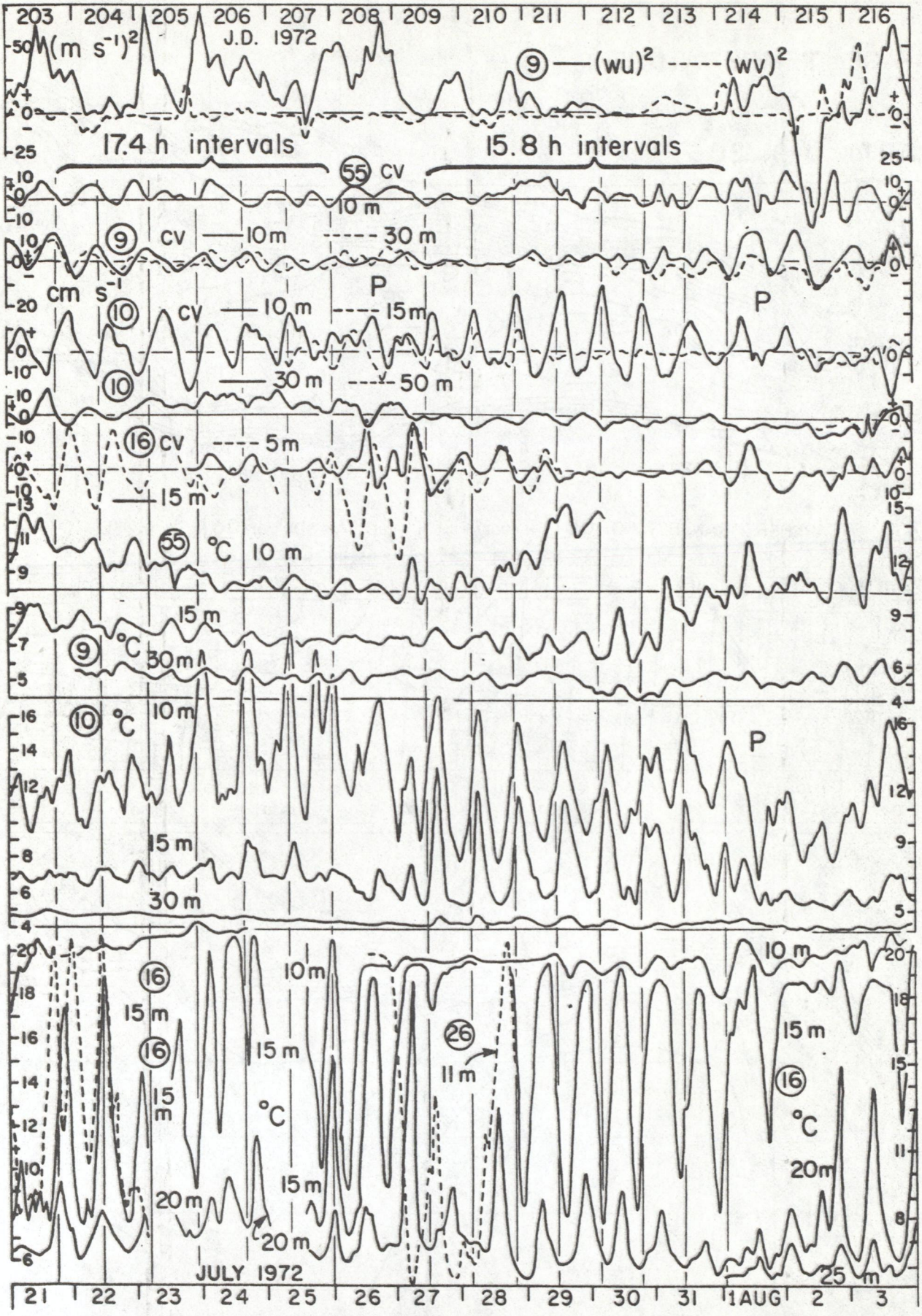

Fig. 43. Composite diagram 9/203-216: wind components $(wu)^2$ and $(wv)^2$ at 9; current component (cv) and temperature (°C) at various depths at 55, 9, 10, 16 and 26. For further details see legend of Fig. 34.

from the upwelling/downwelling displacement. Initially (203/4 in Fig. 41) the low temperatures at 10 m and 15 m depth at 2, 3, and 4 demonstrate that, at that time, the thermocline there was either absent or at a level above 10 m. When, after the disturbance, the surface, warm layer returned to the western end, it did so as a warm front arriving at 4, 3, and 2 in sequence, followed by regular thermocline oscillations at each of those stations. The non-sinusoidal form of the temperature (and current) oscillations at 2 suggests that the thermocline at the western end was also narrow and near the surface at that time, and that the 10 m recorders, situated just beneath it, came to lie alternately in an upper layer with actively rotating currents and then in a lower layer with little current activity. It may also be noted (Fig. 41) that, over the interval 208 to 211, both the current and temperature oscillations were approximately out of phase between 2 and 3, and that the temperature oscillation was also nearly out of phase between 3 and 4. But to interpret that behavior as the signature of a second cross-basin Poincaré mode, for example, does not appear to be realistic so near the end of the basin.

5.4 Evidence for generation of internal surges and of a second mode Poincaré-type response.

Records from cross-section 9 during the same interval (203-216) show that after the eastgoing wind pulses on 208, the best APB fit for both current and temperature oscillations at 10 and temperature oscillations at 16 is 15.8 h (Fig. 43); and the same periodicity is also a good fit for station 6 (6/203-216 A). That period is close to that calculated (16.0 h, Fig. 15) for the second Poincaré mode in a 60 km-wide two-layered channel model with dimensions

---

Figure 44. See following page, 100.

Phase relationships between current and temperature records from stations 55, 9, 10, and 16, JD 207 to 215 (25 July to 2 August) 1972. Small arrows indicate transit times of vessel transects as explained in the text. For further details see legend of Fig. 34.

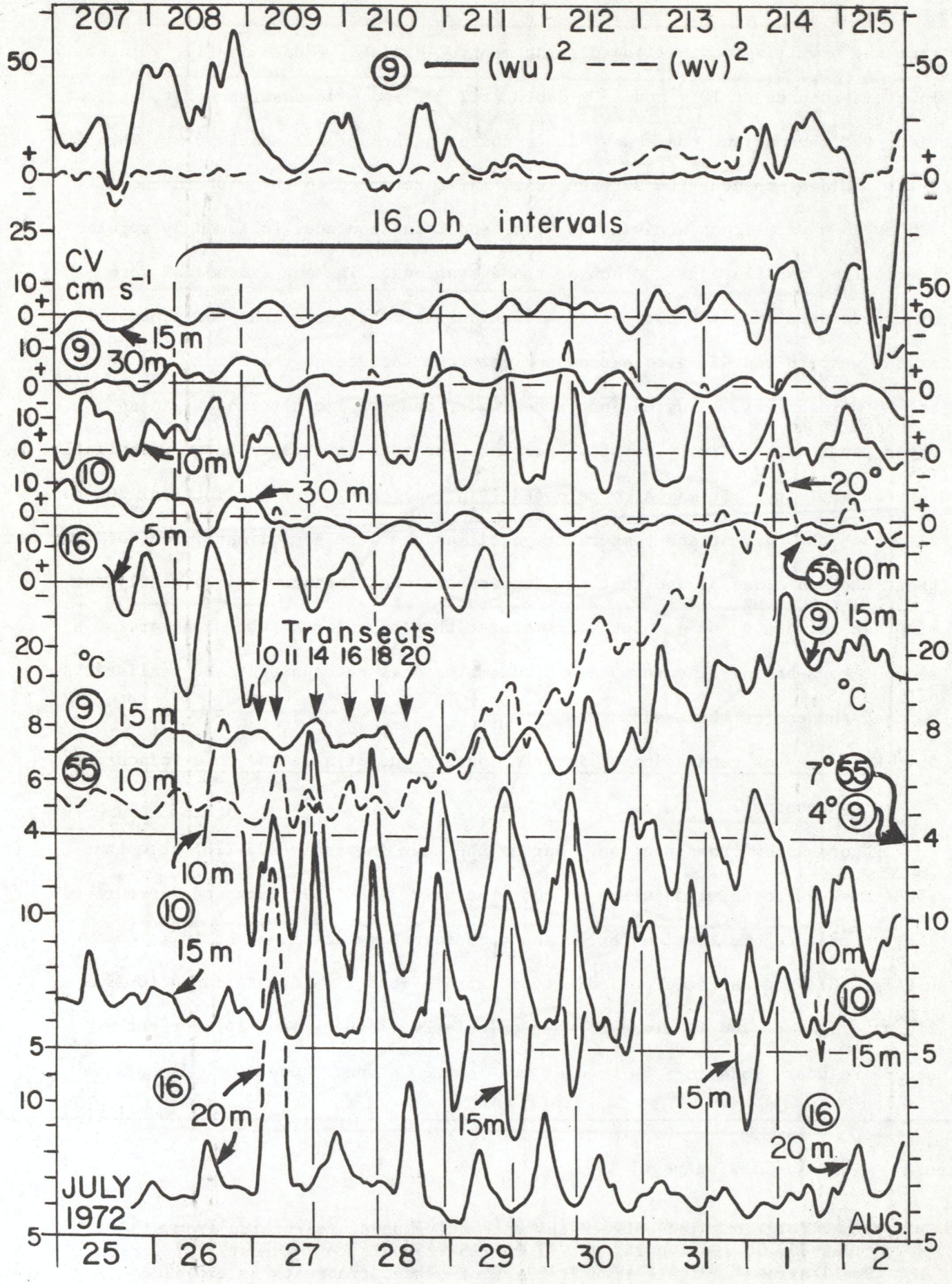

Figure 44. Legend on previous page, 99.

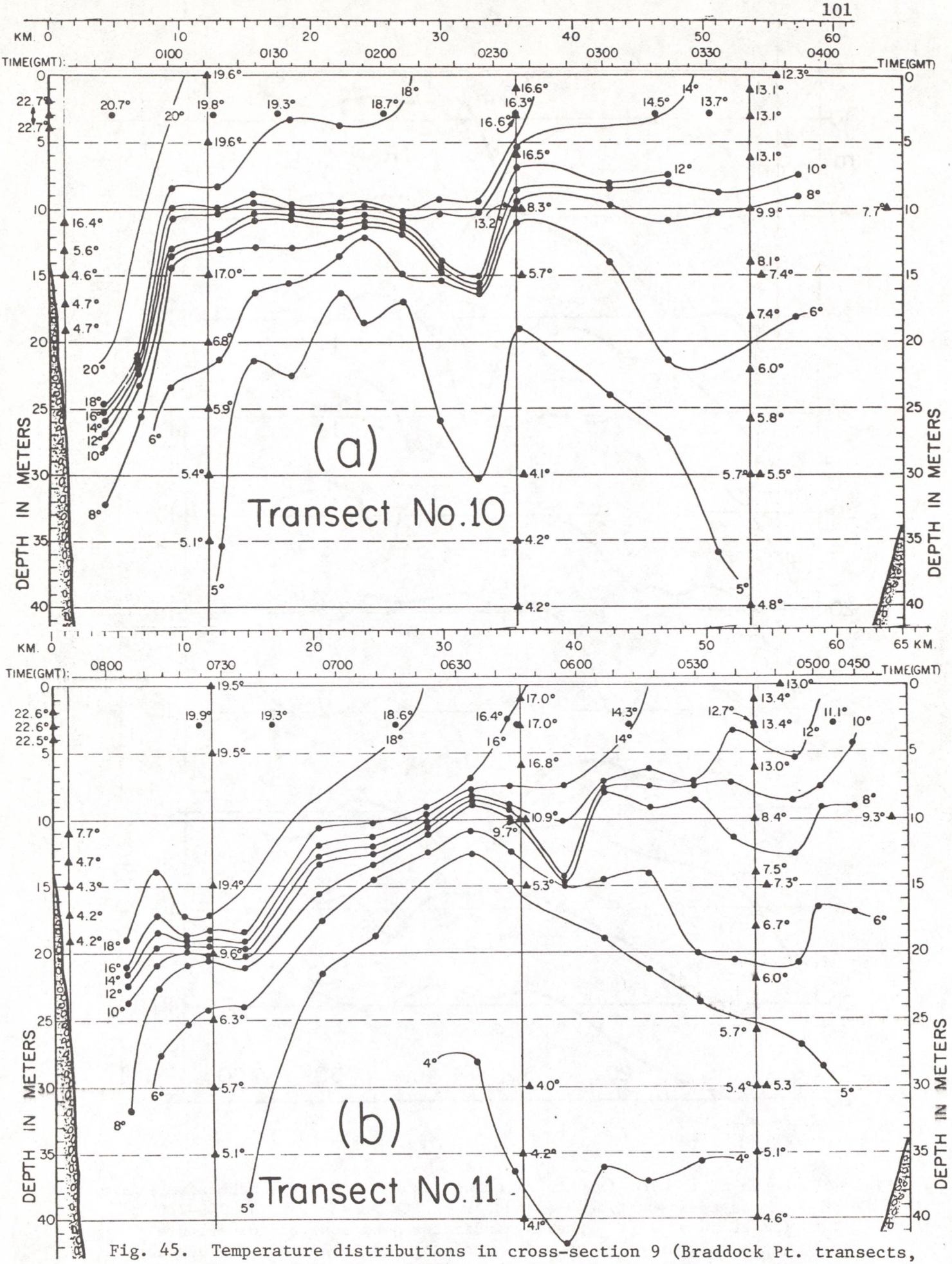

Fig. 45. Temperature distributions in cross-section 9 (Braddock Pt. transects, Boyce and Mortimer 1977) on JD 209, 27 July 1972.

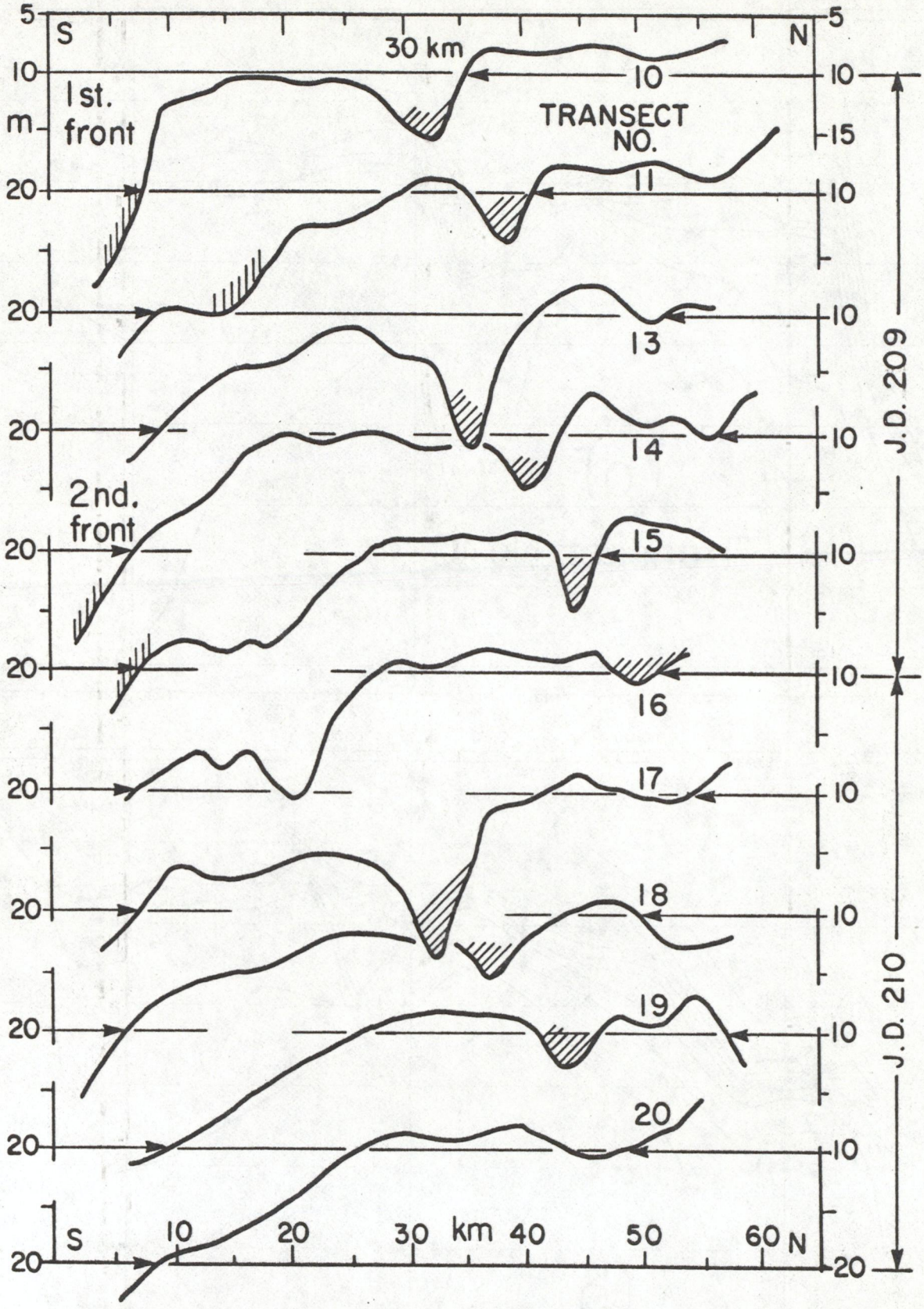

Fig. 46. Depth of the 10° (mid-thermocline) isotherm during successive transects across cross-section 9 (Braddock Pt. to Presquile), JD 209-210 (27-28 July) 1972. Shading indicates positions of temperature fronts (internal surges), the northward progression of which is discussed in the text.

and densities fitted to Lake Ontario conditions (c_i = 40 cm s^{-1}). The evidence for a cross-channel bimodal response in the real lake may be sought (i) in the phase relationships between current and temperature records at 9, 10, and 16 (Fig. 44) and (ii) contemporary cross-channel temperature structure disclosed by repeated transects with the towed, depth-undulating temperature recorder (Boyce and Mortimer 1977).

The windy weather from 203 to 208 culminated in a strong eastgoing impulse (stress >1.5 dyn cm^{-2} at 9) during the evening of 208. This produced a strong downwelling front at the southern end of section 9 (Fig. 45a) which then propagated northward as an internal surge (Fig. 45b) in the manner described by Mortimer (1977, see Figs. 53-57 there) modelled by Simons (1978) and discussed in Section 2.10. When the surge passed 16, a large upswing of temperature occurred there at 20 m depth (16/209, Fig. 44). Further progress of the surge, and of a second one which followed 15 h later, can be followed in Figures 46 and 47. (There are also signals, in Figures 45 and 46, of an earlier surge sequence, seen at 32 and 39 km in transects 10 and 11, respectively, and probably initiated by downwelling along the southern shore during the early hours of 208).

Figure 46 displays the depth variation of a mid-thermocline (10°C) isotherm across the section in ten successive transects (no. 12 incomplete and omitted) with the downwelling fronts and subsequent surges shown shaded. In Figure 47 are plotted the encounter times and distances of the surge front from the S. shore. The average rate of northward progress was 2.2 km h^{-1}, with an indication (broken line) that the front travels slower near shore and faster in deep water. This is similar to the propagation speed (2.3 km h^{-1}) of a later surge (J.D. 223/4) previously described by Mortimer 1977. The time spacing (15 h) between the first and second frontogenesis is the same in both cases. In both cases, also, the eastward wind stress fell to low values after the initial

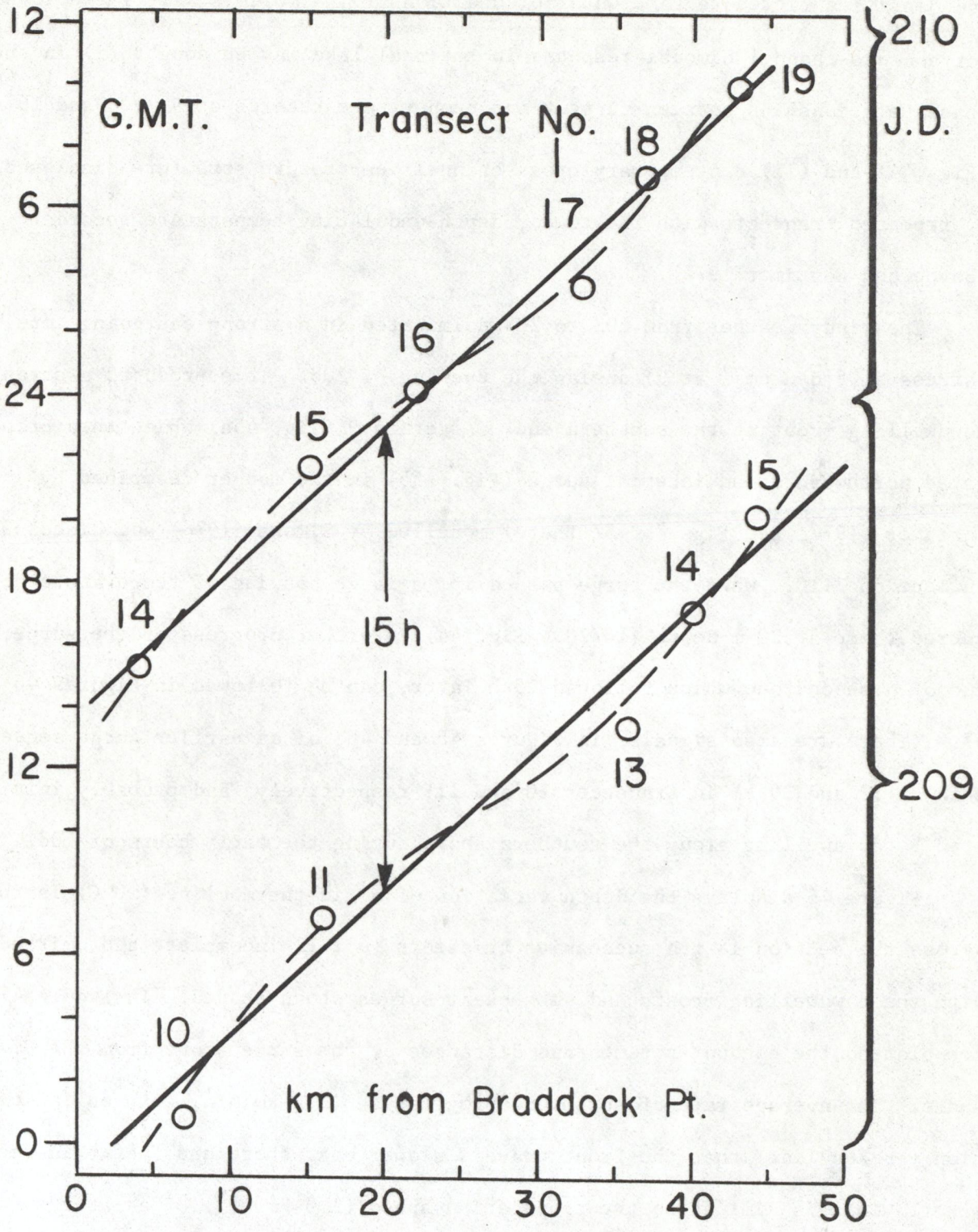

Fig. 47. Time-distance plot showing northward progress of the internal surges illustrated in Figure 46. For further details, see text.

impulse had generated the downwelling front along the southern shore. The surge responses must therefore be viewed as free oscillations, but with conspicuous non-linear wave features, discussed in Section 2.10. These features arise because the amplitude of the initial nearshore downswing of the thermocline is large compared with water depth there. The result is generation of an internal surge or solitary wave, which then propagates away from the shore. In the meantime, the thermocline continues to oscillate up and down with near-inertial periodicity and, if the next downswing is large enough, a second surge is generated.

Turning to cross-section 11, there was also strong downwelling at the S. shore before midnight on 208; and thereafter the APB fit was also close to 16 h (shown fitted to 16.5 h in 11/203-216 A) but no stable phase relationships developed between 11 and 19 (or 20). However, the current and temperature oscillations at 10 and 11 were approximately in phase during 208 to 210; but there is not enough evidence to confirm or deny oscillatory coherence between sections 9 and 11. Examination of the corresponding transect runs across the Oswego section (Boyce and Mortimer 1977, pp. 234-242) discloses a strongly "domed" thermocline with oscillations about a mid-section "node," not further identified. Examination of transects 10 and 11 (JD 209, pp. 236, 237) also reveals weak evidence of a surge propagating northward at about 2 km h^{-1}.

The internal surges, when they occur, are superimposed on larger-scale cross-channel oscillations. For example in cross-section 9, the wind impulse

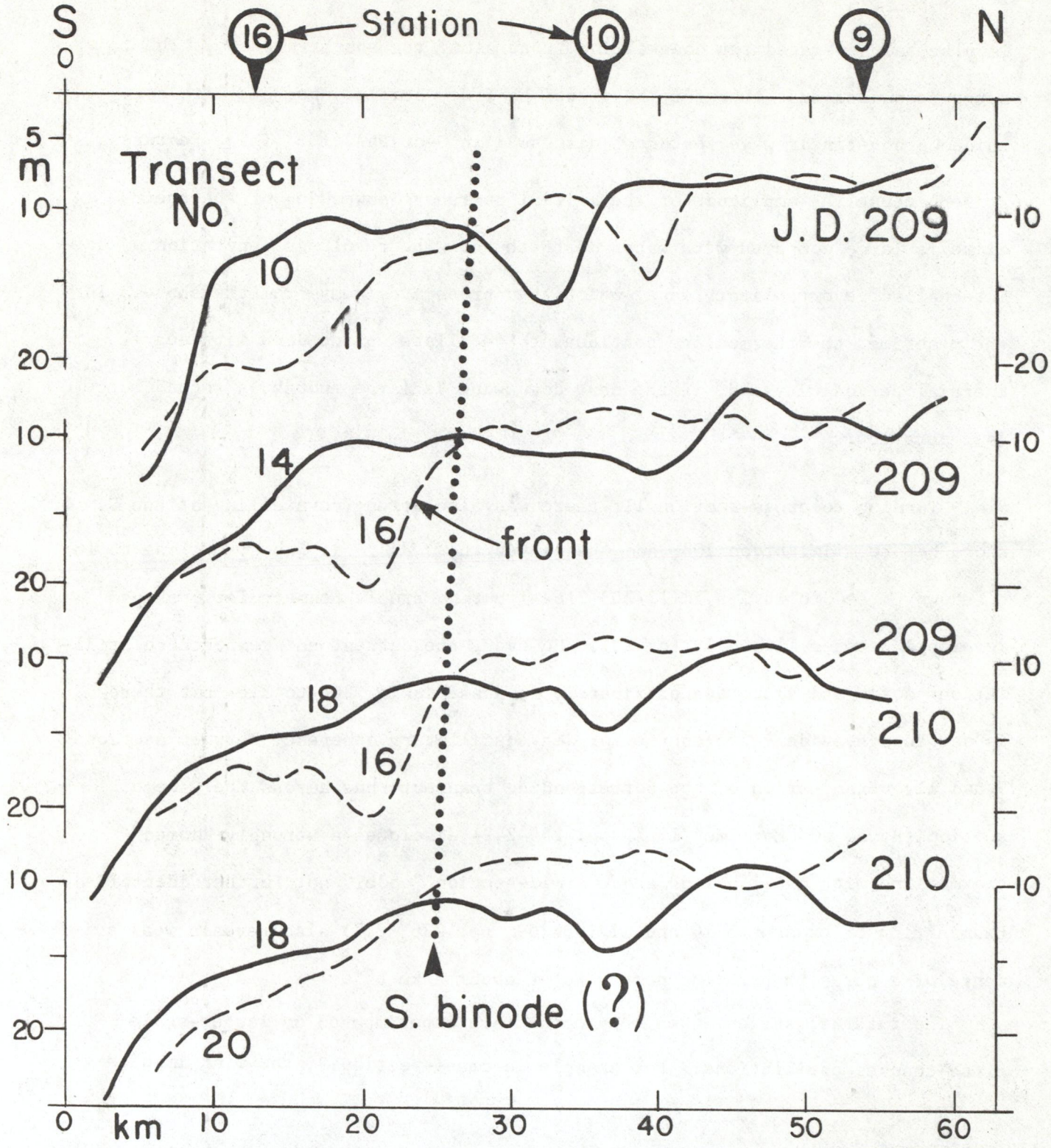

Fig. 48. Depth of the 10° (mid-thermocline) isotherm during selected pairs of transects across cross-section 9 (Braddock Pt. to Presquile, from Boyce and Mortimer 1977). Transect pairs were selected to coincide as closely as possible with maxima and minima in thermocline elevation at stations 9 and 16 (see Fig. 44).

on 208 and the ensuing south-shore downwelling (Fig. 45a) were followed by a near-inertial cross-basin oscillation of the thermocline which is illustrated in Figure 48. In that figure the cross-basin thermocline topography is represented by 10°C isotherms taken from Braddock Pt. to Presqu'ile transects (examples in Fig. 45) covering the interval 209-210. The isotherms are displayed for pairs of transects, selected so that one member of the pair coincides as closely as possible with a peak in the temperature wave at 16 (transit times shown in Fig. 44) and the other coincides with a trough. Selected in this way, the transect pairs display a near-maximum swing of the thermocline and may be expected to disclose the positions of nodes, if present. The average arched shape of the thermocline, sloping upward toward north, changed little during the two days here reviewed. Initially (transect Nos. 10 and 11) the topography was dominated by downwelling and internal surge propagation. Later pairs disclose the presence of a distinct node near 25 km, which moved a little to the south as time progressed, occupying a position well to the south of the uninode later clearly identified in examples of first Poincaré-type mode response. The position of the node, labelled S. binode in Figure 48, and the evident antiphase behavior of temperature oscillations at 10 and 16 in Figure 44, provide strong evidence of second mode response; but the existence and position of a northern binode cannot be clearly demonstrated.

During the interval occupied by transects 14 to 20 (Figs. 44 and 48) the temperature oscillations at 9 were weak but were approximately in phase with those at 10, consistent with the presence of a binode north of 9. (Contemporary, weak temperature oscillations at 59 are too irregular to settle the question.) But during the three days (211-213) which followed, 9 and 10 become clearly out of phase in temperature; and this (with the persistence of 10/16 antiphase behavior) would be consistent with the development of a node south of 9 (e.g., near 50 km) and the persistence of a node near 25 km. And, as already

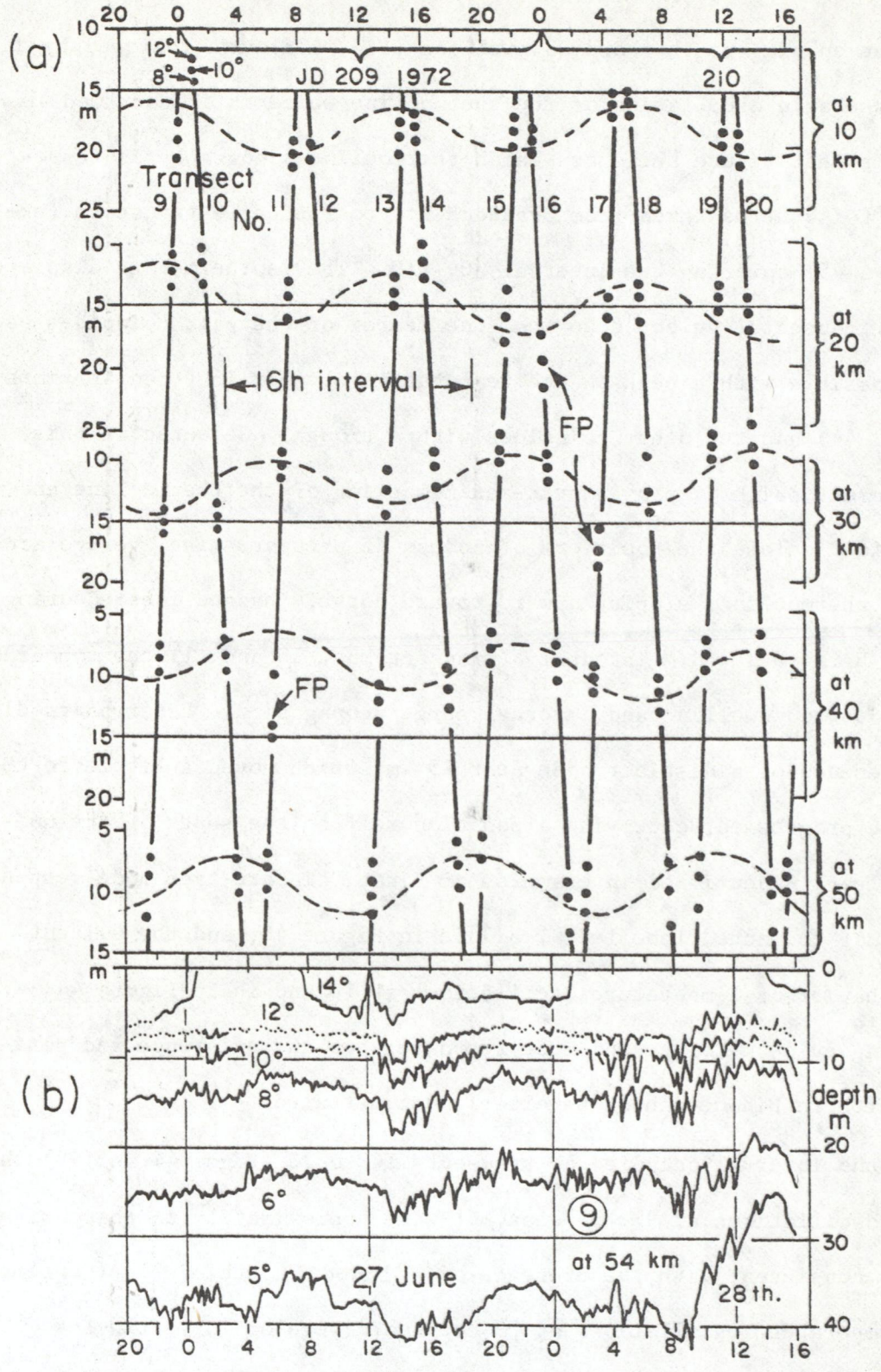

Figure 49. Variation in isotherm depth in cross-section 9, JD 209-210 (27-28) July) 1972: (a) dots show depths of the 12°, 10°, and 8° isotherms at the times of vessel transit at the following distances from Braddock Pt. -- 10, 20, 30, 40 and 50 km; (b) isotherm depths interpolated from temperatures measured at 19 depths by a thermistor chain near station 9 (data by courtesy of Canada Centre for Inland Waters). FP indicates passage of a temperature front, described with other details in the text.

noted, the 16 h periodicity in temperature and current responses suggests second mode dominance; but the phase relationships of the currents do not yield conclusive evidence of this. In a second mode structure, currents at stations 9 and 16 would be in antiphase. This may have been the case on 210 and 211 (see the 30 m records, Fig. 44), but the current oscillation at 9 is too weak and too irregular to yield a conclusion. If station 10 was near the central antinode in a binodal system, currents there would be weak (in fact they were strong) and, depending on which side of the antinode station 10 was located, the currents at 10 would be out of phase with those at 9 and in phase with those at 16, or vice versa. But a clear picture of current phases does not emerge from Figure 44. In fact, the only consistent phase relationship seen there is the 10 m/30 m antiphase at station 10, i.e., a phase change across the thermocline generally found at all stations.

Some additional, independent evidence is provided by the time-variation of isotherm depth at station 9 during 209-210, interpolated from thermistor chain records (Boyce, personal communication). Those interpolations are plotted in Figure 49 (bottom panel) and compared there with isotherm-depth variations at 10 km intervals across the Braddock Pt. cross-section, as deduced from successive transect runs (Nos. 9 to 20). Apart from depth aberrations caused by passages of the internal surge front (examples marked FP), the oscillations in isotherm depth (range about 4 m) display a fair fit with a 16 h wave and a clear phase change between 20 and 30 km, consistent with the presence of a node near 25 km. The oscillations at 10 and 20 km are roughly in phase, as are also the oscillations at 30 and 40 km. The phase relationship between 40 and 50 km is less clear, and the interpolated isotherm depths at station 9 (54 km) show a better fit with the transect results at 40 km than at 50 km. In other words, the northern binode of the presumed binodal response cannot be unambiguously identified or located.

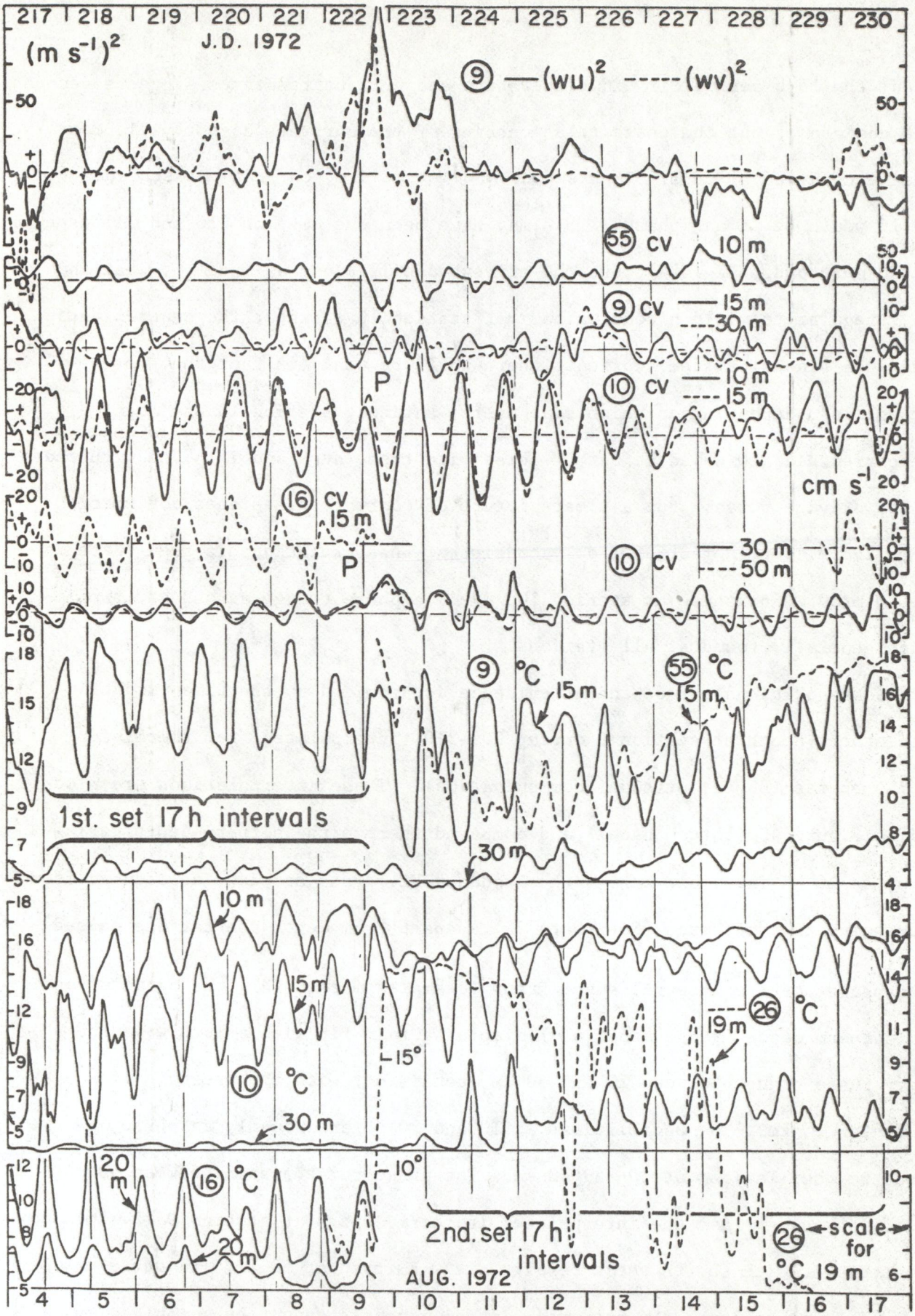

Figure 50. Composite diagram 9/217-230: wind components $(wu)^2$ and $(wv)^2$ at 9; current component (cv) and temperature (°C) at various depths at 55, 9, 10, and 16. For further details see legend of Fig. 34.

5.5 Responses before and after a severe storm on day 222 (9 August).

At stations 2 and 3, a regular current oscillation (fitting a 17 h APB) was in progress before the storm on 222 (2/217-230 A). The temperature oscillations at 2 and 4 at that time (217-221) were less regular or were intermittent; but the oscillation at station 3 was dominated by a higher frequency component (fitted to 14.4 h APB in 2/217-230 A). The strong wind on 222 lasted for about 8 h and, perhaps as expected, was followed by strong inertial oscillations in current and temperature at 3 and at 2 (only 30 m records are available). Allowing for the anticipated phase reversal between currents at 10 and 30 m, the records show that currents at 2 and 3 (less clearly at 4) were approximately in phase and that the period was indistinguishable from inertial (APB 17.4 h). The same held true for the temperature oscillations. Similar inertial oscillations in both current and temperature were also seen at 6 (6/217-230 A) for as long as eight cycles after the storm and also during the episode before the storm. At the nearshore tower 23, however, the brief episode of temperature oscillation (218-219) showed a better fit with a shorter period. The general conclusion is that the 222 wind impulse generated predominantly inertial responses at offshore stations 2, 3, and 6 with no visible contribution from whole-basin Poincaré-type motion.

On the other hand in cross-section 9, a distinctly better fit to both current and temperature oscillations is obtained with a 17 h APB (Fig. 50). That figure combines the records from two episodes: one set of oscillations initiated by the short southgoing wind pulse during the morning of 217 and persisting until destroyed by strong wind on 222; and a second set of oscillations set in motion by the 222 storm. In both cases, the current oscillations at 10 exhibit the character of a damped oscillation. However, in the absence of strong wind after the storm, the diminution and subsequent growth of current amplitude at 10, 227-230, may have been partly the consequence of a "beat" between two or more modes (see Fig. 20)

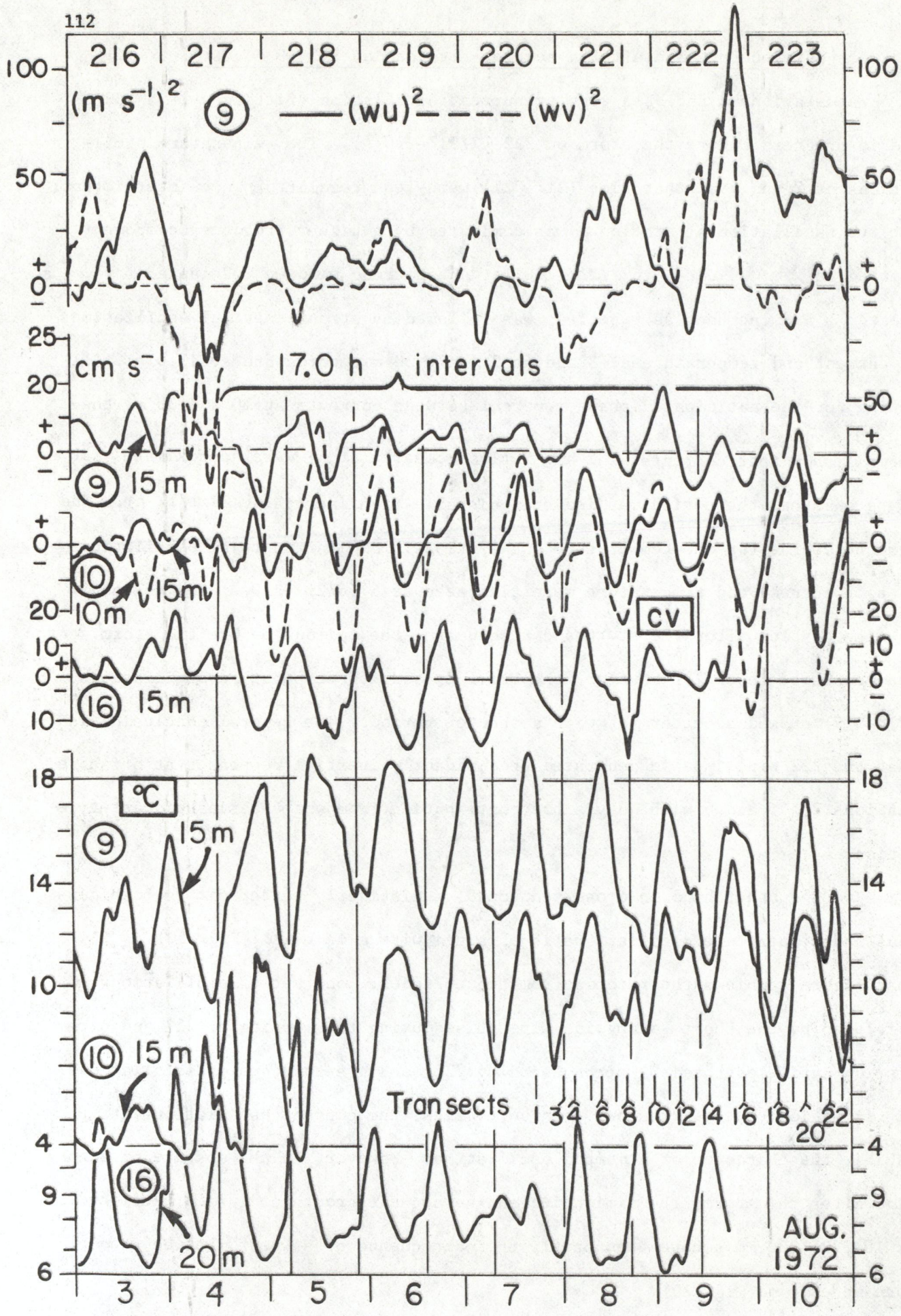

Figure 51. Legend identical with that of Fig. 53 except for interval covered (216 to 223).

In any case, it will be helpful to consider the two episodes separately, starting with Figure 51, in which the current oscillation at 10 was very regular with a average APB of 17 h. Seven cycles covered the interval 218 to 222, at which point there was a marked increase in amplitude (produced by the storm peak in the late hours of 222) with little change in phase. The contemporary current oscillations at 9 and 16 were less regular, but generally in phase with those at 10. Temperature oscillations, less regular than those of the currents, also fit a 17.0 h APB, with 9 and 10 approximately in phase and with 10 and 16 clearly out of phase. Those interstation phase relationships for current and temperature, and the 17.0 h average period, are all consistent with a cross-basin internal seiche of the first mode. This conclusion is also supported by the transect-deduced isotherm-depth variations at 10 km intervals along cross-section, compared (in Fig. 52) with isotherm-depth oscillations interpolated from thermistor chain records at 9. Figure 52 discloses that an oscillation of about 17 h period and 3 m range was nearly in phase at 10, 20, and 30 km, that there was a phase reversal between 30 and 40 km, and that the 17 h oscillation was again nearly in phase at 40 km, 50 km, and at the thermistor chain recorder at station 9 (54 km). This structure and the good fit to a 17 h APB (except for the obvious deviations attributable to surges at FP) is also consistent with a cross-basin first mode response with a node between 30 and 40 km, presumed to be a little south of 10, because of the temperature-phase coincidence at 9 and 10 (Fig. 51).

But the picture changed after the 222 storm. Although a 17.0 h APB remains the best fit to the succeeding episode (Fig. 53) the current oscillation at 10 (and even more so at 9) was less regular than before the storm; the temperature oscillations at 9 and 10 became nearly out of phase (whereas they were in phase before the storm). Unfortunately, the record for 16 is missing except for 229/30, at which time Fig. 53 shows it to be out of phase with the record from 10. It appears, therefore, that the 222 storm brought about a large

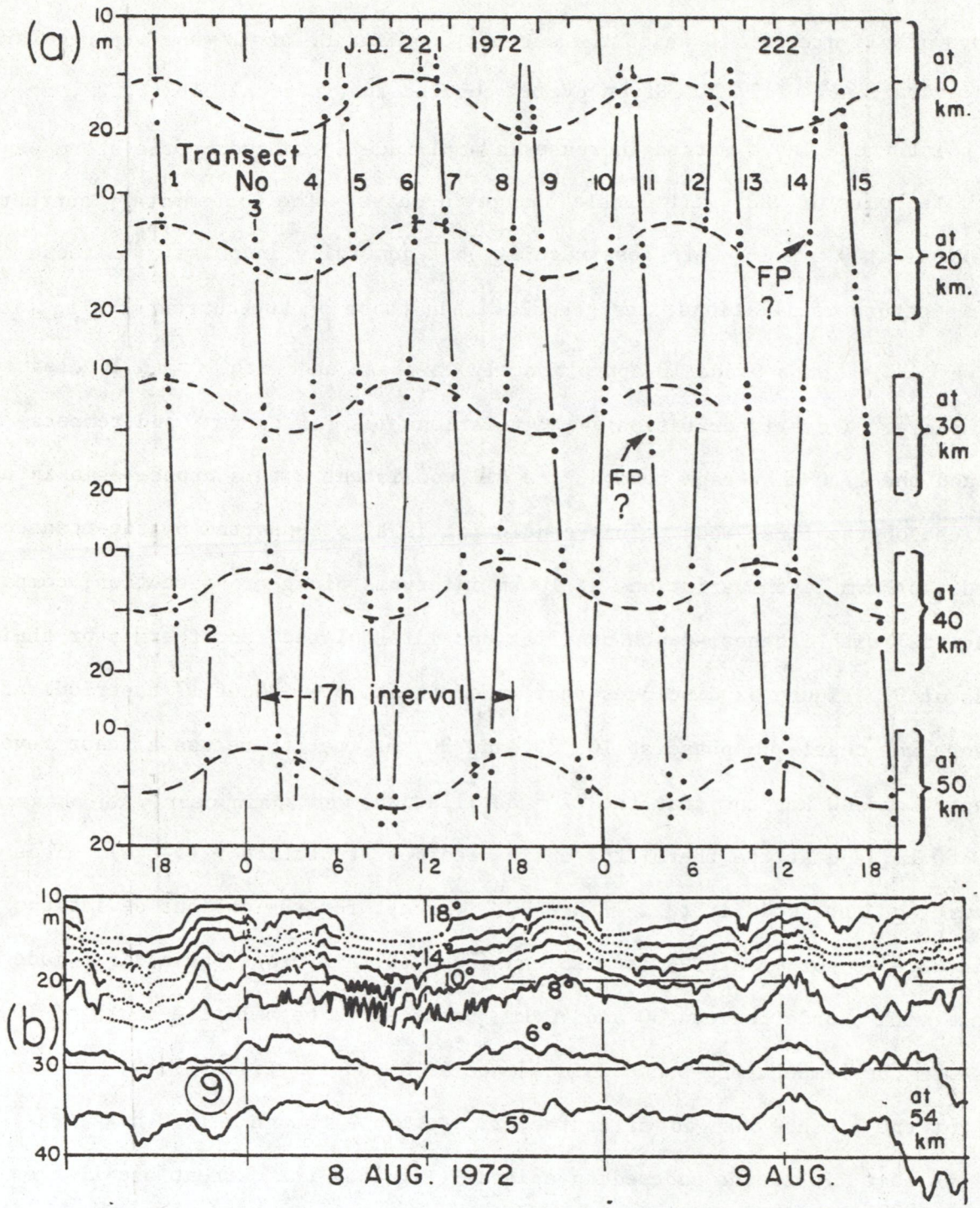

Figure 52. Legend identical with that of Fig. 49 except for interval covered (220-222).

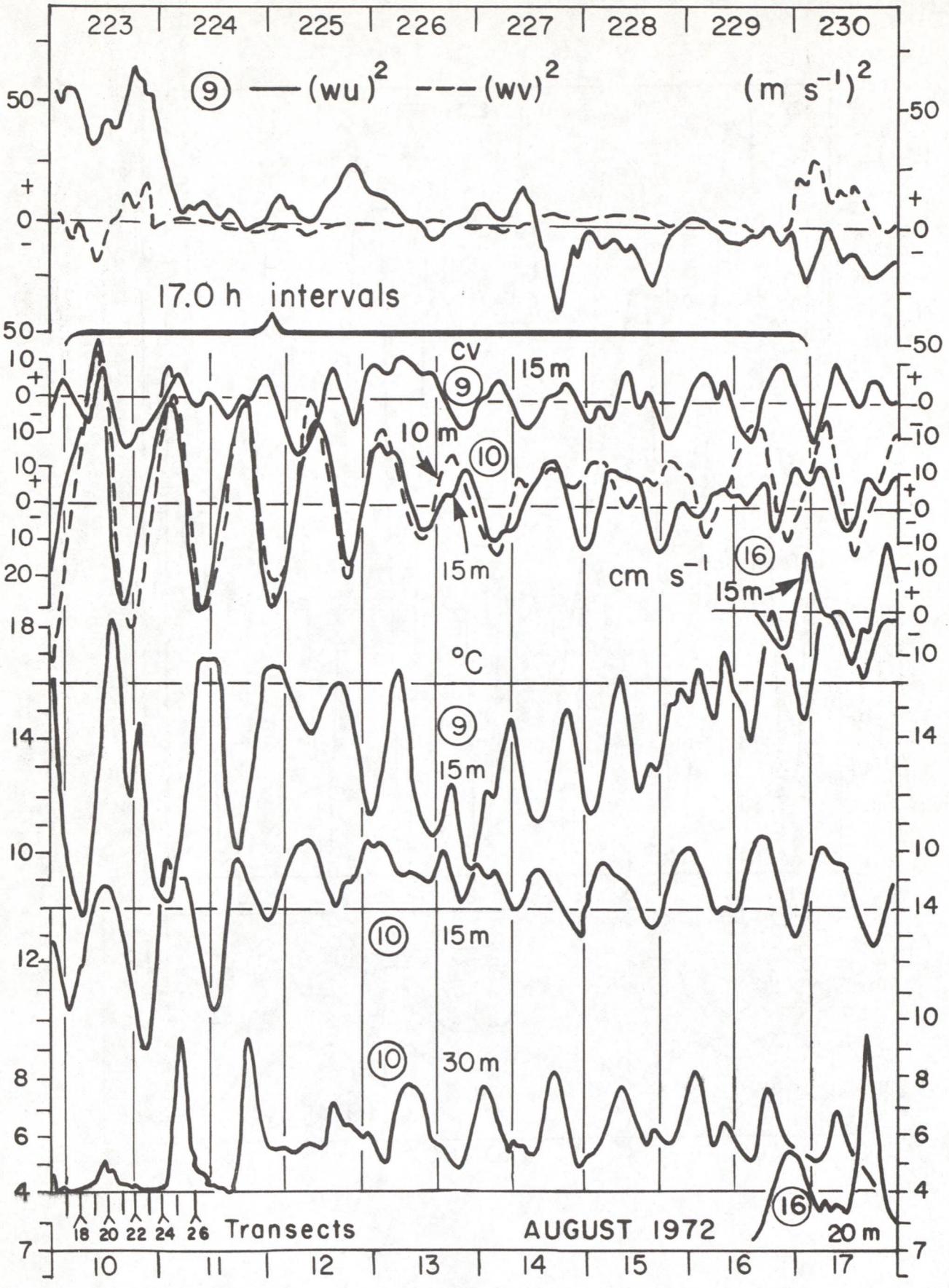

Figure 53. Phase relationships between current and temperature records from stations 9, 10, and 16, JD 223 to 230 (10 to 17 Aug.) 1972. Small arrows indicate transit times of vessel transects as explained in the text. For further details see legend of Fig. 34.

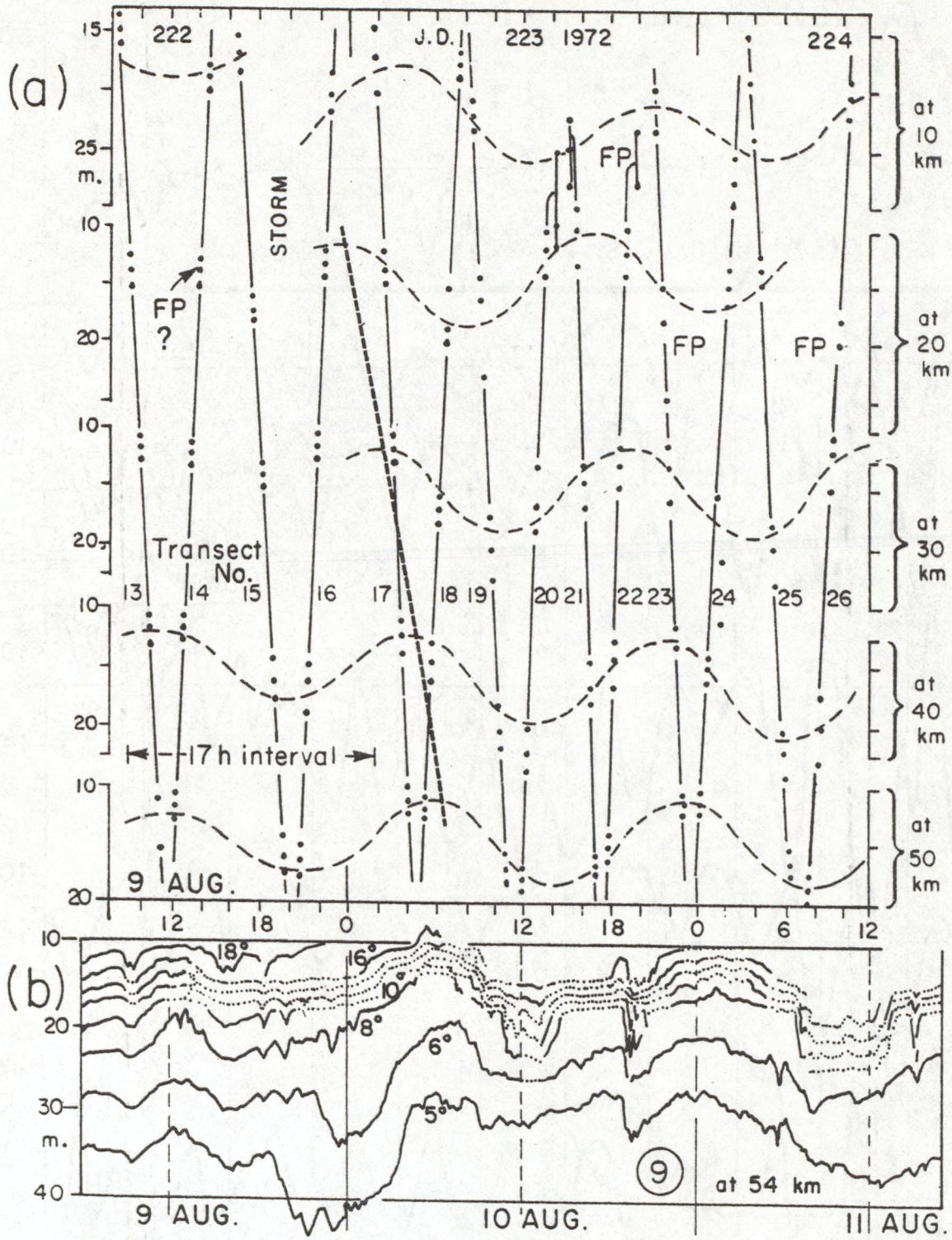

Figure 54. Legend identical with that of Fig. 49 except that the interval covered is 222 to 224. This figure overlaps and extends Fig. 52.

enough change in mean conditions (thermocline deepening, presence of persistent downwelling zone along the southern shore) to cause the node of the predominantly first mode oscillation to shift to the north of station 10, thus bringing the temperature oscillations at 9 and 10 into an out-of-phase relationship. Evidence for a small northward shift of the node during 223-224, bringing it north of 10, is seen in later Figure 55, in which cross-basin distributions of the 10°C isotherm are illustrated for selected Braddock Pt. transect pairs (transit times shown in Fig. 53) timed to show the maximum excursions of the thermocline topography. However, too much reliance cannot be placed on that figure, because thermocline structure was obviously much perturbed by the progression of the internal surge sequences described in Mortimer (1977).

Evidence for a large change in internal wave dynamics after the 222 storm is contained in Figure 54, which is a continuation of Figure 52 with some overlap. Whereas before the storm (Fig. 52) the picture was one of a uninodal standing wave with a node situated between 30 and 40 km, the oscillation after the storm has the character of a wave (still of 17 h period) progressing from south to north at a speed of roughly 5 km h^{-1} between 20 and 50 km, i.e., across that part of the cross-section which lies outside the strongly downwelling-perturbed region within 15 km of the southern shore. That rate of progress is slower than that calculated for a progressive internal Poincaré wave fitted to the dimensions and density distribution in the section, but is (it may be noted) over three times faster than c_i calculated from equations (6 or 16) and a little more than twice as fast as the speed of progress of the internal surges described earlier. Figure 54 may perhaps therefore be taken to represent intial and transition stages in the generation of a whole-basin Poincaré-type response to the storm, starting with a downwelling/upwelling event, in which the downwelling motion is the stronger (see Fig. 6 in Mortimer 1977) followed by a cross-channel internal progressive wave pair (of which the northgoing member is the stronger) which will

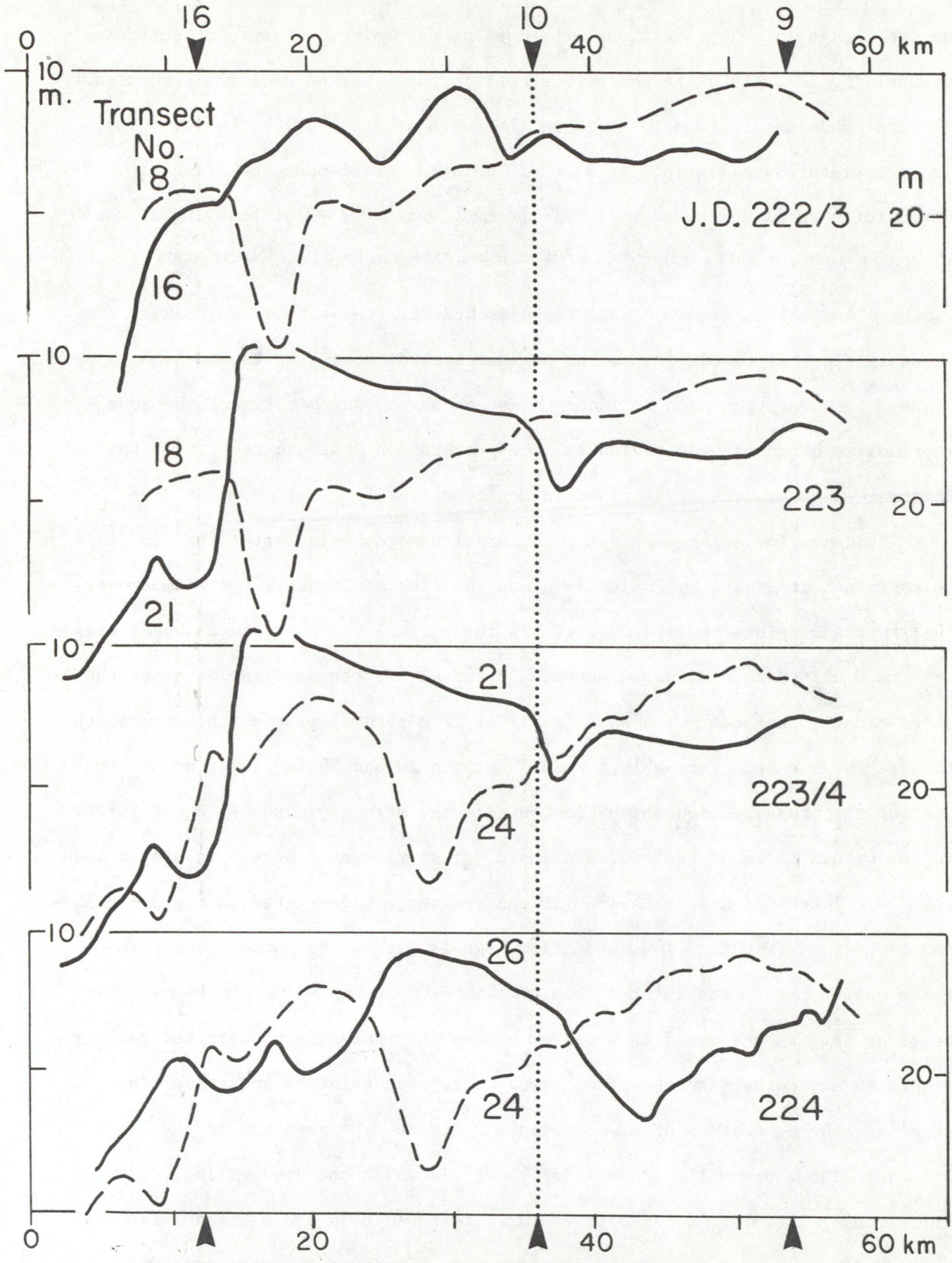

Figure 55. Depth of the 10° (mid-thermocline) isotherm during successive transects across cross-section 9 (Braddock Pt. to Presqu'ile), JD 272-224 (9-11 Aug.) 1972.

later combine to form a standing wave pattern. It is unfortunate that the transect cruises did not continue long enough to allow Figs. 54 and 55) to confirm and display the transition during this particular episode; but a clearer example will be shown later of an episode with uninodal seiche dominance (Sept. 30 to 6 Oct., see section 5.8). Figure 55 also displays the persistence of downwelling in the southern 15 km-wide part of the cross-section. That persistence signals the presence of a strong east-going current in approximate geostrophic balance. Motions in the downwelling zone make it difficult to observe the cross-basin oscillation there. That oscillation is best seen in the central part of the section including the presumed uninode near station 10.

Whereas the dominance of a first mode response has been established in cross-section 9 with certainty for the interval 217-222 and with fair probability for the interval 223-229, such dominance is not visible in other cross-sections. In cross-section 2, as already noted, the strong and persistent current oscillation at 3 could not be distinguished in period from inertial; and in cross-section 6 the same was true for current oscillations at station 6 during both intervals, although for a short interval (217-219) the temperature oscillations at that station were of distinctly shorter period (16 h) and apparently in antiphase with oscillations of similar period at 23 (6/217-230 A).

The interval 217 to 230 was marked in cross-section 11 by a best fit to a 17.0 h ^{APB} (11/217-230 A), but with much less regular oscillations in current and temperature than in cross-section 9. Persistent temperature antiphase between 11 and 20 (or 21) -- expected if a uninodal internal seiche had dominated the section -- was not observed. We must conclude therefore that, if the clear first mode response in section 9 was the expression of a whole-basin oscillation, its signals were masked elsewhere by other motions, including strong inertial motions in currents at 3 and 6.

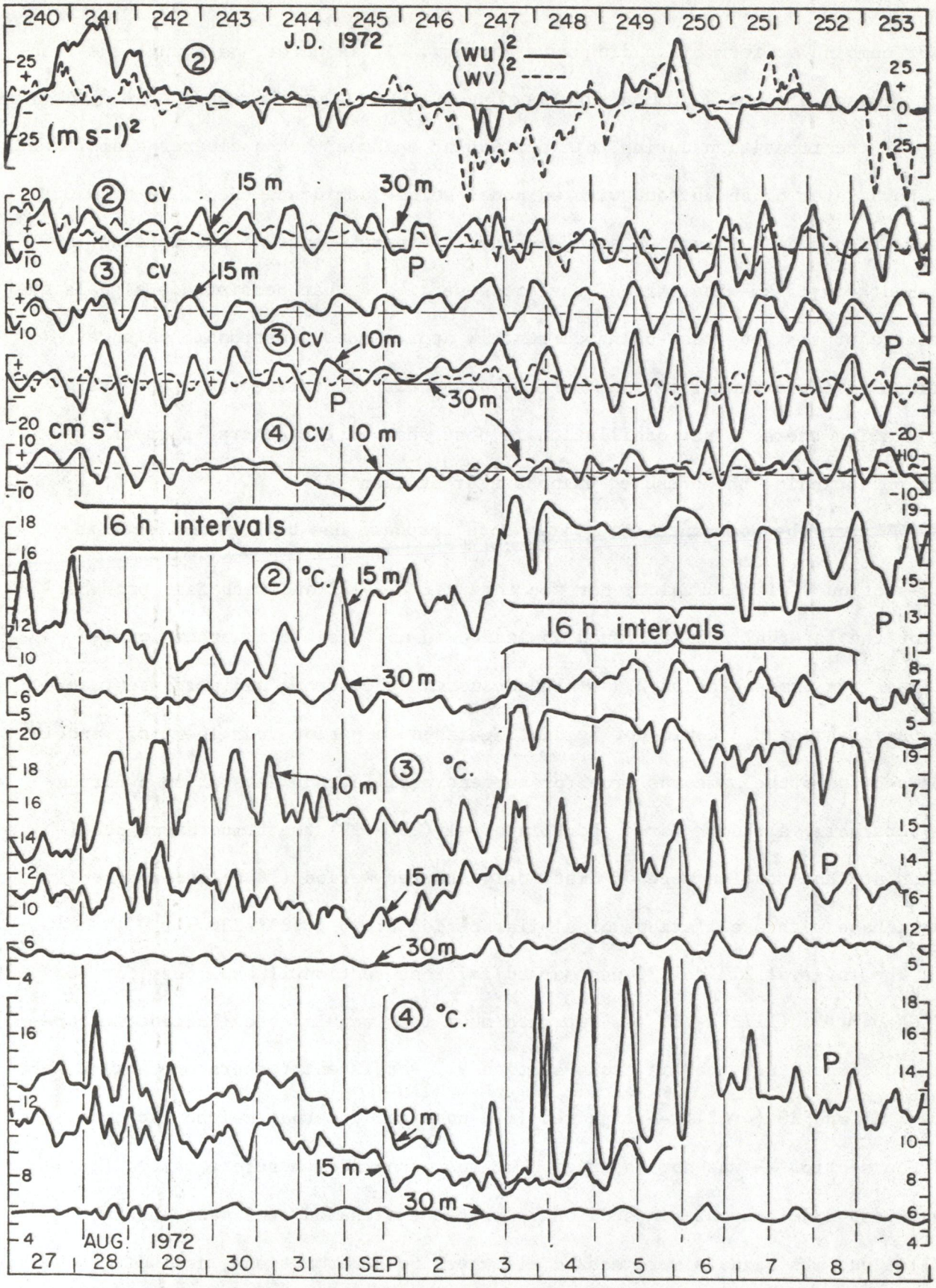

Figure 56. Composite diagram 2/240-253: wind components $(wu)^2$ and $(wv)^2$ at 2; current component (cv) and temperature (°C) at various depths at 2, 3, and 4 (further details in legend of Fig. 34).

5.6 Mixed responses during a month (231-259) of moderate, variable wind.

The interval 231-259 is marked by a series of brief and often interrupted responses often associated with irregular oscillations to which period-fitting is of doubtful value. In such cases 17.4 h lines were drawn, intended more as a guide to the eye than to suggest that an inertial oscillation was, in fact, in progress. In many cases, the temperature oscillations were obviously of shorter period than the current oscillations. Although the 231-259 interval contains no clear example of dominance of a particular mode, some episodes merit brief description to demonstrate the variability encountered. For further details, the diagrams in the appendix may be consulted.

In cross-section 2 the interval 231-259 was marked by calm weather and by weak but regular inertial oscillations in current at station 3 with variation in amplitude reminiscent of a beat phenomenon (2/231-239 A). Currents were generally even weaker at station 4. Temperature oscillations at station 3 (and at 4) exhibited a periodicity distinctly shorter than inertial. After three windy days (239-241, westgoing wind veering to eastgoing) the current oscillations at 2 showed a better fit with 16 h, while the temperature oscillations (quite strong at 3) were irregular and generally of period shorter than 16 h (2/240-253, Fig. 56). The same figure displays a more regular and more cross-section-coherent oscillation during and after three windy days (247-249). Current oscillations fitting a 16 h period were in phase at 2, 3, and 4; and temperature oscillations (of slightly shorter or irregular period) were generally nearly out of phase between 3 and 4 and sometimes nearly in phase between 2 and 3. No other information is available to determine whether this oscillation might be a signal from a particular Poincaré-type mode (the second cross-basin mode?); but it should be noted that the contemporary current oscillation at 6 (6/240-253 A) could not be distinguished in period from 17.4 h, i.e., distinctly longer than the average periods

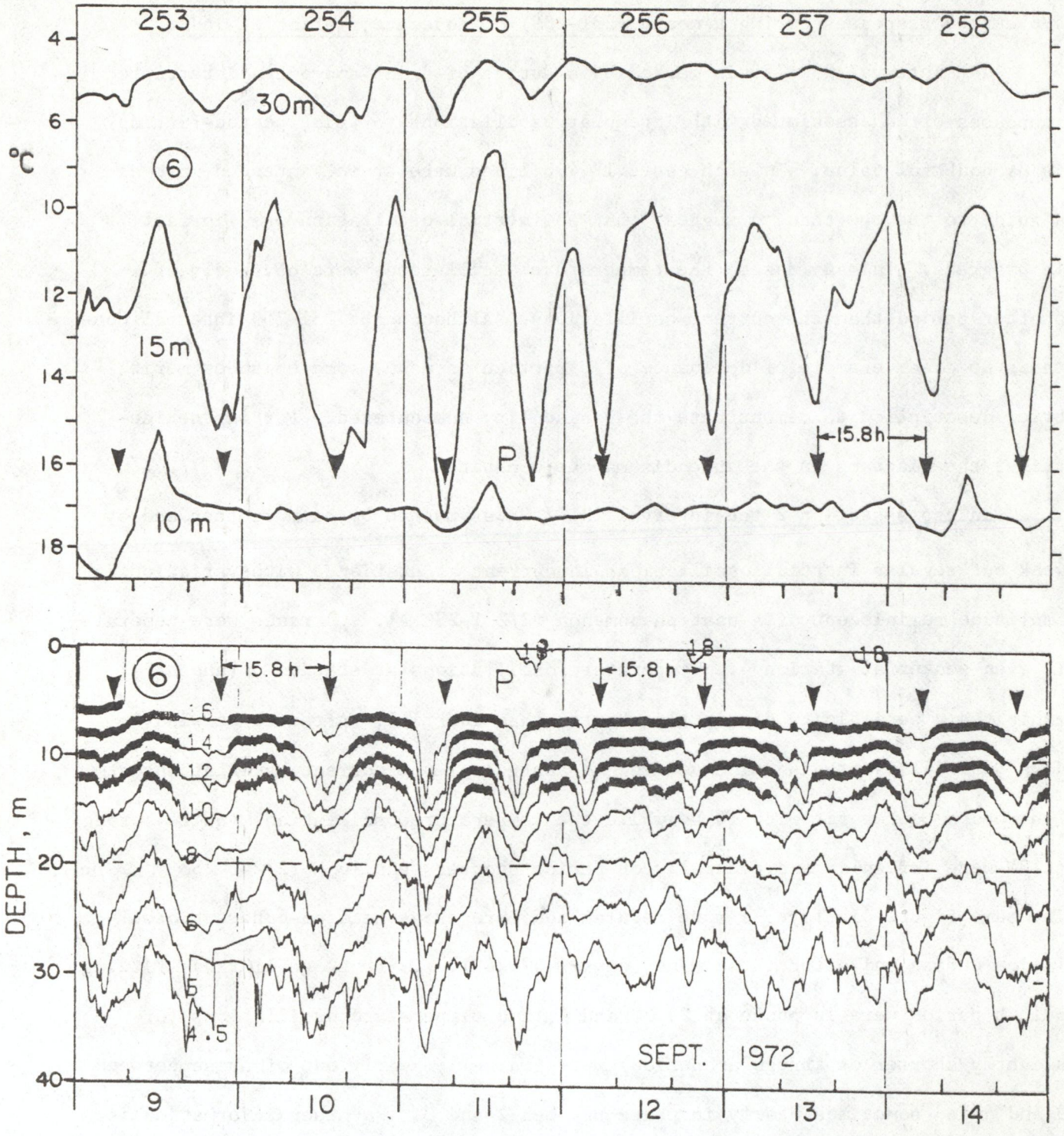

Figure 57. Station 6, JD 253-258 (9-14 Sept.) 1972): (upper portion), temperature fluctuations (°C scale inverted) at three depths at station 6; and (lower portion) isotherm depth fluctuations interpolated from temperature measurements at 19 depths at a thermistor chain near station 6. The thermistor chain data were supplied by the Canada Centre for Inland Waters. The records are fitted to 15.8 h APB (arrows), and P indicates a phase change during JD 225.

at the western stations. Another short episode of relatively coherent oscillation occurred in cross-section 2 after a wind impulse on 254 (see 2/254-258, plotted on the same sheet as 2/231-239 A); but in this case a phase difference was maintained between 3 and 4 and the APB fit is 17 h. The temperature oscillations (15.8 h APB) were regular and out of phase at 2 and 3; those at 4 were less regular.

Turning now to cross-section 6 (6/231-244 A) the picture is one of irregularity in both current and temperature oscillations. For example, the period of the current oscillation at station 6 in that figure was initially close to inertial, but becomes distinctly shorter after 234. There was no conspicuous change in wind to explain this. In the succeeding figure (6/245-258 A) a short burst of near-inertial current oscillation was associated with southgoing wind on 247/8 and later disturbed by a wind pulse centered on midnight 249/50. Following that pulse, a longer series (9 cycles) of inertial current oscillation ensued, not much perturbed by southgoing wind on 253. Temperature oscillations showed some coherence with the inertial current at 6 for four days (251-254), but became irregular and of much shorter average period. No regular oscillations occurred at 5 or 13. An independent check on the temperature record at station 6 is provided by Figure 57, which displays isotherm depths for the interval 253 to 258, interpolated by the Canada Centre for Inland Waters from thermistor chain records at a station near 6. Plotted on an inverted temperature scale for comparison are the contemporary temperature records at three depths at station 6. The temperature peaks (pointing downward) correspond generally, as expected, with the isotherm troughs, although with a small, unexplained time difference of about two hours (clock error?). The irregular internal waves illustrated in Figure 57 are asymmetric with broad peaks and narrow troughs (higher harmonics present?), their average period is 15.8 h with a phase change during 255, and their amplitudes are

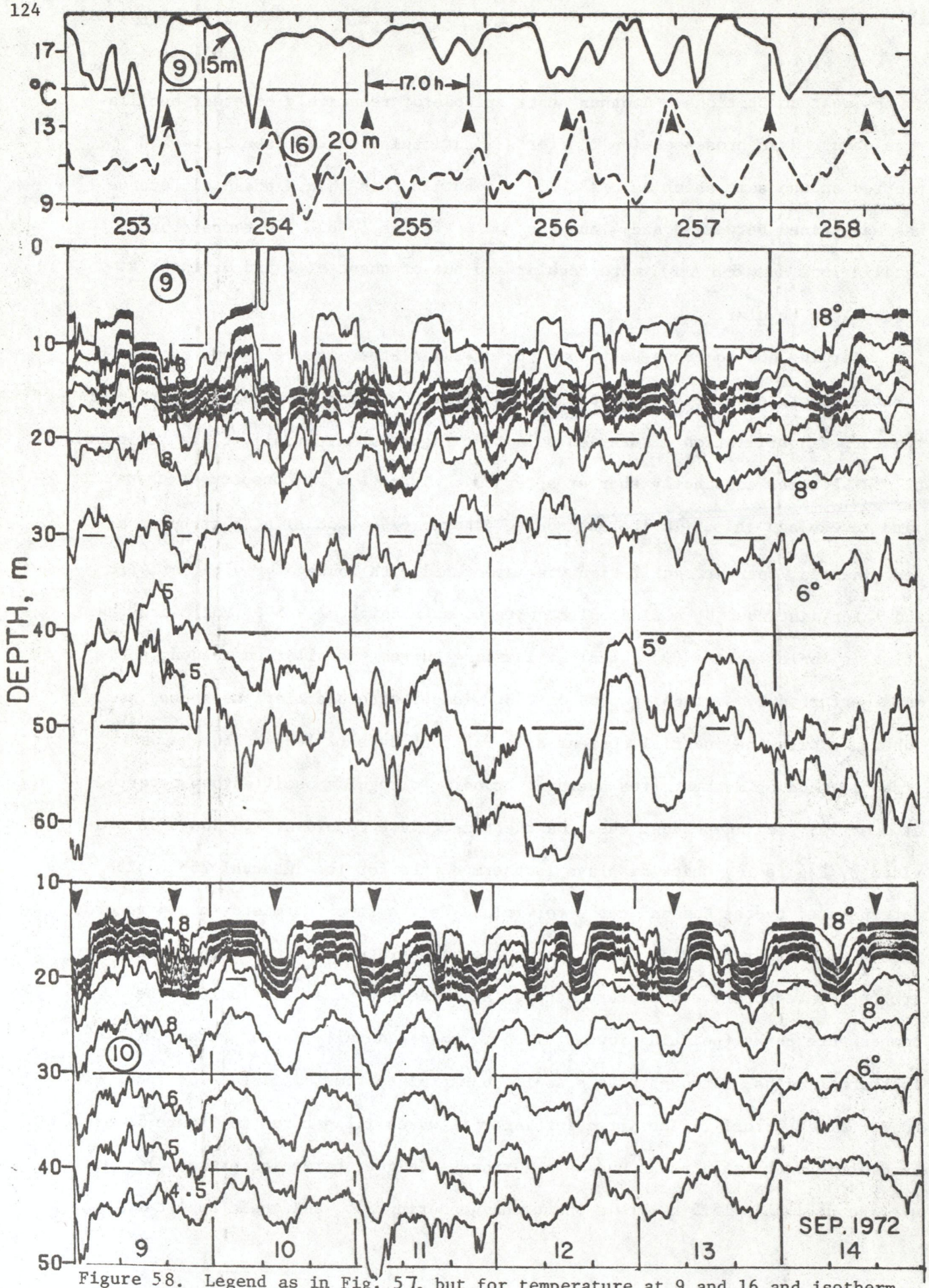

Figure 58. Legend as in Fig. 57, but for temperature at 9 and 16 and isotherm depths (thermistor records) at 9 and 10.

small compared with those seen after stronger wind pulses, as described in the following section, 5.7.

In cross-section 9, the previous dominance of a 17 h current oscillation at 10 (set in motion by the 222 storm) gave way after 231 to a distinctly shorter periodicity (fitted to 15.8 h in 9/217-240 A and to 16.5 h in 9/230-249 A, the latter presented on two sheets). But only the currents at 10 showed this regularity. Current oscillations at stations 9 and 16 and temperature oscillations at all stations were generally irregular. The strong wind on 241 had the effect of damping down existing oscillations rather than generating new ones, although some large temperature oscillations persisted at station 16 with a mean periodicity, after the storm, of 15.8 h and generally out of phase with temperature oscillations at 9.

After the wind pulse on 250, the response was again a mixed one (9/250-263 A). There was a very short burst (3 cycles) of a near-16 h oscillation in current at 55, 59, and 9 (in phase) but little in current elsewhere and only very irregular temperature fluctuations. After southgoing wind on 253, a short burst of inertial oscillation in currents was seen at 55, 59, 9, and (in a scrap of record) at 16, all nearly in phase and fitted in that figure to a 17.4 h period. During the short interval 254-257 there was some evidence of a temperature oscillation at 9, initially coherent with the current and generally out of phase with a more regular series of oscillations at 16, which in turn were nearly in phase with temperature waves at the nearshore tower, 26. The coherence of currents and the phase opposition between 9 and 16/26 (see upper portion of Fig. 58) are consistent with first mode cross-channel response, for which the anticipated period would be 16.95 h, i.e., nearly 17 h; but for so short an episode (254 to 257) there is little to choose in period-fit between 17.4 and 17.0 h.

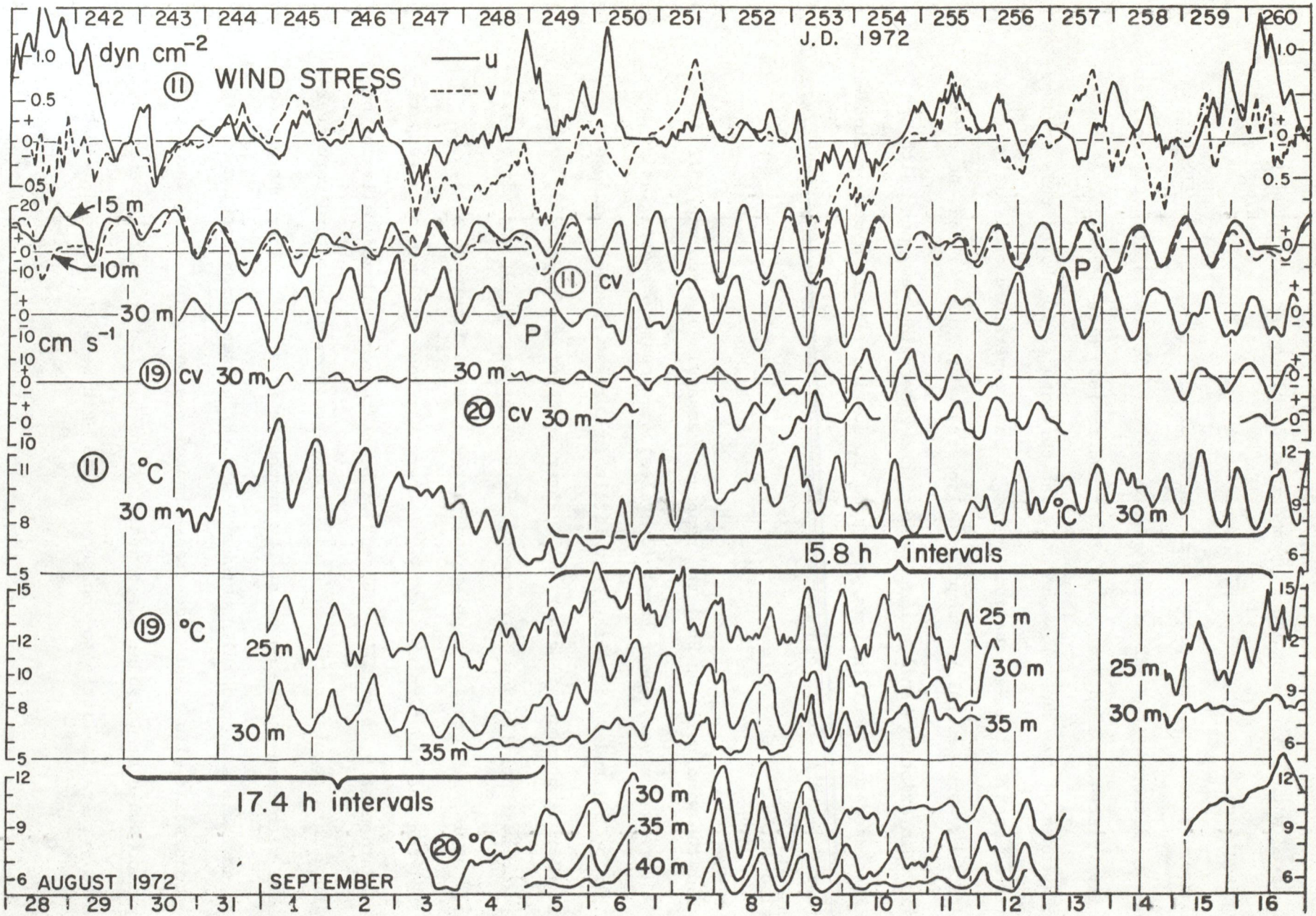

Figure 59. Composite diagram 11/241-60: wind component $(wu)^2$ and $(wv)^2$ at 11; current component (cv) and temperature (°C) at various depths at 11, 19, and 20 (further details in Fig. 34 legend).

Independent evidence is again provided by thermistor chain records (Fig. 58) in which a fairly regular 17.0 h oscillation in isotherm depth is seen at 10, approximately in phase with a much less regular oscillation at 9. There is also evidence at both stations of a double-frequency component of about 8 h period. Temperature peaks at 9 (generally broader than the troughs) approximately coincide, as expected, with isotherm troughs; and the 9/16 temperature antiphase (displayed for this 253-258 interval in 9/250-263 A), coupled with approximate phase coincidence in temperature between 9 and 10, and an average period of 17 h, combine to suggest the dominance of a cross-basin uninodal oscillation with the node south of 10.

In cross-section 11 the effect of a series of wind impulses following each other with a few intervening calm spells, is clearly seen (Fig. 59). The 241/2 storm generated a short burst of inertial oscillation at station 11 (seen in temperature as well as current and with temperature antiphase between 11 and 19) which was destroyed by the 248/9 storm, to be followed by six cycles of shorter period (fitted to APB 15.8 h) in which 11 and 19 were again generally out of phase. The amplitude of the 15.8 h current oscillation decreased after wind on 253 (beat effect?) but picked up again for five cycles (256-259) to be again disturbed by a wind impulse on 260. Also, in the earlier figure for cross-section 11 (11/230-243 A, which preceeds Figure 59) the responses were mixed. After wind on 230/1 there was no marked current response at 11, but a temperature oscillation of short period (fitted to APB 14.4 h) appeared at 20; and the temperature record at 11 showed irregular fluctations with an even shorter mean period.

The month (231-25, 18 Aug. to 15 Sept.) reviewed in this section may be taken as an example of mixed responses to mixed mid-summer wind regimes. The autumnal sequence, now to be reviewed, was marked by stronger, more isolated storms which evoked clearer lake responses.

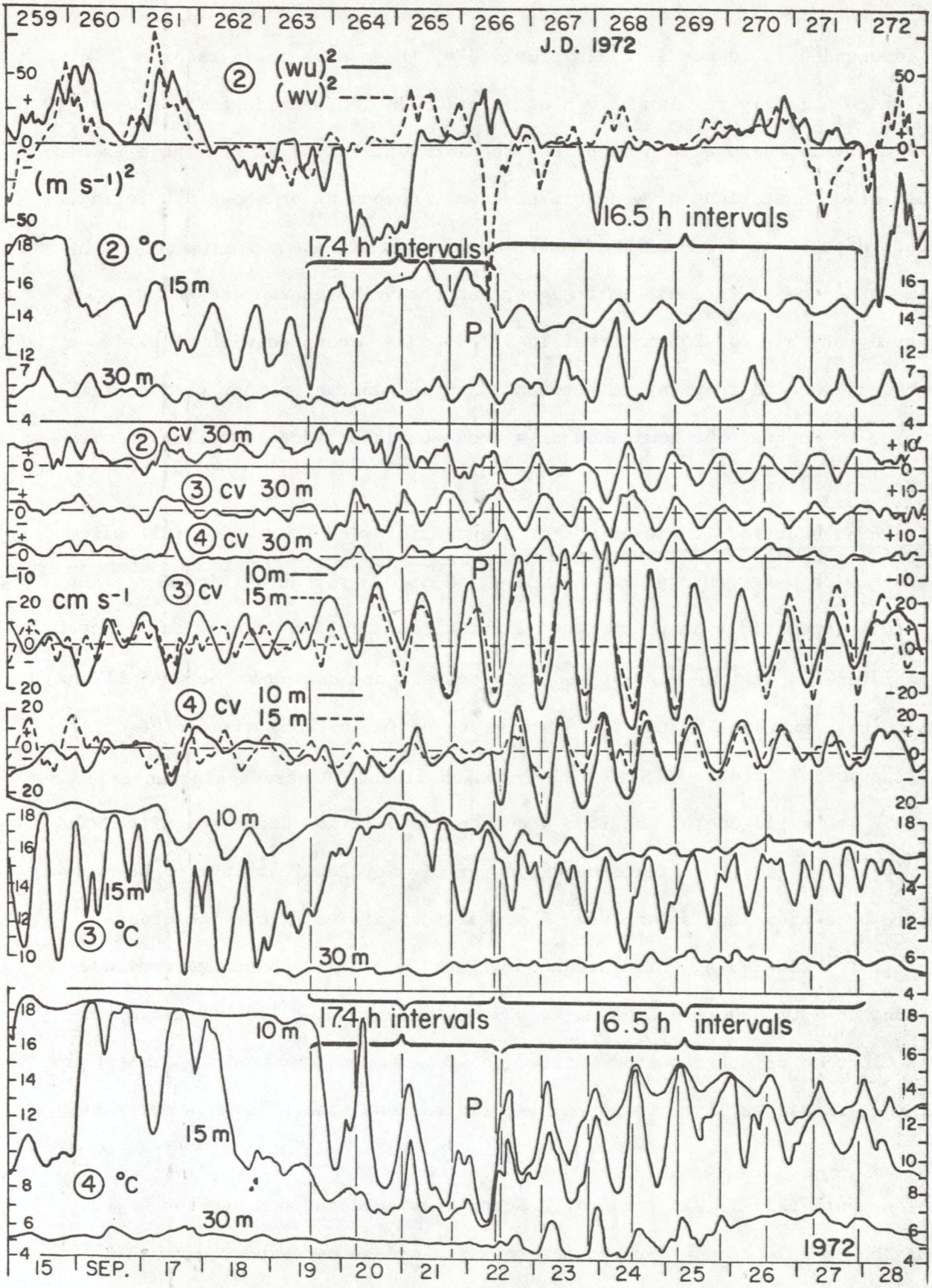

Figure 60. Composite diagram 2/259-272: wind component $(wu)^2$ and $(wv)^2$ at 2; current component (cv) and temperature (°C) at various depths at 2, 3, and 4. Further details in legend of Fig. 34.

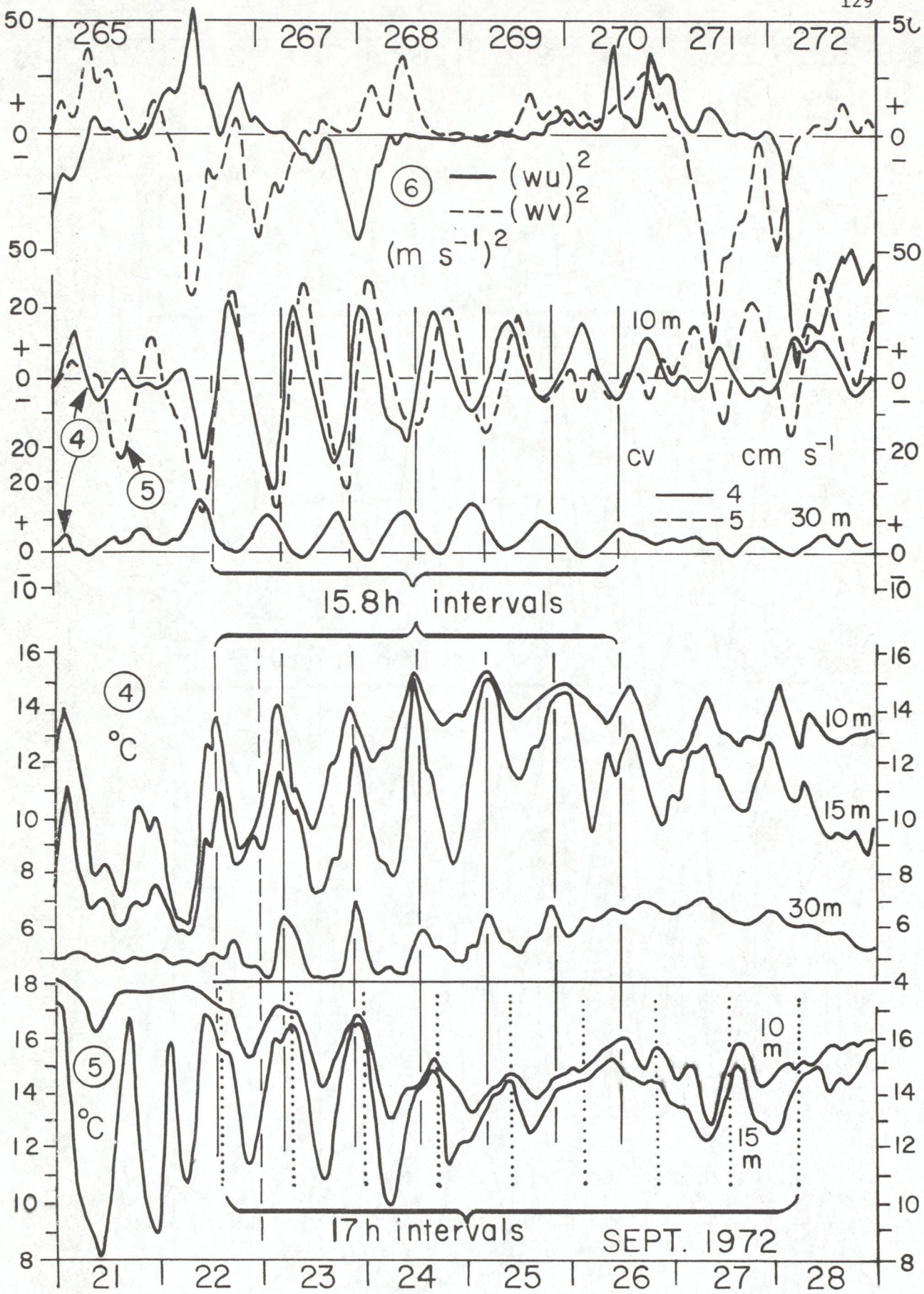

Figure 61. Phase comparisons between the NS components of current (*cv*) and temperature (°C) at various depths at stations 4 and 5, JD 265-272 (21-28 Sept.) 1972. For further details, including explanation of the wind record, see legend of Fig. 34.

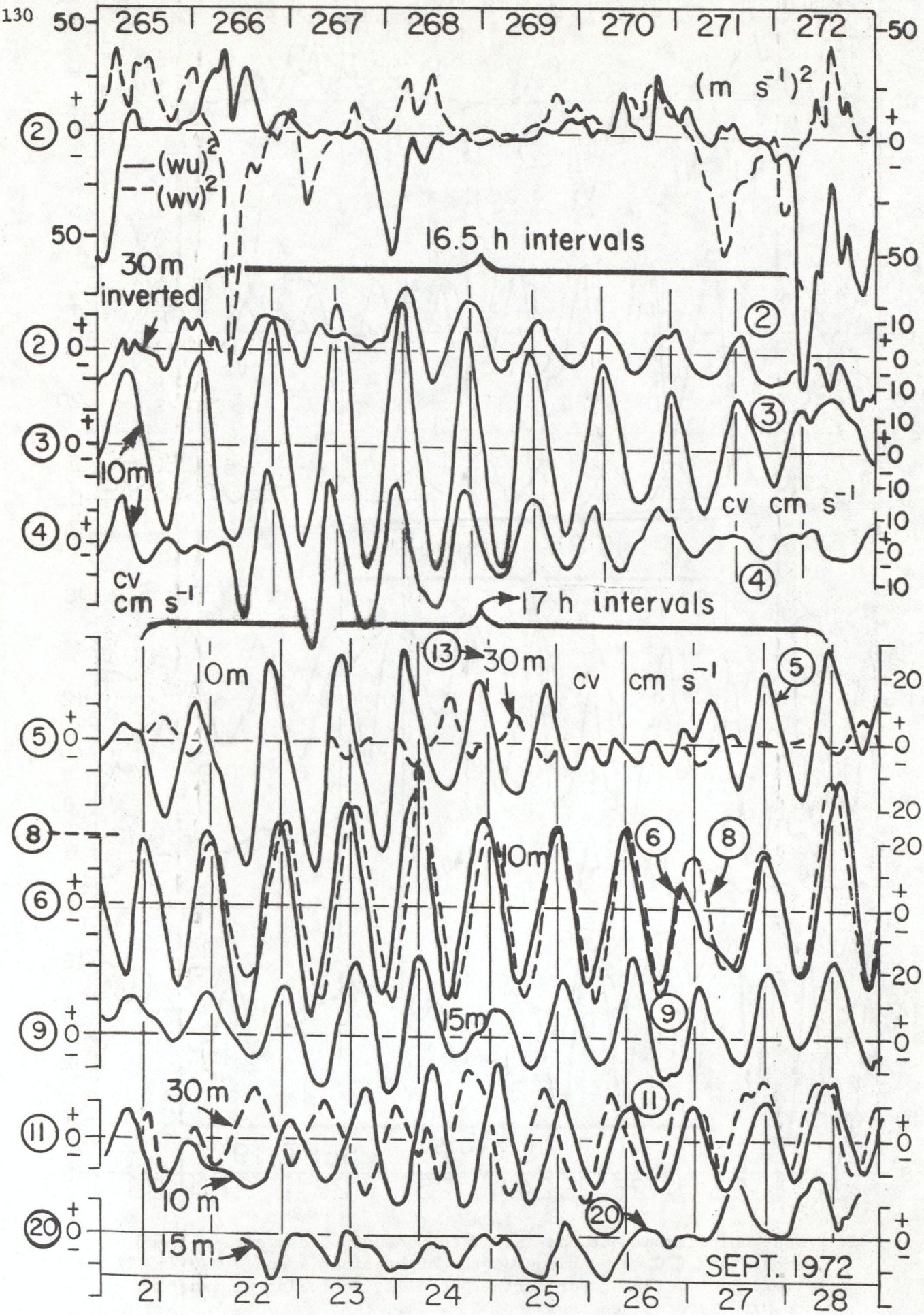

Figure 62. Legend on facing page 131.

5.7 Exploration of the oscillation structures observed during a five-day episode following a wind impulse on 266 (22 September).

Following the same cross-section sequence as before -- 2, 6, 9, and 11 -- we find that wind impulses on 260 and 261 generated no regular oscillations at any stations in cross-section 2 (Fig. 60) but, after a long westgoing wind pulse on 264, near-inertial oscillation in current began at 3 which, after a short but strong southgoing wind pulse on 266, changed into a regular oscillation of mean period 16.5 h which lasted for eight cycles during the calmer days (267-271) which followed. At station 4 (Fig. 61) however, 15.8 h APB is a closer fit to both current and temperature records, while at station 5, dotted vertical lines suggest that 17 h is a better fit.

Figure 62 extends the comparison of current oscillations at all stations from which records were available at that time. At the beginning of the episode (day 267) the currents were not far from an in-phase condition at all stations, although close inspection reveals a general clockwise progression of the peaks 5, 6, 9, and 11 covering an interval of about 6 h. The current at 30 m depth at station 11 (shown as a broken line) was unusually strong, displaying an amplitude not much less than that at 10 m. During the early part of the episode, the 10 m and 30 m currents were nearly out of phase, which is the usual pattern. Later they came nearly into phase.

Of interest for the present analysis is the overall pattern in phase relationships between the current oscillations at various stations illustrated in Figure 62. As the episode advanced, the western group, 2, 3, 4, became more

---

Figure 62, on facing page 130.

Phase comparisons between the NS components of current (cv) at various depths at stations 2, 3, 4, 5, 6, 8, 9, 11, and 20, JD 265-272 (21-28 Sept.) 1972. For further details and explanation of the wind record, see legend to Fig. 34.

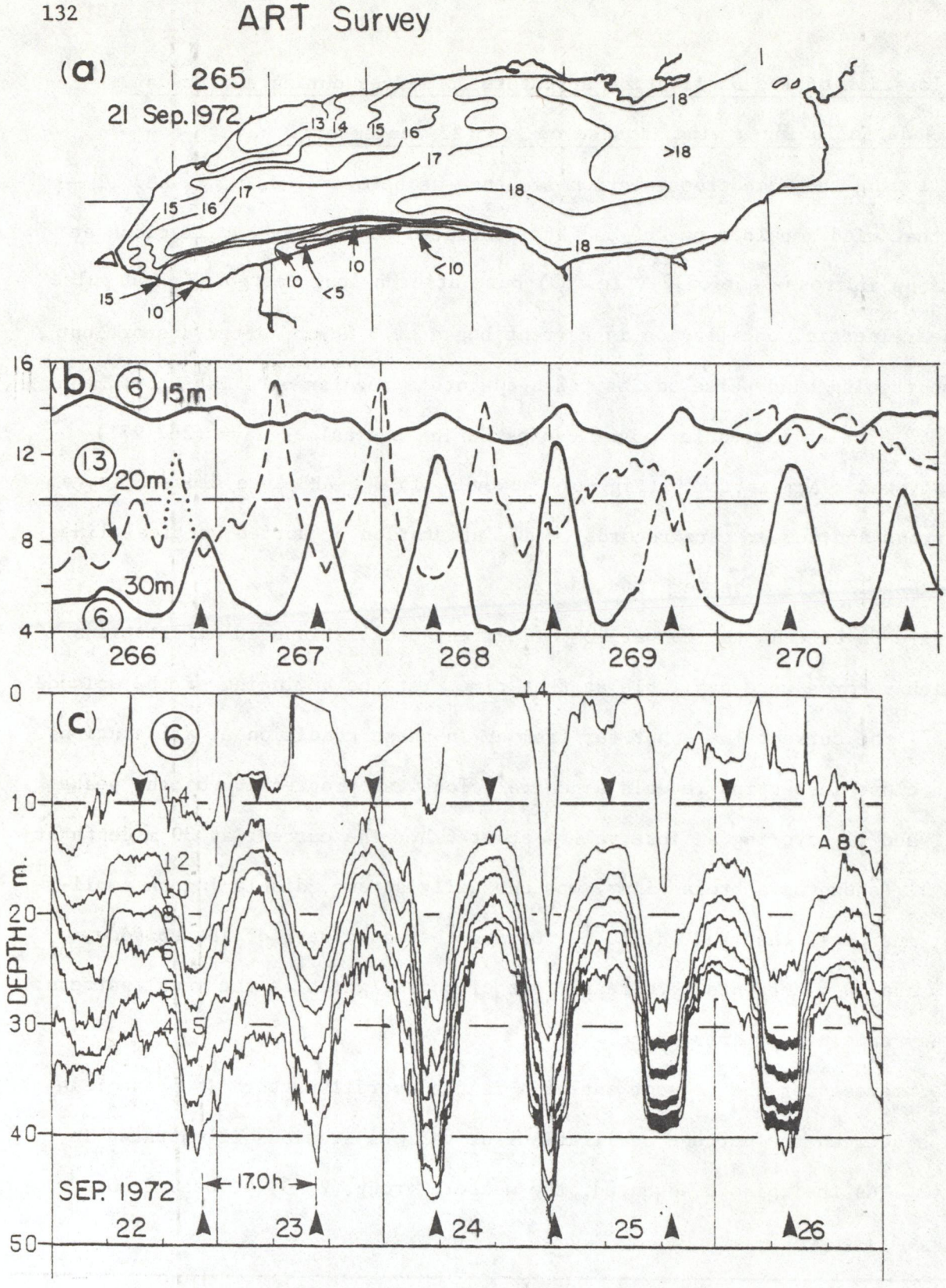

Figure 63. (a) Surface temperature (°C, ART survey, Irbe and Mills 1976) JD 265 (21 Sept.) 1972; (b) temperature at 15 and 30 m, station 6, and at 20 m, station 13; (c) isotherm depth fluctuations near station 6. Portions (b) and (c) occupy the 266-270 (22-26 Sept.) interval. Data in (c) were supplied by the Canada Centre for Inland Waters. An APB of 17.0 h is fitted to (b) and (c) in which six cycles occupy the interval OB. Comparable intervals for APB 16.5 and 17.4 h are OA and OC, respectively.

and more out of phase with stations elsewhere in the basin, in accordance with the respective average period bands 16.5 and 17.0 h. (The current record from 20, from which little can be learned, is included for completeness and because the temperature record from that station is the subject of later discussion.) The fact that the other (non-western) stations, as widely separated as 5, 6, 9, and 11, maintained a regular periodicity of 17 h and were nearly in phase during most of this episode is consistent with the presence of a strong component of cross-basin first-mode oscillation in all except the western extremity of the basin, which is also suggested by the following analysis of the temperature records.

The overflight on 265 with a radiation thermometer measuring surface temperature disclosed (Fig. 63a) that west-going wind on the previous day had produced a narrow but extensive band of upwelling along the southern shore (see also the dip in temperature records at the southshore tower 23 in Fig. 64). The regularity of the subsequent oscillation and its good fit to APB 17.0 h are illustrated for cross-section 6 in Figures 63 and 64 and for cross-section 9 in later Figure 66. However, a closer look (in Fig. 65) at the western group of stations (which were fitted to a common APB of 16.5 h in Fig. 60) reveals that better individual fits are to APB 17.0, 14.4 h and 15.8 h for stations 2, 3 and 4, respectively.

This result suggests that, while signals from the lst-mode oscillation were strong at many other stations, higher modes (second and third?) were also excited, and that stations 3 and 4 were located in regions in which the higher mode response was large while the response to the first mode was relatively small. Obviously, the interplay between station position and the different mode structures is an important factor in the analysis. At all the non-western stations the 17.0 17 h APB is the best fit. For example at station 6 (Figs. 63c and 64) an APB of 17.0 h is clearly a better fit (six cycles during the interval OB) than are either 16.5 h (OA) or 17.4 h (OC). The isotherm-depth oscillations in 63c exhibit an asymmetry between broad peaks and narrow troughs. The latter generally correspond,

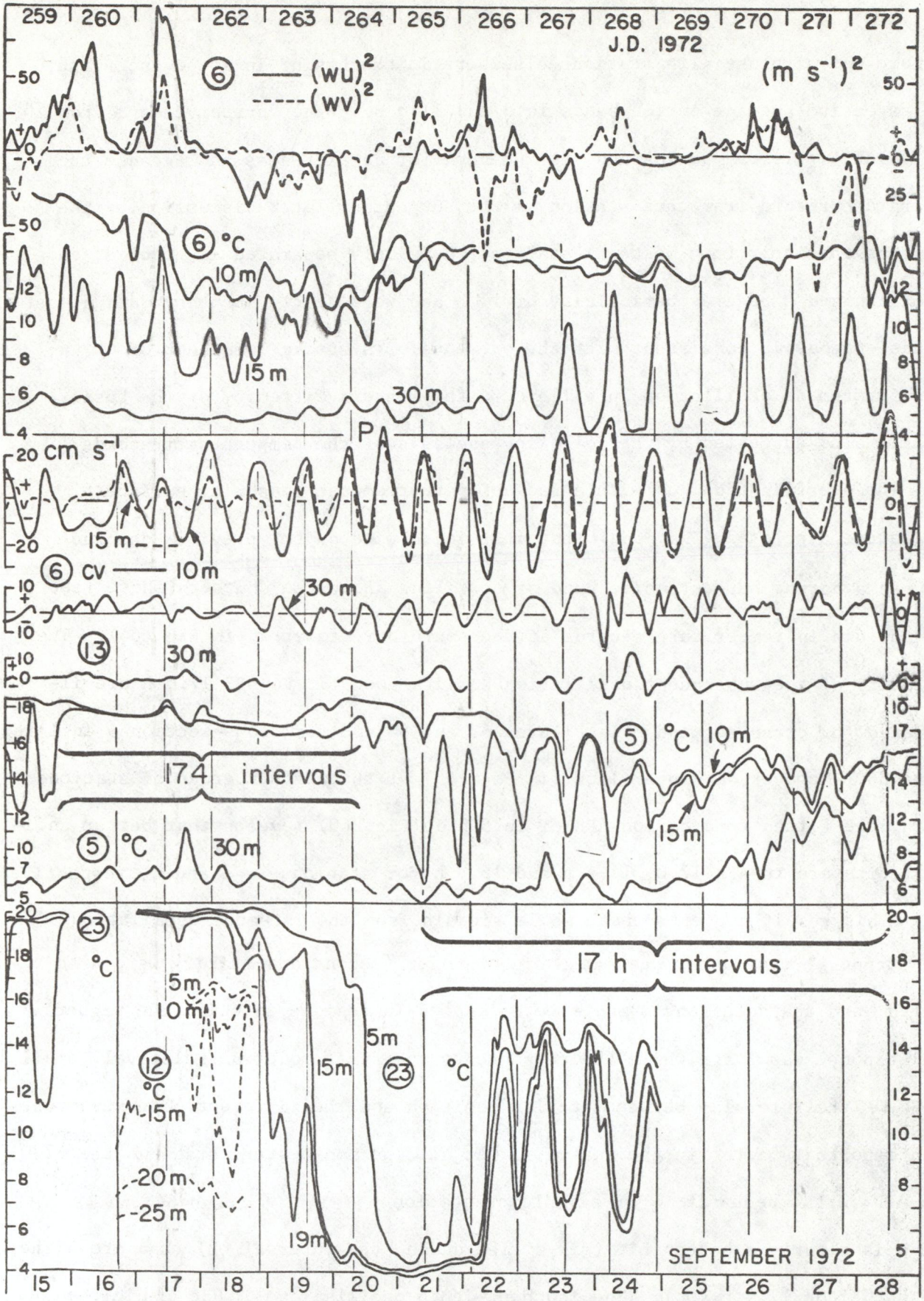

Figure 64. Composite diagram 6/259-272: wind components $(wu)^2$ and $(wv)^2$ at 6; current component (cv) and temperature (°C) at various depths at 5, 6, 13, and 23 (further details in legend of Fig. 34).

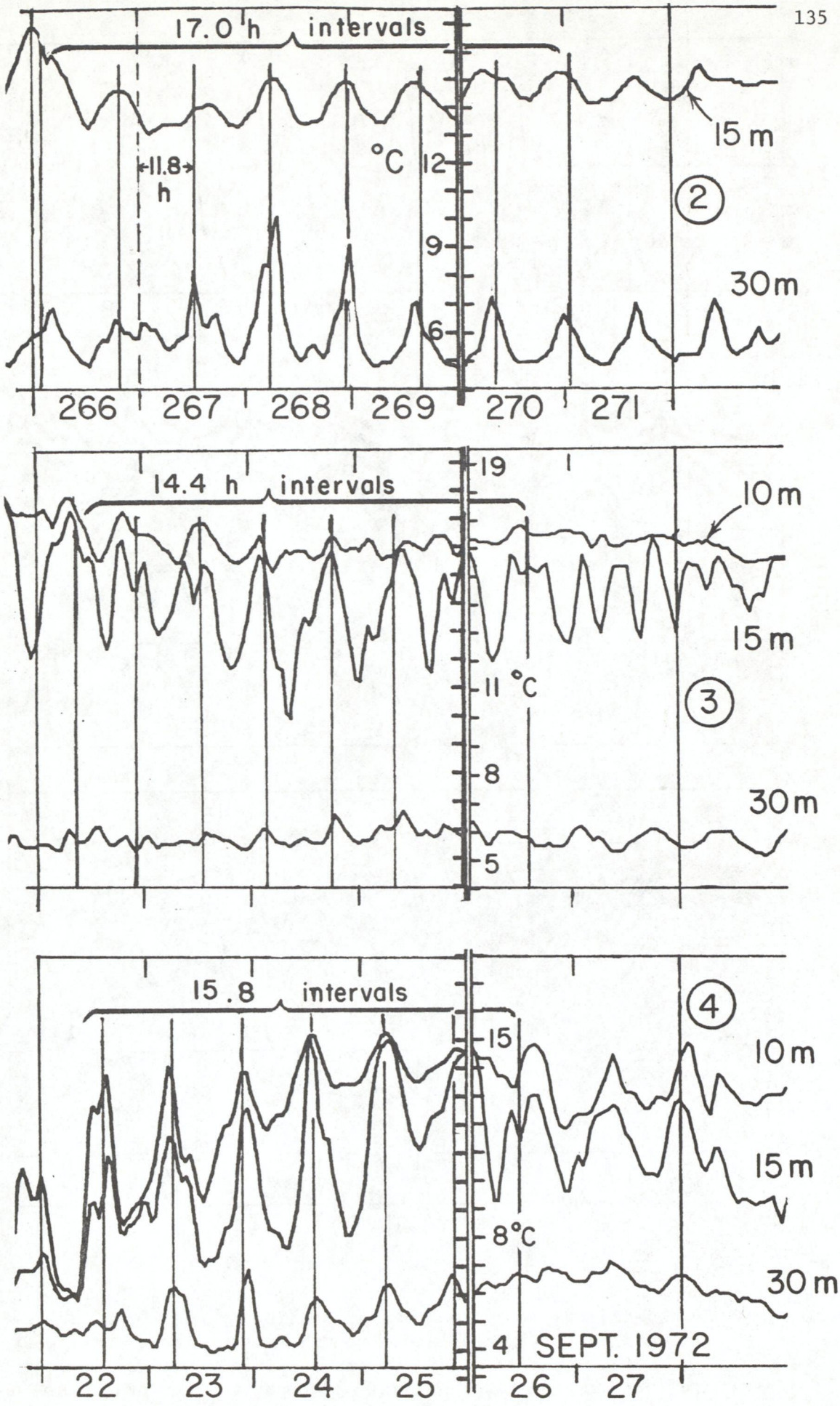

Figure 65. Temperature fluctuations at various depths at stations 2, 3, and 4, JD 266-271 (22-27 Sept.) 1972, illustrating interstation differences in APB fitting.

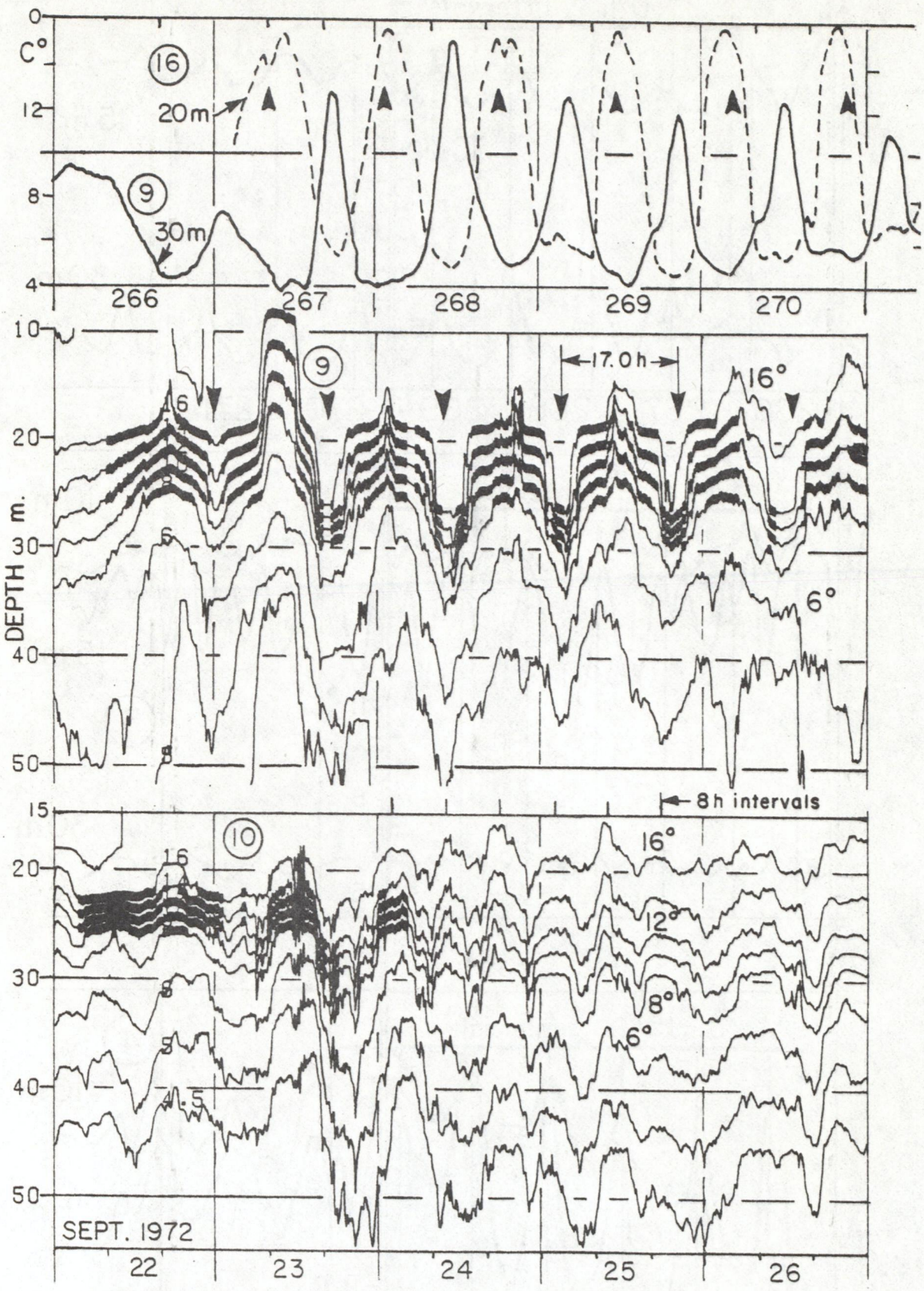

Figure 66. Fluctuations in isotherm depth at stations 9 and 10, JD 255-270 (22-26 Sept.) 1972, interpolated from thermistor chain records at 19 depths (supplied by Canada Centre for Inland Waters) and compared with temperature fluctuations (upper portion) at stations 9 and 16.

as expected, with temperature peaks at 30 m depth at 6 (not shown on an inverted temperature scale in this case) although, as in Figure 57, the temperature peaks in 63b appear to lag behind the isotherm troughs in 63c by one or two hours with no obvious explanation. For three cycles during 267-268 there is a clear antiphase relationship between the temperature oscillations at 6 and 13, at opposite ends of the cross-section. Unfortunately no records are available from station 12 for this interval, or indeed for most of the year.

A similar cross-channel antiphase relationship in temperature is seen in cross-section 9 between stations 9 and 16 (Fig. 66, and 9/260-273 A), and again the temperature peaks at 9 correspond closely in time with the isotherm troughs at the nearby thermistor chain. A 17.0 period is marked in that figure, although perhaps a slightly shorter period (16.6 h) would have been a better fit. The asymmetry of the isotherm oscillation is even more marked at thermistor chain 9 than at 6, and the troughs are not found at the mid-point in time between the crests. The thermistor chain record at station 10 is particularly interesting. If, as the 9/16 antiphase and the near-17 h APB at the top of Figure 66 suggests, a first-mode cross-channel oscillation was in progress, station 10 would be close to the node, as noted earlier. The first response at 10 to wind forcing on 266 appears to have been (i) a single cycle of oscillation of about 17 h period, followed by (ii) five cycles of shorter waves of approximately 8 h period. In (i) we may be seeing the initial progressive-wave response to the wind impulse (suggested earlier in connection with Fig. 54) which later, through reflection and interaction with the opposite shore would generate the cross-channel standing wave pattern. That pattern may not have been conspicuous at 10 because of the close proximity of the node to that station, thus permitting the 8 h or double inertial frequency component (often seen in spectra, for example in Figs. 18, 27, and 36 in Marmorino and Mortimer 1978) to become visible. This 8 h signal is not to be interpreted as a higher mode of the Poincaré-type response. Rather it reveals the non-linear features of the largest amplitude

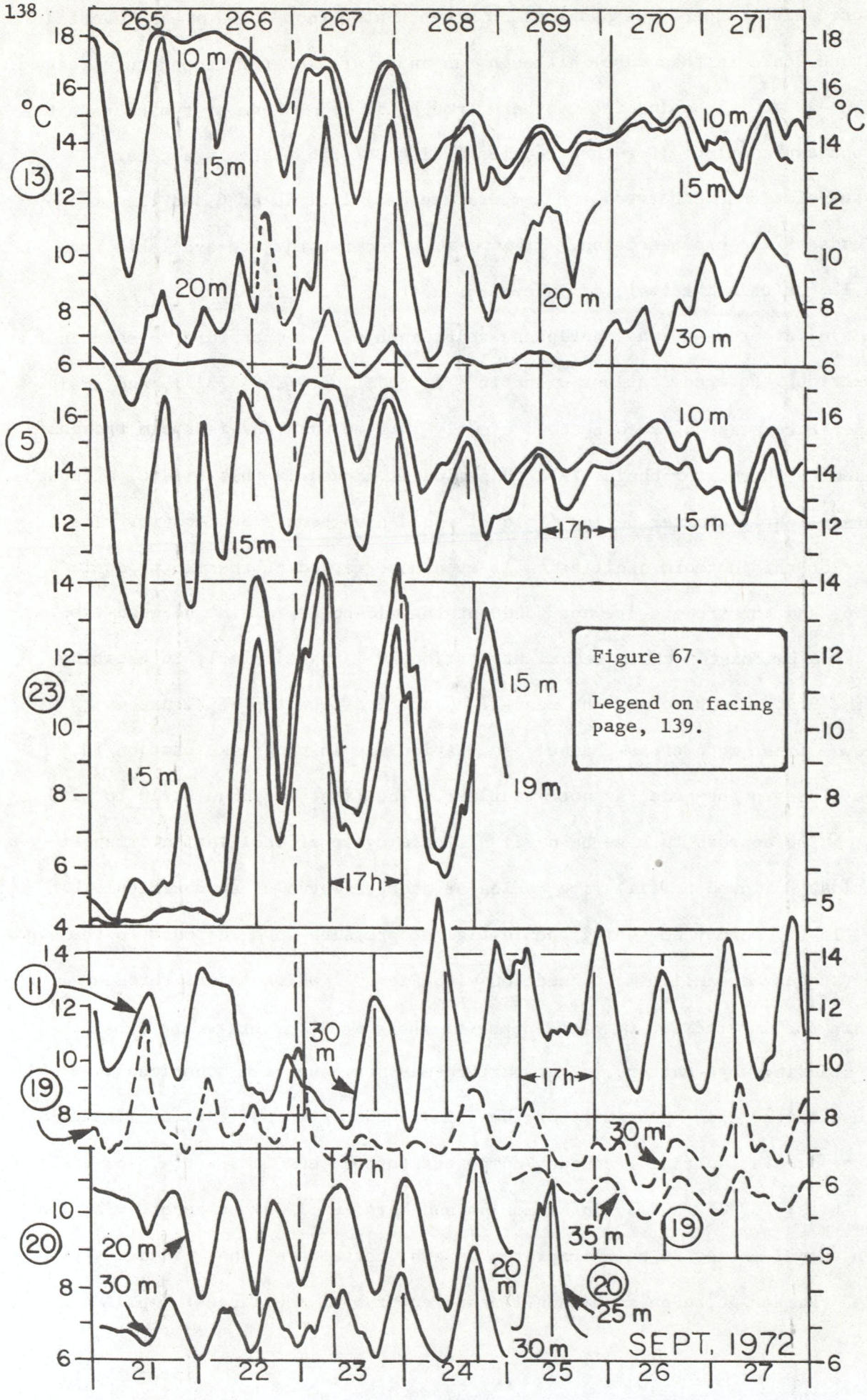

Figure 67.

Legend on facing page, 139.

Poincaré mode present, taken to be the first mode in this episode.

In cross-section 11, the picture is not clear (11/261-280 A). The wind history there differed somewhat from that in other sections (note the strong northgoing wind on 268, not seen at 2). Temperature records from 11 and 20 are reproduced in Figure 67, which assembles records from all those stations (except 2, 6, and 9 which were portrayed in previous figures) which show evidence of a near-17 h oscillatory component. The 265/6 record at station 20 displays short-period oscillations, which later gave way to three near-17 h cycles. That record ceased on 269. The record at station 19 was irregular (11/261-280 A) but is shown dotted in Figure 67 for comparison with station 11. If the oscillations on 269/70 are taken as weak evidence of a 17 h component at 19, the corresponding lag with respect to 11 is about 2 h.

Although the temperature oscillations displayed in Figure 67 are less regular than those of the currents in Figure 62, their peaks match a 17 h period fairly closely over the 3-day interval 267-269, although the timing of those peaks differs from station to station. Of interest is the comparison between records at stations 5 and 13, obtained from instruments moored within 1 km of each other and installed and processed independently by a Canadian (CCIW) and a U.S. agency (NOAA). The similarity between the 10 m and 15 m records from those two stations is satisfactorily close. Within the accuracy of the period fit, they are in phase, a point to be noted later. A short portion of record from a nearshore instrumented tower station, 23, installed to the south of stations 13 and 5, provides evidence of coastal upwelling on 265; and although the record is short, the approximate fit of a 17 h APB to the peaks suggests that the oscillation at 23 lagged behind that at stations 13 and 5 by about two hours.

Figure 67. See facing page, 138.

Phase comparisons of temperature records from stations 13 and nearby 5 and from stations 11, 19, 20, and 23, JD 265-271 (21-27 Sept.) 1972.

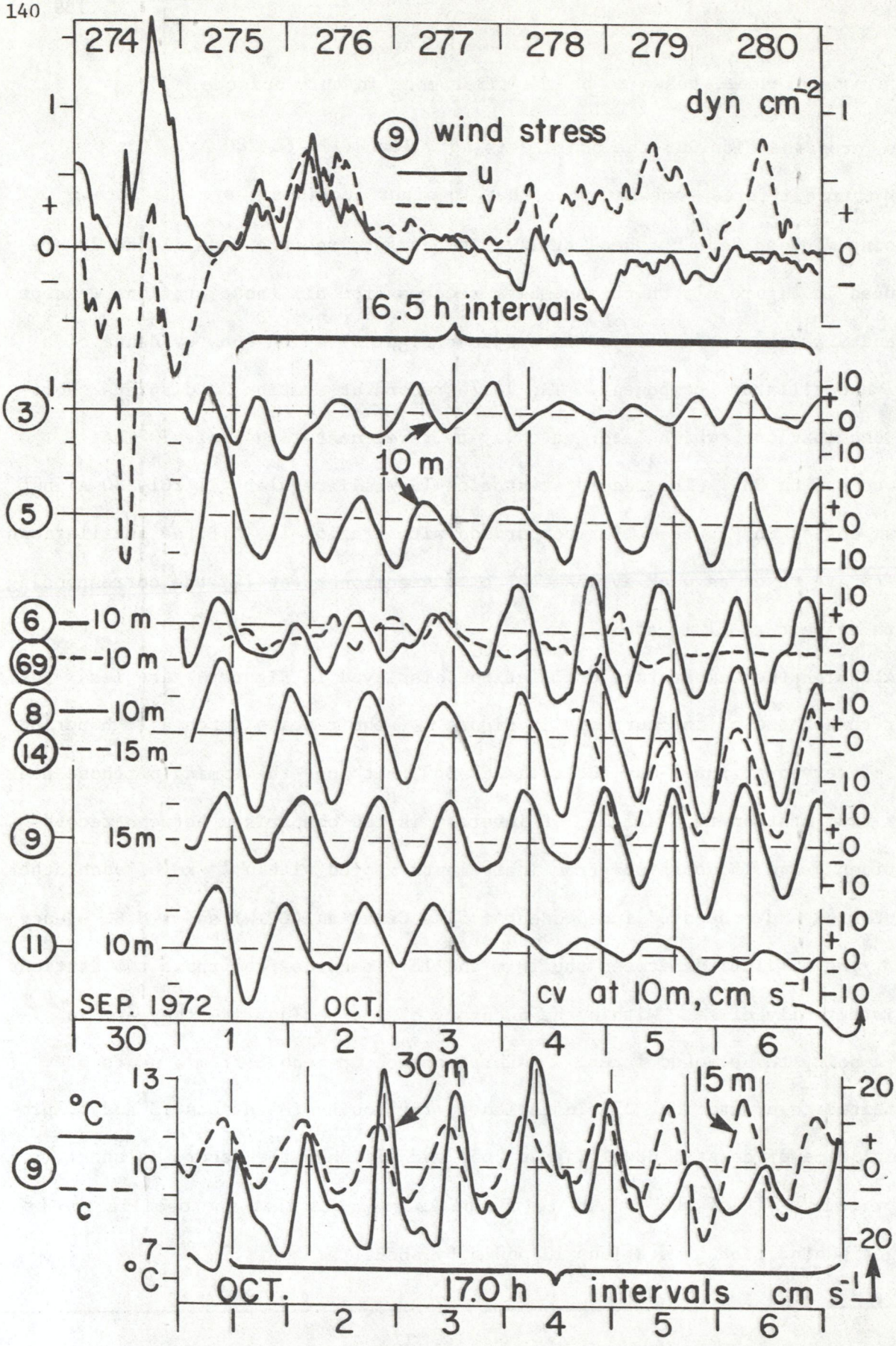

Figure 68. Legend on facing page, 141.

5.8 The responses, in various regions of the basin, to a wind impulse on 274 (30 September) deduced from station and transect comparisons.

The next spell of windy weather arrived on 272 (an eastgoing pulse) and continued changeable during 273. Then a strong, very short southgoing pulse arrived at about mid-day on 274 followed that afternoon by another short eastgoing pulse later that day (Fig. 68). It so happened that 274 was the day on which many of the moored instruments were replaced, resulting in a gap in data (including wind) for that day at many stations. The NS components (cv) of current records from all stations showing distinct oscillations during the ensuing episode of weak winds, 275-280, are assembled in the upper main portion of Figure 68 and fitted to 16.5 h APB intervals centered on the peaks at station 9. This period is a good fit at 9 and a reasonably good fit elsewhere, although evidently a slight underestimate for some stations, 5 for example. But it should also be noted that the temperature record at 30 m depth at station 9 was a remarkably close fit to a 17.0 APB (9/274-287 A). This fit is illustrated in the bottom panel of Figure 68, in which that temperature record is compared with the current record at 15 m, superimposed as a broken line. This is a rare example in which the periodicity of the current oscillation is apparently slightly less than that in temperature. The phase progression of the current oscillations (an eastward progression 5, 6, 8, 9 spanning approximately 3 h) in Figure 68 is similar to that seen during the previous episode (Fig. 62). But, whereas the phases of stations 3 and 11 fell into the same sequence in Figure 62, during the present episode they did not fit; station 11 for example showed a 3 or 4 h lead over 9.

Figure 68. See facing page, 140.

Phase comparisons between near-shore NS current components (cv) at stations 3, 5, 5, 8, 9, 11 and 14, JD 275-280 (30 Sept. to 6 Oct.) 1972. Further details, with explanation of the wind record, are found in the legend of Fig. 34. In the bottom panel cv at 15 m is compared with temperature at 30 m, both at station 9.

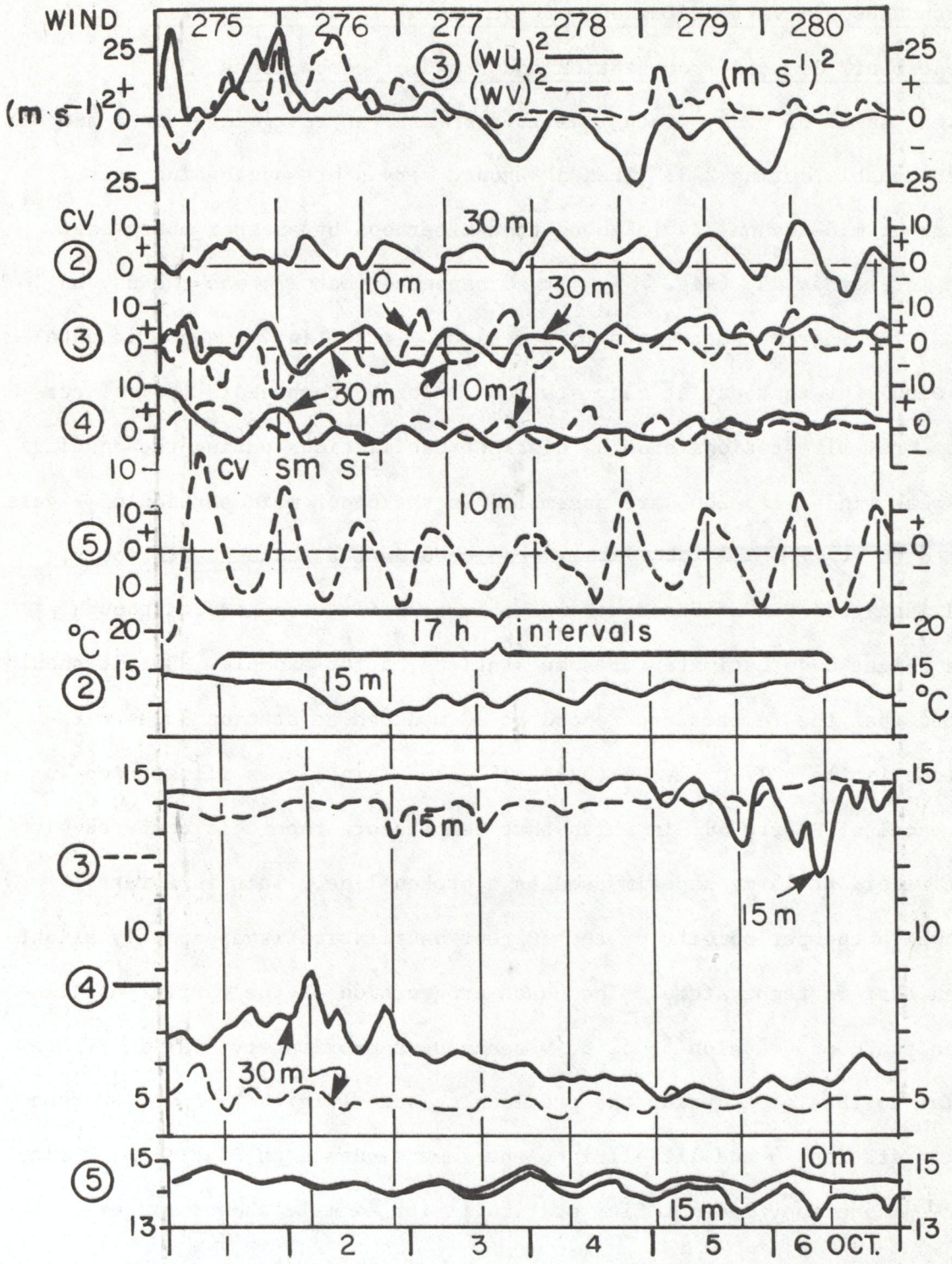

Figure 69. Legend as for Fig. 68, but relating to current and temperature records at various depths from stations 2, 3, 4, and 5.

The difference between the behavior of currents in the end regions and the patterns seen in the main body of the basin is paralleled by differences in the patterns of temperature. In cross-sections 6 and 9, the wind impulse on 274 was followed by fairly regular oscillations. These persisted with an APB near 17 h for ten cycles during a week of weak winds, until a fresh disturbance on 281 was followed by the most violent storm of the stratified season on 282-3. At the western end of the basin, however, the stations in group 2, 3, and 4 showed only minor responses during this episode of very weak winds (Fig. 69). Stations further east, as we have seen in previous figures and can see in the record at 5 in Figure 69, responded much more actively to the wind impulse on 274. Why the response at 2, 3, and 4 was so weak is not evident. Perhaps the answer lies in horiztonal inhomogeneity in wind stress, impossible to confirm because 274 was the day on which many instruments were replaced. Because of the small amplitudes in current and temperature oscillations at 2, 3, and 4, period-fitting is unreliable. All that can be concluded from Figure 69 is that 17 h is a fairly good fit to the current oscillation at station 3 and to the current and temperature oscillation at station 5.

The complexity of the responses at the eastern end of the basin, in cross-section 11, will be described in subsequent paragraphs and in Part II of this report. Here we examine briefly the simpler picture seen in cross-sections 6 and 9, deferring more detailed analysis of that picture to Part II. It was fortunate that the 276-280 episode coincided with temperature transect cruises, shuttling to-and-fro across cross-sections 6, 9, and 11. Temperature records from the moored stations can therefore be compared with cross-basin isotherm structures. Such comparisons will be illustrated in Part II by means of figures similar to earlier Figures 49, 52, and 55, in which isotherm depths are plotted at transect-intersect times at several selected distances across the section.

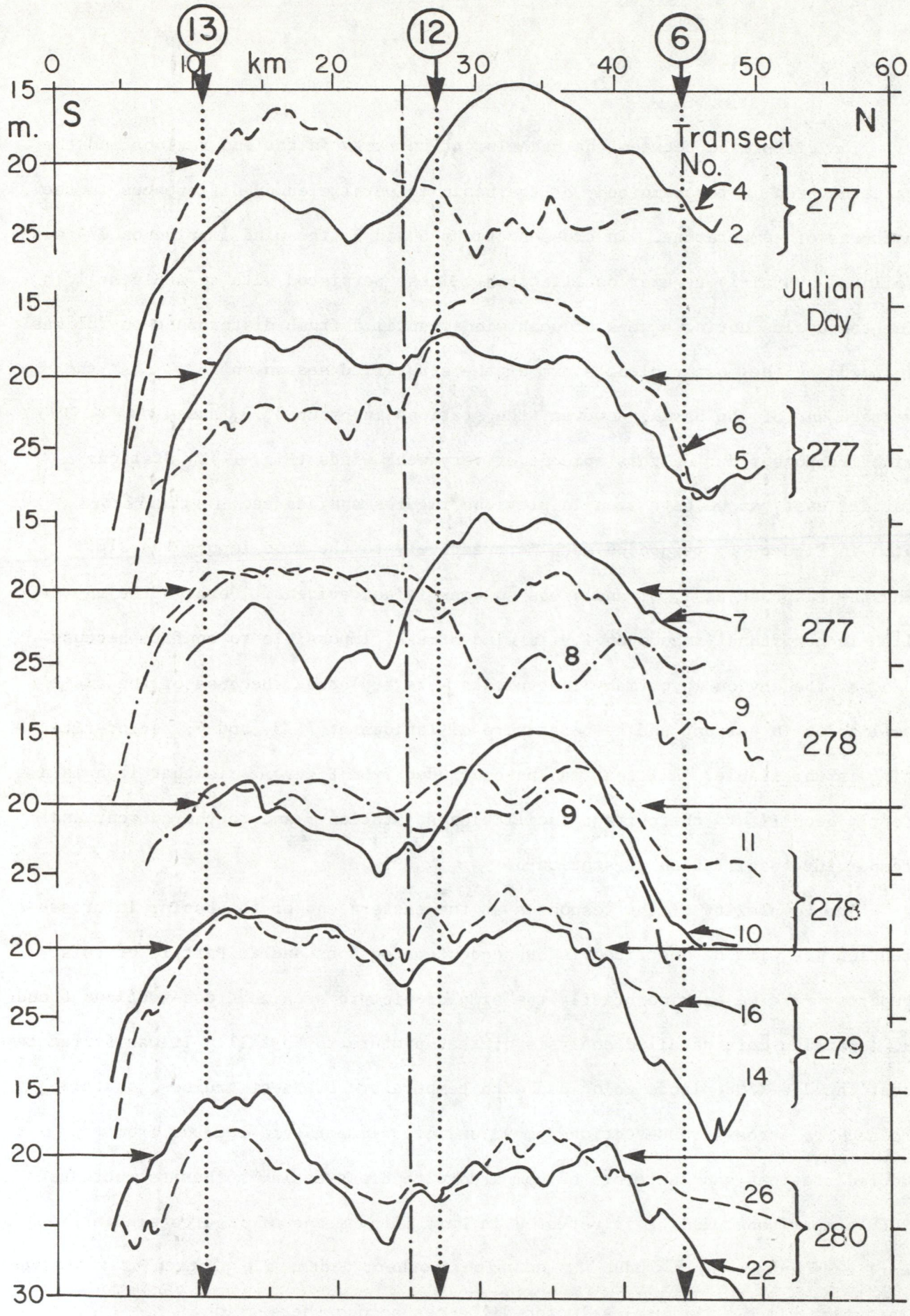

Figure 70. Legend on facing page 145.

In the case of cross-section 6 during the 276-280 episode, undulatory trends were evident and can be approximately fitted to a 17 h sinusoid, conforming to the 17.0 h APB fitted to current and temperature oscillations at stations 6 and 13 in 6/276-290 A. This conformity justifies the attempt (in Part II) to assign an approximate phase structure elsewhere in the cross-section (i.e., at points other than 6 and 13).

When groups of 10° isotherms, taken to represent mid-thermocline levels in the transects across cross-section 6, are plotted as in Figure 70, evidence of a uninodal cross-basin internal seiche appears. This is superimposed upon a strongly arched thermocline topography with downwelling near both the N and S shores. The mid-section crossover points, indicating the region of the presumed node, lay close to 25 km during the first eight transects but were less clearly defined during later transects.

A similar transect-isotherm figure for this episode was published for cross-section 9 in Mortimer (1977, Fig. 18). In that cross-section the uninodal cross-basin seiche structure, corresponding to the 17 h oscillation seen in 9/274-287 A, was clearly evident and will be treated more extensively in Part II of the present report. Some features were described in Mortimer (1977, Figs. 47, 48).

Figure 70. See facing page 144.

Depth of the 10° (mid-thermocline) isotherm during selected pairs of transects across cross-section 6 (Braddock Pt. to Presqu'ile), from Boyce and Mortimer 1977; an extended version of Fig. 21 in Mortimer 1977). Transect pairs were selected to coincide as closely as possible with maxima and minima in thermocline elevation at stations 6 and 13 (see 6/276-290 A).

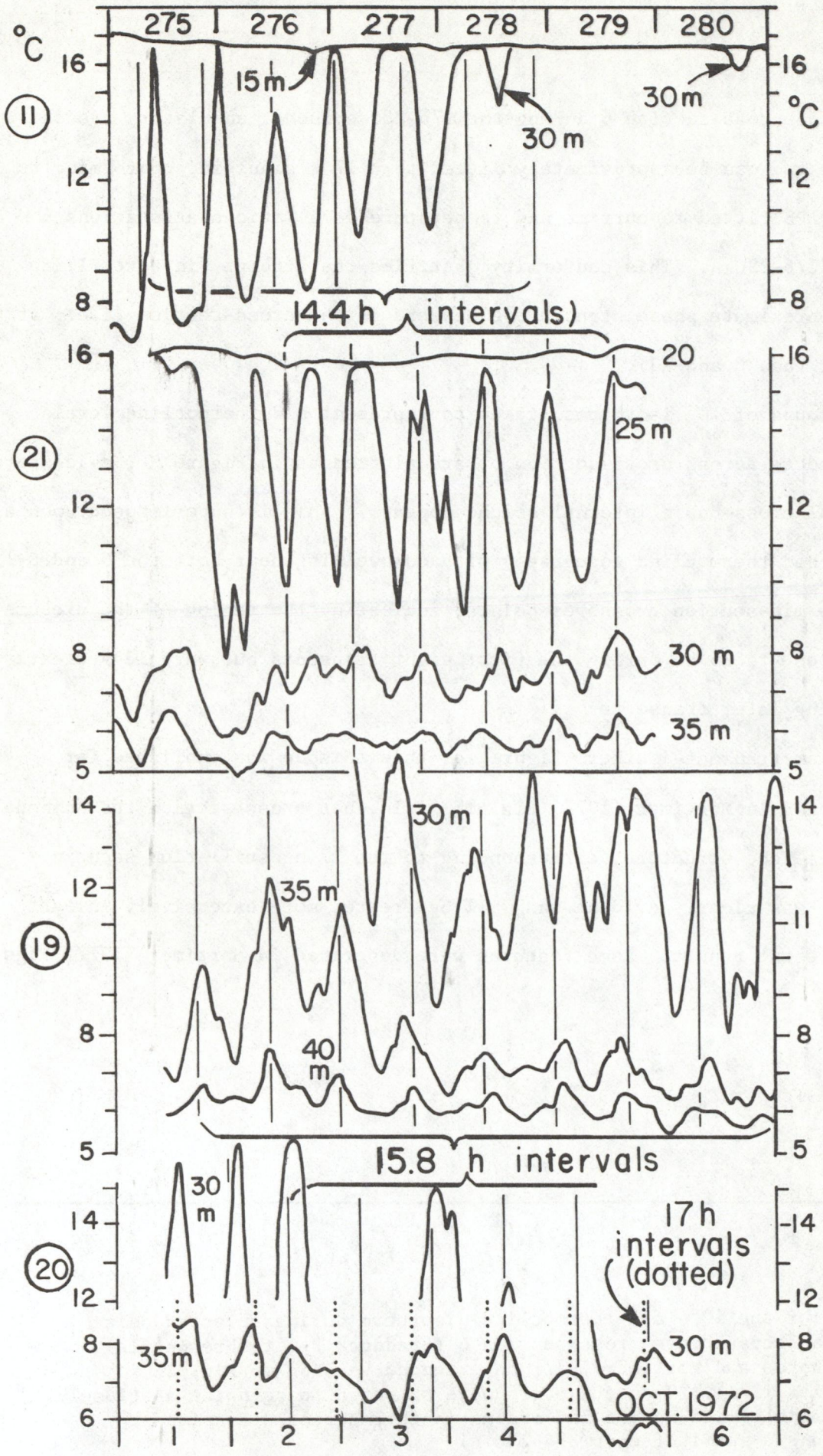

Figure 71. Legend on facing page, 147.

At the eastern end of the basin, in cross-section 11, the 275 to 280 interval was marked by a fairly regular, decaying oscillation of 16.5 h APB in current rotation at station 11, but with no regular current rotations at the other stations (11/261-280 A). The temperature records were even less regular and showed evidence of periodicities distinctly shorter than the unmistakable 17 h oscillation dominant in cross-sections 6 and 9. A 14.4 h APB was fitted in 11/261-280 A; but closer inspection (in Fig. 71) of temperature records from cross-section 11 (stations 11, 19, and 20) and from station 21 show that, in spite of the irregularity, a 14.4 h APB can be fitted to portions of the record at 11 and 21, while 15.8 h is a better fit to most of the record at 19. The record at 20 is too fragmentary and irregular for a reliable period fit, but 15.8 and 17 h intervals are shown in Figure 71. Further evidence of lack of regularity and inter-station coherence in cross-section 11 during this episode is illustrated in Part II of this report by means of a figure similar to previous figures 49, 52, and 54, displaying isotherm depths at selected transit points across the section. Coherence or lack of it between cross-sections will also be discussed more fully in Part II.

Figure 71. See facing page, 146.

Phase comparisons of temperature records from stations 11, 19, 20 and 21, JD 275 to 280 (1 to 6 Oct.) 1972.

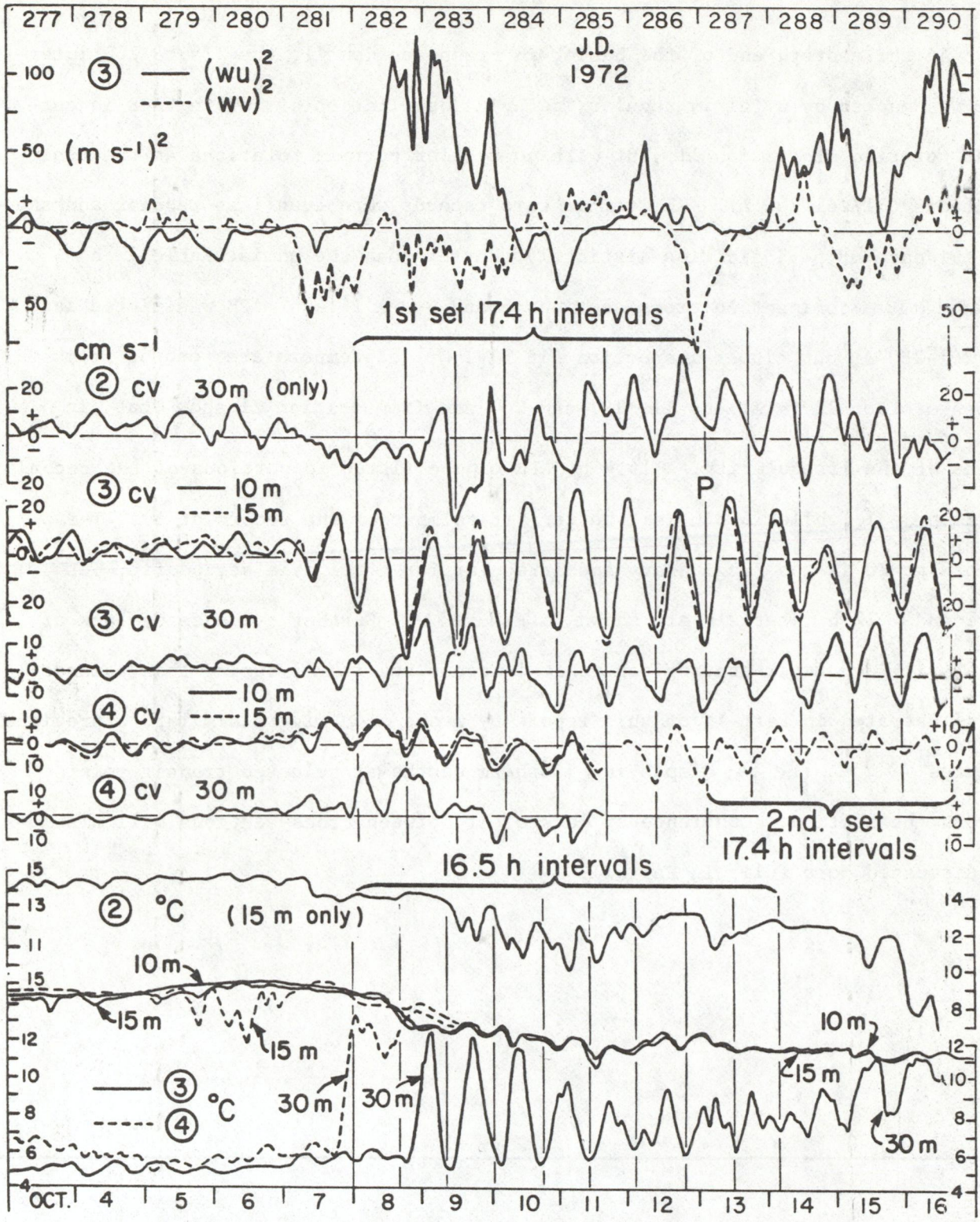

Figure 72. Composite diagram 2/277-290: wind components $(wu)^2$ and $(wv)^2$ at 3; current component (cv) and temperature (°C) at various depths at 2, 3, and 4 (further details in legend of Fig. 34).

5.9 Events during the breakdown of stratification.

In the westernmost cross-section there was little activity during the previously described episode (276-280, Fig. 72); but a southgoing wind on 281 succeeded by a strong eastgoing two-day storm (282/3) generated strong current and temperature oscillations at station 3 and less conspicuous but equally persistent current oscillations at 4. That storm mixed the upper layer to greater depths over the whole basin, for example, to below 30 m at station 4 and to near 30 m at station 3. That thermocline descent, shown in the temperature record from 3, probably explains the double-peaked appearance of the current record from 30 m depth, where the current meter may have been recording alternately in the upper and lower layer as the thermocline rose and fell. The 30 m current record at station 2 was also irregular and showed large velocities. The violence of the storm and its effect in deepening and cooling the upper layer is illustrated by the heat content surveys in Figure 73, which also includes the ART survey of surface temperature on day 284. Five days earlier, the ART survey disclosed a very uniform surface temperature of 15-17°C whereas, one day after the 284 storm, it showed extensive upwelling along the northern shore and a surface temperature near 12°C elsewhere (Fig. 73). The upwelling effect can also be seen in cross-sections 6, 9, and 11 (6/276-290 A, 9/274-287 A, and 11/281-287 A). At station 6 there was a nearly steady drop in surface temperature; at station 9 the upwelling condition lasted for several days; and at 11 there was a rapid recovery by 285, but the water column remained mixed to at least 30 m depth.

Examination of Figure 72 also discloses that the APB for the current oscillation at station 3 (and also for the weaker oscillation at 4) was 17.4 h, the inertial period, while that for the temperature oscillation at station 3 was 16.5 h. This again describes a situation, commonly encountered earlier in the year, in which a mixture of inertial and standing-wave responses are respectively dominant in the current and temperature records. Records of currents

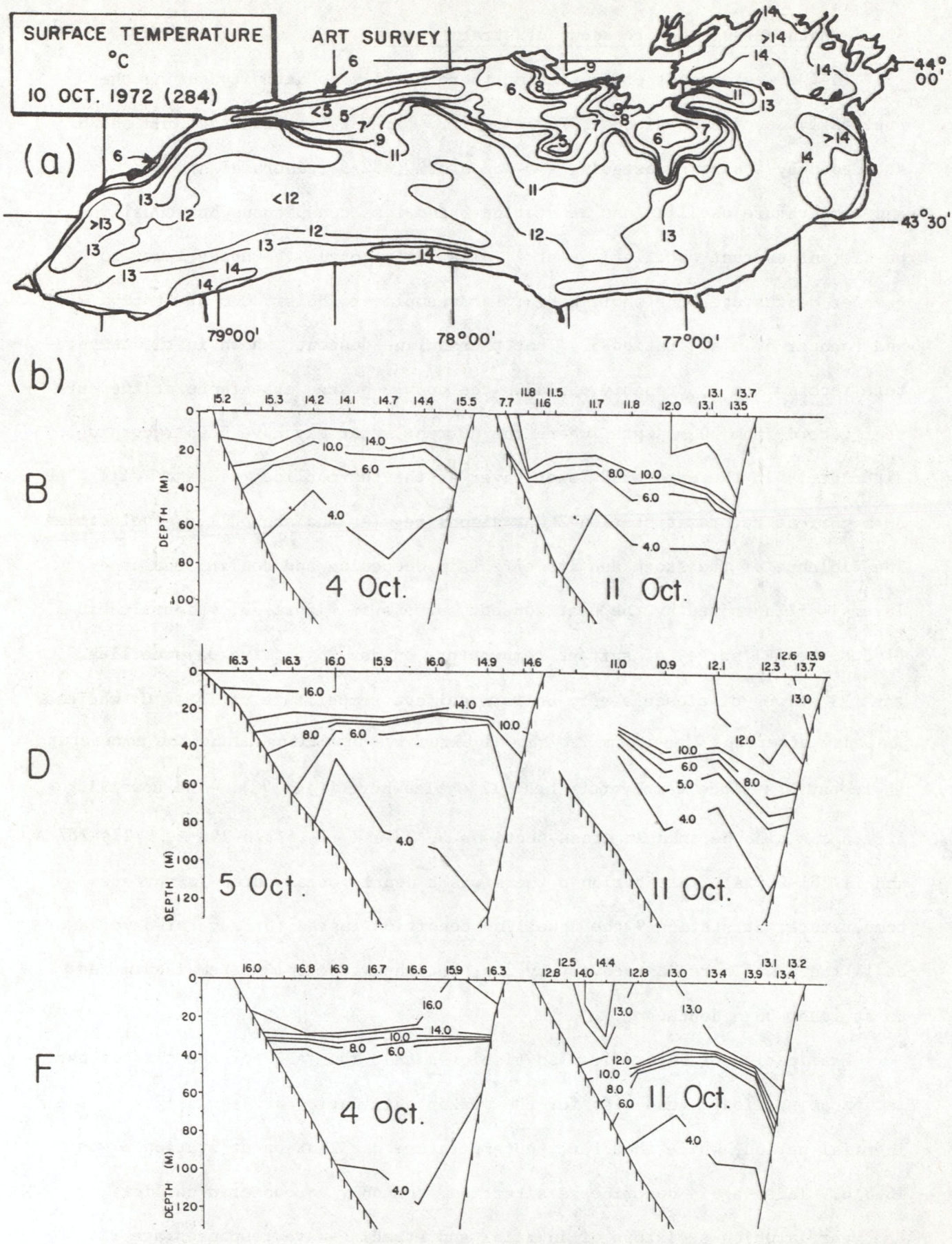

Figure 73. Legend on facing page, 151.

during the episode 283-289, at all stations which exhibited more or less regular oscillations, are assembled in Figure 74. Stations 3 and 4 were the only ones which showed a relatively regular oscillation during the whole episode. The short burst of oscillation at station 6 lagged behind that at 3 by about 4 h and would fit an APB of less than 17.4. Station 8 and the mid-lake station 14 started off roughly in phase but were almost in antiphase by 287/8. The oscillations at stations 9 and 11 were too irregular to permit reliable phase deductions; but stations 8 and 9 appear to have been nearly in phase (and out of phase with 14) during 287/8. In attempting to interpret the picture of current phases, it should be noted that the stations (8, 9 and 11) in the northern half of the basin were then strongly influenced by the upwelling. The extent and the complex topography of the upwelling front during day 284 is illustrated in Fig. 73; and the temperature records from stations 8, 9, and 11 (Figs. 75, 76) testify to the strength of that disturbance. Also, during the days following the main storm on 282/3, the wind was variable and sometimes strong. For example, 284 which was calm was followed by two days with peak wind stresses approaching 1.0 dyn cm^{-2} at most stations and exceeding 2.0 at station 11 (the large temperature rise at 50 m at 11 can be attributed to this); and a relatively calm day on

---

Figure 73. See facing page, 150.

Lake Ontario 1972: (a) Surface temperature (ART survey, Irbe and Mills 1976) on 10 October; (b) sub-surface temperature distribution in sections B, D and F (heat content survey) on 4, 5 and 11 October.

Figure 74. On next page, 152.

Phase comparisons of near-surface current records (NS component, *cv*) at stations 3, 4, 5, 6, 8, 9, 11 and 14, JD 283-289 (9 - 15 Oct.) 1972. For further details, including explanation of the wind record, see legend of Fig. 34.

Figure 75. Follows on page 153.

Phase comparisons of temperature records at stations 3, 6, 8, 12, 13 and 14, JD 283 to 289 (9 to 15 Oct.) 1972. Also shown are the EW and NS components of wind stress at station 8, computed by the method of Hamblin and Elder (1973). For further dtails see legend of Fig. 34.

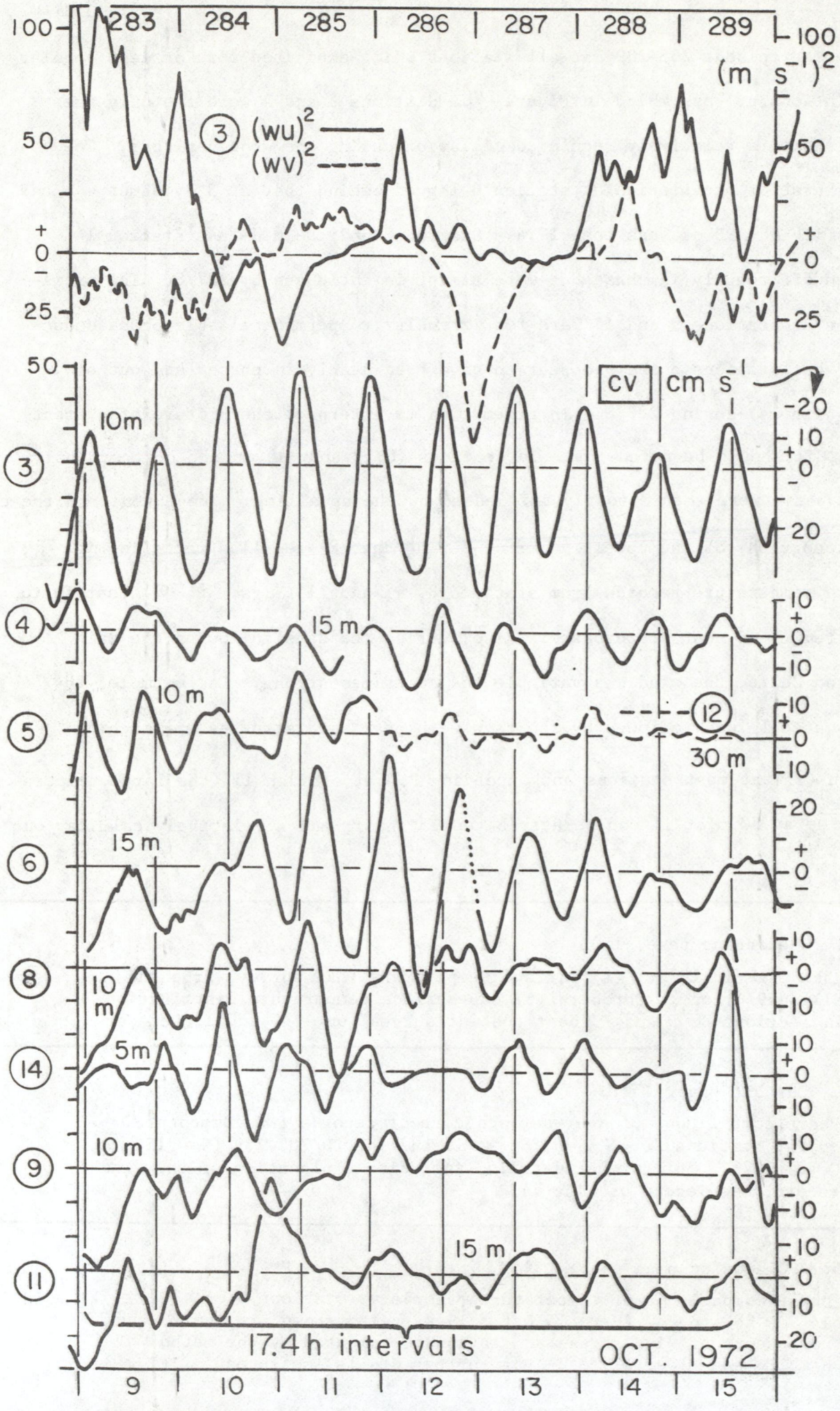

Figure 74. Legend on previous page, 151.

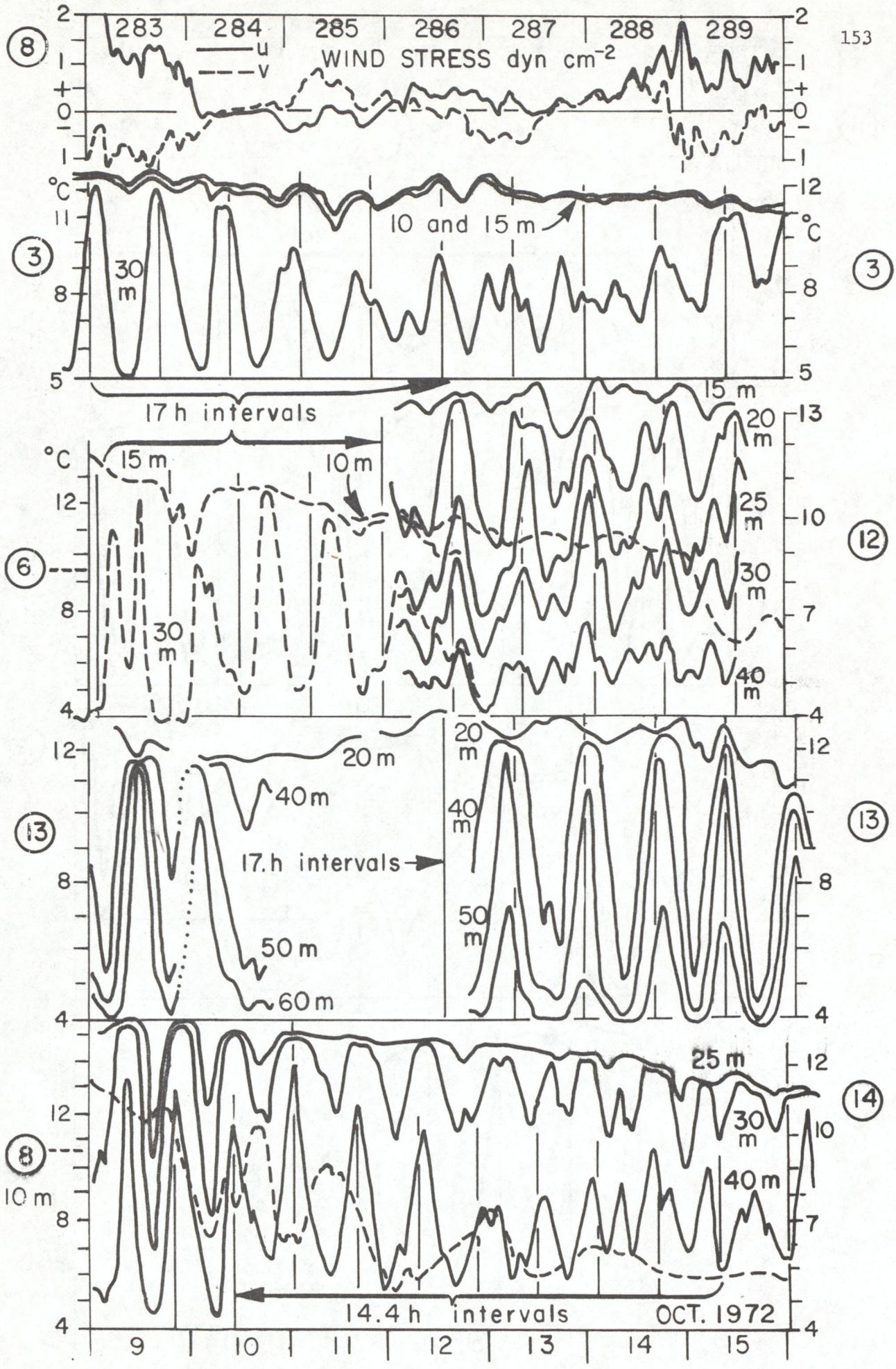

Figure 75. Legend on page 151.

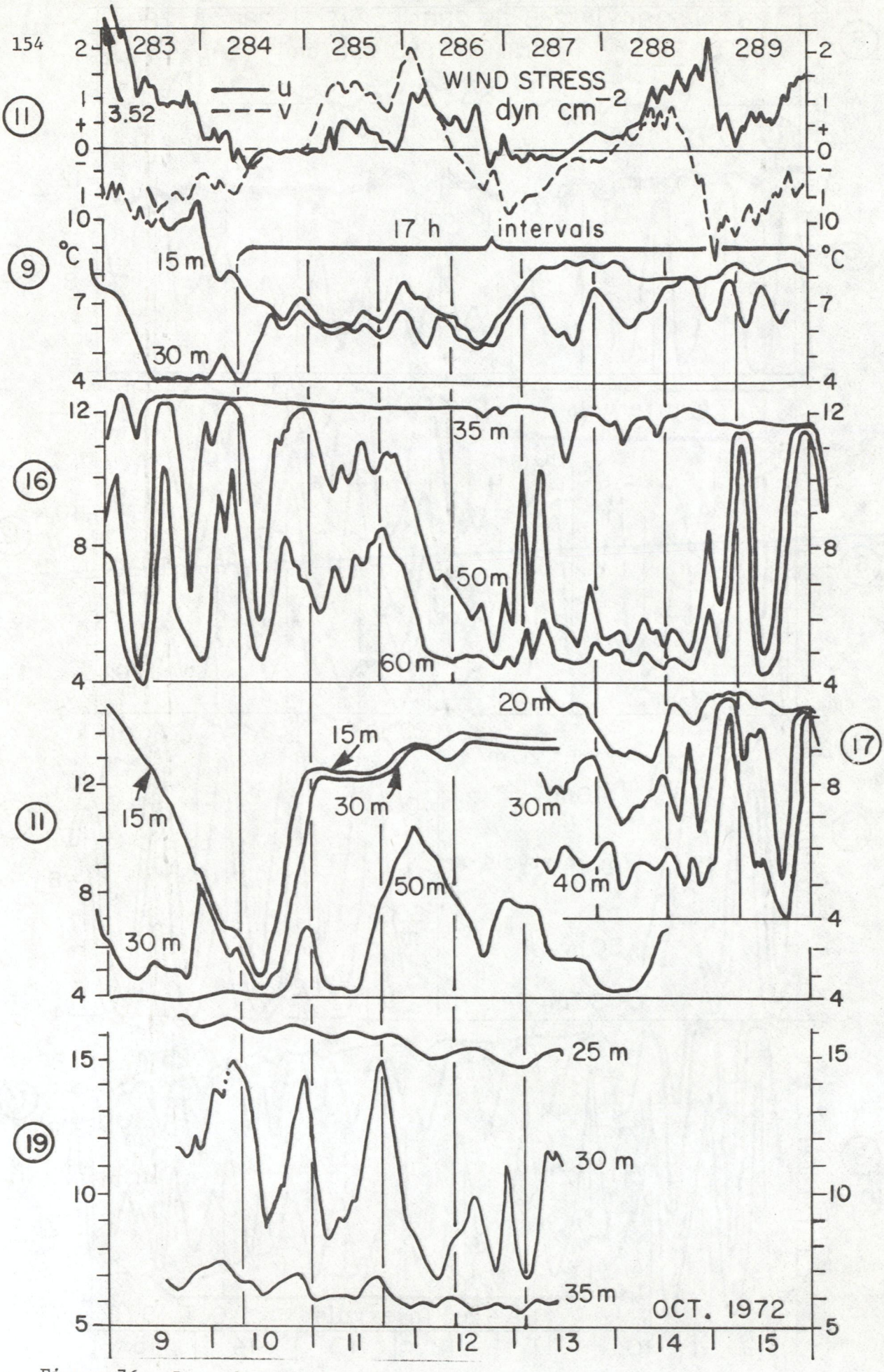

Figure 76. Legend on facing page, 155.

287 was followed by wind (again stronger at station 11) on 288/9 (Fig. 74).

While the response to the storm, to the ensuing upwelling, and to subsequent wind pulses was apparently far from simple, short bursts of temperature oscillations appeared at mid-lake stations (3, 12, 14, 19) and at stations nearer the southern shore. All the temperature information for the interval 283-289 is assembled in Figures 75 and 76. The oscillation bursts are too short for reliable period-fitting; but to aid discussion, 17 h time intervals are shown for all stations except 11 (which showed evidence of a nearly diurnal oscillation at 50 m) and 14. The latter station showed a better fit at 40 m with 14.4 h, although there was evidence at 25 m of a component of longer period during the middle of the episode. At stations 9 and 16 (Fig. 76) no regular oscillation was sustained and there was little evidence of interstation coherence. What evidence there was, during 287-289 for example, suggests an in-phase relationship, in contrast to the expected out-of-phase relationship of these two stations during a 17 h cross-basin oscillation.

In cross-section 6, stations 12 and 13 differed in phase by only 2 h during 287 and 289; and, when the 17 h intervals ruled for station 12 in Figure 75 are extrapolated back in time, it appears that station 12 may have been out of phase with 6 during the earlier part of the episode. However, the short, isolated scrap of record on 283/4 from station 13 shows that it is difficult if not impossible to determine which are predominantly free responses and which are forced -- adjustments to the upwelling disturbance, for example. No sequence of calm days occurred, during which the interstation coherence of free responses could be explored.

Figure 76. On previous page, 154.

Phase comparisons of temperature records at stations 9, 11, 16, and 19, JD 283-289 (9 to 15 October) 1972. Also shown are the EW (u) and NS (v) component of wind stress at station 11, computed by the method of Hamblin and Elder (1973). For further details see legend of Fig. 34.

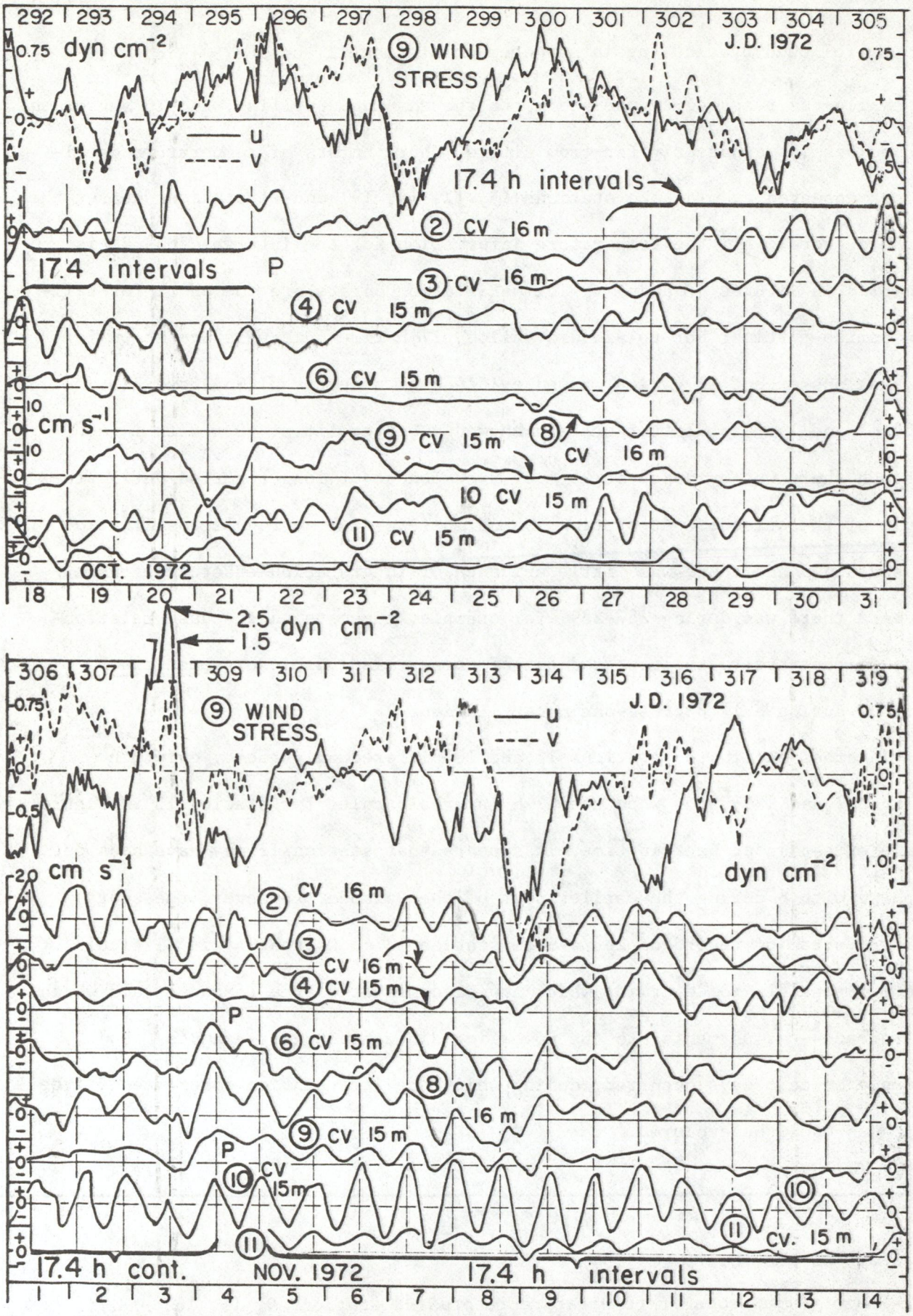

Figure 77. Phase comparisons of near surface current records (NS component, *cv*) from stations 2, 3, 4, 6, 8, 9, 10, 11, JD 292 to 319 (18 Oct. to 14 Nov.) 1972. Also shown are the EW and NS components of wind stress, computed by the method of Hamblin and Elder (1973). For further details see the legend of Fig. 34.

In fact (as the wind record in Fig. 77 shows) a series of storms occupied the remainder of October and early November, with very few intervening days of weaker winds. Strong wind stress toward the east on day 291 again produced extensive upwelling along the northern shore (4° water at the surface) and a marked whole-basin tilt of the thermocline isotherms, downward to the south (Fig. 78). Another severe storm occurred on day 308 (maximum eastward stress 2.5 dyn cm^{-2}), and by that time the thermocline had been pushed down to a mean depth of about 60 m and the surface temperature had fallen to below 10°C. Although the thermocline gradient had weakened, there was still sufficient stratification to permit inertial current oscillations to develop in the upper layer in response to wind impulses. All available current records for the 28-day interval 292-319 (18 October to 14 November) are assembled in Figure 77. When oscillations occurred, they were intermittent in time and space; they appeared in bursts of a few cycles at a few stations or at a single station, but not at others. The significant feature of these sporadic and apparently local responses is that the APB is indistinguishable from the local inertial period. We saw earlier that inertial oscillations arose in the spring, as local responses to wind impulses, as soon as stratification arose locally and before it became established over the whole basin. In Figure 77 are examples of what also appear to have been local inertial responses at a time when thermal stratification was being destroyed.

5.10 Inertial motions observed in Lake Ontario during the 1972/3 winter.

Figure 77 which runs until mid-November, illustrates the last examples of what might be termed conspicuous inertial motion during the 1972 season. By the end of November a "slippery" thermocline layer of suppressed turbulence and relatively low friction was no longer present, and inertial responses in the form of current rotation with 17.4 h APB were no longer conspicuous. But such

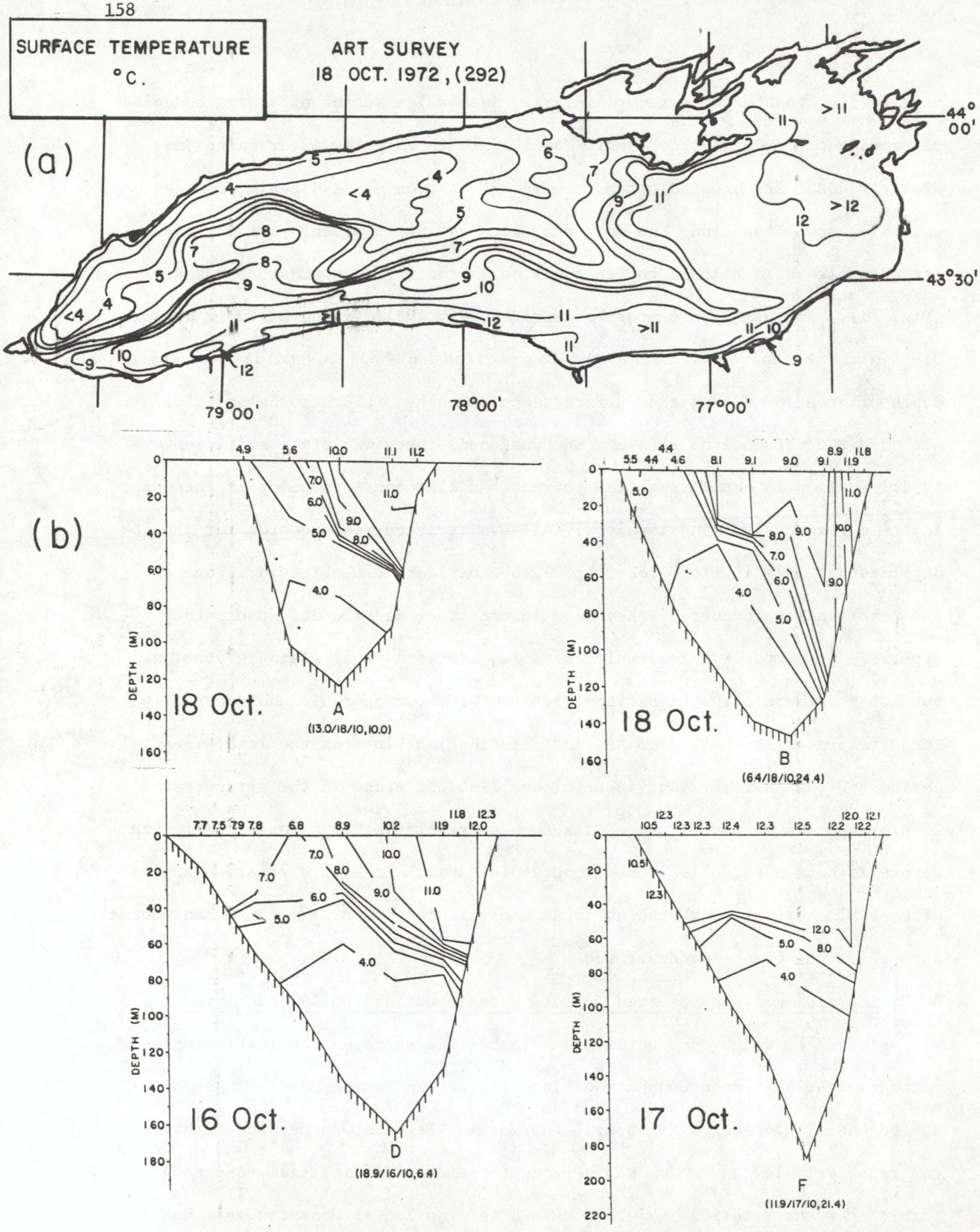

Figure 78: (a) Surface temperature (ART survey, Irbe and Mills 1976) on 18 October; (b) sub-surface temperature distribution in sections A, B, D, and F (heat content survey) 16-18 October 1972.

oscillations were nevertheless observed occasionally during the winter (Marmorino 1978) particularly when a slight thermal stratification was present. Those episodes of inertial motion lasted less than five days and exhibited speeds of less than 15 cm s^{-1}, averaging (for example) 10% of the total current variance at station 10.

> "Some inertial events in midlake had no counterpart nearer shore. In contrast, a lakewide episode of inertial currents was induced by a storm during a two to three week period of vertical stratification. The average hodographs during the stratified period, calculated from bandpassed shallow currents, were ellipses with major axes oriented generally alongshore and axis ratios of 1.05 to 1.64. Some of the data can be interpreted in terms of internal-inertial waves with downward energy propagation and a vertical wavelength equal to the basin depth. Observed shifts to frequencies higher and lower than the inertial value were most likely caused by an interaction with lower frequency currents (Doppler effects)."

6. SUMMARY OF THE FINDINGS (PART I).

Although prefaced by a section which recapitulates some theory, this portion (Part I) of the report on inertial and near-inertial responses to wind impulses in two of the St. Lawrence Great Lakes is mainly descriptive in nature and assembles, in archival form as a series of diagrams, the entire body of observations upon which the analysis is based. Some preliminary analysis, particularly relating to observed average periodicities of current and temperature responses during selected episodes, has been carried out in this portion of the report and in Mortimer (1977); but a closer look will be taken in Part II at the extent of interstation and inter-cross-section coherence during particular episodic responses, in order to explore the whole-basin structure (or lack of it) during those responses. As a consequence, much of the concluding discussion is deferred until Part II; but the following summary of the principal findings in Part I is designed to enable this Part to stand on its own. Those findings were:

1. During the season of stratification, inertial or near-inertial responses to wind impulses were frequent, but intermittent and short-lived.
2. Inertial motion proper, defined as an oscillation with an average

periodicity indistinguishable from inertial, was the common response before whole-basin thermal stratification became established in the spring (Mortimer 1977) and after it began to break down in the fall.

3. During the season of fully developed stratification, intermittent bursts of inertial motion proper (as defined above) occurred occasionally at individual stations (but not at all stations) in response to short wind impulses, characteristically of <10 h duration; but the more typical responses exhibited distinctly sub-inertial periodicities, commonly with periods of 17 or 16.5 h dominant in current and/or temperature records, interpreted as individual or mixed Poincaré mode excitation; i.e., defined as "basin-tuned," near-inertial motion.
4. Changes in amplitude and phase of pre-existing oscillations were often seen during episodes of wind-forcing; but other apparent phase changes in the response, not obviously related to wind, may have been the result of beat effects between Poincaré wave modes or between such modes and inertial motion proper (see Fig. 20).
5. A frequently occurring pattern was seen, in which the current records fitted a slightly longer average period than did the contemporary temperature records at the same station. This pattern is interpreted as the consequence of a theortetical prediction that the ratio of potential to kinetic energy in the Poincaré wave increases with mode number. Therefore, if a mixture of modes was present, signals from the lower modes (longer periods) were more strongly expressed in current oscillations (kinetic energy), whereas signals from the higher modes (shorter periods) were relatively stronger in temperature oscillations (potential energy).
6. Using the current and temperature records from various depths at sixteen

stations located on four cross-sections of Lake Ontario (results from June to October 1972 assembled in a series of text figures or in the appended diagrams of this report) it was possible to determine the degree of inter-station (and inter-depth) coherence in some responses to selected episodes of wind-forcing. Evidence of whole-basin coherence, even for the most readily excited and the most often seen first Poincaré-type mode, was rare; cross-lake coherence over a given cross-section was more common; less frequent was coherence between neighboring cross-lake sections.

7. Occasionally, individual stations displayed oscillations indistinguishable in period from inertial, while at the same time the dominant period at other stations was closer to that predicted for a particular Poincaré mode in a channel model fitted to conditions in the local cross-section. Review of this complexity suggests that, for short wind impulses, the true inertial responses were predominantly local and depended on the strength, fluctuation, and timing of the wind stress and upon its direction (or changing direction) relative to pre-existing current patterns. But when strong impulses of longer duration caused extensive displacements of the thermocline from equilibrium, cross-channel (Poincaré-predicted) coherence in the responses became more evident; and this may have obscured any local inertial responses present.

8. In most cases the expectation is that a mixture of local inertial and various Poincaré mode responses will be generated; and the response at a given station at a given moment will depend, not only upon which oscillation modes are excited at that time, but also upon that station's position within the structures of those particular modes.

7. REFERENCES

Bennett, J.R. 1973. A theory of large amplitude Kelvin waves. J. Phys. Oceanogr., 3: 57-60.

Boyce, F.M.* and C.H. Mortimer.* 1978. IFYGL Temperature transects, Lake Ontario, 1972. Environment Canada, Inland Waters Dir., Tech. Bull. No. 100, 315 pp. (*principal investigators with collaboration of: D.N. Baumgartner, J.A. Bull, D.L. Cutchin and W.J. Moody.)

Brown, P.J. 1973. Kelvin-wave reflection in a semi-infinite canal. J. Mar. Res. 31: 1-10.

Cahn, A. 1945. An investigation of the free oscillations of a simple current system. J. Meteorol. 2: 113-119.

Clarke, A.J. 1977. Observational and numerical evidence for wind-forced coastal trapped long waves. J. Phys. Oceanogr. 7: 231-247.

Crépon, M. 1967. Hydrodynamique marine en region impulsionnel, Part 2. Cah. Oceanogr. 19: 847-880.

_____. 1974. Geneèse d'ondes internes dans un milieu à deux couches. LaHouille Blanche, 1974: 631-636.

Csanady, G.T. 1978. Water circulation and dispersal mechanisms. in Lakes: chemistry, geology, physics (A. Lerman ed.) Springer Verlag, 363 pp.

Dantzig, D. and H.A. Lauwerier. 1960. The North Sea problem. I. General considerations concerning the hydrodynamical problem of the motion of the North Sea. Konink. Ned. Akad. Wetensch., Proc. Ser. A., 63: 170-180. IV. Free oscillations of a rotating rectangular sea. Ibid.: 339-354.

Djordjevic, V.D. and L.G. Redekopp. 1978. The fission and disintegration of internal solitary waves moving over two-dimensional topography. J. Phys. Oceanogr. 8: 1016-1024.

Galazii, G.I. ed. 1969. Baikal Atlas. Limnol. Inst. Acad. Sci. U.S.S.R. Siberian Section. publ. by Govt. Dept. Geodesy and Cartography, Irkutsk and Moscow, 30 pp.

Gardner, C.S., J.M. Greene, M.D. Kruskal, and R.M. Miura. 1967. Method for solving the Korteweg-deVries equation. Phys. Rev. Lett., 19: 1095-1097.

Gonella, J.A. 1974. Effet d'écran d'une thermocline observations faites sur la bouée-laboratoire. La Houille Blanche, 1974: No. 7/8: 607-613.

Gustafson, T. and B. Kullenberg. 1936. Untersuchungen von Trägheitsströmungen in der Ostsee. Svensk. Hydrogr.-Biol. Komm. Skr. (New Series) Hydrogr. 13: 28 pp.

Hamblin, P.F. and F.C. Elder. 1973. A preliminary investigation of the wind stress field over Lake Ontario. Proc. 16th Conf. Gt. Lakes Res. (Int. Assoc. Gt. Lakes Res.) 1973: 723-734.

Hammack, J.L. and H. Segur. 1974. The Korteweg-deVries equation and waterwaves. Part 2. Comparison with experiments. J. Fluid Mech., 65: 289-314.

Houghton, D.D. 1969. Effect of rotation on the formation of hydraulic jumps. J. Geophys. Res., 74: 1351-1360.

Hunkins, K. and M. Fliegel. 1973. Internal undular surges in Seneca Lake: a natural occurrence of solitons. J. Geophys. Res., 78: 539-548.

Irbe, J.G. and R.J. Mills. 1976. Aerial surveys of Lake Ontario water temperature and description of regional weather conditions during IFYGL -- January 1972 to March 1973. Environ. Canada (Downsview) Atmos. Environ. Rept. CL1-76, 151 pp.

Kadomtsev, B.B. and V.I. Karpman. 1971. Nonlinear waves. Sov. Phys. Usp. (English translation) 14: 40.

Kanari, S. 1975. The long-period internal waves in Lake Biwa. Limnol. Oceanogr., 20: 544-553.

Krauss, W. 1966. Interne Wellen, in Methoden und Ergebnisse der theoretische Ozeanographie, Vol. 2, Bornträger, Berlin, 248 pp.

_____. 1979. The erosion of a thermocline by breaking internal waves in a field of inertial waves. Int. Assoc. Phys. Sci. Ocean, Proc.-Verb. No. 15 (XVII Gen. Ass., Int. Ass. Geodesy Geophys., Canberra, Australia), abstract only, p. 72.

Lauwerier, M.A. 1961. The North Sea Problem IV. Non-stationary wind effects in a rectangular bay. (Theoretical Part). Proc., Koninklijke Nederlandske Akademie van Wettenschappen, Series A, 64, 104-122.

LeBlond, P.H. and L.A. Mysak. 1978. Waves in the ocean. Elsevier, 602 pp.

Lerman, A. (ed.) 1978. Lakes: chemistry, geology, physics. Springer-Verlag, 363 pp.

Marmorino, G.O. 1978. Inertial currents in Lake Ontario, Winter 1972-73 (IFYGL). J. Phys. Cceanogr., 8: 1104-1120.

_____ and C.H. Mortimer. 1977. Internal waves observed in Lake Ontario during the International Field Year for the Great Lakes (IFYGL) 1972: II. Spectral analysis and modal decomposition. CGLS Spec. Rept. 33.

Millot, C. and M. Crépon. 1980. Inertial motions on the continental shelf: observations and theory. J. Phys. Oceanogr. (in press)

Mortimer, C.H. 1963. Frontiers in physical limnology with particular reference to long waves in rotating basins. Proc. 5th Conf. Great Lakes Res., Univ. Michigan, Great Lakes Res. Div., Publ. No. 10: 9-42.

_____. 1971. Large-scale oscillatory motions and seasonal temperature changes in Lake Michigan and Lake Ontario. Pt. I, text, 111 p., Part II, illustrations, 106 p., with the collaboration, in Chapter III on internal wave theory, of M.A. Johnson. Ctr. Great Lakes Stds., Univ. Wisconsin-Milwaukee, Spec. Rept. No. 12.

1977. Innternal waves observed in Lake Ontario during the International Field Year for the Great Lakes (IFYGL), 1972: I. Descriptive survey and preliminary interpretations of near-inertial oscillations in terms of linear channel-wave models. Ctr. for Great Lakes Stds., Spec. Rept. No. 32, Univ. Wisconsin-Milwaukee, 122 p.

_____. 1978. Internal waves and associated currents in Lake Ontario observed during the IFYGL Program. Verh. Int. Ver. Limnol., 20: 280-287.

Mortimer, C.H. 1979. Strategies for coupling data collection and analysis with dynamic modelling of lake motions, p. 183-277. In Lake Hydrodynamics (W.H. Graf and C.H. Mortimer, Eds.), Proc. Symp., Lausanne, Switzerland, Oct. 1978. Elsevier Devel. in Water Sci. 11, Amsterdam.

Neumann, G. and W.J. Pierson. 1966. Principles of Physical Oceanography. Prentice-Hall, Englewood Cliffs, N.J.

Osborne, A.R. and Burch, T.L. 1980. Internal solitons in the Andaman Sea., Science, 208: 451-460.

Platzman, G.W. 1970. Ocean tides and related waves. Amer. Math. Soc., Lectures in applied mathematics, 14: 239-291.

Poincaré, H. 1910. Théorie des marées. Lecons de mécanique céleste, 3. Paris.

Pollard, T.T. 1970. On the generation by winds of inertial waves in the ocean. Deep-Sea Res., 17: 795-812.

_____ and R.C. Millard. 1970. Comparison between observed and simulated wind-generated inertial oscillations. Deep-Sea Res., 17: 813-821.

Rao, D.B. 1977. Free internal oscillations in a narrow, rotating rectangular basin. Mar. Sci. Directorate, Dept. Fish. Environ., Ottawa, Ms Rept. Ser. No. 43, 391-398.

_____ and D.J. Schwab. 1976. Two-dimensional normal modes in arbitrary enclosed basins on a rotating earth: Application to Lakes Ontario and Superior. Phil. Trans. R. Soc. London A 281: 63-96.

Sato, G.K. and C.H. Mortimer. 1975. Lake currents and temperatures near the western shore of Lake Michigan. 98 p., 216 figs. Center for Great Lakes Studies, Spec. Rept. No. 22, Univ. Wisconsin-Milwaukee.

Schwab, D.J. 1977. Internal free oscillations in Lake Ontario. Limnol. Oceanogr., 22: 700-708.

Simons, T.J. 1978. Generation and propagations of downwelling fronts. J. Phys. Oceanogr., 8: 571-581.

_____. 1980. Circulation models of lakes and inland seas. Canadian Bull. Fish. Aquat. Sci., 203: 146 pp.

Sverdrup, H.U. 1926. Dynamic of tides on the North Siberian sehlf: results from the Maud Expedition. Geofys. Publ. 4. 75 pp.

Taylor, G.I. 1920. Tidal oscillations in gulfs and rectangular basins. Proc. Lond. Math. Soc., 2nd Ser., 20: 148-181.

Thorpe, S.A. 1977. Turbulence and mixing in a Scottish loch. Phil. Trans. Roy. Soc. London, A., 286: 125-181.

U.S. Dept. Interior. 1967. Water quality investigation, Lake Michigan basin: Lake currents. Fed. Water Pollution Control Admin. (FWPCA), Gt. Lakes Reg., Chicago., Mimeo rep. 364 pp.

Zabusky, N.J. and M.D. Kruskal. 1965. Interacation of "solitons" in collisionless plasma and the recurrence of initial states. Phys. Rev. Lett., 15: 240-243.

8 APPENDICES

8.1 Table of Julian dates for June to November 1972 (leap year).

DAY \ MONTH	6	7	8	9	10	11
1	153	183	214	245	275	306
2	154	184	215	246	276	307
3	155	185	216	247	277	308
4	156	186	217	248	278	309
5	157	187	218	249	279	310
6	158	188	219	250	280	311
7	159	189	220	251	281	312
8	160	190	221	252	282	313
9	161	191	222	253	283	314
10	162	192	223	254	284	315
11	163	193	224	255	285	316
12	164	194	225	256	286	317
13	165	195	226	257	287	318
14	166	196	227	258	288	319
15	167	197	228	259	289	320
16	168	198	229	260	290	321
17	169	199	230	261	291	322
18	170	200	231	262	292	323
19	171	201	232	263	293	324
20	172	202	233	264	294	325
21	173	203	234	265	295	326
22	174	204	235	266	296	327
23	175	205	236	267	297	328
24	176	206	237	268	298	329
25	177	207	238	269	299	330
26	178	208	239	270	300	331
27	179	209	240	271	301	332
28	180	210	241	272	302	333
29	181	211	242	273	303	334
30	182	212	243	274	304	335
31		213	244		305	

8.2 Complete list of composite diagrams, including text figures and those appended in Section, 8.3.

The following table (indicating Julian dates) includes all the composite diagrams (prepared, as described in Section 3, to display wind, current, and temperature records from selected IFYGL stations, Lake Ontario, June to November 1972) presented and examined in Parts I and II of this Report. Composite diagrams used as text figures in Part I are so numbered in the table. The remainder appear (in order of beginning date and in cross-section sequence 2, 6, 9, and 11, in section 8.3) referenced by cross-section number, followed by Julian dates, by A (indicating Appendix), and by page number.

Cross-Section 2		Cross-Section 6		Cross-Section 9		Cross-Section 11	
	p.		p.				p.
161-174 A	167	161-174 } A	168	161-174 (Fig. 31)		161-174 A	169
175-188 A	170	175-188 }		175-188 (Fig. 34)		175-188 A	171
189-202 A	172	189-202 A	173	189-202 (Fig. 38)		189-202 (Fig. 40)	
203-216 (Fig. 41)		203-216 A	174	203-216 (Fig. 43)		203-216 A	175
217-230 A	176	217-230 A	177	217-230 (Fig. 50)		217-230 A	178
				217-240 A	p. 179		
231-239 A*	180	231-244 A	181	230-249 A (on 2 sheets)	pp. 182/3	230-243 A	184
240-253 (Fig. 56)		240-253 A	185		p.	241-260 (Fig. 59)	
254-258 A*	180	245-258 A	186	250-263 A	187		
259-272 (Fig. 60)		259-272 (Fig. 64)		260-273 A	188	261-280 A	189
273-276 A**		273-275 A**		274-287 A	190		
277-290 (Fig. 72)		276-290 A	191			281-287 A	192
				292-319 (Fig. 77)+			

*assembled on a single sheet, p. 180

**included with sheet 11/281-287 A, p. 192

+wind at station 9 and near-surface currents only at stations 2, 3, 4, 6 and 11.

8.3 Composite diagrams, other than those included as text figures in the main body of the Report (Part I).

Sheet No. 2/161-174 A.

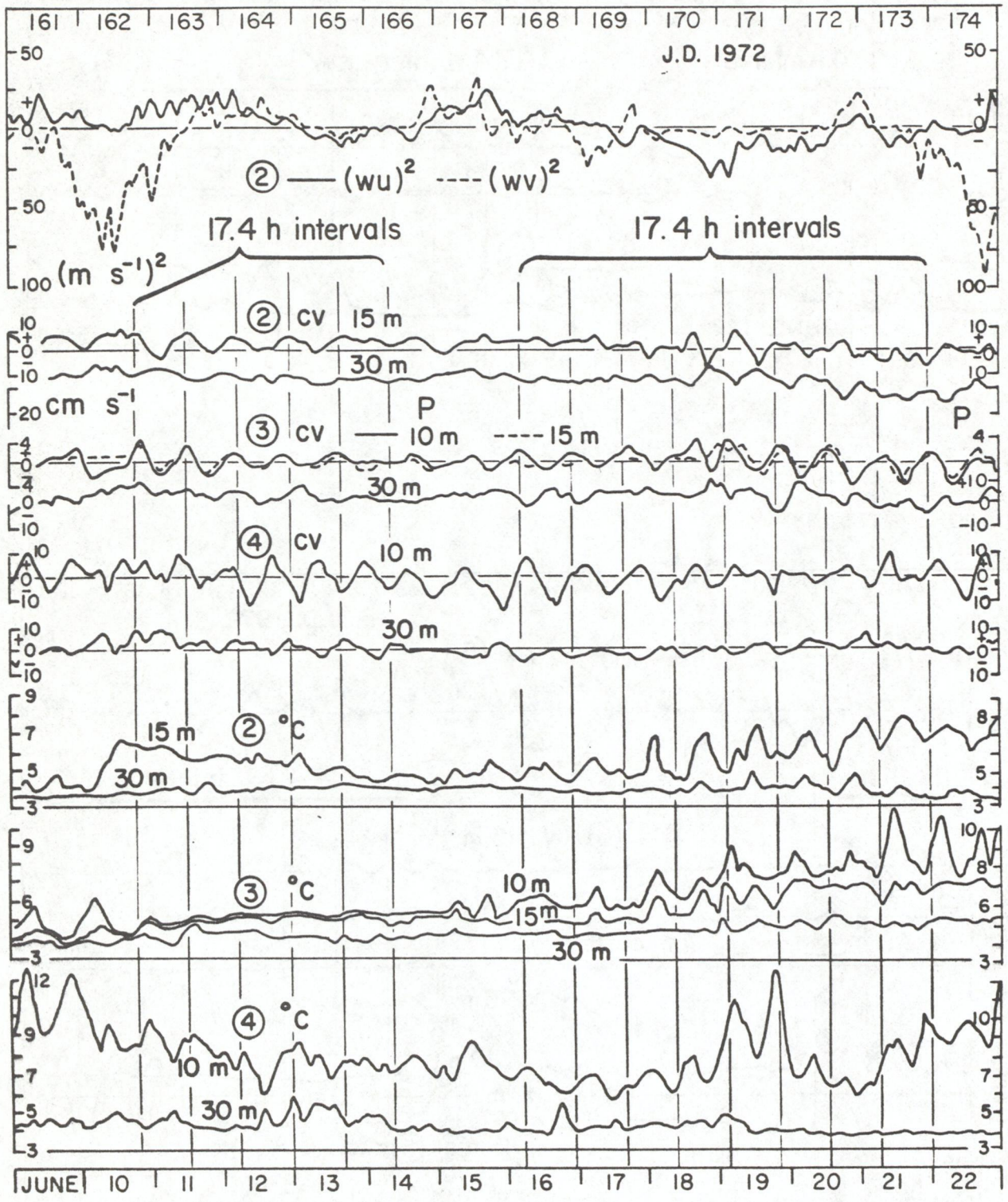

Sheet 6/161-174 A

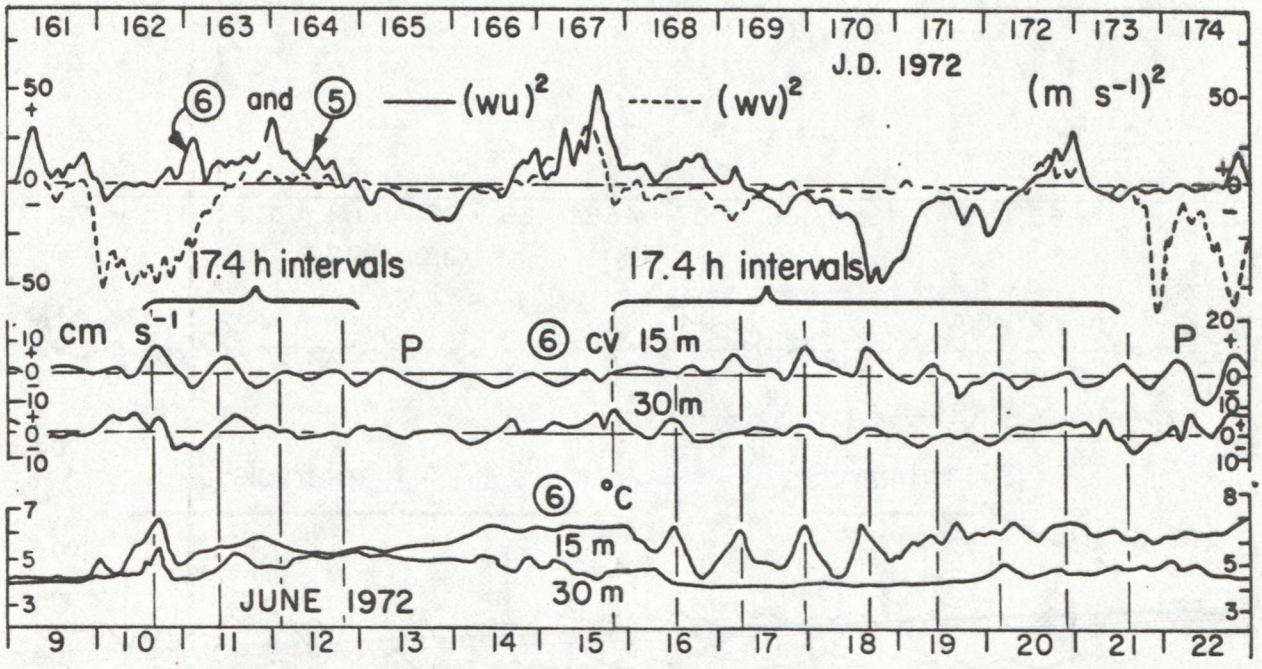

Sheet 6/175-188 A

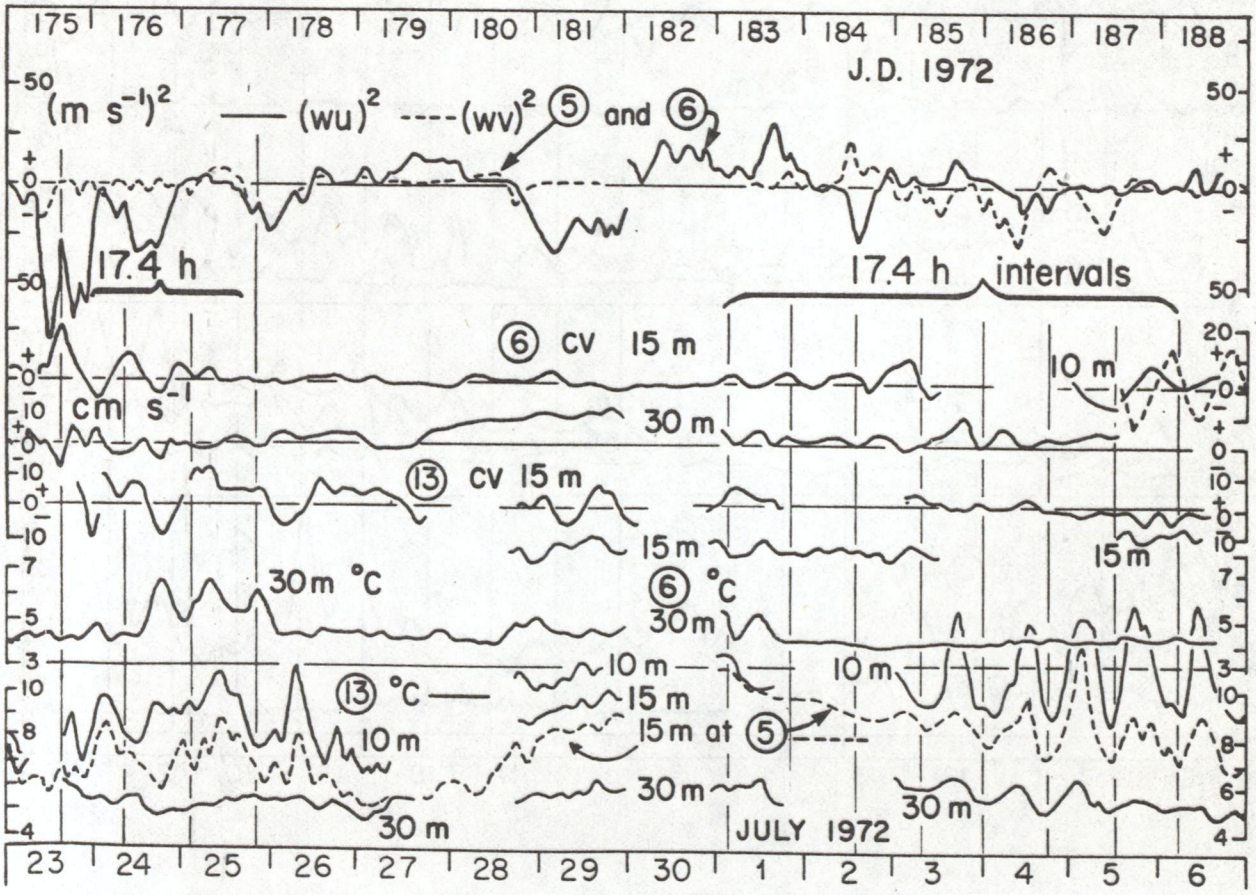

Sheet 11/161/174

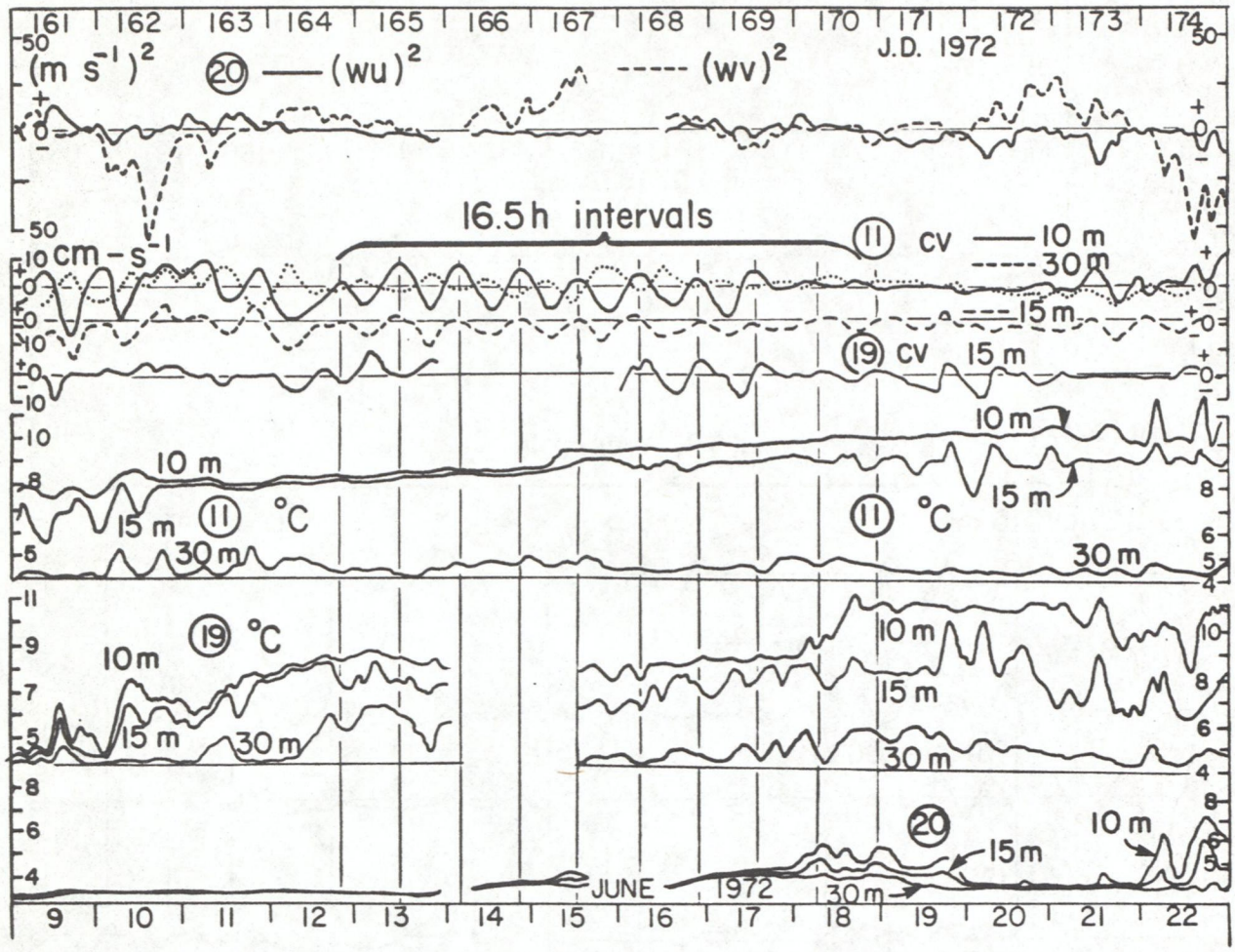

Sheet 2/175-188 A

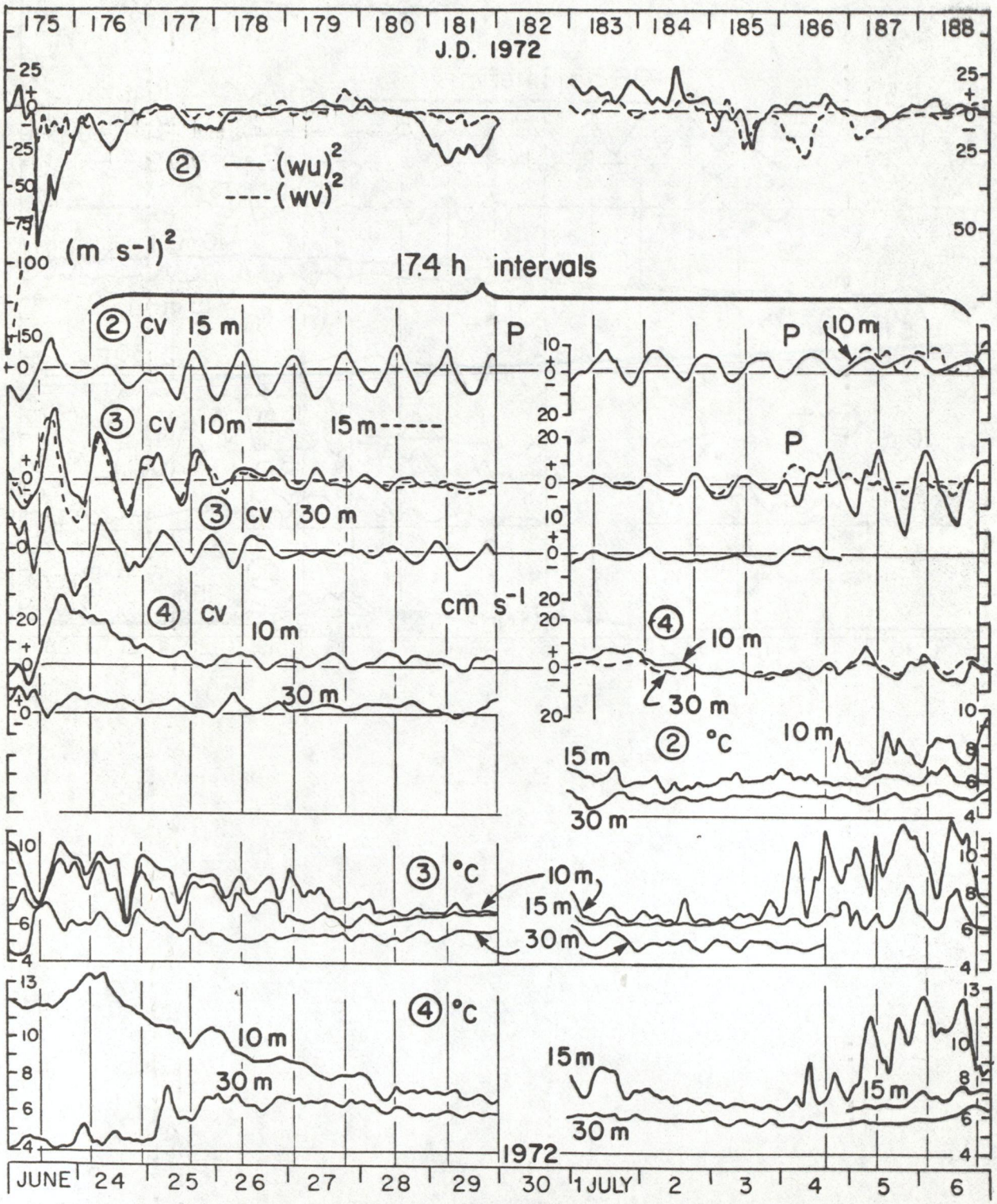

Sheet 11/175-188 A

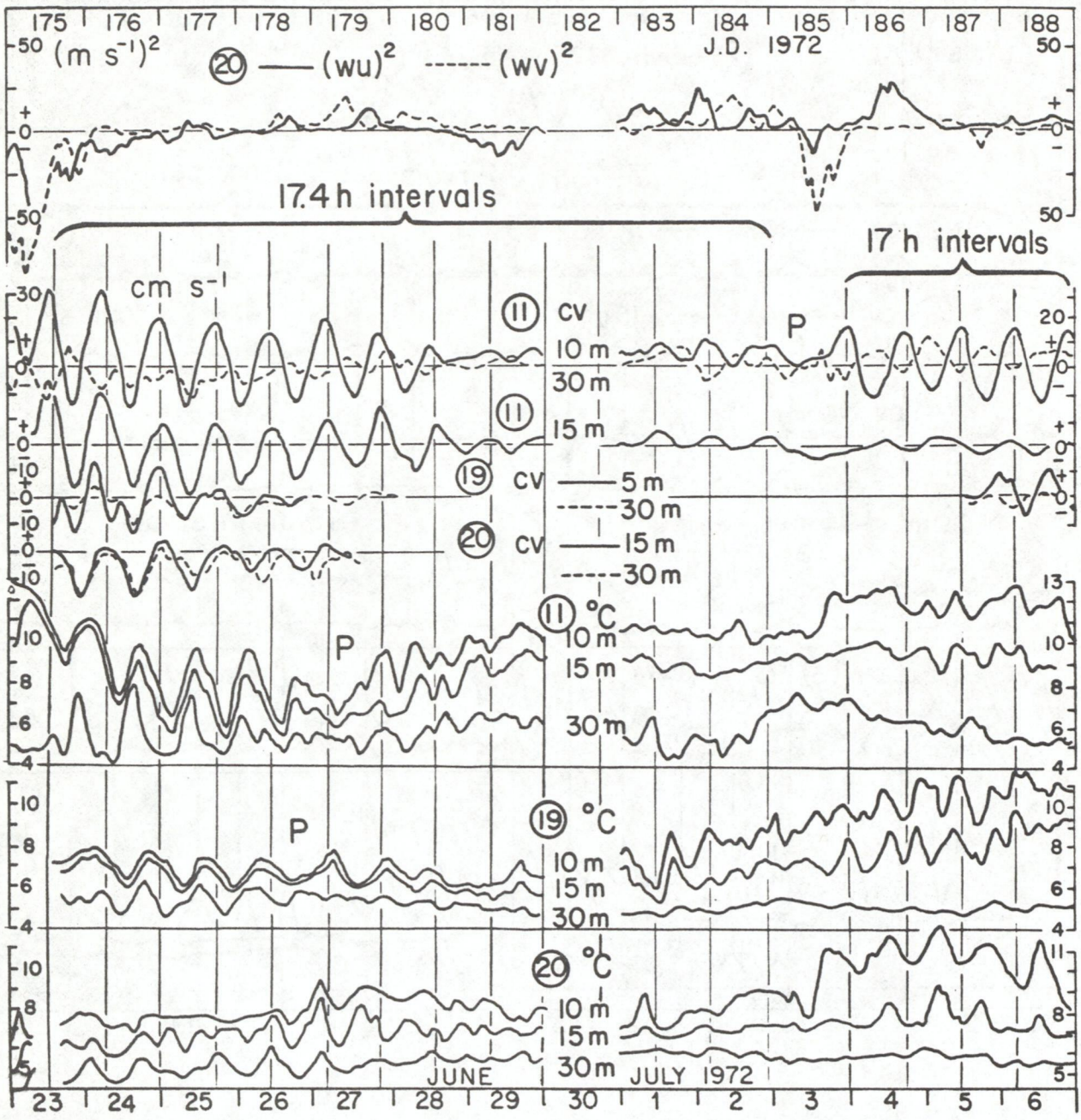

Sheet 2/189-202 A

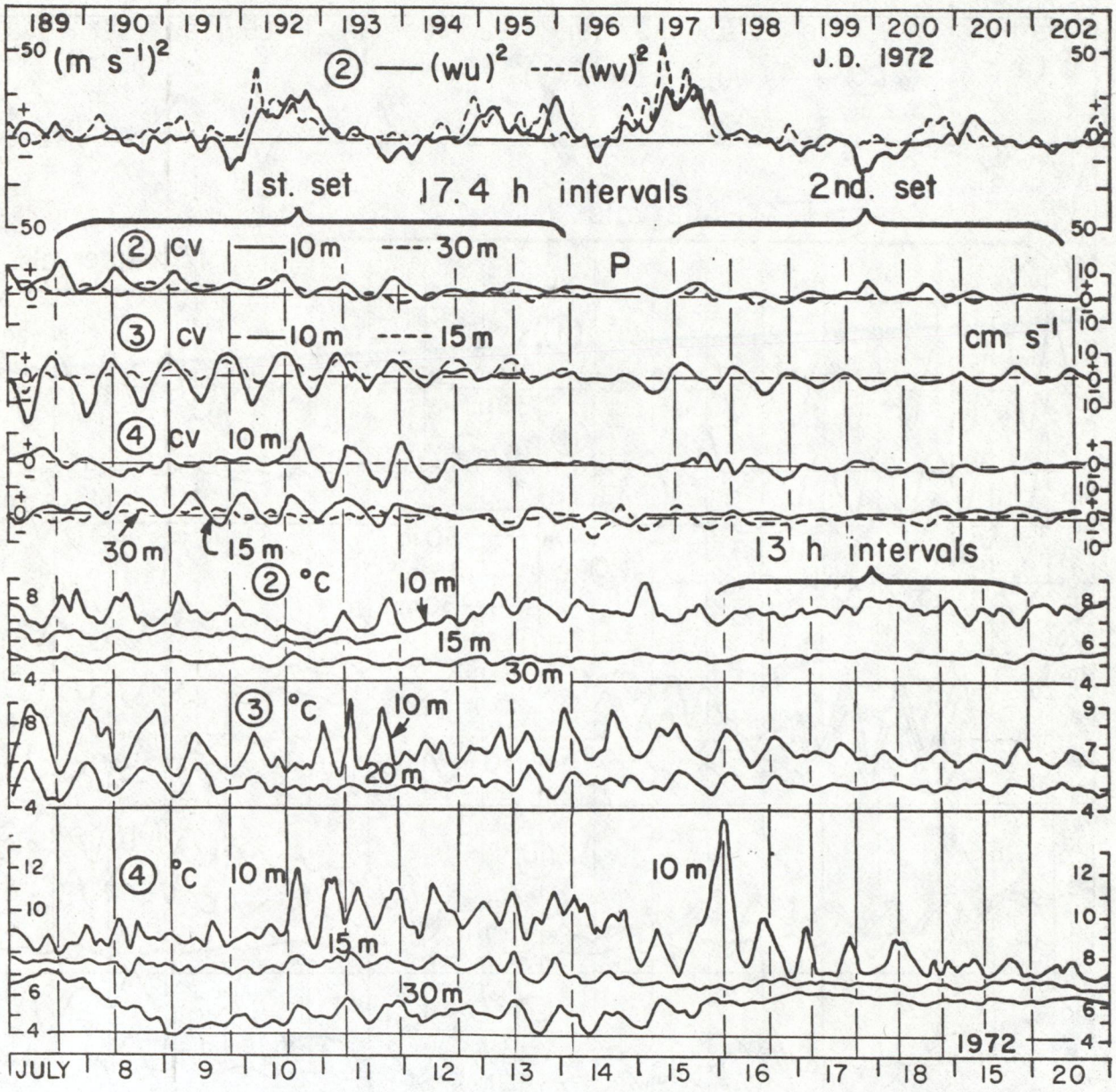

Sheet 6/189-202 A

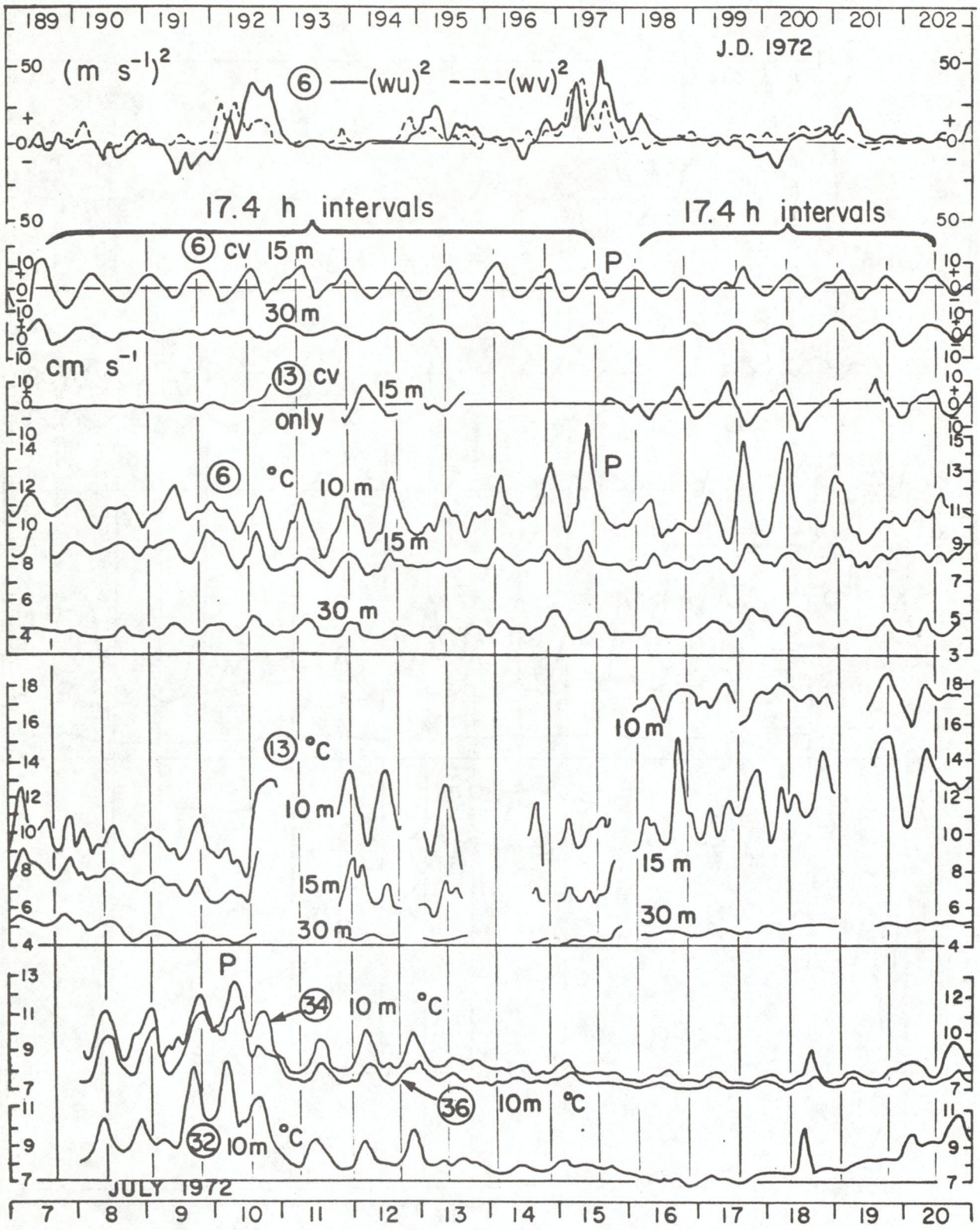

Sheet 6/203-216 A

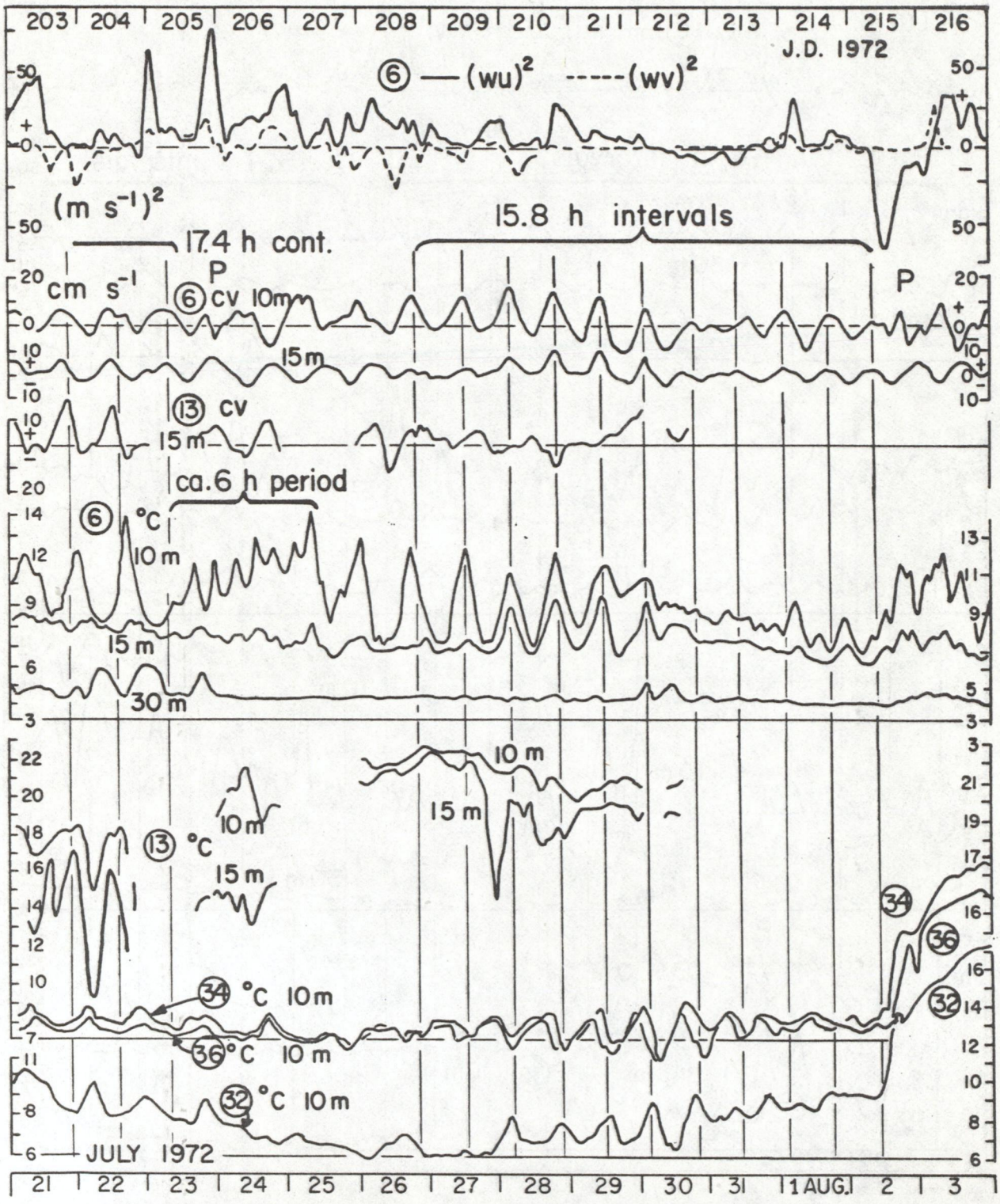

Sheet 11/203-216 A

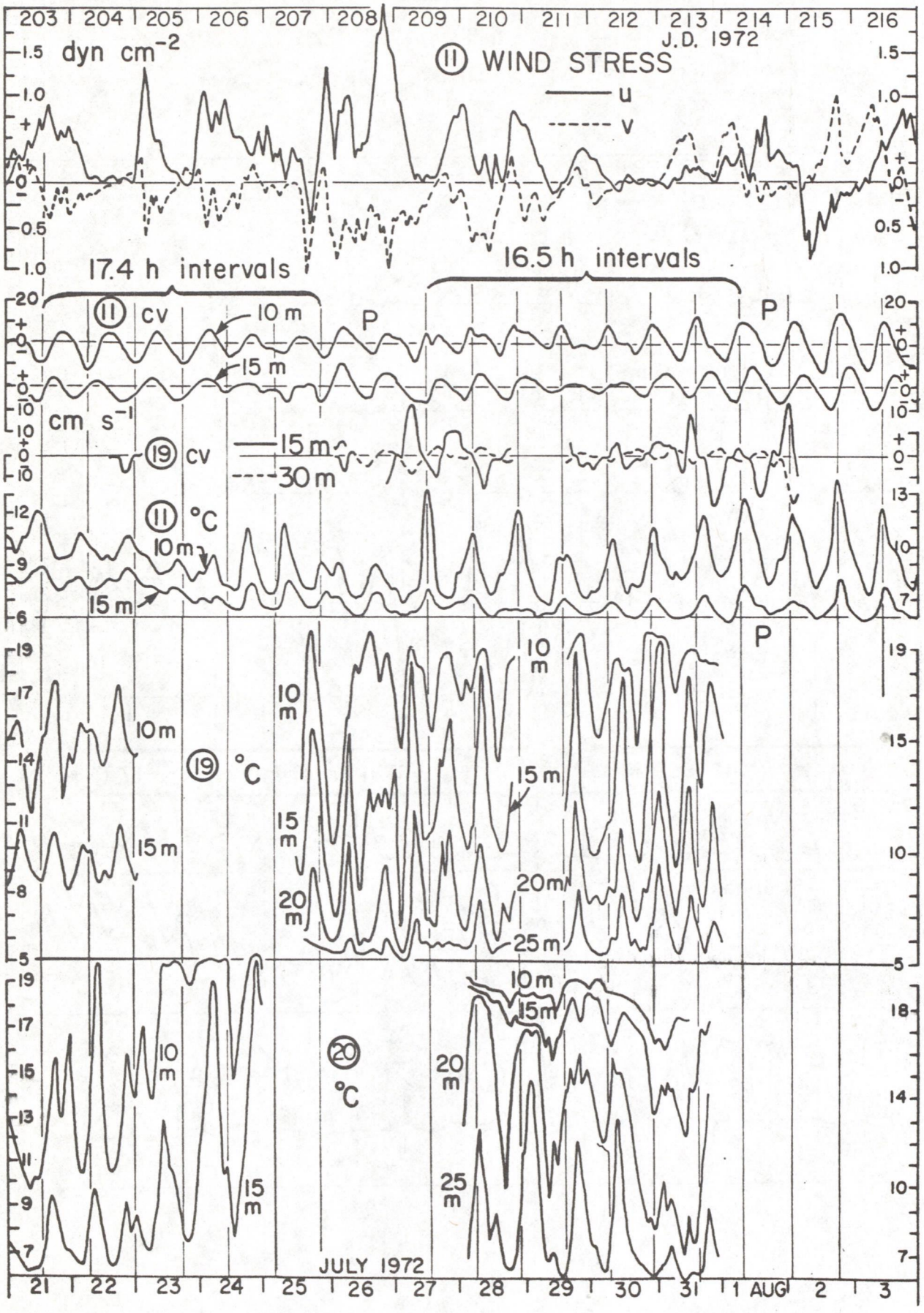

Sheet 2/217-230 A

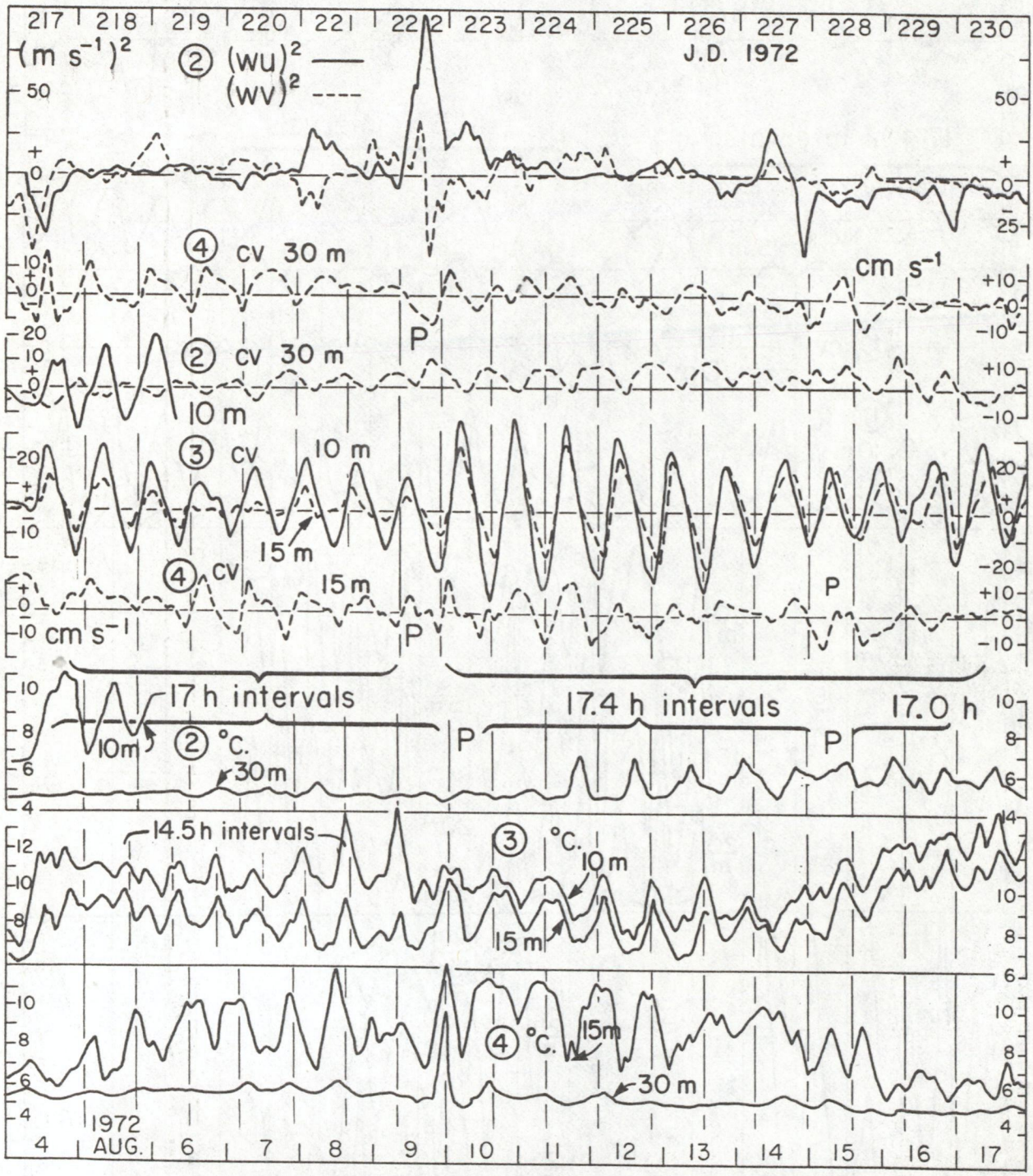

Sheet 6/217-230 A

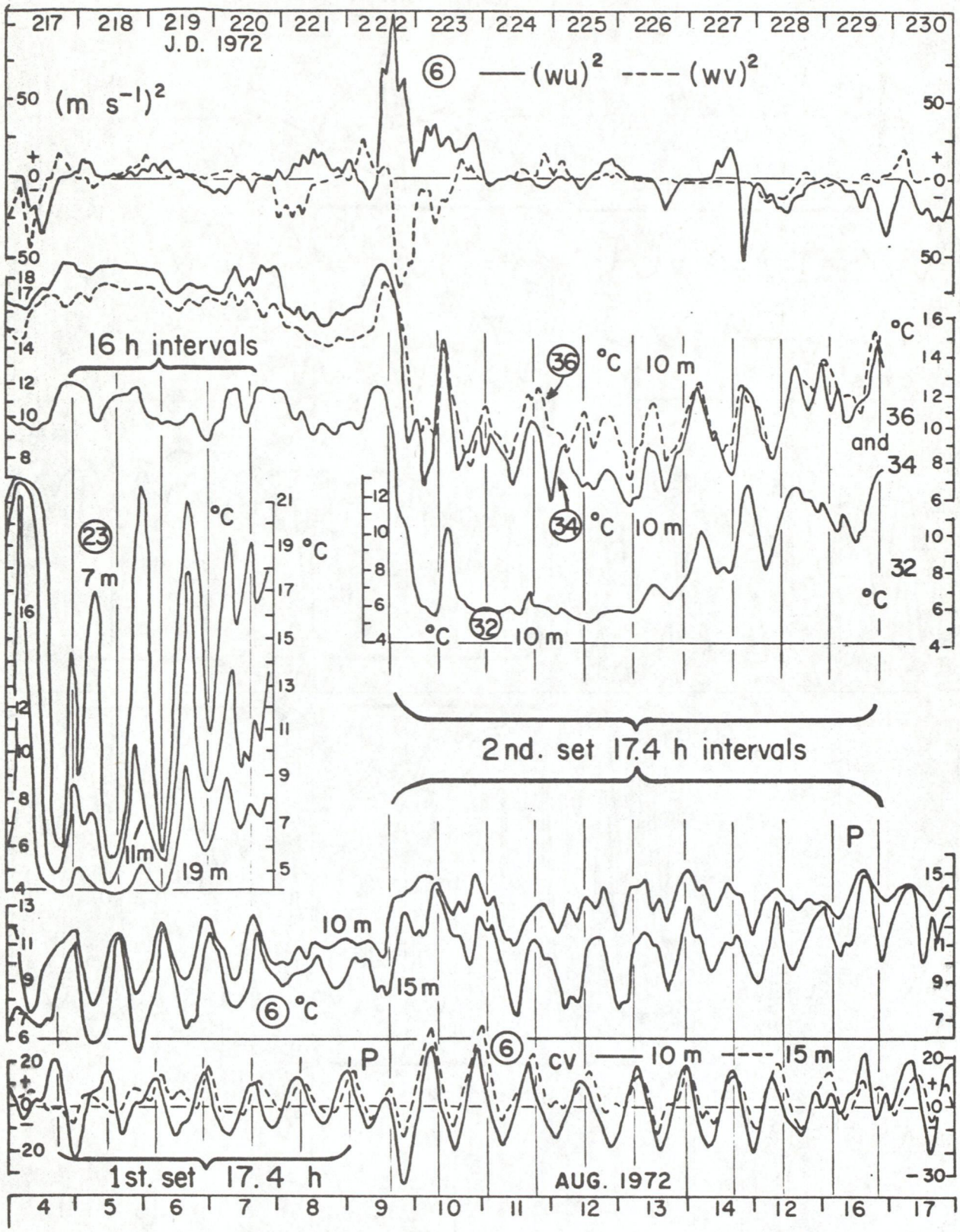

Sheet 11/217-230 A

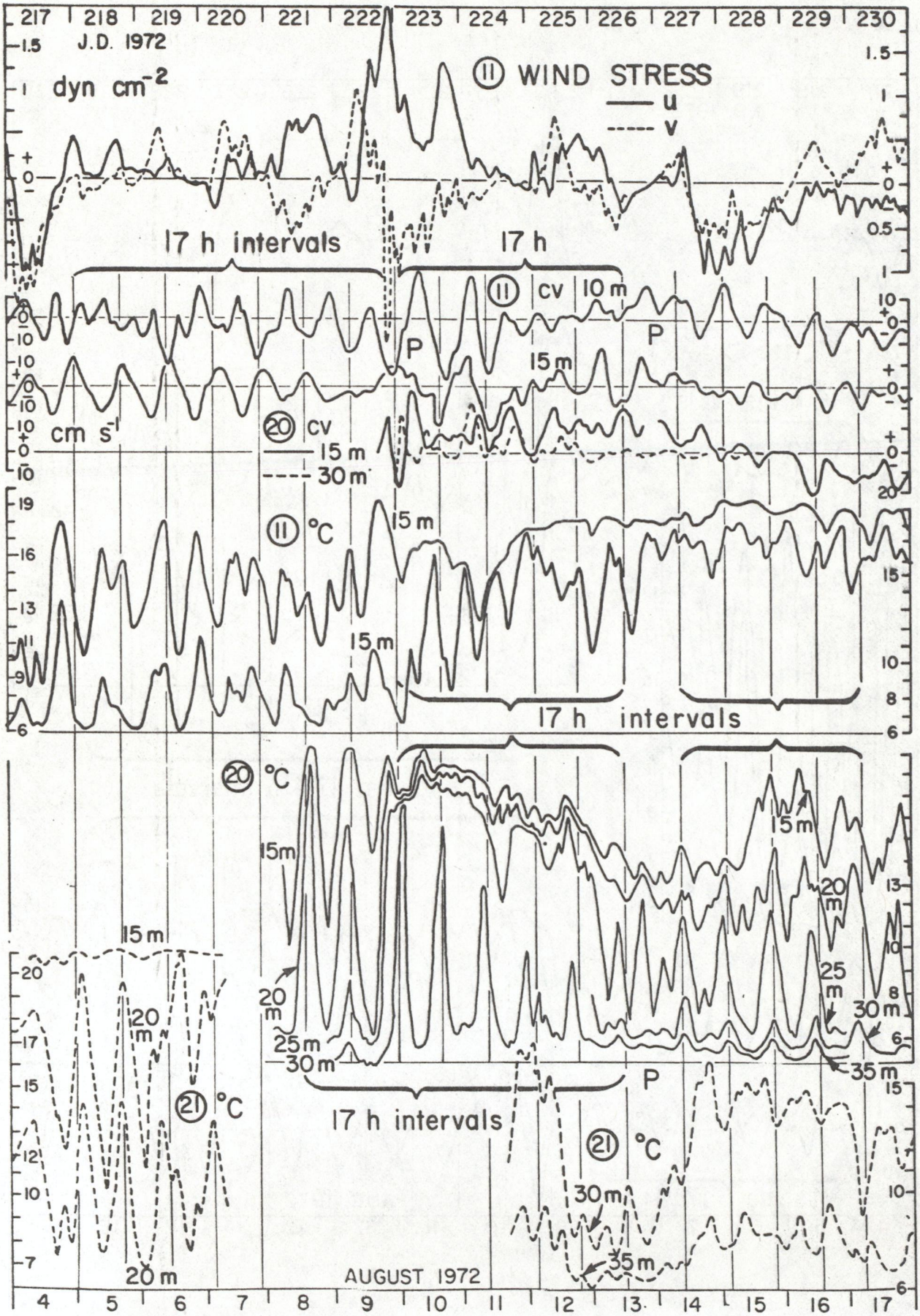

Sheet 9/217-240 A

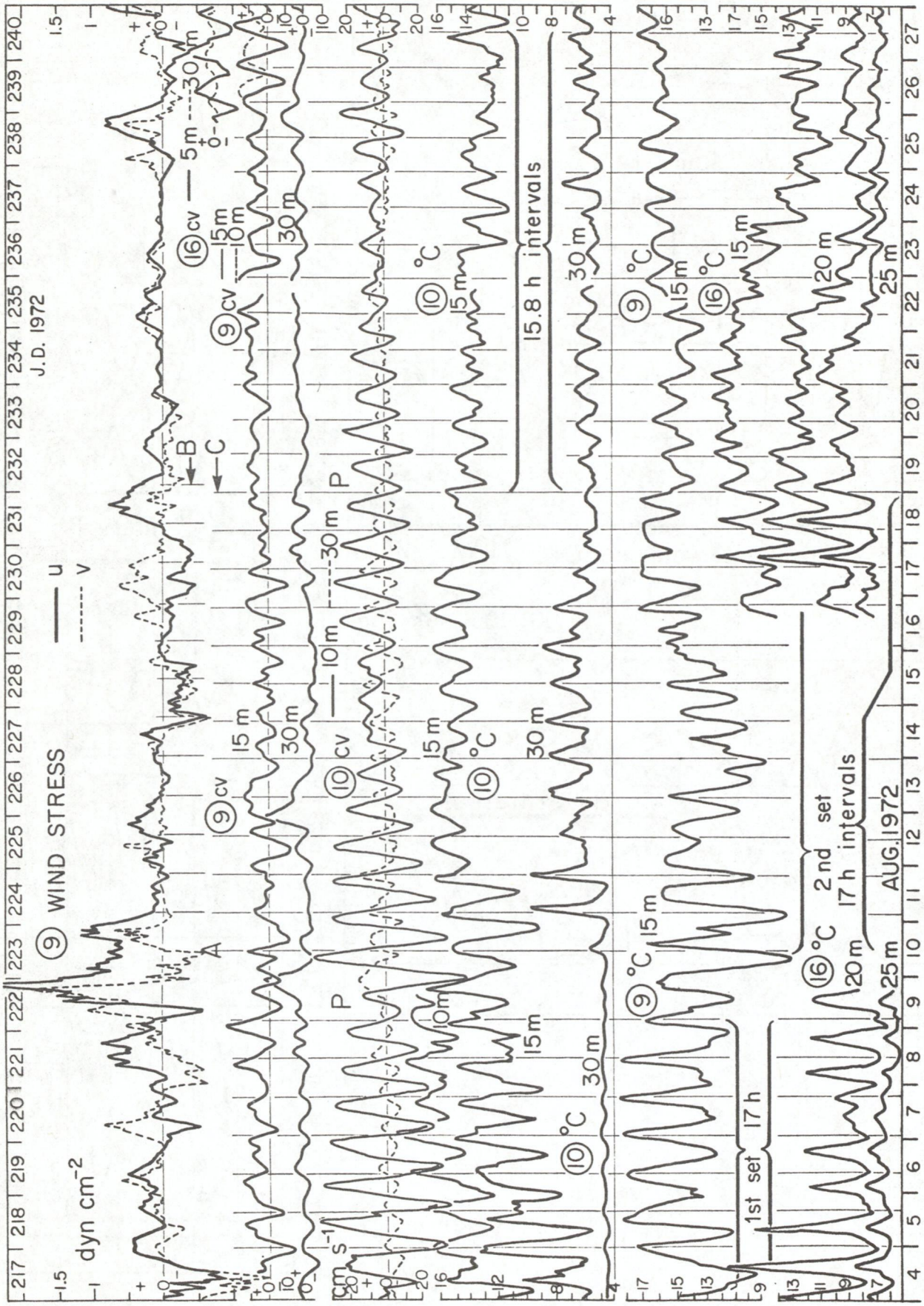

Sheet 2/231-239 A

2/254-258 A

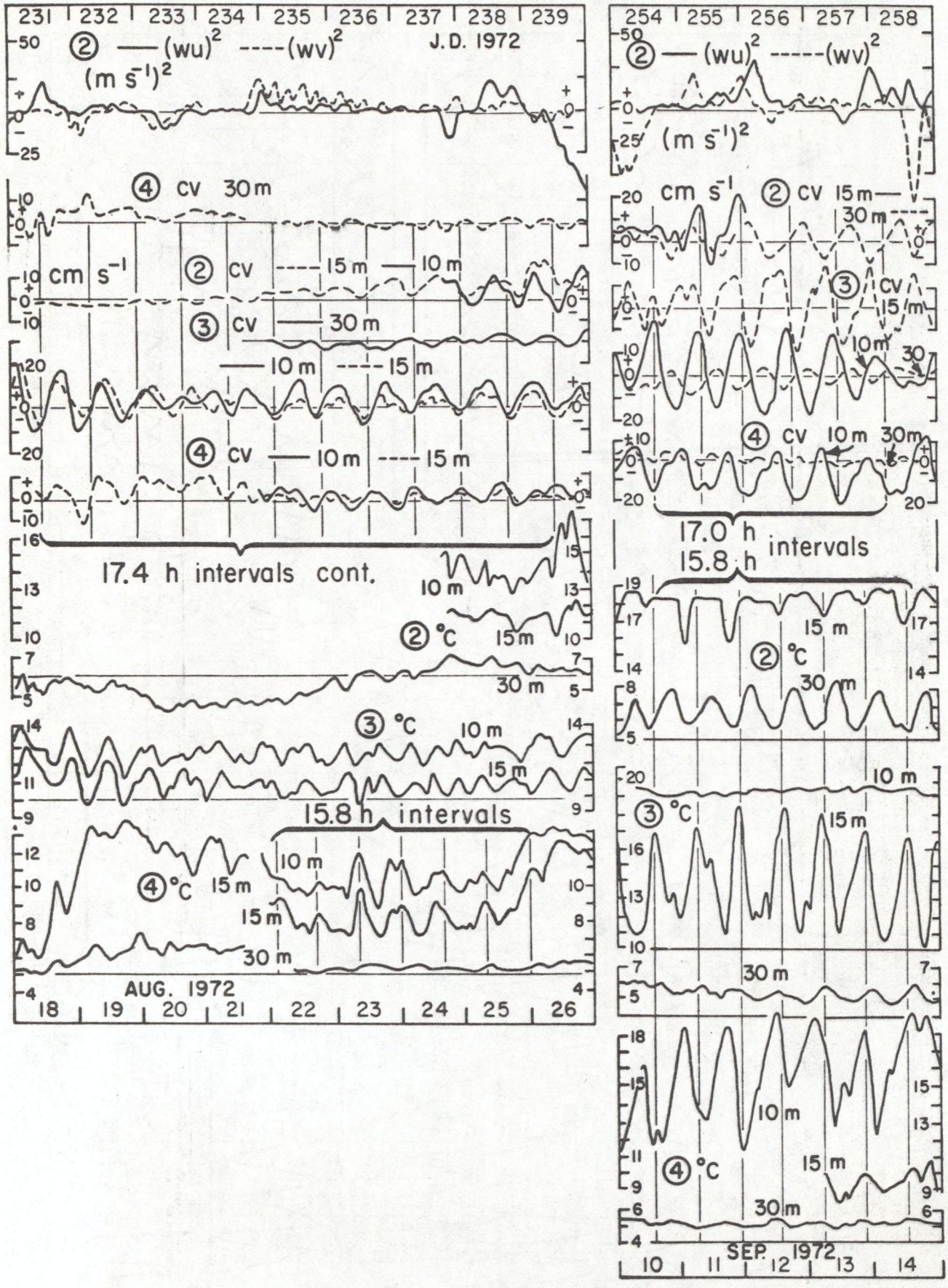

Sheet 6/231-244 A

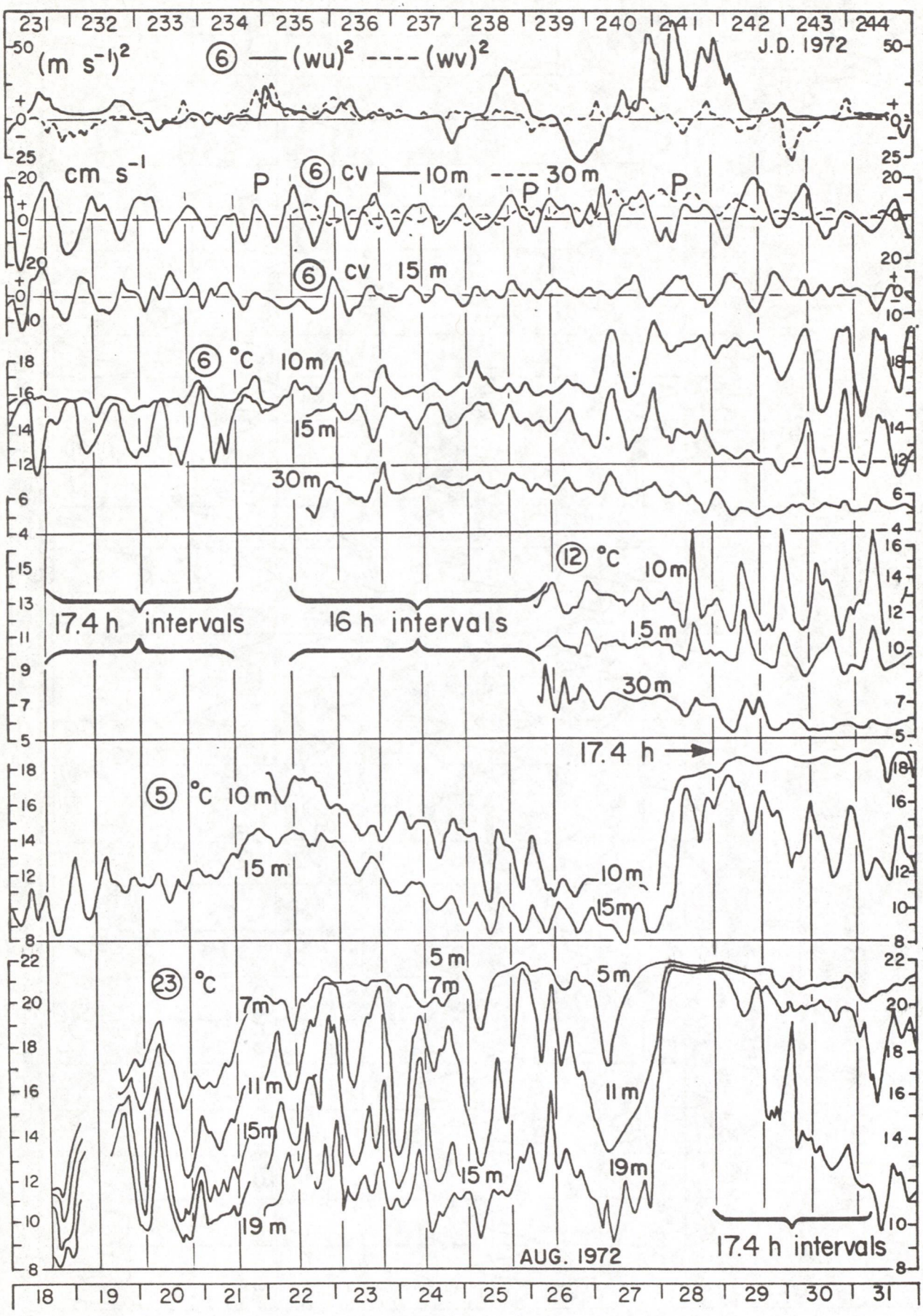

Sheet 9/230-249 A (top portion)

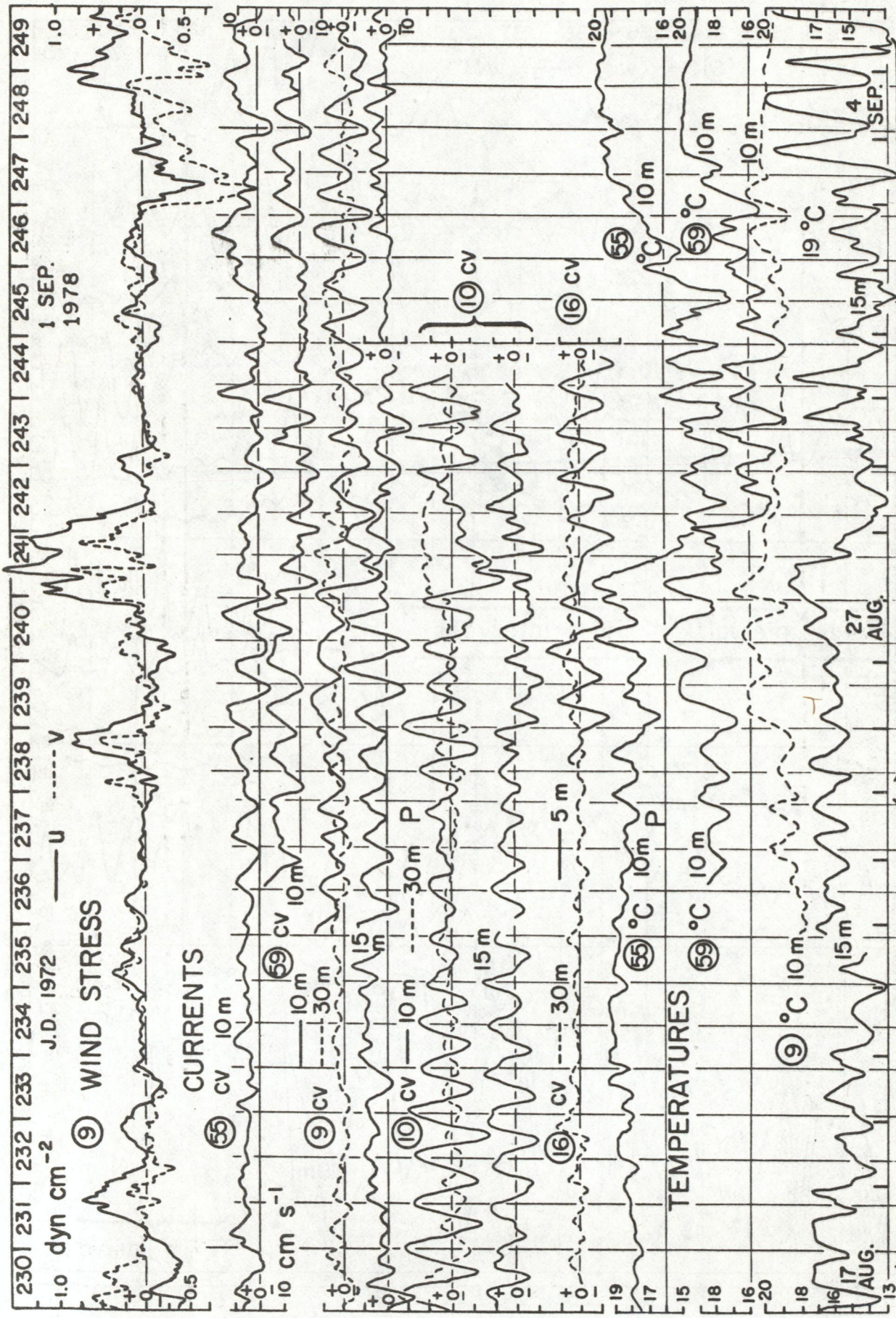

Sheet 9/230-249 A (bottom portion)

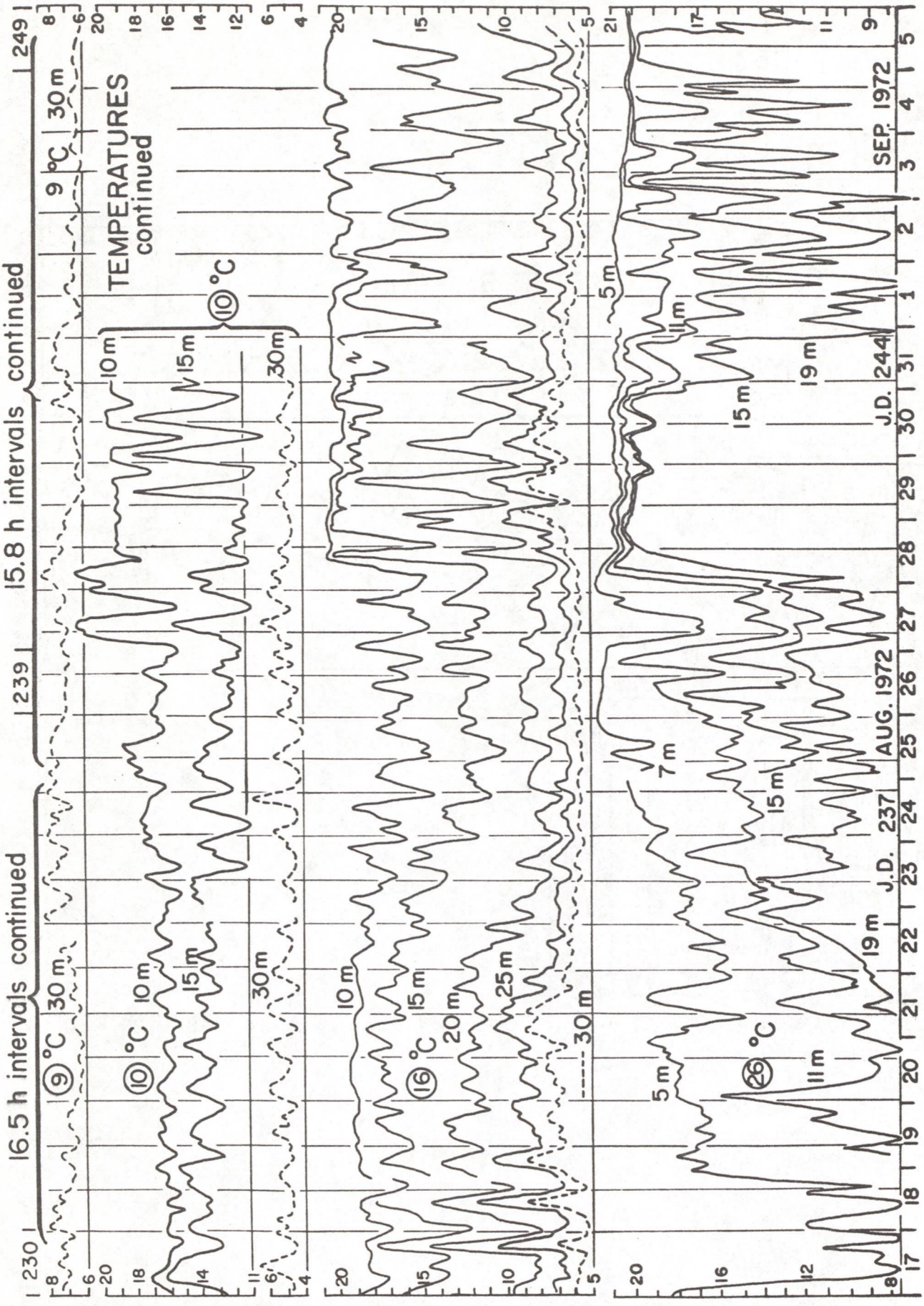

Sheet 11/230-243 A

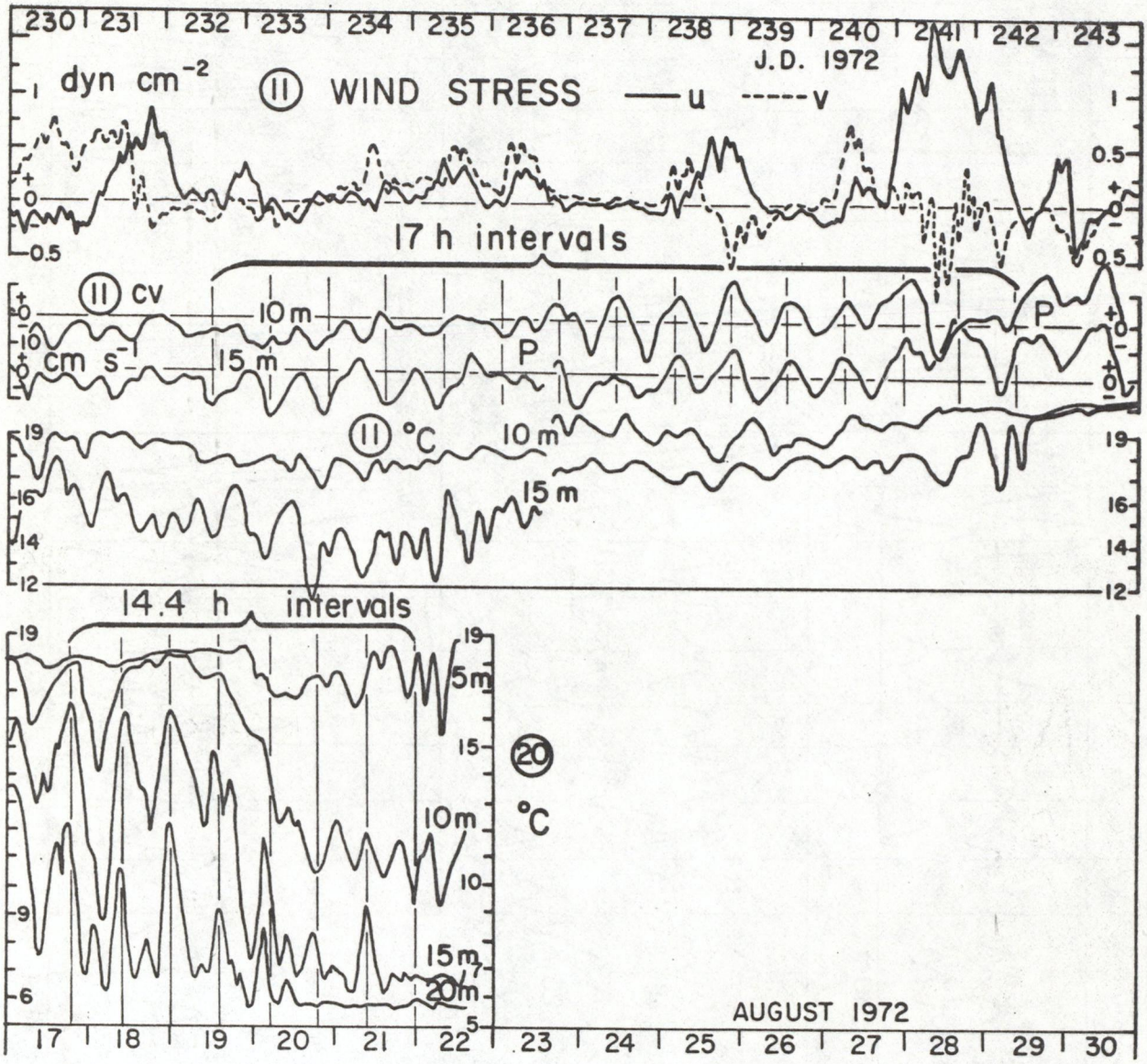

Sheet 6/240-253 A

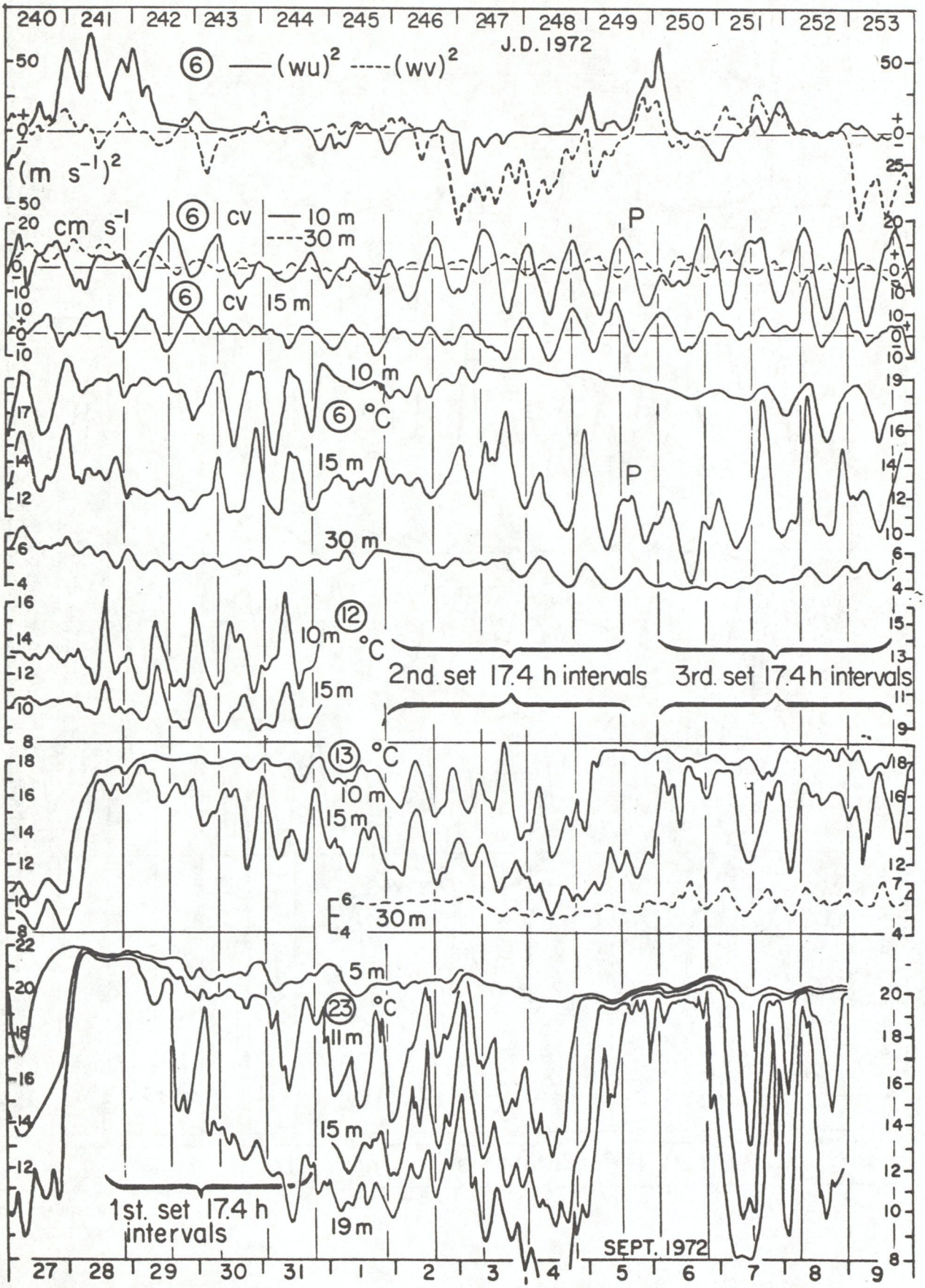

Sheet 6/245-258 A

Sheet 9/250-263 A

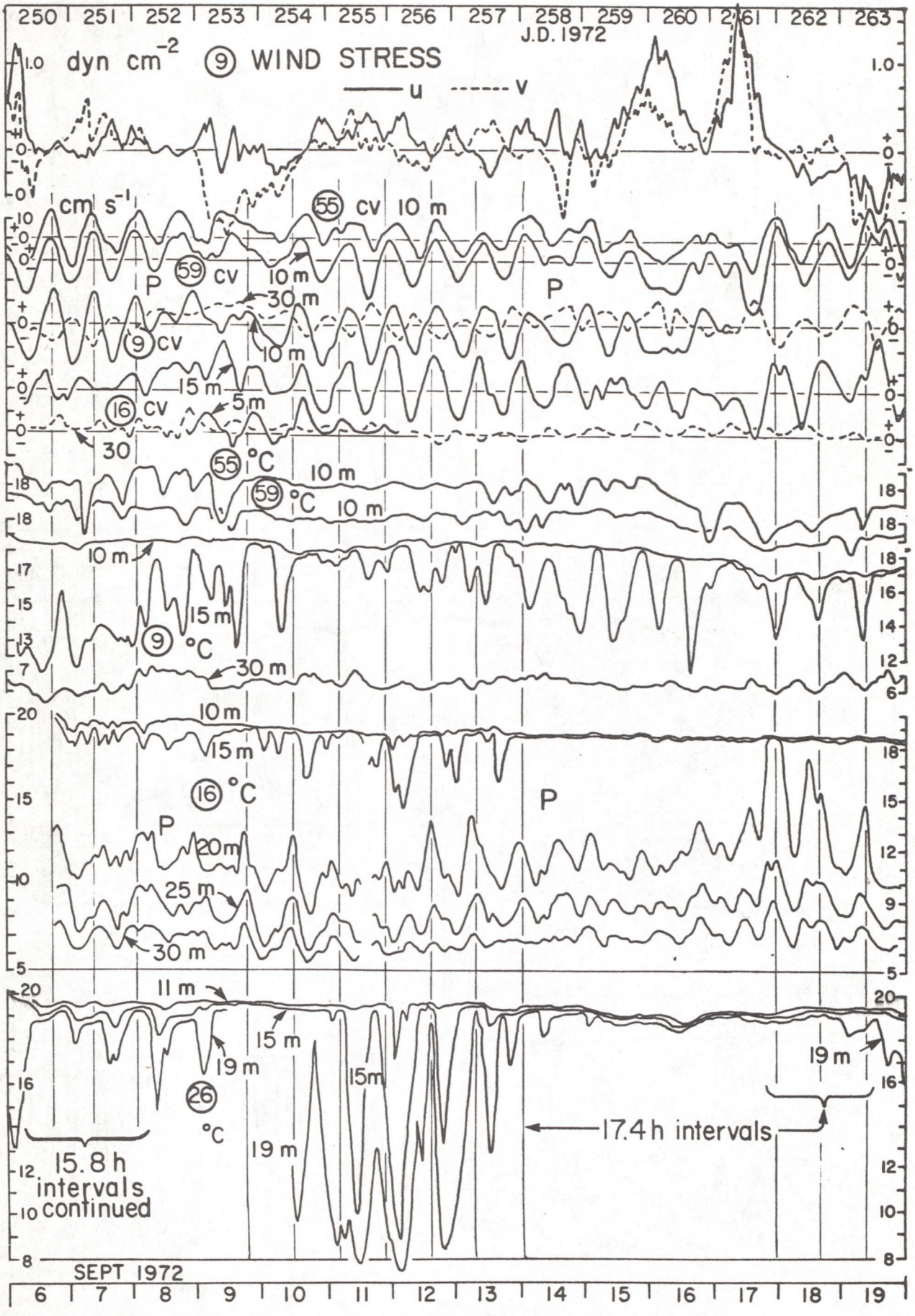

Sheet 9/260-273 A

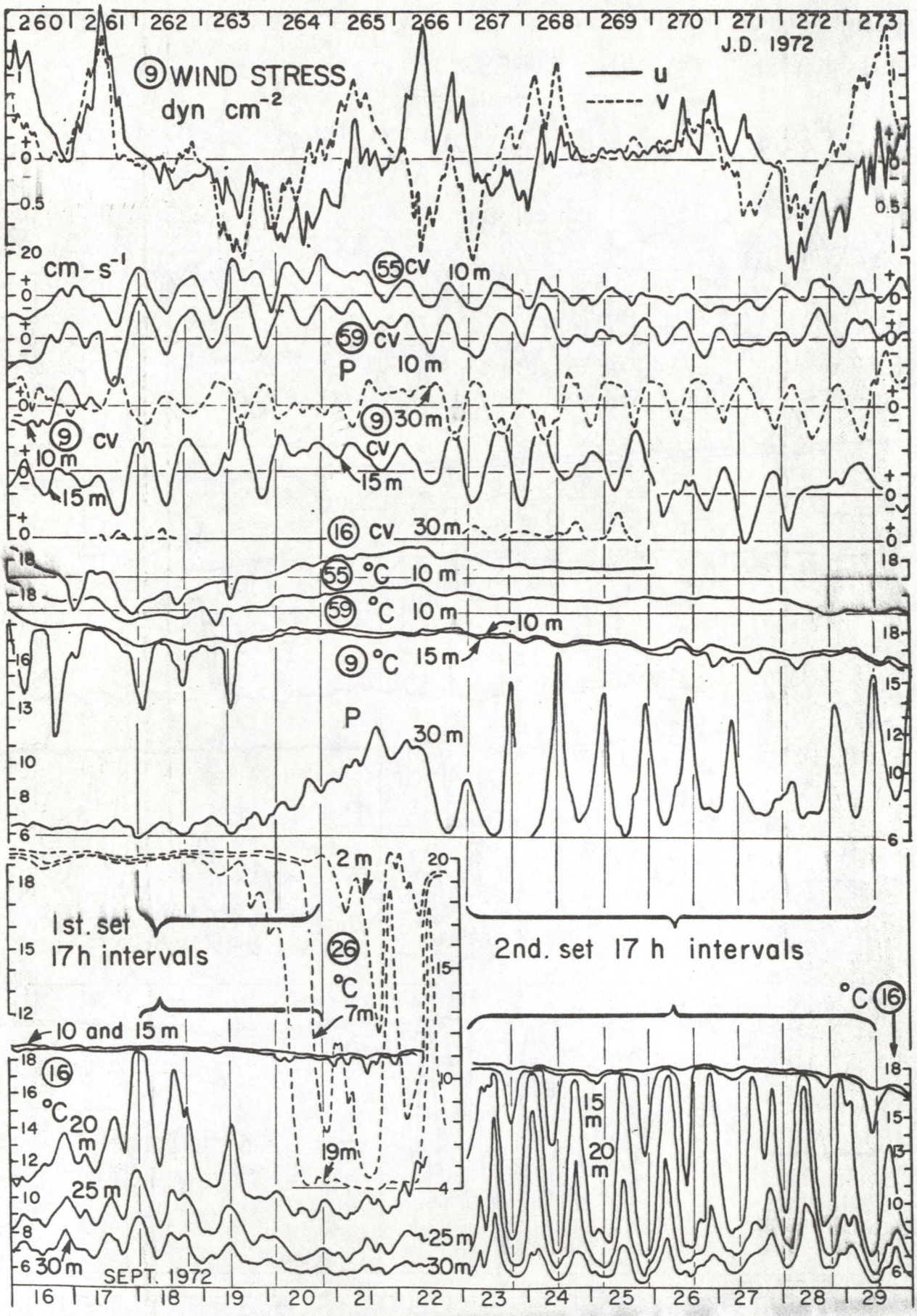

Sheet 11/261-280 A

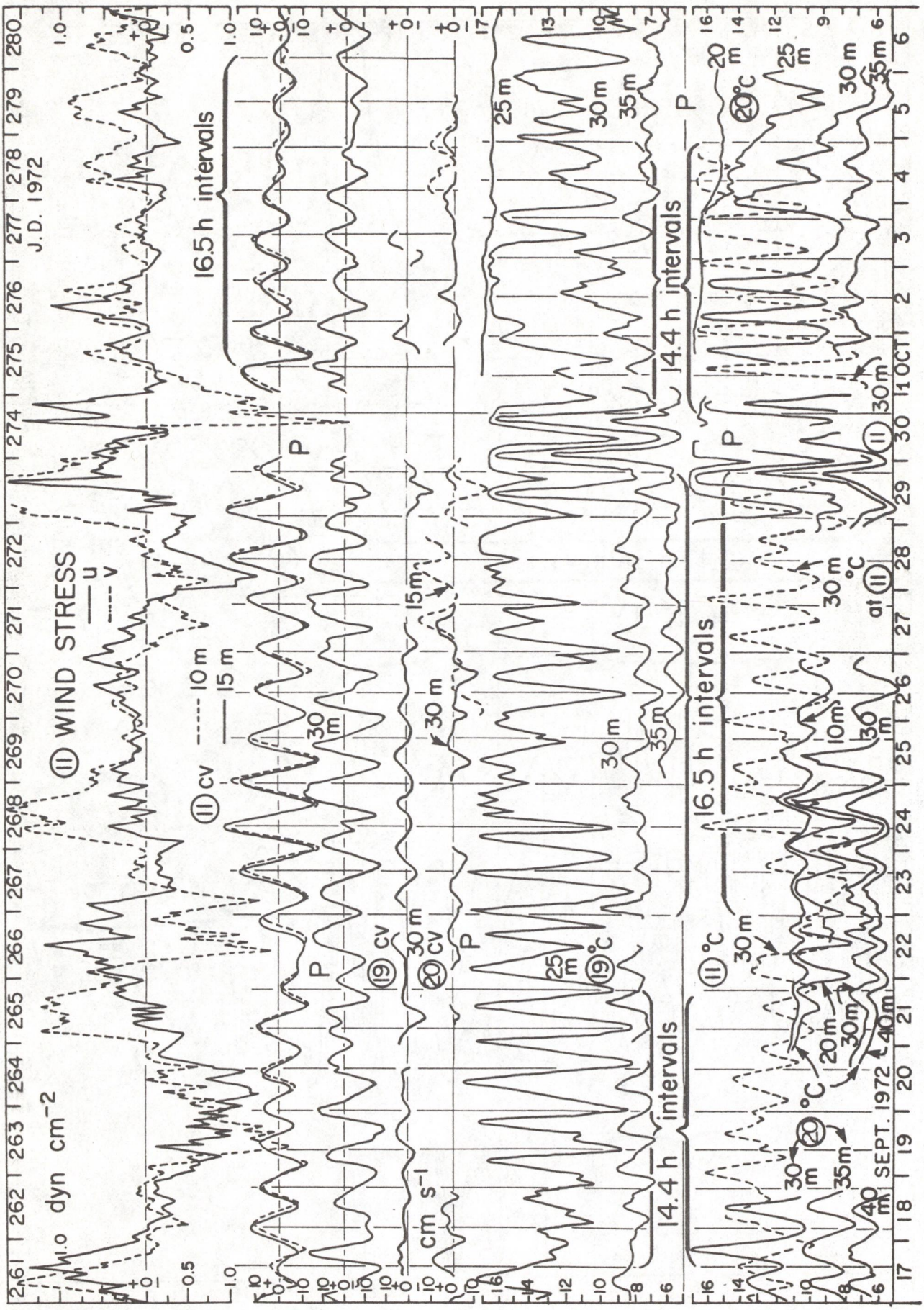

Sheet 9/274-287 A

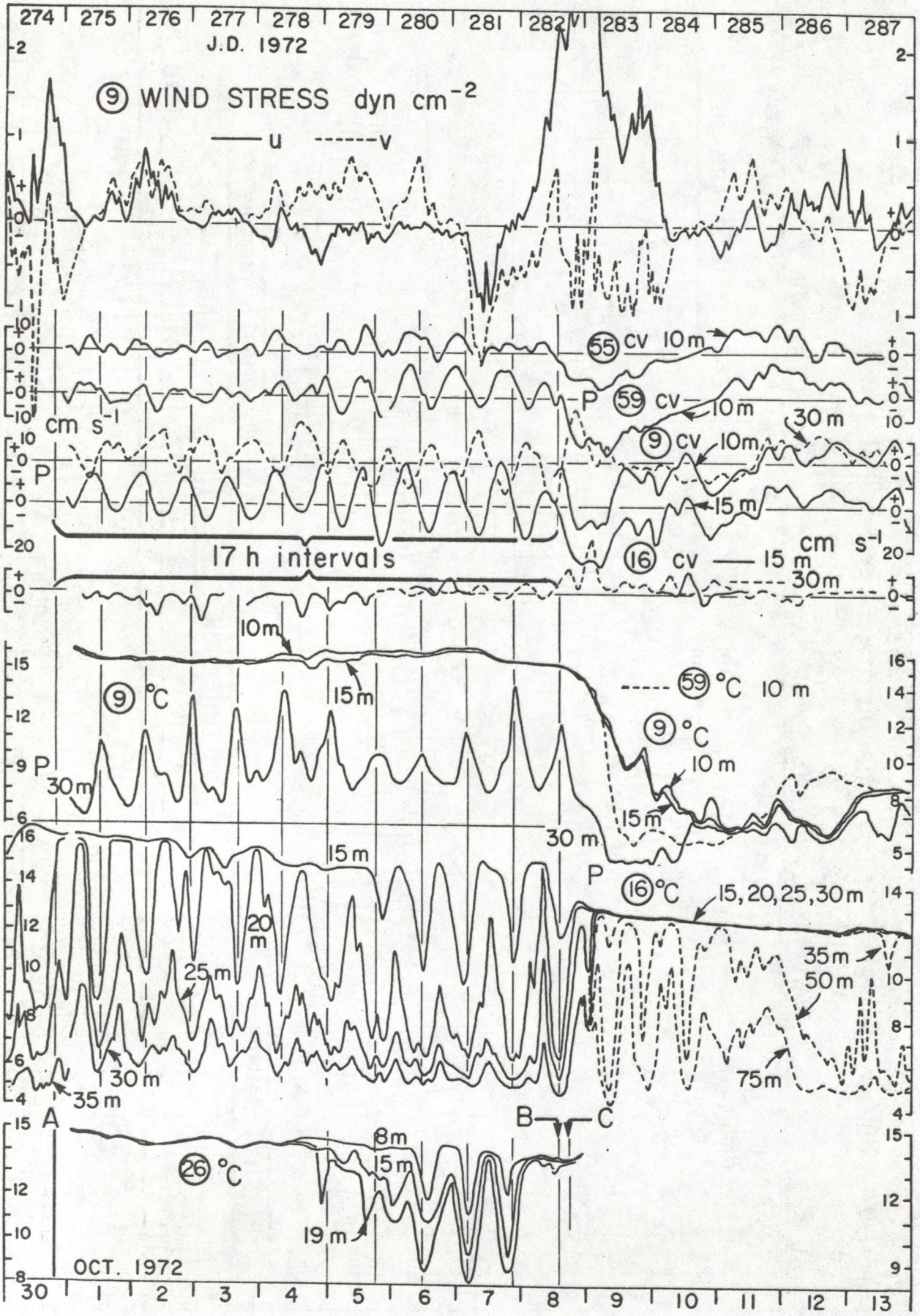

Sheet 6/276-290 A

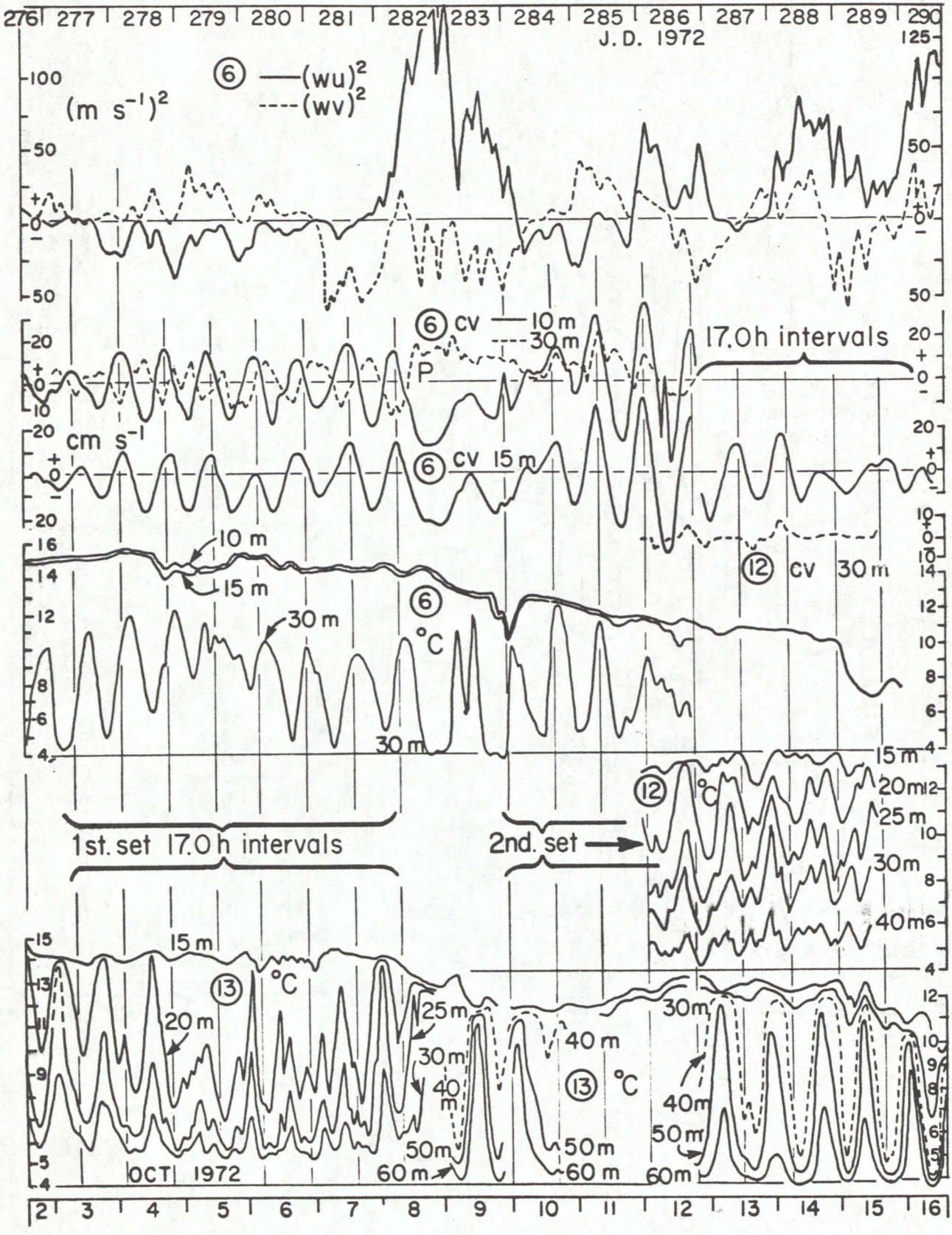

2/273-276 A 6/273-276 A Sheet 11/281-287 A